UNIVERSITY OF NAIROBI

SYNTHESIS AND APPLICATIONS OF *TRIS*-HOMOLEPTIC CYCLOMETALATED IRIDIUM (III) COMPLEXES

BY

RACHAEL E. NJERI NJOGU

I80/52381/2017

A Thesis Submitted in Fulfillment of the Requirements for Award of the Degree of Doctor of Philosophy in Chemistry of the University of Nairobi

DECLARATION

I declare that this thesis is my original work and has not been submitted elsewhere for research. Where other people's work or my own work has been used, this has properly been acknowledged and referenced in accordance with the University of Nairobi's requirements.

Signature ..... Date.....

Rachael E. Njeri Njogu

This thesis has been submitted with our approval as research supervisors:

	Signature	Date
Lydia W. Njenga Department of Chemistry, University of Nairobi	…….	……
David K. Kariuki Department of Chemistry, University of Nairobi	…….	……
Ola F. Wendt Centre for Analysis and Synthesis Department of Chemistry Lund University	…….	……
Amir O. Yusuf Department of Chemistry, University of Nairobi	…….	……

DEDICATION

This thesis is dedicated to my parents Reverend Alex Njogu and Mrs. Sophia Wanjiru Njogu and my siblings; Ms. Ruth E. Wanjiku Njogu, Dr. Leah J. Muringo Njogu and Mr. Antony R. Muriuki Njogu.

ACKNOWLEDGEMENT

Firstly, I extend my sincere gratitude to my Supervisors; Professor Lydia W. Njenga, Professor David K. Kariuki, Professor Amir O. Yusuf and Professor Ola F. Wendt who went over and above their mandate and provided invaluable support, guidance and timely assistance throughout the entire duration of my PhD.

I'd also thank the entire Department of Chemistry, University of Nairobi for first not only for employing and giving me study leave to pursue research in Lund University but also for the moral support of my fellow colleagues. To Dr. Farida Were, Dr. Joyce Githure and Dr. Solomon Derese, a big thank you for teaching my courses when I was abroad for the research.

International Science Programme (ISP), are acknowledged for their financial support through KEN 01 project without which this work would not have been possible. I acknowledge Lund University in particular Center for Synthesis and analyses (CAS) Sweden, where majority of experimental work was carried out. I acknowledge the KEN01 group members for their invaluable support. Professor Carl-Johan Wallentin and Dr. Peter Fodran from Gothenberg University, Professor Ivan Scheblykin and Dr. Yuxi Tian from Lund University, Department of Physics, are acknowledged for collaborating with us for part of redox photocatalysis application and transient spectroscopy measurements respectively.

Most of all I thank my family for the all their love, unwavering support and constant encouragement to achieve my goals. Finally, I thank the Almighty God for life, strength and tenacity and enabling me to bear this work to conclusion.

ABSTRACT

Tris-cyclometalated homoleptic iridium(III) complexes have been shown to harbor immense potential as functional materials constituents and actively play a critical role in the field of photocatalysis and photosensitization. Herein, this study reports the synthesis, characterization, photophysical and electrochemical properties of iridium(III) complexes of 2-(1-naphthyl)-pyridine (npy) and 1-phenyl isoquinoline (piq) ligands synthesized via Suzuki coupling protocol with subsequent cyclometalation to generate; $Ir(npy)_3$, C-L_1; $Ir(npy\text{-}OMe)_3$, C-L_2; $Ir(npy\text{-}CF_3)_3$, C-L_3; $Ir(npy\text{-}Me_2)_3$, C-L_4; $Ir(npy\text{-}Me)_3$, C-L_5; $Ir(npy\text{-}Me)_3$, C-L_6; $Ir(piq\text{-}F)_3$, C-L_7; $Ir(piq\text{-}CF_3)_3$, C-L_8; $Ir(piq\text{-}t\text{-}Bu)_3$, C-$L_9$ and $Ir(piq\text{-}Me)_3$, C-L_{10}. They were characterized using ^{1}H, ^{13}C, ^{19}F, 2D COSY and HSQC, single crystal XRD, HRMS and elemental (CHN) analyses. Their photophysical and electrochemical properties were also probed through UV-VIS, PL, τ, Φ and CV. In the results, a systematic investigation of ligand substitution patterns showed an influence on the lifetime of the excited state, with slight changes in the absorption and emission spectral features. Specifically, the emission lifetime of a complex of a npy ligand substituted with a strongly electron-withdrawing trifluoromethyl group was longer than that of the corresponding complex with the electronically non-perturbed ligand (3.7 μs versus 1.5 μs). Electronically complementary ligands and complexes with orthogonal configurations showed slightly shorter excited state lifetimes compared with unsubstituted npy (1.4–3.0 μs). All complexes displayed reversible or quasi-reversible redox-couple processes, with the complex of the trifluoromethylated ligand showing the highest ground-state oxidation potential $Eox_{1/2}$ [Ir^{III}/Ir^{IV} = 0.95 V vs. SCE in CH_2Cl_2]. This study showed that these complexes can be used as efficient photoredox catalysts, as demonstrated by the six of the complexes (C-L_1-C-L_6) in their application in a regioselective methoxytrifluoromethylation in which the npy complexes showed equal or better performance compared with the archetypical photoredox catalyst *tris* 2-phenyl pyridine iridium(III). Their second photoredox application was in photobleaching of morin, as model reaction. C-L_1 to C-L_6 were found to catalyse the degradation of morin in 12 minutes under ambient temperatures in O2 environment at pH 10 with degradation rate constants, K_{obs} 0.023 s^{-1} to 0.036 s^{-1}. C-L_4, exhibited the highest K_{obs} = 0.036 s^{-1}. The photoredox catalytic degradation reaction of Morin dye was found to follow first order kinetics. The third photoredox application was on photooxidation of alcohols; benzyl alcohol and 4-methoxy benzene alcohol to corresponding aldehydes. C-L_1 had higher yields of 30% and 58% for both reactions under study as compared to the rest of the complexes. In all cases selectivity was >

99% for the product. Complexes C-L_1 to C-L_6 selectively hydrogenated furfural to furfuryl alcohol with C-L_1 giving the highest 21% yield. In conclusion, the chemistry of *tris* homoleptic cyclometalated Ir(III) complexes bearing variants of 2-(naphathalen-1-yl) pyridine and 1-phenyl isoquinoline ligands and their various applications has been reported. The complexes, C-L_1-C-L_6, were successful in photoredox catalysis and selective hydrogenation of furfural.

TABLE OF CONTENTS

LIST OF SCHEMES

LIST OF FIGURES

LIST OF TABLES

LIST OF ABBREVIATIONS AND SYMBOLS

δ	Chemical Shift
Φ	Quantum Yield
τ	Emission Lifetime
Ac	Acetyl
AO	Atomic Orbitals
acac	Acetylacetonate
APCI	Atmospheric Pressure chemical Ionization
BzH	Benzyl Aldehyde
BzOH	Benzyl Alcohol
CE	Counter Electrode
CFT	Crystal Field Theory
CFSE	Crystal Field Stabilization Energy
CI	Chemical Ionization
C^N	Carbon-nitrogen cyclometalating ligands
COSY	Correlation Spectroscopy
CT	Charge Transfer
CTTS	Charge Transfer to Solvent
CV	Cyclic Voltammetry
DFT	Density Functional Theory
E_f	Formal Charge
E_{ox}	Oxidation Potential
E_{red}	Reduction Potential
EDGs	Electron Donating Groups
EI	Electron Impact
ESI	Electron spray ionization
EWGs	Electron Withdrawing Groups
FAB	Fast Atom Bombardment
GC	Gas Chromatography
GPC	Gel Permeation Chromatography
HOMO	Highest Occupied Molecular Orbital

HPLC	High Pressure Liquid Chromatography
HRMS	High resolution Mass Spectroscopy
HSQC	Heteronuclear Single Quantum Coherence
IL	Intraligamd
IR	Infrared
ISC	Intersystem Crossing
LC	Ligand Centered
LC	Liquid Chromatography
LFT	Ligand Field Theory
LLCT	Ligand to Ligand Charge Transfer
LMCT	Ligand to Metal Charge Transfer
LUMO	Lowest Unoccupied Molecular orbital
MALDI	Matrix Assisted Laser Desorption Ionization
MC	Metal Centered
MLCT	Metal to Ligand Charge Transfer
MO	Molecular Orbital
MOT	Molecular Orbital Theory
NMR	Nuclear Magnetic Resonance
npy	2-(napthalen-1-yl) pyridine
NHC	N-heterocyclic carbene
Ph	Phenyl
PL	Photoluminescence
ppy	2-phenyl pyridine
RE	Reference Electrode
RE	Reductive Elimination
SEC	Size exclusion Chromatography
SET	Single Electron transfer
SFC	Super Critical Fluid Chromatography
SIMS	Secondary Ion Mass Spectrometry
SOC	Spin Orbit Coupling
TLC	Thin Layer Chromatography

THFA	Tetra Hydro Furfuryl Alcohol
TMCs	Transition metal complexes
UV-Vis	Ultra Violet – Visible
WE	Working Electrode
XRD	X-ray Diffraction

CHAPTER ONE

INTRODUCTION

1.1 Background

Organometallic chemistry is a branch of coordination chemistry that deals with the chemistry of compounds containing metal-carbon bonds (M-C). Transition metals usually have empty or partially filled d orbitals, imparting their characteristic properties. The metal or metal ions can therefore be bound to ligands by accepting electron pairs from the ligands, to form coordination complexes of the type ML_n, where the metal ion act as lewis acids whereas the ligands are lewis bases forming a coordinate bond (Crabtree, 2009).

In organometallic chemistry, one of the distinctive aspects is the ability of the metal ions to coordinate with ligands containing π electron systems. These ligands can be hydrocarbons both linear and cyclic and those containing heteroatoms such as sulfur, phosphorous and nitrogen. They are normally classified through denticity (number of points at which they are bound to the metal center), which leads to classes such as mono- and poly- ligands such as bi-, tridentate. Ligands with two or more attachment to the metal are referred to as chelating ligands and the complexes formed thereof are chelates. These chelating ligands can form five or six membered chelates i.e., organometallic intramolecular-coordination complexes. Chelate effect leads to increased stability in the chelated complexes as opposed to the non-chelated congeners. Typical chelating/cyclometalating ligands include; 2,2- bipyridine, 1,10-phenanthroline, 2-phenylpyridine, 1-phenylisoquinoline and 2-(naphthalen-1-yl) pyridine, which can be synthesized through cross-coupling reactions that leads to formation of new C-C bonds (Tian *et al.*, 2011).

Organometallic intramolecular-coordination (metallacyclic) five (Omae, 2014) or six membered (Kondrashov *et al*., 2015) ring complexes with either N or O exhibit high stability of the ring (chelate effect). These can be synthesized using cyclometalation reactions, hence have been used widely and are considered a basis for organometallic synthetic methods. These reactions are highly regioselective and have high reactivities. The ease of the formation of the five membered ring arises from; i) metal activation by the coordination of lone pair of electrons of the hetero atom (N, P, O, S) to the metal; ii) the chelate effect due to the formation of the ring and; iii) the metal

activation of the ligands bonding with the metal atom e.g. hetero groups (bipyridines, phosphines, carboxylates), unsaturated groups, carbonyl groups, N-heterocyclic carbenes (NHCs) and halogens (Omae, 2014).

Selective activation of C-H bonds involves cleavage of these bonds, which are considered to be relatively strong and inert. In alkanes for instance, the molecules have no empty orbitals of low energy as in the case of unsaturated hydrocarbons. Therefore, activation of the unreactive C-H bonds remains a key challenge in the synthetic chemistry, and has become a fast-growing field with promising approaches. To this end, cross-coupling and cyclometalation reactions offer an easy way of C-H activation and are extensively studied in organometallic chemistry (Polukeev *et al.,* 2015; Li 2014a; Labinger & Bercaw, 2002). The d_z^2 and $d_{x^2-y^2}$ orbitals form the sigma bond while if an element carrying the lone pair has empty low energy orbitals with appropriate symmetry overlaps with d_{xy}, d_{xz} or d_{yz}, of the metals and accept the electron density, this leads to back-bonding/ synergic bond that gives double bond character to the M-L interaction. For instance pyridines have empty π* orbitals hence display the backbonding (Mathey, 2013).

Coordinated complexes thus prepared offer extensive applications and have shown significant advances and improvements for their use in organic light emitting diodes (OLEDs), dye-sensitized solar cells, sensors, biological labels, catalysts, and therapeutics. Further, they are utilized as photocatalysts in chemical transformations that take place via catalytic addition or removal of electrons as well as serving as photosensitizers owing to their long-lived light induced excited states with favorable reducing and/or oxidizing properties compared to the ground states (Singh *et al*., 2015). Cyclometalated $4d^6$ and $5d^6$ transition metal complexes with aromatic ligands are considered to be suitable systems for photoredox processes such as catalysis, due to the σ-donor and π -acceptor properties of the ligands that give rise to low-lying metal to ligand charge-transfer (MLCT) states. The MLCT character of the lowest excited state is supposed to be highest with the maximum number of metal-C σ –bonds. Subsequently, preparing complexes with a maximum number of coordinating C atoms is commonly preferred (Colombo *et al.,* 1994).

d^6 transition metal complexes (TMCs) such as those of Re (I), Pt (IV), Os (II), Ru (II) and Ir (III) are of interest and have been increasingly developed since they have the ability to emit both singlet and triplet excitons as well as having high internal efficiencies. In particular, studies indicate that Ir(III) complexes have attracted most attention due to efficient emission, excellent thermal stability and broadly tunable emission colors at both the molecular and device levels due to the strong spin

orbit coupling associated with the Ir(III) metal ion. In *tris* homoleptic Ir(III) complexes, i.e., complexes where the metal center is coordinated to three identical cyclometalating ligands, represented as $(C\hat{}N)_3Ir$, all the cyclometalating ligands (C^N) influence the electro and optical properties such as emission color, oxidation potential, lifetime, and quantum yield. On the other hand, in *bis* heteroleptic Ir(III) complexes, i.e., where the metal center is coordinated to two identical cyclometalating ligands and the third being ancillary ligand, represented as $(C\hat{}N)_2Ir(LX)$, the ancillary ligands (LX) such as acetylacetonate (acac) typically have no influence on the electro-optical properties of the complexes but rather influence properties like solubility, thermal stability, and essential electron/hole transmittability. This allows for specific functionalization of the complex with insertion of moieties that may improve charge recombination and/or interconnection of units to increase solubility. It is noteworthy that homoleptic Ir(III) complexes have higher chemical stability and stronger lifetimes than their heteroleptic *bis* cyclometalated counterparts. It has been reported that introduction of electron withdrawing groups such as F, $-CF_3$ lead to stabilization of highest occupied molecular orbital (HOMO) since it depletes electron density at the metal center, to yield a wide HOMO-LUMO (lowest unoccupied molecular orbital) gap hence high energy triplet levels are observed giving rise to blue/hypsochromic shifts, with electron donating groups displaying a reverse effect and giving red/bathochromic shifts (You and Park, 2005; Chen *et al.,* 2007; Tian *et al.,* 2009; Tian *et al*., 2011; Zhuang *et al.,* 2014; Okamura *et al.,* 2016).

Characterization of these *tris* cyclometalated complexes includes physical methods such as IR, MS, ^{1}H, ^{13}C NMR spectroscopy, UV-VIS, photoluminescence and cyclic voltammetry. The study of these photophysical and electrochemical properties, gives a basis for establishing the relationships between structure and properties of the complexes (Zhuang *et al.,* 2014; Huang *et al.,* 2015).

Amongst the popular applications of *tris* homoleptic cyclometalated Ir(III) complexes is photoredox/visible light photocatalysis due to the efficient utilization of solar energy/light, which is an abundant, endless, renewable, inexpensive and nonpolluting reagent, hence, promotes green and sustainable chemistry. Polypyridyl complexes of ruthenium and iridium constitute the most commonly investigated visible light photocatalysts. Utilizing the said photocatalysts, in electron/energy transfer processes to sensitize organic molecules leading to significant photochemical reactions is of utmost importance. Irradiation of the complexes with visible light

leads to population of the excited states via MLCT and these states can easily serve as potential oxidants or reductants i.e. they serve as oxidative and reductive quenchers through single-electron-transfer (SET) events (Narayanam and Stephenson 2011; Shi and Xia 2012; Liu *et al.*, 2016).

Transition metal complexes have found use in hydrogenation reactions involving moieties such as aldehydes (Xuefeng *et al.*, 2016). Furfural is an aldehyde that can be derived from waste biomass for example, maize cobs, sugarcane molasses and rice husks. These are rich in pentoses and through acid catalyzed hydrolysis can yield furfural, which in turn can be selectively reduced to yield Tetrahydrofurfuryl alcohol (THFA), a solvent with extensive industrial applications. THFA is water miscible, biodegradable, has low toxicity and volatility (Ho *et al.*, 2009).

The aim of this study was to utilize 2-(1-Naphthyl) Pyridine (npy) and 1-phenyl isoquinoline (piq) ligands, and their various modified forms in exploring the synthesis and characterization of the corresponding *tris* homoleptic cyclometalated Iridium(III). The C-H activation of these ligands has been previously studied and reported active (Kondrashov *et al*., 2015). Subsequently, potential applications of the resulting complexes as photoredox catalysts was explored. Further selective hydrogenation of furfural to THFA as a potential application was also explored.

1.2 Statement of the Problem

Activation of unreactive C-H bond remains a challenge in the field of synthetic organic chemistry. Cross coupling and cyclometalation offers a pretty successful route of circumventing this conundrum via directed activation and have been found to strongly affect the redox, electronic and photophysical properties of the resulting complexes. There's a growing need to continually search for new types of C^N ligands which tune the energy levels of excited states making them versatile with regard to potential applications in diverse fields. Despite rich exploration in the properties of these complexes, many facial homo/heteroleptic variants often lack complete chemical, photophysical, crystallographic and electrochemical characterization. The most archetypical ligand used to form coordinated complexes with iridium is 2-phenyl pyridine and its derivatives. Considering ruthenium, which has also been widely studied, mostly the ligand 2,2- bipyridine (bpy) is utilized. However, reports on synthesis and applications of the slightly more conjugated ligand, 2-(1-naphthyl) pyridine are scanty hence the need to explore this ligand and its tunability

in terms of photophysical and electrochemical properties. 1-phenyl isoquinoline ligand was used for comparison due to similarity in structure with 2-(1-naphthyl) pyridine.

Photoredox catalysis is still under infancy yet it's an emergent robust and transformative driving force that uses mild conditions and utilizes visible light, an abundant, nonpolluting and endless renewable resource for chemical transformations such as difunctionalization of alkenes, hitherto inaccessible under normal thermal conditions. Despite selective difunctionalization of alkenes being a potent chemical transformation, only a limited number of reports involving trifluoromethylation have been shown. Moreover, while trifluoromethylation of aromatic compounds has been extensively studied and effective methodologies established, trifluoromethylation in simple alkenes is still lacking. Hence there is need to establish new methodologies for highly efficient and selective insertion of CF_3 group into diverse skeletal structures of organic molecules. Photoredox catalysis can also be extended to photodegradation of industrial dyes, which has been studied under heterogeneous catalysis utilizing nanoparticles but not with Ir(III) complexes. The catalytic effect of Ir(III) complexes on photooxidation of alcohols has not been exhaustively researched on.

Selective hydrogenation of the carbonyl group in furfural to produce unsaturated compounds is a challenge since the olefinic group also gets easily hydrogenated to give undesirable saturated products. Shortcomings of metal catalysts and supports that have been previously utilized in this reaction include activity, selectivity, toxicity and recyclability issues. The Ir (III) complexes haven't been evaluated for their activity and selectivity in such a reaction. In Kenya, availability of raw materials for fine chemicals is a challenge. THFA, used for this purpose and as a high purity solvent is also unavailable locally and expensive, yet it can be manufactured locally from agricultural wastes through selective hydrogenation of furfural.

1.3 Objectives

1.3.1 Main objective

To synthesize and characterize 2-(1-naphthyl) pyridine *tris*-homoleptic cyclometalated iridium(III) complexes for photoredox catalysis and selective hydrogenation of furfural

1.3.2 Specific objectives

1. To synthesize and characterize 2-(1-naphthyl) pyridine modified ligands
2. To synthesize and characterize *tris* cyclometalated homoleptic Ir(III) complexes
3. To evaluate the photoredox catalytic ability of Ir(III) complexes
4. To utilize the Ir(III) complexes in selective hydrogenation of furfural

1.4 Justification

While enormous advances in cyclometalated Ir(III) complexes have been made and many complexes developed, it has been demonstrated that structural changes in the skeletal as well as substituent groups of the cyclometalating ligand (C^N) afford significant tuning of photophysical, electrochemical and electrophosphorescence properties due to increased ligand-field stabilization energy.

Luminescent metal complexes are attractive for diverse applications. The usefulness and applicability of new luminescent materials can be assessed according to their stability, external quantum yield, excited-state lifetime, and emission energy. Therefore, it is highly desirable to design and synthesize novel ligands and tailor transition-metal complexes that will emit across the visible spectrum and to produce molecules in which light emission predominates over nonradioactive decay. These properties can be evaluated using both photo and electroluminescent methods. Among these applications is photoredox catalysis and selective reduction/ hydrogenation of aldehydes.

Photoredox catalysis has become popular since it involves efficient utilization of solar energy/light, which is an abundant, inexpensive, nonpolluting and an endless renewable reagent, hence promotes green chemistry leading to significant photochemical reactions under mild

conditions. Through photocatalysis there is efficient conversion of light to chemical energy with simultaneous selective molecule activation, which open pathways to access otherwise inaccessible transformations and functionalizations under normal thermal conditions. The significance of ability to fine-tune the photocatalyst for specific application through adjusting the ligands emphasizes the importance of photoredox processes. As such, transformations such as oxytrifluoromethylation, photodegradation of dyes is therefore possible under safe, mild conditions.

Trifluoromethyl (CF_3) group can influence chemical and metabolic stability, lipophilicity and binding selectivity in biologically active molecules with trifluoromethylated and organoflourine compounds finding extensive use in agrochemical, material sciences and pharmaceutical fields.

Photodegradation of Morin is an example of photo redox catalysis application. This catalytic degradation of Morin and related dyes has been studied under heterogeneous conditions using manganese oxide nanoparticle (NP) catalysts with H_2O_2 as the oxidant or Au NPs as a model reaction but has not been studied using Ir(III) complexes as photoredox catalysts.

2-Furanaldehyde (Furfural) can be derived from waste biomass for example maize cobs, sugarcane molasses and rice husks, which are locally available but without any economic applications yet. These are rich in pentoses which through acid catalyzed hydrolysis can yield furfural which in turn can be selectively reduced by the aforementioned synthesized complexes to yield THFA, a solvent with extensive industrial applications and by so doing add value to the agricultural wastes which would improve the economy of the farmers and in principle environmental sustainability. Reduction of aldehydes, abundant natural products, to their corresponding alcohols is critical in synthetic chemistry especially by using catalytic hydrogenation with transition metal complexes as opposed to traditional stoichiometric methods using reducing agents such as $NaBH_4$.

Overall, synthesis of novel tris cyclometalated phosphorescent Ir(III) complexes will contribute to achievement of Kenya's big four agenda mainly manufacturing & universal healthcare and vision 2030 since the complexes synthesized can be utilized in making products that would be useful in aforementioned industries.

CHAPTER TWO

LITERATURE REVIEW

2.1 Coordination Compounds

Coordination compounds comprises of a metal atom or ion, as the central coordinating substituent, with electron-donating ligands to form complexes. Complexes containing metal-carbon coordinating bonds are referred to as organometallic compounds (Miessler *et al.,* 2014). Organometallic chemistry therefore is the study of coordination compounds that bridges organic, inorganic and bioinorganic chemistry disciplines and contributes to the understanding of material science (Riess, 1985). Ligands are lewis bases as they donate lone pairs of electrons to metals via coordinate bonds with chelating ligands coordinating to the metal center with two or more bonds to form chelate complexes. Chelates are more thermodynamically stable than their corresponding monodentate complexes of similar metal center due to chelate effect that may arise from ligands' interaction with metal centers, either by sigma (σ) or *pi* (π) electrons coordination (Housecroft and Sharpe 2005; Miessler *et al.,* 2014). Bidentate ligands are grouped by the number of atoms separating the donor atoms and subsequently, the size of the chelate ring formed. Hence, from 1,1-ligands chelate ring a four-membered is formed whereas 1,2-ligands, a five membered chelate ring. Complexes in which the metal is bound to only one kind of ligand are homoleptic whilst those in which the metal is bound to more than one kind of ligand are heteroleptic (Jones, 2002).

Coordination environments are often described in terms of regular geometries for coordination number (CN) between two and six, with CN 6 being typical for *d*-block metal ions with O_h geometry (Jones, 2002). The variety of coordination numbers provides a large number of isomers, which can be classified into two groups: stereo or configurational isomers and structural or constitutional isomers. Octahedral complexes also display geometric isomerism subject on the orientation of the three ligands. If all lie in the same plane, they give a meridional, or *mer*, isomer, while if they are adjacent, they form a triangular face of the octahedron in a facial, or *fac*, isomer. X-ray crystallography allows for elucidation of isomeric structures (Jones, 2002).

The *d*-block metal ions form complexes, which are accompanied by color change due to their ability to absorb light in the visible region. Absorptions arise from transitions between electronic

energy levels: i) transitions between metal centered orbitals that possess *d*-orbital character, the *d-d* transitions; and ii) transitions between metal and ligand centered molecular orbitals which transfer charge from metal to ligand or vice versa, known as charge transfer. Charge transfer leads to intense absorptions whereas *d-d* transition bands are relatively weak. Low intensity colors are consistent with them originating from *d-d* transitions. Therefore, the pale colors indicate that the probability of the transitions occurring is low since the transition is forbidden by laporte selection rule. (Housecroft and Sharpe 2005; Miessler *et al.,* 2014).

The electronic structures of organometallic compounds are based on the 18-electron rule. Electron count done through donor pair or neutral-ligand method, allows determination of the number of shared electrons between the metal and the ligands that coordinate through their lone pairs thereby forming π-bonds. Magnetic data allows for the determination of the number of unpaired valence electrons in octahedral d^6 complexes and subsequent classification of complexes into two categories namely paramagnetic and diamagnetic complexes, which constitute high spin and low spin complexes, respectively (Mathey, 2013; Miessler *et al.,* 2014).

Back bonding (back donation) is the metal to ligand (M-L) π bonding that involves *d* orbital electrons occupying π orbitals of the ligands thus the metal transfers some electron density "back" to the ligands, which is in contrast with sigma interactions where the metal accepts and the ligand donates the electrons. Ligands having appropriate symmetry and empty π antibonding orbitals that can accommodate the donations from the metal through the π interactions are called π acceptors for example, CO, N_2, NO, phosphines and alkenes. Conversely, ligand to metal π bonding entails the π electrons from the ligands being donated to the metal ion and hence the ligands are π donors for example, halides (Cl^-, F^-, I^-). This interaction results when either filled ligand p orbitals or π* orbitals interact with metal valence orbitals with compatible energies. Therefore, ligand classification is based on their donor (σ or π donation) or π acceptor abilities and more so in their abilities to cause the d orbitals splitting, summarized in the spectrochemical series. The spectrochemical series runs in order from strong π-acceptor ligands to π-donor ligands with ligands high in the series causing larger d-orbital splitting hence high values of Δ and favors low spin configurations whilst ligands low in the series have lower values of Δ and generate high spin configurations (Mathey, 2013; Miessler *et al.,* 2014; House, 2018).

The bonding of coordination compounds can be explained using various theories. Among these is the molecular orbital theory, which considers covalent interactions between the metal center and the ligand. Only the d_z^2 and $d_{x^2-y^2}$ participate in bonding hence, are raised in energy (destabilized) to a greater extent and constitute a set of two degenerate orbitals with e_g symmetry. The d_{xy}, d_{xz}, and d_{yz} form the nonbonding atomic orbitals, are stabilized and constitute a set of three degenerate orbitals possessing t_{2g} symmetry with respect to the barycenter. The energy difference between the two symmetry sets is Δ or 10D*q*. Figure 1A shows molecular orbital diagram of an O_h complex and the possible electronic transitions are shown in Figure 1B. Evidence for metal-ligand covalent bond in coordinated complexes is provided by the nephelauxetic (electron cloud expanding) effect, with soft ligands displaying larger effect than harder ligands.

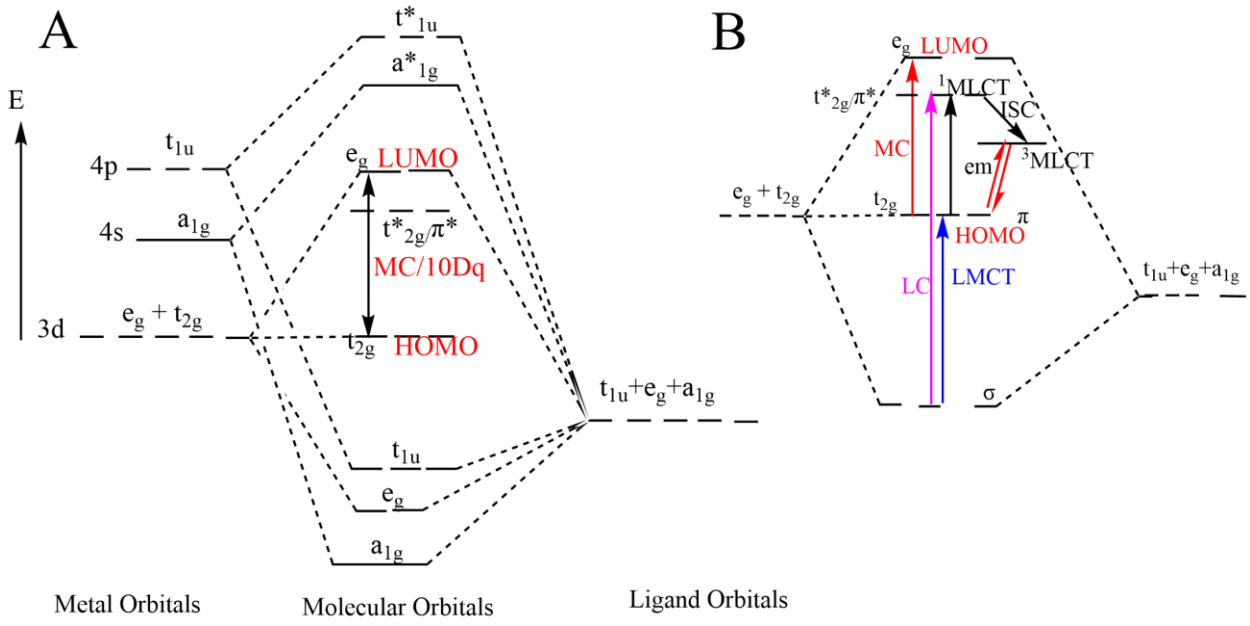

Figure 1: A) Molecular orbital diagram B) MO showing transitions in an O_h complex

Source: (Ball & Key, 2014; House, 2018)

Reported 10Dq values of some Ir(III) complexes include 27000cm^{-1}, 25000cm^{-1}, for $Ir(dtp)_3$, $Ir(dsep)_3$ respectively, which places the diethyldithiophosphate (dtp) and diethyldiselenophosphate (dsep) ligands early in spectrochemical series, between Cl^- and F^- and late in the nephelauxetic series. Complexes with nitrogen ligands report higher 10Dq values and include $[Ir(NH_3)_6]^{3+}$ with 41200cm^{-1}, $[Ir(en)]I_3$ with 41400cm^{-1} and $[Ir(NH_3)_5Cl]Cl_2$ with 40,400cm^{-1} (Livingtstone, 2017). Other studies has shown spectra of Ir(III) with strong field ligands to exhibit spin forbidden

transitions: $^1A_{1g} \rightarrow {}^3T_{1g}$ (16640cm^{-1}); $^1A_{1g} \rightarrow {}^3T_{2g}$ (19140cm^{-1}); $^1A_{1g} \rightarrow {}^3T_{1g}$ (23396cm^{-1}) and $^1A_{1g} \rightarrow {}^3T_{2g}$ (30230cm^{-1}) (Pandey *et al.*, 2010).

2.2 Cross Coupling Reactions

The chemistry of transition-metal-cross-coupling reactions provides an approach that is regio- and stereoselective, to synthesize highly functionalized compounds. This is achieved through the formation of new C-C bonds by direct chemospecific linkage of reaction partners (i.e. via formal replacement of an electronegative group X in R–X with a nucleophilic moiety R^1 carrying an electropositive group m in R–m) under mild conditions and non toxic byproducts (Fihri *et al.*, 2011; Brown, 2015; Stein *et al.*, 2015). Palladium and copper salts are the most favored transition metals with halides being used as electrophilic sources, although other sources such as phosphonates, sulfonates, tosylate and triflates can be used (Stein et al., 2015). These reactions reach across chemistry from materials to molecular biology, are popular in industry and widely utilized there at all scales levels, and rarely require forcing conditions. Since the award of the 2010 Chemistry Nobel Prize to Richard F. Heck, Ei-ichi Negishi, and Akira Suzuki on their pioneering contributions in the field of cross coupling entitled "Palladium catalyzed cross couplings for organic synthesis", the level of activity in both innovation and application has remained high (Brown, 2015).

Conventional methods of cross coupling include; i) Heck cross-coupling which entails Pd-catalyzed alkenylation or arylation of olefins (Li, 2014b); ii) Hiyama cross-coupling involves reaction of organosilicons with organic halides, triflates. In this case, transmetallation requires the presence of activating agents such as fluoride to proceed (Li, 2014c); iii) Kumada (Kumada-Tamao-Curio/ Kharasch) cross-coupling, involving cross coupling of Grignard reagents/ organolithium/ organomagnesium compounds with aryl or alkenyl halides with nickel or palladium catalyst (Li, 2014d); iv) Negishi cross-coupling which features coupling of organozinc compounds with various halides or triflates (aryl, alkenyl, alkynyl, and acyl) catalyzed by either nickel- or palladium-(Li, 2014e); v) Sonogashira cross-coupling are Pd-catalyzed coupling between *sp*, and sp^2 or sp^3 C-atoms under mild conditions (Sisodiya *et al.*, 2015); vi) Stille cross-coupling is palladium catalyzed coupling between organotin compounds and acyl halides (Tian, 2011); vii) Yamamoto cross-coupling involve coupling between dibromo or diiodo monomers using nickel catalysts is widely utilized to synthesize pi-conjugated polymers (Tian, 2011).

Suzuki cross-coupling reaction (also called Suzuki-Miyaura reaction) (Scheme 1), discovered by Nobel laureate Akira Suzuki, is among the most widely used protocols for the formation of carbon–carbon bonds and have become influential for the synthesis of biaryl compounds. The reaction is accredited with high activity and selectivity and is workable with a wide range of substrates with many functional groups being highly tolerated due to the mild reaction conditions. In addition, the boronic acid starting materials are readily available, stable, sustainable and not toxic (Fihri *et al.*, 2011). Tetrahydrofuran (THF) or toluene is commonly utilized as the organic solvents with the addition of a small amount of an alcoholic solvent facilitating the mixing of the organic and inorganic components. The most commonly used base in the reaction is Na_2CO_3, but it is often ineffective when dealing with sterically demanding substrates hence a base such as CsF is used (Tian, 2011).

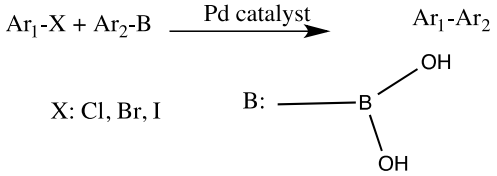

Scheme 1: The Suzuki-Miyaura reaction

Aryl bromides and aryl iodides are commonly used as starting materials. One of the limitations of Suzuki coupling is the poor reactivity of aryl chlorides despite being the most attractive family of aryl halide substrates due to their low cost and their ready availability (Littke *et al.,* 2000). However, the use of bulky halides has led to improvement of this challenge. The different coupling rates of aryl halides are related to the size of X and strength of the Ar-X bond, which increases: I < Br < Cl< F and makes the oxidative addition step increasingly difficult. This means that the relative reactivity for this reaction follows the order: Ar-I>Ar-Br>Ar-Cl under same reaction conditions (Tian, 2011). Since the electronegativity decreases down the halogen group while the size increases, alkyl fluorides and fluorocarbons in general are chemically and thermodynamically quite stable, and do not share any of the reactivity patterns shown by the other alkyl halides. Studies have reported that the poor reactivity can be overcome by utilizing stronger base such as CsF. More vigorous conditions are typically required to effect Suzuki cross-couplings of electron-rich aryl chlorides (Littke *et al.,* 2000). A wide range of palladium (0) catalysts or precursors can be used for cross-coupling reaction. $Pd(PPh_3)_4$ is most commonly used, but $PdCl_2(PPh_3)_2$and

$Pd(OAc)_2$ plus PPh_3 or other phosphine ligands are also efficient since they are stable to air and readily reduced to the active Pd (0) complexes with organometallics or phosphines used for the cross-coupling (Miyaura and Suzuki, 1995). Phosphines (arsines or NHC) are necessary in cross-coupling reactions to prevent catalyst decomposition to metal. A general catalytic cycle for the cross-coupling reaction of organometallic complexes, which involves oxidative addition-transmetalation-reductive elimination sequences, is depicted in Scheme 2.

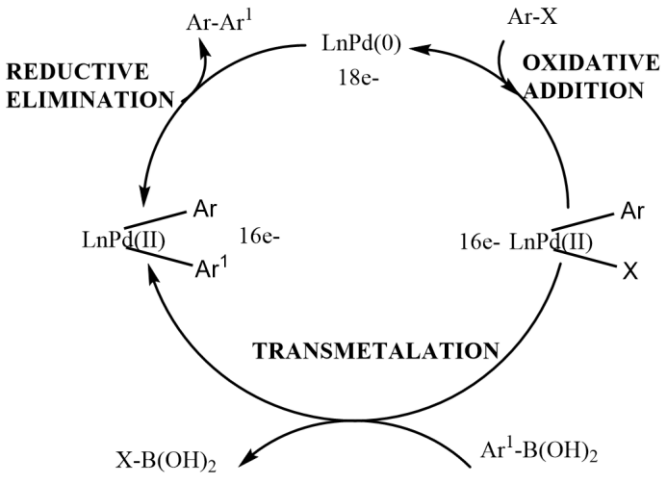

Scheme 2: Catalytic cycle of Suzuki cross coupling reactions

(X is Halide; L is ligand; n is number of ligands attached; Ar is aryl group)

Source: Littke *et al.*, 2000

2.2.1 Oxidative addition (OA)

OA involves the attachment of two groups X-Y to a metal complex of relatively low oxidation state. This produces a new complex with an oxidation state two units higher than before, an increase in coordination number of two, and an electron count two higher than the present starting material as shown in Scheme 3 (Mathey 2013; Spessard and Miessler 2010). It is often the rate-determining step in a catalytic cycle. This reaction can proceed through four mechanisms: i) concerted three-center mechanism, which is followed when homoatomic (H-H, O-O, etc.) or weakly polar (H-Si, H-C, etc.) bonds are involved; ii) similar to S_N2 substitution type mechanism where a highly polar (H-X, R-X) A-B type of a bond is involved and the metal is nucleophilic

hence if B is a good leaving group then this mechanism is favored; iii) ionic mechanism occurs in dissociating solvents with strong acids or nucleophilic anions; iv) concerted, S_N2 mechanism (Mathey, 2013).

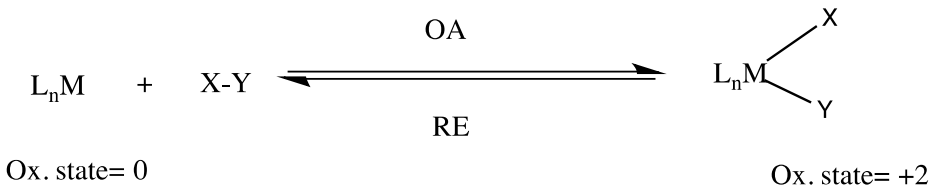

Scheme 3: Oxidative Addition and Reductive Elimination Reaction

2.2.2 Reductive elimination (RE)

RE is the reverse reaction of oxidative addition whereby the oxidation state, coordination number and electron count all decrease, typically by two units. It allows for the recovery of the organic product at the end of the catalytic cycle. The concerted mechanistic pathways of RE are exactly the same as those for OA only that now in reverse *Cf* Scheme 3. RE is favored in complexes with bulky ligands (due to relief of steric hindrance upon ligand loss), a low electron density of the metal (high oxidation state), and the presence of groups that can stabilize the reduced metal fragment upon ligand loss. RE is the last step of the catalytic cycle designed to join two different carbon fragments and regeneration of the metal catalyst. This process can be enhanced through electrochemical oxidation of the metal if it doesn't proceed spontaneously (Miyaura and Suzuki 1995; Spessard and Miessler 2010; Mathey 2013).

2.2.3 Transmetalation

Transmetalation step produces the exchange of organic groups between metals. The ability of organoboron reagents to transmetalate with a variety of metal compounds has been known for many years. In particular, their versatile transmetalation with palladium (II) complexes has allowed the Suzuki–Miyaura reaction to develop into such an important coupling process in academic and industrial settings (Lennox & Lloyd-Jones, 2013). Mechanism of this step is less known as compared to OA and RE since it is highly dependent on organometallics or reaction conditions used for the couplings (Miyaura & Suzuki, 1995). The overarching mechanistic complexity in the transmetalation event arises from the fundamental property of three-coordinate

boron species, which are Lewis acids to varying degrees (Lennox & Lloyd-Jones, 2013). Association of a fourth ligand to generate a four-coordinate "ate" complex is required to facilitate efficient transfer of the organic moiety from an organoboron species to a metal center, for example, Pd.

2.3 Cyclometalation Reactions

The cyclometalation process, introduced by Trofimenko (1968) consists of a transition metal-mediated activation of a C-R (in most cases, C-H) bond to form five or six membered metallacycles (chelate ring) containing a metal-carbon σ bond (Scheme 4) (Bruce, 1977; Hill, 2002; Albrecht, 2010; Ahlstrand *et al.,* 2017). The reaction proceeds via two consecutive steps: initial coordination of the metal center via a donor group, and subsequent intramolecular activation of the C–R bond, which closes the metallocycle (Albrecht, 2010). Cyclometalation can also be regarded as a special case of oxidative addition, in which a C−R bond in a ligand oxidatively adds to a metal to give rise to the metallacycle. Chelation leads to organometallic compounds with increased stability, regioselective and easy to synthesize (Hill, 2002). Recently, it was reported that cyclometalation can proceed without the Csp^3-H activation being chelated assisted (Ahlstrand *et al.,* 2017). The effective bond activation is most often a heteroatom-assisted process, involving classical donors such as N, O, P, S, Se, and As, though cases of carbon-assisted C–R bond activation are known as well. Consequently, the cyclometalated product often includes heteroatoms other than the metal with cases of carbon-carbon, carbon-oxygen, and carbon-silicon bond activation having been reported (Albrecht, 2010).

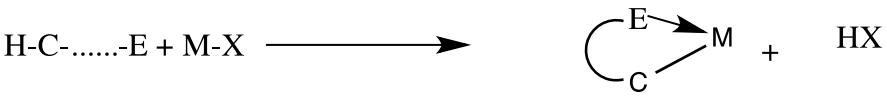

Scheme 4: Cyclometalation (E-donor atom; M-transition metal; X-leaving group)

The cyclometalation reaction has been widely studied since it represents one of the mildest routes for activating strong C-H and C-R bonds. The tendency of transition metal salts to undergo cyclometalation reaction, and, in particular, ortho-metalation (metalation of phenyl-substituted ligands) reaction, with heteroaromatic ligands to give metallacycles has been demonstrated with various metals such as Re(I), Pt(II), Rh(I), Ir(I) and Pd(II) (Bruce, 1977; Hill, 2002).

The reaction mechanisms of these reactions involve the coordination of the metal with a heteroatom followed by the activation of geometrically accessible C–H bonds, which can be adjacent or remote, to generate a template for further functionalization and the subsequent chelate effect from the five or six-membered ring formed (Butschke and Schwarz, 2012; Kondrashov *et al.*, 2014; Omae, 2014). The agostic interactions of these reactions that include but not limited to C-H activation, C-X activation, C-H functionalizations, chelated-assisted reactions and cross-coupling reactions, all follow the same mechanism related to cyclometalated reactions. The products of these reactions include catalysis, CO_2 utilizations, sensors, organic electric devices, pharmaceuticals, and dye-sensitized solar cells (Omae, 2014).

Cyclometalation strongly affects the redox potentials as well as the photophysical properties of the resulting complexes compared to their non-cyclometalated congeners (Wadman *et al.*, 2010). Cyclometalating ligands, coordinating the metal center by an anionic carbon through C-M bonds, are strong σ-donors and induce strong ligand field with high electron density around the metal center. This leads to bigger splitting of the ligand field energy hence more intense luminescence. In principal, cyclometalated complexes tune the frontier orbital energies by changing the electronic properties of the ligand. The pH-responsive transition-metal complexes containing *N*-heterocyclic ligands are one family of fundamental molecular devices with adjustable ground- and excited-state properties (Wadman *et al.*, 2009).

Metal precursor used should provide a coordination site for heteroatom (E = N, O, P, S, As, Se, C) bonding that enable ligand attachment through to M-E interactions. Mechanistically, C-H bond activation in cyclometalation proceeds through three possible pathways; i) electrophilic C-H bond activation observed with electron-poor late transition metals; (ii) oxidative addition which requires electron-rich metal center e.g. Ir(I) and Rh (I) and; (iii) σ-bond metathesis being the most predominant pathway involving electron-poor metal centers such as high valent early transition metals, and in some cases late transition metals through modified versions (Albrecht, 2010).

Early transition metals (group 3-5) are the least prone to undergo C–H bond activation amongst the *d*- block metals with the exception of the high valent tantalum (V). Other early transition metals are rarely considered for cyclometalation because the metal precursors are poor-electron centers containing basic alkyl or amide ligands for scavenging the proton from C–H bond activation leading to σ-bond metathesis due to the strong polarization of the M– N_{amid} and the M–C_{alkyl} bond.

In contrast, in group 6 and 7 metals cyclometalation with tungsten, manganese and rhenium has been reported and involve low-valent configuration at the metal centers to give respective metallacycles, W(0), Mn(I) and Re(I) (Albrecht, 2010).

Cyclometalation using late transition metal centers (groups 8-10) have significant electron density, which assists in stabilizing the σ complex in the cyclometalation mechanism. The process has therefore been termed σ-complex-assisted metathesis (σ -CAM). Cyclometalation could be categorized in to two; first row metals (Fe, Co, Ni) and platinum group metals (Ru, Os, Rh, Ir, Pd and Pt). Iron cyclometalation reports are scarce since its stable oxidation states, (II) and (III), have low tendency to form σ-bond metathesis or 2-electron C-H activation and the Fe-C bond has low stability notwithstanding the utilization of multidentate chelates. Cobaltacycles are synthesized via transmetalation protocols with C-H bond-activation methodologies being less frequent while nickelacycles proceed via both oxidative addition and transmetallation. Ni-mediated cyclometalation is favored in coordination compounds with steric constraints (Albrecht, 2010).

Platinum group metals present the most popular domain of cyclometalation majorly via heteroatom-assisted C-H activation. Cycloruthenation is versatile, broad scoped and has widespread applications due to favorable photophysical and electrochemical properties. Osmium mediated cyclometalation is less popular although it proceeds via oxidative addition pathway and low valent Os(0) complexes are prevalent. In cyclorhodation the low valent Rh(I) complexes have received a lot of attention with the oxidative addition pathway being followed. Iridacylces have roused considerable interest owing to their exceptional activities particularly in catalysis and photophysical applications. For example, pincer ligand complexes are known to be outstanding catalysts for alkane dehydrogenation while *tris* Ir(II) complexes are used in OLEDs and potential dopants. Cycloiradiation affords direct synthetic access to these compounds without laborious prefunctionalization of ligand precursors or manipulation of air or moisture sensitive intermediates (Albrecht, 2010).

Ir(III) complexes are popular due to their environmentally inertness, stability, have appropriate energy levels and favorable phosphorescent lifetimes (Tian *et al.*, 2009). A wide range of facial heteroleptic variants of $Ir(ppy)_3$ have been reported with the synthesis of homoleptic complexes counterparts missing and often lacking complete chemical, photophysical and electrochemical characterization (Singh et al., 2015). Singh *et al.*, have reported an extensive scope of Ir(III)

complexes based on the 2-phenyl pyridine ligand with varied EWGs and EDGs on the phenyl ring and varying the substitution either in *para* or *meta* positions or in both to yield homoleptic complexes of the type $Ir(ppy\text{-}R)_3$ where R was CF_3, F and tBu as well as cationic heteroleptic complexes of the type $[Ir(R1ppy\text{-}R2)_3]^+$. Tian *et al.,* (2009) reported synthesis of Ir(III) heteroleptic complexes with 2-phenyl pyridine and 2-(naphthalen-1-yl) pyridine ligands with carbazolyl and thienyl substituted β-diketones as ancillary ligands to achieve increased functionality for OLED devices. Homoleptic complexes based on 2-(naphthalen-1-yl) pyridine ligands which is more conjugated than the widely used 2-phenyl pyridine ligands have not been explored much yet they offer a route for fine tuning the complexes for exploration in photocatalysis and photosensitization.

2.3.1 C-H Activation

The C-C σ-bonds are the most ubiquitous bonds, relatively electronically unipolar and main constituents of the organic compounds with C-H bonds on the periphery. Transformations of these unactivated σ-bonds remain a challenge in synthesis chemistry hence research into their activation has become a fast growing field with promising approaches (Ahlstrand *et al.,* 2017; Murakami & Ishida, 2017). In order for C-H activation reaction to be of synthetic value, there needs to be selective discrimination of one C-H bonds from all the other bonds which usually are chemically similar (Kuhl *et al*., 2012; Kondrashov *et al*., 2015). This can be circumvented through direct C-H activation. Typically, the position γ to the donor atom undergoes functionalization. The δ-position can be involved if the γ-position is blocked. Since these reactions proceed via the corresponding chelate, with the sum of ideal bond angles in five- membered rings being closer to the ideal angle sum of a polygon than it is in the corresponding four- or six-membered analogues, the five membered metallacycles are easily formed (Kondrashov *et al*., 2015). Additionally, application of molecules with C-H bonds of different reactivity mostly in heterocycles can also solve the problem but in benzene derivatives the discrepancy in reactivity of the bonds is less pronounced hence other regioselectivity controlling methods are applied such as using directing groups (DG) such as pyridine, amides, acetanilides etc. The major limitation of this method is that it leads to mostly *ortho* functionalizations hence restricts the scope of products. It also requires further synthetic steps to install the DG and manipulation after the functionalization (Kuhl *et al*., 2012).

Biaryl moiety is an important structural motif in biologically active compounds, natural products, and materials. Its construction through a direct cross coupling of two arenes is therefore an attractive process that offers superior sustainability and environmental compatibility to conventional transition-metal-catalyzed cross-couplings between aryl halides or triflates and organometallic reagents. In general, C-H arylation reactions can be divided into two classes: 1) the coupling of a simple arene with either an aryl halide (Ar-X + Ar-H) or an organometallic species (Ar-H + Ar-M), also called direct arylation, and; 2) dehydrogenative couplings (Ar-H + Ar-H) in which both reaction partners contain C-H bonds.

2.4 Spectroscopic studies of coordination complexes

Cyclometalated complexes of metals such as Pt(II), Pd(II), Ru(II) and Ir(III) have been extensively studied due to their remarkable photophysical properties with their luminescent properties making them invaluable in diverse applications. Interaction of matter with light leads to crucial processes such as photon absorption, internal conversion, fluorescence, intersystem crossing and phosphorescence all which gives the photophysical properties of complexes (Cîrcu & Micutz, 2011).

2.4.1 Principles of photophysical properties of complexes

In an atom, two angular momenta, spin (m_s) and orbital (m_l), contribute to the total electronic angular momentum and the interaction of these two momenta with each other is termed spin-orbit coupling (SOC) (Cîrcu and Micutz 2011, Khudyakov *et al.,* 1993). The magnetic moment of the particle should be bistable, with an energy barrier between ‘‘up’’ and ‘‘down’’ orientations of the magnetic moment. The occurrence of an energy barrier is intimately linked to magnetic anisotropy, which is the phenomenon that a molecule can be more easily magnetized along one direction than the others i.e., the different orientations of the magnetic moment have different energies. In the absence of orbital angular momentum (for instance, in many transition metal ions), this phenomenon is called zero-field splitting. In coordination clusters of first row transition metal ions without orbital angular momenta, the energy barrier ultimately arises from spin–orbit-coupling-induced mixing of the electronic ground and excited states (Liddle and van Slageren, 2015). SOC arises from interaction of the magnetic field associated with the spin angular momentum with the

magnetic field associated with the orbital motion of the same electron in the electrostatic field of a nucleus (Khudyakov *et al.,* 1993).

SOC provides magnetic interactions, which lead to nonzero matrix elements between states of different spin multiplicity, and thereby a mechanism, which allows the corresponding electronic transitions to occur between states of different spin multiplicity. Crystal field splitting is an important characteristic of a system in determining the magnitude of SOC (Khudyakov *et al.,*1993). The most evident experimental manifestation of SOC in atoms is the fine splitting of the atomic spectra while in molecules it is the violation of prohibition of singlet-triplet (S-T) interconversion (Khudyakov *et al.,*1993).

The operable photophysical processes in a coordination complex is initiated by absorption of light which promotes an electron from a metal-centered t_{2g} orbital to a ligand-centered $\pi*$ orbital which implies that the metal center is oxidized whereas the ligand is reduced electronically corresponding to metal-to-ligand charge transfer (MLCT), a type of charge transfer process (Monos & Stephenson, 2017). Charge-transfer (CT) excited states play an important role in the observed photo-reactivity of metal complexes (Nazeeruddin *et al.,* 1993). These complexes are known to exhibit many of the electronically excited states found in coordination compounds. However, the low-valent metal center and the high degree of covalency associated with the metal-ligand bond in an organometallic complex give rise to some notable differences in the excited-state (Lees, 1987).

Charge transfer transitions occur when transition metal complexes (TMCs) absorb light, which can lead to electron transfer from ligands to empty d orbitals or from the d orbitals to ligand. TMCs have complex electronic structures, since both the metal and ligand contribute to available excited states. When there is irradiation transition occurring between two MOs can be explained using the MO involved but assignment of various bands on a TMC spectra can be challenging due to the complex electronic structure of the complex. Therefore, CT is used to explain these transitions since it involves displacement of electronic charge from metal to ligand or ligand to metal (Housecroft & Sharpe, 2005).

Transition metal complexes transitions are in principle responsible for the luminescent properties and can be classified as charge transfer (CT), intraligand (IL) or metal centered (MC). MLCT

involves transition of an electron from d orbital to π* orbital of the ligand (d-π*) while ligand-to-metal charge transfer (LMCT) involves electronic transition from ligand orbital to metal orbital (π-d). When the transition is between two ligand orbitals, it is referred to as ligand-centered (LC) or intraligand (π-π* or n-π*) transitions. Lastly, metal centered transitions (MC) are observed when the predominant MO is localized on the metal center and essentially constitute the d-d transitions, which are fairly weak. The charge transfer electronic transitions are shown in Figure 1. Charge transfer to solvent (CTTS) and ligand-to-ligand charge transfer (LLCT) constitute the less common transitions that involve transitions from a metal centered orbital to a solvent localized orbital and transitions between two orbitals but on different ligands coordinated to the same metal center, respectively (Brulatti, 2010).

Four types of electronic states in organometallic complexes compete for the lowest unoccupied molecular orbital (LUMO). LUMO and HOMO are shown in Figure 1. Two of them are singlet and triplet metal-to-ligand charge transfer states, ^{1}MLCT and ^{3}MLCT. The remaining two are the singlet and triplet ligand-centered, (^{1}LC) and (^{3}LC) states. The involvement of the d-orbital in the bonding is expected to be higher for MLCT states and this is reflected in the lower intensities of the corresponding absorption bands relative to those involving ligand-centered states (Tian, 2011). Generally, when a molecule absorbs light (steady-state absorption), one t_{2g} d –electron of ground state octahedral complex is excited onto π* orbital of the ligand without flipping its spin, the so-called MLCT, which generates a singlet-excited state which can relax back to the ground state with emission of some light (photoluminescence). The singlet-excited state can also rapidly decay to the long-lived triplet excited state via spin-forbidden intersystem crossing (ISC). The intersystem crossing rate can be enhanced by a heavy atom through increased spin−orbit coupling, which consequently increases the triplet excited-state quantum yield (Li *et al.,* 2014; Angnes *et al.,* 2015).

The selection rules governing d-d transitions between electronic energy levels of transition metal complexes are: The Spin selection rule, $\Delta S = 0$ where the allowed transitions must involve the promotion of electrons without a change in their spin (singlet to singlet or triplet to triplet); and the Laporte (parity/orbital) selection rule $\Delta l = \pm 1$ which provides that if the molecule has a center of symmetry, as in the case of O_h complexes, transitions within a given set of p or d orbitals (i.e. those which only involve a redistribution of electrons within a given subshell) are forbidden. In

other words, electric dipole transitions that maintain parity either symmetry or antisymmetry with respect to an inversion center cannot occur (Laporte allowed: a change in parity occurs i.e. s → p and p → d or g (gerade=even) → u (ungerade=odd) and u → g; Laporte forbidden: the parity remains unchanged i.e. p → p and d → d or g → g and u → u) (Laporte and Meggers, 1925; House, 2018). Tetrahedral molecules are not centrosymmetric thus mixing of p and d orbitals is allowed hence p → p and d → d transitions are not Laporte forbidden. However, this rule is only strictly applicable to states of definite parity (i.e., those belonging to a centrosymmetric point group), meaning that it can be relaxed by altering the symmetry of the electronic states such that they do not have definite parity. This can be done through molecular vibrations, vibronic coupling or spin orbit coupling thus allowing relaxation of the Laporte rule and permits weak transitions such as d-d transitions to be observed (Wisser *et al.*, 2015; Ellis, 1999). Therefore, d-d transitions are observed as weak, less intense transitions since they are Laporte forbidden and are only allowed via vibronic and spin orbit coupling. Moreover, they have lower energy charge transfer bands since they have a smaller 10Dq values

2.4.2 Ultraviolet- Visible spectroscopy/ electronic spectroscopy

Absorption of light in the ultraviolet (UV) and visible (Vis) region leads to transition amongst the electronic energy levels giving rise to a series of absorption bands, which constitute electronic absorption spectra (Anderson *et al.,* 2004). Transitions are accompanied by rotational and vibrational transitions such that electron promotion can happen from ground state level E_1 to any of the vibrational or rotational levels of E_2, clarifying why, for polyatomic molecules, the spectra is characterized by broad bands since in each electronic state, rotational and vibrational energy is considered as per Frank-Condon principle (Anderson *et al.,* 2004; Brulatti, 2010). The strength of electronic spectroscopy lies in its ability to measure the extent of multiple bond or aromatic conjugation within molecules. Compounds that absorb light between 400-800 nm (visible region) appear colored to the human eye and the resultant color is a function of which wavelengths the compound subtracts from white light (Kemp, 1991).

Allowed transitions are determined by selection rules founded on symmetry of ground and excited states of the molecule determine which electronic transitions are allowed (Anderson *et al.,* 2004). In Beer-Lambert law, the absorbance (A) of a solution is directly proportional to path length (l) and concentration (c) of the absorbing molecule according to equation 1.

$A = \varepsilon cl$ ----------(1)

ε, the molar absorptivity or molar extinction coefficient is characteristic of the molecule and a measure of intensity of the absorption, ranging from 0 to 10^6 units. The greater the ε value, the greater the probability of absorption and its associated electronic transition. Forbidden transitions are occasioned by low-intensity bands (ε < 10000) (Anderson *et al.,* 2004). Integration of ε shows the probability of transition from ground to excited and the reciprocal of the transition probability is the lifetime of the excited state before it relaxes to ground start with emission of a photon (Brulatti, 2010).

Chromophores, portion of the molecule bearing electrons that are involved in absorption leading to electronic transition, that are non-conjugated lead to high-energy absorptions with low-intensity (ε) values, although most of these get lost in atmospheric oxygen absorptions. Generally, UV spectra are of interest in unsaturated systems; the greater the degree of unsaturation the more intense the absorptions and at longer wavelengths. Conjugation increases the chromophore resulting into greater intensity absorption bands with larger ε values. On the other hand, conjugation reduces the HOMO-LUMO energy gap for a system implying that less energy is required for promoting an electron from ground state energy level. Therefore, the longer the chromophore the longer the maxima wavelength, λ_{max} of absorption. Occurrence of an electron donating substituent on an aromatic ring extends the chromophore and increases the absorption's wavelength. An increase in the λ_{max} towards the red end of the absorption spectrum is called red/bathochromic shift (shift to longer λ, lower energy). The reverse effect is a shift to the blue end of the spectrum called blue/hypsochromic shift (Anderson *et al.,* 2004).

UV spectroscopy is utilized to identify a key chromophore of an unknown molecule for instant in analysis of pharmaceuticals. It has been utilized for the detection of analytes in analytical separation techniques e.g. thin layer chromatography (TLC), for rapid qualitative analysis of reaction mixtures and as detectors in HPLC (Anderson *et al.*, 2004).

Measurements are mostly done using a double beam spectrophotometer consisting of a UV-visible light source, two cells through which the light passes and a detector. The double beam spectrophotometer splits the light into two parallel beams, each passing through a cell; one with the sample dissolved in solvent and the other cell with the solvent only. The intensity of the light

transmitted through the solvent alone (I_0) and that transmitted through the sample cell (I) are measured and compared using a detector.

2.4.3 Photoluminescence spectroscopy

Once a complex absorbs light after irradiation, energy is utilized in the formation of the excited state and this can be liberated in different ways; i) radiative decay which involves emitting photons, ii) non radiative decay which can either be vibrational, transitional and translational energy within the same molecule or to another or solvent, or thermal degradation where the energy is discharged as heat to the environment, or the molecules taking part in chemical reactions whilst still in their excited state. If the excitation involves light, the subsequent emission is called photoluminescence. Excitation, which is donated by the orbital of origin, e.g. (π- π*) initially produces a singlet excited electronic state (S_n) whose spin is anti-parallel to that of the ground state orientation, which undergoes rapid relaxation through non-radiative pathways to give lowest singlet excited state (S_1). From this state, two types of emissions can be observed, fluorescence and phosphorescence as depicted in Jablonski diagram in Figure 2 (Brulatti, 2010).

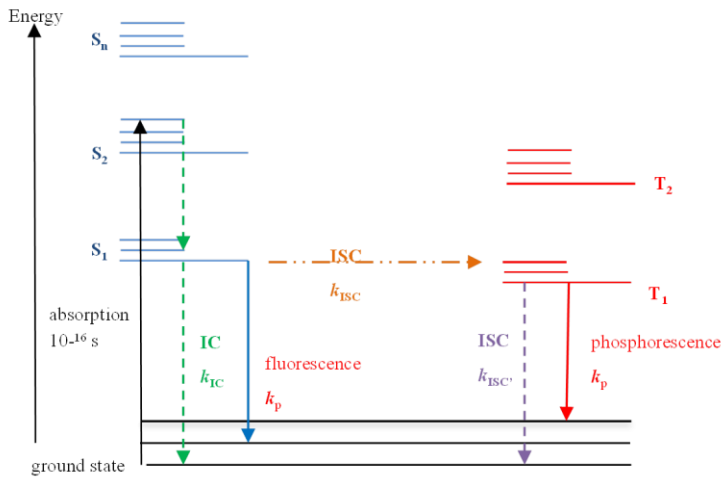

Figure 2: Jablonski Diagram

Source: (Brulatti, 2010)

Fluorescence

Typically, an excited molecule undergoes internal conversion, a non-radiative process, which involves reverting the molecule from S_n to lower excited states or singlet ground state and the energy difference is converted to vibrational energy and then heat. When this radiative relaxation is from S_n to ground state this is referred to as fluorescence (Figure 2), which happens at lower frequency than excitation energy and it fundamentally does not lead to change in spin multiplicity (Brulatti, 2010).

Phosphorescence

Primarily, when crossing of the excited state to a second excited but of different spin occurs, this is referred to as intersystem crossing (ISC) with a rate constant k_{ISC}, which happens due to singlet (S) and triplet (T) energy curves crossing each other. Subsequently, conversion from ↑↓ to ↑↑ of the spins, which is normally forbidden, becomes possible, essentially converting the molecule to a triplet state. The radiative relaxation from the triplet state to a singlet ground state is phosphorescence with a rate constant $k_{ISC'}$ (Figure 2) and it involves a change of spin quantum number (Brulatti, 2010). Singlet to triplet transitions are favored when spin orbit coupling (SOC) is strong as in the case of heavy metals, and this promotes mixing of singlet and triplet states breaking down selection rules at which point, the spin forbidden transition is competing with spin-allowed processes. Phosphorescent emission is lower in energy than fluorescent emission since triplet states are lower in energy than singlet state as per Hund's rule. Luminescence quantum yield, quantifies the efficiency with which a compound emits light.

Quantum Yield, Φ

Photoluminescence/radiative quantum yield, Φ, for an emissive species is a direct measure of the efficiency of conversion of absorbed photons into emitted photons and is hence given as a ratio between the number of photons emitted by a sample and the number of photons absorbed **(**Equation 2). Φ, can also be expressed in terms of kinetic competition where the ratio between relative rate(s) of processes giving rise to emission and the rates of all processes that serve to deplete the population of that emissive state is considered **(**Equation 3). Φ, determines the achievable sensitivity in luminescence analysis hence is a fluorometric vital parameter in determining the

suitability of a chromophore in various applications such as sensors, labels, photoredox probes and converters in OLEDs (Würth *et al.,* 2011; Arias-Rotondo *et al*., 2016)

$$\phi = \frac{\#\ photons\ emitted}{\#\ photons\ absorbed} = \frac{I_{em}}{I_{abs}} \text{ ---------- (2)}$$

$$\phi_o = \frac{K_r}{K_r + K_{nr}} = \frac{K_r}{K_o} \text{ ---------- (3)}$$

Where I_{em} and I_{abs} is the number of photons emitted and absorbed, respectively; K_r, K_{nr} and K_o are rates of processes giving rise to emission and those depleting the population of that emissive state

Φ, can be measured either relative to a standard with a known absolute value (method 1) (Equation 4) for example, $[Ru(bpy)3]^{2+}$; or as an absolute value (method 2) that necessitates the detection of every emitted photons per number of absorbed photons and is labor intensive; or indirect measurements by utilizing dissipated heat using photoacoustic spectroscopy or thermal sensing (method 3).

$$\phi_x = \phi_{std} \left(\frac{I_x/A_x}{I_{std}/A_{std}}\right) \left(\frac{\eta_x}{\eta_{std}}\right)^2 \text{ ---------- (4)}$$

Where; *x* is molecule of interest, I_x and I_{std} are integrated areas of corrected emission spectra for molecule and standard, A_x and A_{std} are absorbance's at excitation wavelength for molecule and standard while η_x and η_{std} are indices of refraction of solutions for molecule and standard. Choice of standard used depends on the emission properties of the substrate of interest.

Relative Φ measurements involve either using same excitation wavelength for the sample and standard (method 1a). This is commonly used since it is comparatively simple, cheap and has higher sensitivity thus minimizes amount of sample required for the measurements and allows measurement of small fluorescence Φ. Alternatively, different excitation wavelength for the sample and standard (method 1b) can be measured. This is considered to be more efficient but faces the challenge of excitation correction mandatory to account for wavelength dependence on photon flux getting to the sample. Therefore, absolute measurements are considered to be the most straightforward method for determination of Φ, which exploits an integrating sphere and essentially circumvents uncertainties arising from fluorescence standards integral to all relative

measurement methods. The accuracy of absolute Φ measurements is dependent on how reliable the radiometric characterization of the integration sphere is and proper considerations of reabsorption effects since these can result in substantial systematic errors (Würth et al., 2011). Factors affecting Φ include; i) transition type, ii) structural rigidity where the more rigid the structure the higher the yields, iii) substitution where the nature of substituent affects the yields. Substitution with heavy atoms such as halogens may lead to high quantum yields and is typically indicative of phosphorescence, iv) temperature, where lower the temperatures suppress non-radiative processes hence increasing Φ, v) solvent, where decrease in viscosity could reduce rate of non-radiative de-excitation, increasing Φ, vi) pH, where changes strongly alter Φ since this could lead to the luminophores changing in basic and acidic media (Omary & Patterson, 1999).

Emission Lifetimes

By following the kinetics of time-resolved emission, the radiative and non-radiative decay processes are first-order with respect to the excited states. The rate at which the excited state is lost can be expressed as a rate law and the inverse of the rate constant in this is called the lifetime (τ_0) of the excited state, which is measured using time-resolved emission spectroscopy also called transient absorption (TA). It has been found that longer excited state lifetimes lead to faster SET. Classically, excitation is done at λ_{max} or near it and the emission collected at 90^o with respect to excitation beam with the aim of minimizing scattering of light. Solvent, oxygen concentration in the sample and temperature among others, affect lifetime of the excited state. TA exploits laser pulses that excite the sample and a white light source to probe the absorption of transient species formed after excitation. Consequently, a TA signal is the change in absorbance of sample before and after the excitation (Arias-Rotondo *et al*., 2016; Ochola & Wolf, 2016). The main advantage of lifetimes is that it can be used for spectral assignment specifically by assigning if luminescence bands are either fluorescence where they emit in sub-microseconds level (nanoseconds, picoseconds) or phosphorescence where τ is in the microseconds and longer (milliseconds, seconds) although this is subjective (Omary & Patterson, 1999).

2.4.4 Nuclear Magnetic Resonance (NMR) spectroscopy

Atomic nuclei with odd mass or atomic numbers spin due to among spin $I \neq 0$, when placed into a magnetic field B_0, exhibit quantization with their orientation depending on spin quantum number,

I. The nuclei can assume (2*I* + 1) orientations in the field, with m_I (magnetic quantum numbers) values of –*I*, -*I*+1,.. *I*. NMR selection rules states that transitions with $\Delta m_I = \pm 1$ are allowed. Such nuclei display the NMR effect while nuclei with both even mass and even atomic numbers with I = 0 can never exhibit the NMR effect. For nuclei with spin, $I = ½$ (half-spin nuclei) (such as ^{1}H, ^{13}C, ^{19}F and ^{31}P), two arrangements are possible: either aligned "with" (lowest state energy, α, $m_I = + ½$; "spin up"*)* or aligned "against" (β, $m_I = - ½$; "spin down"*)* the applied field B. Thus, NMR measurements comprises of moving atomic nuclei α state to β state and observing this effect on nuclei of interest for a given sample (Anderson *et al.,* 2004). Consequently, NMR is a very popular and powerful analytical technique for identifying, characterizing and structure elucidation of chemical species (Willard *et al.,* 1986; Skoog *et al.,* 1998). NMR transitions occur in the radiofrequency end electromagnetic spectrum owing to their low energy with the relationship between the frequency of the transition and magnetic field being depicted by equation 5.

$$\nu = \gamma B_{eff}/2\pi \text{----------(5)}$$

Where ν is the frequency at which NMR transition occurs and has units Hz or s^{-1}, γ is the magnetogyric ration, measure of the size of the magnetic field or magnetic moment generated by a particular nuclear species and has units $s^{-1}T^{-1}$ and B_{eff} is the strength of magnetic field experienced by nucleus and has units T (Tesla) (Anderson *et al.,* 2004).

Therefore, the strength of B_0 determines the energy difference between the possible alignments of the nuclear magnetic dipole: the stronger the applied field, the greater the energy gap and the greater the frequency. NMR effect cannot be observed without the applied field, since there would be no energy difference between the nuclei's possible alignments (Anderson *et al.,* 2004). Poor signal-to-noise ratio is a feature of NMR arising from the small energy gap between the possible alignments of nuclear magnets. Moreover, the energy difference is proportional to the population, with the Boltzmann distribution for a nucleus with spin $I = ½$ at room temperature being 50:50 *i.e.,* nearly 50% of the nuclei will be aligned "with" and 50% will be aligned "against" the magnetic field. Subsequently, NMR experiments are conducted at the highest frequency possible; since γ is constant, this is achieved by increasing the strength of the magnetic field (Anderson *et al.,* 2004). The NMR spectrum is affected by environmental effects such as chemical shift (δ) and spin-spin splitting both of which are monumental in structural analysis and elucidation.

Chemical shift (δ) is caused by small secondary magnetic fields that are generated by electrons as they circulate around the nuclei giving rise to diamagnetic currents, which oppose and decreases the strength of the applied field B_0 at the nucleus. Consequently, the nucleus experiences a reduced subsequent field from the full effect of the primary field and is described as shielded. Hence, the external field must be increased to give rise to nuclear resonance. δ is used to identify functional groups and aids in determination of structural arrangements of groups based upon empirical correlations between structure and shift (Skoog *et al.*, 1998).

The decrease of the main field due to spinning electrons is tiny but detectable in NMR experiment. This is why equation 5 has the term B_{eff}, effective magnetic field, rather than B_0, applied magnetic field, which is the chemical shift effect. The electron density around the nucleus determines the magnitude of this effect: high electron density causes a large effect while low electron density causes less effect. An atom attached to an EDG has increased electron density around the nucleus, which decreases B_{eff}. This adjustment of B_0 by surrounding electrons is referred to as shielding; higher electron density leads to greater the shielding (low frequency). Conversely, an EWG reduces the electron density around the nucleus hence increases B_{eff}, which is deshielding. A deshielded nucleus thus resonates at higher frequency than would have been expected (Anderson *et al.*, 2004). Nuclei in the same chemical environments display similar shifts and have units' ppm due to the effect being very small as compared to the main field. The unwanted magnetic field dependence chemical shift measurement is removed by in defining δ to be the ratio of the frequency at which NMR transition occurs to the strength of the applied field as measured by the frequency at which protons resonate as illustrated in equation 6 (Anderson *et al.*, 2004).

$$\delta = ((\nu_{sample} - \nu_{reference}) / \nu_{spectrometer}) \times 10^6 (ppm) \quad \text{----------(6)}$$

Where ν_{sample}, $\nu_{reference}$ and $\nu_{spectrometer}$ are frequencies due to sample, reference and spectrometer

Factors affecting the chemical shifts include electronegativity, magnetic anisotropy, inductive effects, van der waal deshielding and hydrogen bonding. Shielding of nucleus is directly related to the electron density surrounding it. Therefore, in absence of other factors shielding decreases with increasing electronegativity i.e., the nucleus is deshielded. Magnetic anisotropy attempts to explain the effects of multiple bonds on δ. In aromatic compounds when the plane of the ring is perpendicular to the magnetic field, the field induces a flow of π electrons around the ring, creating

a ring current that corresponds to an induced secondary field opposing the applied field. In turn, the induced field exerts a magnetic field on the protons attached to the ring hence aromatic protons resonate at a lower external field. Ring current is absent in other orientations of the ring (Skoog *et al.*, 1998).

Spin-spin splitting/ spin-spin coupling/ J coupling involves mutual splitting of the sharp resonance lines into multiplets, splitting patterns, when nuclei interact with each other (Willard et al., 1986). Spinning nuclei create a magnetic field, which affects the distribution of electrons in its bonds to other nuclei leading to splitting of energy levels that give rise to multiple transitions. Coupling constant (*J*) is the spacing in hertz of multiplets in a spectrum and it indicates the strength of coupling. Its magnitude is dependent on the bonding between the nuclei; the fewer bonds the larger the J values. Its noteworthy that equivalent protons both chemically and magnetically do not couple with each other (Skoog *et al.,* 1998; Anderson *et al.,* 2004). In an aliphatic system, proton-proton coupling is transmitted only through two or three bonds although in some rigid structures with favorable geometry, coupling through four bonds is relatively large. Conversely, in unsaturated systems, long-range couplings are enhanced, up to ^{7}J. In aromatic rings, couplings of protons in *ortho* positions (through three bonds, ^{3}J) are 7-9Hz, *meta* (four bonds, ^{4}J) 2-3Hz and *para* (five bonds, ^{5}J) 0.5-1Hz (Willard et al., 1986). In saturated systems, a favorable arrangement for long-range coupling is when bonds adopt a W arrangement (Anderson *et al.,* 2004).

Rules governing first order spectra interpretation: chemically equivalent nuclei, those that have identical chemical shifts or are related by some symmetry element, do not interact to give multiple absorption peaks. Coupling constants decrease appreciably with separation of groups with coupling being rarely observed at distances greater than four bonds (^{4}J). Moreover, coupling constants are independent on applied field (B_0) hence multiplets can be distinguished from closely spaced δ by running spectra at two differing field strength. Multiplicity of a band is determined by *n*, number of magnetically equivalent protons, those that have identical coupling constants to all others, on the neighboring atom and is given by the quantity n+1. For protons on an atom (A) that are affected by protons on two different nonequivalent atoms (B and C), multiplicity A in this case is given by $(n_B+1)(n_C+1)$ (Willard *et al.,* 1986; Skoog *et al.,* 1998).

Vicinal coupling is a three-bond (^{3}J) coupling that is commonly observed while geminal or two-bond coupling (^{2}J) is less frequent but displays the largest coupling constant ^{3}J in an aliphatic

region. The presence of electronegative elements directly attached to the same carbon atom decreases the magnitude of the coupling constants, while the presence of electropositive elements increases it. The effect is small in chains but more pronounced in rigid systems such as alkenes. Geminal coupling constants increase by: i) introduction of an electronegative substituent on an adjacent carbon atom, ii) introduction of an electropositive substituent on the same carbon atom as the geminally coupled hydrogen's and iii) having an adjacent π-bond, so that the C-H sigma orbital can overlap with the π-orbitals of the π-bond. Conversely, they are decreased by: an increase in the H-C-H bond angle, introduction of electronegative substituent on the carbon atom as the geminally coupled hydrogen's and introduction of an electropositive substituent on an adjacent carbon atom (Anderson *et al.,* 2004).

Proton (^{1}H) NMR is a powerful and indispensable tool that plays a vital role in identification, characterization of pure compounds, structure elucidation of biochemical, organic and metal-organic molecules as well as being utilized for quantitative determination of absorbing species (Skoog et al., 1998). A ^{1}H NMR spectrum gives the number of ^{1}H in each molecular environment since the number of ^{1}H nuclei giving rise to the peak are proportional to the area under each peak (Anderson *et al.,* 2004). δ typically ranges between 0-15 ppm since the δ is influenced only by the s electron. ^{1}H δ are a measure of electron density with higher chemical shift of that ^{1}H being observed when the carbon bearing the proton is attached to a more electronegative group (Anderson *et al.,* 2004).

Carbon-13 (^{13}C) has a natural abundance of 1.1% and a nuclear spin of ½ and gives rise to NMR signals thus, ^{13}C NMR spectroscopy has become important in structure confirmation and elucidation as it provides information about the backbone of molecules rather than about just the periphery as in the case of ^{1}H NMR (Skoog *et al.,* 1998; Anderson *et al.,* 2004). The effects of substituents on ^{13}C shifts is not confined to the nearest atom as in ^{1}H (Skoog *et al.,* 1998). A convectional. ^{13}C NMR spectrum is referred to as being proton decoupled and consists of chemical shift against intensity, with one peak for each carbon atom in the molecule. Quaternary carbons (which have no attached protons) have no nearby nuclei with spin to which they can transfer their energy, so they don't have sufficient time to "relax "back to equilibrium before the next pulse is applied. As a result, their peak intensities are normally reduced compared to other groups for example, methyl (CH_3) (Anderson *et al.,* 2004). The chemical shift of carbon atoms lies between

0-220 ppm, which translates to less overlap of peaks such that it becomes possible to observe individual carbon peaks. Deshielding or shielding effects of atoms and groups influences the chemical shifts in a manner similar to that of protons but do not necessarily match the relative positions of the corresponding protons in the ^{1}H spectrum. Signals of carbon atoms in an alkyl chain appear at the high-end of the spectrum, about δ 10-30; the greater substitution on a carbon, the more deshielded the signal. Aromatic carbon atoms usually give rise to signals in the region δ 120-140 although the exact chemical shift is affected by the substituents on the ring with EWG or EDGs leading to different patterns of deshielding or shielding (Anderson *et al.,* 2004). The most significant effects, regardless of whether the substituent is withdrawing or donating are seen at the 2- (*ortho*) and the 4- (*para*) positions with 3- (*meta*) carbon being rarely affected by more than a few ppm. Carbonyl carbons with sp^2 carbon bonded by a π-bond to the highly electronegative O, have a characteristic chemical shift of δ 160-220, with the aldehyde and ketones being most deshielded and resonating at δ185-220, while those of carboxylic acids and their derivatives resonating at δ 160-180 (Anderson *et al.,* 2004).

Two-dimensional, 2D Correlated SpectroscopY (COSY) NMR, presentation makes it possible to unravel complex spectra, and determines all the coupling interactions in a single experiment. It permits the presentation of spectra as a function of two independent frequency parameters. These experiments involve two pulses separated by a variable time period and observation of the free induction decay signal in a sequence of; pulse, evolution, pulse and detection. In other words, the data is acquired as a function of time t_2 just as in 1D NMR, but prior to obtaining this FID signal the system is normally perturbed by a pulse for a period t_1 (Willard *et al.,* 1986; Skoog *et al.,* 1998; Anderson *et al.,* 2004). HH COSY allows correlation of ^{1}H shifts of all the coupling partners in the molecule. The COSY spectrum is symmetrical about the diagonal axis, and the cross-peaks all appear on either side of the diagonal axis and are symmetrical about it. This symmetry makes identification of cross peaks easy since the two-coupled peaks (on the diagonal) and the cross-peaks (off the diagonal) form the four corners of a square. Therefore, for one to determine the coupling partner for any peak, go down directly vertically or horizontally from any give peak until a cross-peak is encountered, then going vertically or horizontally from this peak to the diagonal gives the peak for the coupling partner (Anderson *et al.,* 2004).

Fluorine-19 (^{19}F) has natural abundance of 100% and a spin of ½ hence it is NMR-active. ^{19}F NMR spectroscopy provides information about fluorine in the molecule. Fluorine absorption is sensitive to the environment and resulting δ extend over a range of 300ppm. Solvent plays more significant role in determination of the ^{19}F peaks than in ^{1}H (Skoog *et al.*, 1998).

2.4.5 X-ray diffraction

X-rays avail a potent technique for the study of crystal structure since they can undergo diffraction as in the case of visible light. Typically, the ordered arrangement of atoms in a crystal with interatomic spacing of the order of few angstroms behaves like a three-dimensional diffraction grating for X-rays. The characteristic difference between a crystal and ordinary grating is that for the former, the diffracting centers are not in the same plane, crystals act as space grating rather than plane grating used to study light diffraction. Laue pattern is a grating pattern that consists of symmetrical pattern of spots, which consists of a central spot surrounded by series of spots arranged in a definite pattern. According to Bragg, the spots are produced due to reflection of some incident X-rays from various sets of parallel crystal planes, Bragg's plane, which contain a large number of atoms. The Bragg's law of X-ray diffraction, which governs how reflection takes place (Equation 7),

$$2d \sin\theta = n\lambda \text{----------(7)}$$

Where: θ, glancing angle, is the angle between the incident ray and the planes of reflection; d is interplanar spacing of plane i.e., distance between the same set of planes and n is 1,2, 3 implying first, second and third order respectively. From Bragg's law, reflection occurs only for $\lambda \leq 2d$ (Kakani & Kakani, 2004).

2.4.6 Elemental Analyses

This is a fundamental quantitative analysis technique of the major elements namely carbon, hydrogen and nitrogen and fluorine, of an organic substance in new compounds, using either classical or automated analyzers. The ability to measure these elements accurately is extremely vital in the characterization and identification of organic compounds, which entails reliable identification and verification of purity by means of proper organic elemental analysis methods. The organic compound undergoes oxidative decomposition and subsequent reduction of nitrogen

and any sulfur oxides followed by formation of final products such as carbon dioxide, water, elemental nitrogen and sulfur dioxides. Elemental analyses for fluorides in polyfluoroaromatic/ fluorine containing compounds is possible although this requires stringent decomposition conditions since such compounds are thermally stable and require removal of fluorine as an interfering elemental in the combustion zone due to aggressiveness of F and HF formed which can lead to corrosion of the analyzers (Ma & Gutterson, 1970; Fadeeva *et al.,* 2008).

2.5 Electrochemistry

Electrochemistry is a quantitative analytical technique that deals with interconversion of electrical energy and chemical energy with the principal objective being to study the behavior and reactions of ions in a variety of environments (Atkins, 1978; Chang, 2005). Therefore, electrochemistry has been used extensively to study heterogeneous electron transfer kinetics commonly at a metal-solution interface (Nicholson, 1965; Rackus *et al.,* 2015).

Voltammetry is the most comprehensively used electrochemical technique to access the ground-state potentials of a complex and as such derive their redox behaviors. It has the ability to probe the reversibility of the system under study (Wang *et al.,* 2012; Rackus *et al.,* 2015; Arias-Rotondo *et al.,* 2016). Ideally, a system whose electrochemical equilibrium is always maintained at the electrode would be deemed reversible if the separation of cathodic and anodic peak potentials is *ca.* 60mV (Nicholson, 1965). Derivative voltammetry possesses the distinct advantage in that vital information seemingly lost in the original current is readily recovered from analysis of the either 1^{st} or 2^{nd} derivatives and can be used to inform on reversibility of the systems. In 1^{st} derivative CV, analysis of peak potential, peak heights and peak widths can determine satisfactorily whether a system undergoes reversible, quasi-reversible or irreversible processes (Kim *et al.,* 1993)

Measurements are done using an electrochemical cell comprising of a set of electrodes that act either as a source of electrons or as a sink (Atkins, 1978). In most cases, a three electrode-system is used; i) a working electrode (WE) which measures the occurring redox reactions of the analyte of interest, (ii) a counter electrode (CE) which sets the WE potential, balances the current and is typically controlled by the potentiostat and (iii) a reference electrode (RE) providing the feedback of the WE potential to the potentiostat. During measurement, the analyte moves from the bulk solution to the electric double layer through one or more of the three genres of mass transfer which

includes; migration, diffusion, and convection. Subsequently, the analyte participates in reduction-oxidation (redox) reaction due to electric potential, *E*, that is measured between RE and WE. Electric potential *E*, and concentrations of reductants [Red] and oxidants [Ox] vary according to Nernst relationship shown in Equation 8 (Rackus *et al.*, 2015).

$$\boldsymbol{E = E^{o} + \frac{RT}{nF} \ln \frac{[Ox]}{[Red]}} \text{----------(8)}$$

Where: E = standard potential; E^{o} = the formal potential; R = gas constant; T = temperature; n = number of electrons transferred; F = Faraday's constant; [Ox] and [Red] = the surface concentrations of the oxidized and reduced species at the electrode/solution interface, respectively (Rackus et al., 2015).

In cyclic voltammetry, *E*, which is varied with time, is applied between WE and CE and the resultant current, *I* measured. Typically, *E* is swept in a linear cycle at a scan rate *v*, i.e., rate of change of potential with time. Initially a forward potential scan is applied and then the direction of the scan is subsequently reversed at the end of the first scan (first switching potential) and the potential range is scanned again in the reverse direction and stopped at the final potential (BASi Epsilon, 2009). As *E*, becomes increasingly positive the analyte is oxidized and conversely as *E* becomes more negative, the analyte is reduced with each step of the redox process being associated with peak current, i_p (Rackus *et al.*, 2015). In the initial forward scan, an increasing oxidizing potential is applied and as the cathodic peak potential, E_{pc} is approached, there is a net cathodic peak current, i_{pc} that increases exponentially with potential. After i_{pc}, current decays due to depletion of the analyte in the interfacial region. Upon reversal of direction of potential scan the current continues to decay until potential nears anodic peak potential, E_{pa} at which point there begins a net reoxidation of the reduced species to analyte which causes an anodic current, i_{pa} (BASi Epsilon, 2009). Randles-Sevcik equation (9), gives the relationship between i_p and *v*.

$$i_p = (2.69 \times 10^5) A C D^{\frac{1}{2}}\ n^{\frac{3}{2}}\ v^{\frac{1}{2}} \text{----------(9)}$$

Where: A = electrode area; C = concentration of analyte in bulk solution; D = diffusion coefficient of analyte; n = number of electrons involved in reaction; *v* = scan rate in V/*s*

Consequently, the magnitude of i_p can be used for determination of the analyte concentration and reductive/ oxidative potentials can be used for qualitative identification of the analyte (Rackus *et al*., 2015). A typical cyclic voltammogram is shown in Figure 3 where E_{pa} and E_{pc} are anodic and cathodic potential peaks respectively whereas i_{pa} and i_{pc} are anodic and cathodic current peaks respectively.

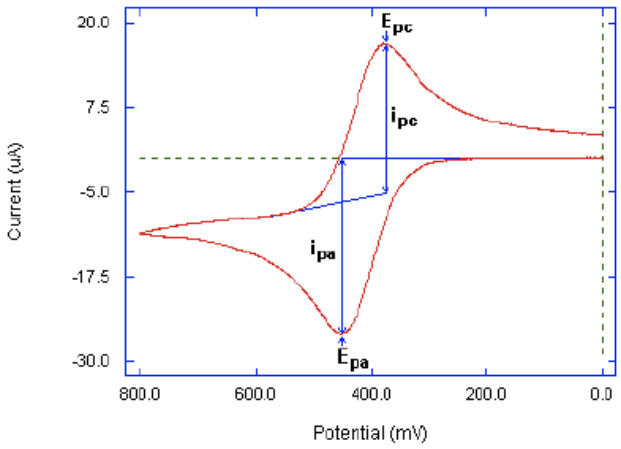

Figure 3: Cyclic Voltammogram

Source: BASi Epsilon 2009

2.6 Chromatography

Separation of mixtures using chromatographic techniques is an integral part of analytical and preparative chemistry. The methods include; i) liquid chromatography, LC (in columns or on thin layers, TLC, or in high-performance liquid chromatograph, HPLC); ii) gas chromatography, GC (in packed or capillary columns); and iii) specialized ion exchange chromatography, gel permeation chromatography (GPC), size exclusion chromatography (SEC) and super critical fluid chromatography (SFC) (Kemp, 1991).

Liquid Column Chromatography is utilized to separate volatile and nonvolatile solutes (Kemp, 1991), and is a strategic technology in analysis and production of value added chemicals, enables monitoring of changes in the environment through provision of tools able to control emission of pollutants and determine their distribution and metabolism; and provides a platform for medical and therapeutics. In column chromatography, separation occurs in a column that has a stationary

and a mobile phase, which transport a mixture of analytes to be resolved through the column with subsequent separation of analytes into individual species through selective distribution between the two phases exiting the column outlet as narrow bands that are then detected (Fadeeva *et al.*, 2008).

Flash Chromatography is an absorption LC for routine purification of organic compounds which is an alternative to the traditional gravity column chromatography that is tedious, time consuming and tends to give poor recovery due to band tailing with the shortcomings being magnified if samples greater than 1 or 2 g must be separated. It is an air pressure driven hybrid of medium pressure and short chromatography, optimized for mostly quick separations (Still *et al.,* 1978).

2.7 Mass spectrometry

This analytical technique is utilized since it provides three critical pieces of information: i) to measure with high accuracy relative molecular masses (molecular weights), from which exact molecular formulae can be deduced; ii) to detect within the molecule the preferable fragmentation patterns, from which the presence of recognizable groupings can be inferred; and iii) as a technique to identify analytes through comparison of their mass spectra with libraries of digitized mass spectra of known compounds (Kemp, 1991).

MS works on the premise that the instrument generates gas-phase ions, separates them by their mass-to-charge ratio in an evacuated volume by utilizing an electric field and counts the number of ions. Solvated analytes are introduced to the MS through a combined inlet/ionization source, where introduction, desolvation and ionization of the sample are closely related. This solution is introduced either as effluent from LC or directly via syringe pump (Henderson and McIndoe, 2005). Conversion of some translational energy of an accelerated ion to internal energy occurs after collision with residual gas leading to collision-induced dissociation (CID) or CAD (collision-activated decomposition), with decomposition/fragmentation of the ion being induced by increase in internal energy. The first step involves the collision between accelerated ions with an immobile neutral target leading to increased internal energy of the ion, which then rapidly redistributes this extra energy amongst its vibrational nodes. The second step is much slower and is the unimolecular fragmentation of the excited ion into product ions and neutral fragment, with their abundance each mass-to-charge ratio (*m/z*) values being measured by a detector. Typically, mass resolution

represents the ability of MS to separate ions of varying *m/z,* which is represented in the peak's sharpness while mass accuracy, is the difference between the calculated mass of an ion and the observed mass, $\Delta m = m_{calculated} - m_{observed}$, expressed relative to the observed mass. High resolution MS (HRMS) provide a mass accuracy of 5ppm or better and as such provide accurate mass data (Henderson and McIndoe, 2005).

There exist a number of vaporization and ionization processes such as electron impact (EI), chemical ionization (CI), fast atom bombardment (FAB), matrix assisted laser desorption ionization (MALDI), electrospray ionization (ESI), field desorption (FD) and secondary ion mass spectrometry (SIMS). Vaporization process occurs before the ionization except for the case of electro-spray ionization (Anderson *et al.,* 2004).

Electron Impact (EI) is a relatively harsh technique and involves the sample being volatilized into gas phase by heating in a vacuum, and then bombarded by a stream of electrons in order to cause ionization of the sample. Chemical ionization (CI) also uses a stream of electrons in the ionization process. However, a reagent gas such as ammonia or methane, present in high concentrations, is in this case ionized and not the sample molecules. CI results in the production of $[M + 1]^+$ ion with little excess energy, hence the fragmentation is less evident than EI. CI is capable of producing negatively charged ions unlike EI owing to the presence of high concentrations of the reagent gas (Anderson *et al.,* 2004).

Fast atom bombardment (FAB) involves bombarding a solution of the analyte in a matrix with a beam of fast-moving atoms, generally xenon atoms with energy in the range 6-9 keV. FAB can also generate negatively charged ions and gives $[M + 1]^+$ peaks (corresponding to MH^+ ion) with little fragmentation. In negative ion mode the most abundant peaks observed are $[M - 1]^-$ peaks corresponding to $[M - H]^-$ (Anderson *et al.,* 2004). Matrix assisted laser desorption ionization (MALDI) uses similar principle to FAB except in this case the energy transferred to the matrix from a laser beam and the matrix employed must have a chromophore which absorbs at the wavelength of the laser. (Anderson *et al.,* 2004).

Electrospray ionization (ESI) is a popular soft ionization technique where the analyte is dissolved in a mixture of an organic solvent (usually methanol or acetonitrile) and water with a pH modifier (for example, methanoic or ethanoic acid for positive ion model). pH modifier ensures that

ionization takes place in the solution state, the only common case where ionization occurs before ion vaporization. Depending on the pH modifier used, ionization takes place by deprotonation or protonation of the analyte, hence, the molecular species detected is almost exclusively $[M + H]^+$ in positive ion mode and $[M - H]^-$ in negative ion mode, with both species undergoing very little fragmentation. ESI's advantage is that it gives multiply charged ions for large molecules with many ionizable functional groups, which lowers the *m/z* ratio thereby allowing determination of the masses of large molecules without the need for a detector that has a large mass range. On the other hand, ESI is very sensitive to contaminants in the solvents, particularly alkali metal is such that ions corresponding to $[M + Na]^+$ or $[M + NH_4]^+$ can be observed. These peaks can often be used in accurate mass determination using ESI (Anderson *et al.,* 2004). Atmospheric pressure chemical ionization (APCI) uses similar processes as in CI, but at atmospheric pressure. The reagent gas (water) becomes protonated and can act as an acid towards the analyte, leading to the addition of a proton. The species formed in in positive ion mode is $[M + H]^+$ while in negative ion mode the reagent acts as a base towards the analyte leading to deprotonation and subsequent formation of $[M - H]^-$ (Anderson *et al.,* 2004).

Ion mass analysis methods characterize the type of instrument. The most common are: i) magnetic sector mass spectrometers (and double-focusing mass spectrometers); ii) quadrupole mass filters; iii) ion trap mass spectrometers; iv) time-of-flight (TOF) spectrometers; and v) ion cyclotron resonance-Fourier transform (ICR-FT) mass spectrometers (Anderson *et al.*, 2004).

Magnetic sector mass spectrometers (and double-focusing mass spectrometers) utilize a magnetic field to analyze ions produced in the ion source. Quadrupole mass filters used to provide low-resolution spectra, have analyzers that consist of two parallel rods providing the quadrupole field while in ion trap mass spectrometers the quadrupole field is generated within a three-dimensional cell using a ring electrode and no filtering of the ions occurs (Anderson *et al.,* 2004).

Time-of-flight (TOF) spectrometers generate the mass spectrum by separating ions according to the time it takes them to reach the detector. The separation takes place in a region without applied magnetic or electric field, the field-free region. All ions of the same charge are given similar kinetic energy accelerating them through a known potential difference. If kinetic energy is constant, the ions with smaller masses have greater velocities hence take shortest time to reach the detector while those with greater masses travel more slowly and takes longer to reach the detector. Ions

with the same charge will thus reach the detector in order of increasing mass. TOF MS are among the most sensitive analyzers and can operate up to very high molecular masses (very low velocities) (Anderson *et al.*, 2004). Ion cyclotron resonance-Fourier transform (ICR-FT) mass spectrometers utilize an ion trap where the ions are trapped within a cell situated within a strong magnetic field at right angles to the trapping plates. Ions in such strong magnetic field undergo ion cyclotron resonance and move in a circular orbit perpendicular to the magnetic field direction, at a frequency dependent upon their *m/z* ratio (Anderson *et al.*, 2004).

The biggest difference between MS of organic and organometallic compounds is the extensive incidence of polyisotopic elements**.** Since the MS separates individual ions, if the ion contains one or more polyisotopic elements it results into a couple of isotope peaks, having distinctive patterns of spacing and intensities and is dependent on the masses and relative abundance of the isotope in the ion, the so-called isotope pattern of the ion. Isotope pattern matching involves comparing theoretical and experimental isotope pattern but experiences difficulties arising due to: i) low signal-to-noise ratio where the lower intensity isotope pattern vanish into the noise; ii) low resolution causes overlap of peak which is a problem for high molecular weight species that are multiply charged; iii) poor calibration; iv) overlap of two patterns arising from competing ionization pathways are e.g. between oxidation to form $[M]^{\bullet+}$ and protonation to form $[M+H]^+$ or the appearance of $[M+NH_4]^+$ and $[M+H+H_2O]^+$. The best approach to sort this is to promote one ionization pathway at the expense of the other (for instance, add H+) or look for a different ionization source all together in this case one can use atmospheric pressure chemical ionization (APCI) instead of the commonly used electron spray ionization (ESI); v) When two patterns overlap from different compounds. This is more rare in organometallics than in organics but can be resolved through separation by either LCMS or GCMS; and vi) When two patterns overlap with one from $[M]^{+/-}$ and the other is from the dimer, $[2M]^{2+/-}$ (Henderson and McIndoe, 2005).

2.8 Cyclometalated Iridium(III) Complexes

Iridium is a heavy atom, platinum group metal with a high atomic number, 77, [Xe] $4f^{14}$ $5d^7$ $6s^2$. The heavy atom offers increased spin-orbital coupling (SOC) in an Ir(III) complex. Formation of neutral complexes which allows for sublimation *in vacuo* is facilitated by the stable oxidation state of Ir(III) (Tian, 2011). Ir(III) d^6 complexes are usually kinetically inert, low spin, diamagnetic O_h

complexes with high stabilization influence of CFSE, 12/5 Δ_0, the maximum possible for any d^x configuration (Greenwood & Earnshaw, 1998).

The *tris* cyclometalated iridium complexes are d^6, 18-electron complexes, which are remarkably stable in the ground state. However, upon absorption of photons of the appropriate energy, the complexes undergo excitation to produce an excited singlet state initially which rapidly relaxes via spin forbidden intersystem crossing to the long-lived triplet state which has undergone a metal-to-ligand charge transfer (MLCT) (Li *et al*., 2014) leading to remarkable photophysical and photochemical properties. Consequently, the complexes have found use in a number of applications in diverse fields including being utilized as photocatalysts in removal or addition of electrons and serving as photosensitizers (Dedeian *et al*., 2005; Singh *et al.,* 2015; Hofbeck and Yersin, 2010). The popularity of the molecules arises mainly from the relatively intense emissions (in terms of color and efficiency), which can be tuned by varying the electronic structures (utilization of functional groups bearing electron withdrawing and electron donating properties) of the ligands or combination of different ligands (Felici *et al.,* 2010). The Ir(III) complexes display high phosphorescence efficiencies and triplet quantum yields as a result of mixing of singlet and triplet excited states via SOC. Interpretation of the electronic spectra of Ir(III) complexes can be done using spin allowed d-d bands due to the small 10Dq values required to induce spin pairing. However the second d-d bands are usually masked by C-T transitions (Greenwood & Earnshaw, 1998).

The majority of Ir(III) complexes developed to date are based on C^N chelating ligands such as 2-phenylpyridine (ppy), which play a crucial role in modulating the energy of the emissive lowest-lying triplet excited states such as ^{3}MLCT and $^3\pi$–π^* (LC^3). By varying the electronic structure C^N ligand, the phosphorescence of the C^N-chelate Ir(III) complexes can be fine-tuned over the entire visible region (Bae *et al.,* 2013)**.**

2.9 Photoredox Catalytic Application of Ir(III) Complexes

Catalysis aims at developing novel methods of activating small molecules, with visible light, photoredox, catalysis being on the forefront. Photocatalysis is based on the premise that photonic energy is selectively targeted to a specific photon absorbing catalyst, a photocatalyst (PC), which after excitation induces an accompanying substrate to engage in chemical transformations that were otherwise inaccessible under thermal conditions. Typical modes by which a PC can convert

light to chemical energy and simultaneously participate in selective molecule activation include: i) energy transfer; ii) organometallic excitation; iii) light-induced atom transfer; and iv) photoredox catalysis (Shaw *et al.*, 2016). When selecting an appropriate PC, factors to consider include: i) PC stability under reaction conditions; ii) PC's ability to effectively absorb visible light and to give and sustain long-lived excited states for SET to occur; and iii) suitable ground- and excited state redox potentials that facilitate catalysis to proceed. In this regard, Ir(III) and Ru(II) compounds are commonly utilized due to their ability to form charge transfer excited states after absorbing visible light and have long lifetimes (Ochola & Wolf, 2016). Photoredox catalysis entails electron transfer processes initiated by absorption of a photon by a coordination metal complex or organic dyes leading to single electron transfer (SET) events. Scheme 5, with organic substrates (Prier *et al.*, 2013; Arias-Rotondo *et al.*, 2016). Polypyridyl complexes of ruthenium and iridium constitute the most commonly investigated visible light photocatalysts.

The key step is usually the absorption of a photon by photocatalyst in its ground state leading to an excited state, which then participates in a chemical reaction (Arias-Rotondo *et al.*, 2016). An excited electron is promoted from the photocatalyst's HOMO to its LUMO creating an intermediate excited state that can be viewed as charge-separated electron-hole pair. This intermediate can then engage in intermolecular conversions if they contain adequately long enough emission lifetimes, since the decay to singlet ground state is spin-forbidden, by either filling its partially occupied d-orbital from an electron-rich donor (**D**) or donating a high energy electron to an acceptor (**A**). These species are the reductive and oxidative quenchers respectively (Skubi *et al.*, 2016).

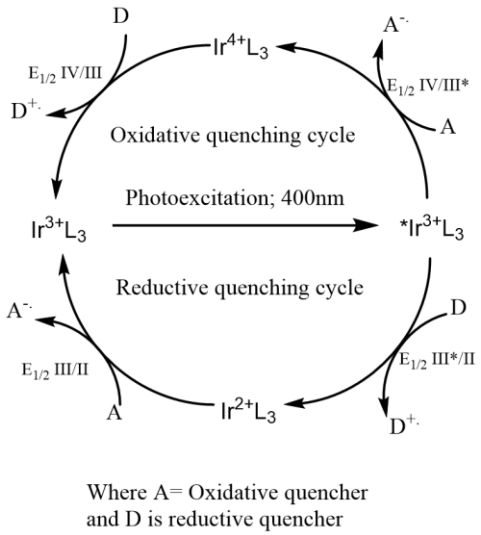

Scheme 5: Single Electron transfer (SET)

Source: Arias-Rotondo *et al*., 2016

The intermediate is both more oxidizing and more reducing than its corresponding ground state species and is said to have a dual nature hence redox transformations may proceed via either reductive or oxidative quenching (Scheme 5), to yield both strong reductant or strong oxidant respectively. Therefore, in photoredox catalysis, there is formal transfer of electrons with subsequent formation of reactive radical ions (reduced acceptor $\mathbf{A}^{\bullet-}$and oxidized donor $\mathbf{D}^{\bullet+}$) but only one radical is engaged in any particular transformation with subsequent introduction of a complementary redox equivalent species to initiate the second electron transfer event which is paramount for the regeneration of the active state (Skubi *et al.*, 2016).

Redox reactions are associated with radical reactions and traditional strategies such as electrolysis, photolysis and use of stoichiometric amounts of reductants or oxidants experience disadvantages such as: waste derived from oxidants and reductants; need for specialized equipment for both photochemical and electrochemical experiments. In the event that UV light is utilized in photo-initiating organic reactions the following disadvantages are observed: i) specialized UV reactors are of high cost and impose serious size constraints; ii) side products formed due to light absorption by the photo-products and other chromophores of reactants; iii) UV wavelengths for organic photochemistry are not abundant in the solar spectrum; and iv) they are not feasible on a large scale and have little impact on industry. Hence, the need for easy, mild, and safe to use protocols

that afford selective and efficient outputs is enormous and exploiting sunlight/visible light can easily solve this. As such, redox potentials of the photocatalyst and the organic reactants are vital in the design of the reaction. (Narayanam and Stephenson 2011; Shi and Xia 2012; Koike and Akita 2014a; Liu *et al.,* 2016).

When designing or choosing a suitable photocatalyst (PC), the factors to consider include: i) good absorption cross section such that the PC can absorb over a broad range of wavelengths that the other species present does not absorb at; ii) the quantum yield, i.e. the efficiency with which the reactive species is formed after photon irradiation, of the PC should be high since it affects the yield of the formed reactive excited state; iii) sufficient long lifetime of the PC so that the reactive excited state is able to persist as long enough to undergo the expected reaction with the substrate since lifetimes act as an intrinsic clock of that particular PC; iv) PC should exhibit reversible electrochemical potentials, there shouldn't be any photodegradation in the absence of a quencher; v) ground and excited state redox potentials must provide for an exothermic reaction especially if electron transfer events are to proceed; and vi) that the PC's excited-state properties should be easy to tune through synthetic modifications (Arias-Rotondo *et al*., 2016).

Photoredox catalysis heavily relies on the redox potentials of the ground-and excited-state hence cyclic voltammetry comes in handy in establishing these parameters. Reversibility is paramount and is defined by the difference between cathodic and anodic peak potentials and should be ca. 59mV for a 1e transfer event although in non-aqueous medium, the value observed is usually between 70-80mV. Values contrary to these imply that the system is either quasi-reversible or irreversible. Scheme 5 is a one-electron approximation that shows that the configuration of the excited state can be obtained through promoting an electron of an occupied orbital in the ground state to an empty orbital in the excited state. However, this approximation is insufficient in explaining the chemical nature of the excited state with regards to its potential reactivity, and this is better illustrated through potential energy surface diagrams, Figure 4, where the parabolic curves represent the electronic states shown in Scheme 5 bearing in mind electron-electron interactions and changes in equilibrium geometry. Hence relevant MLCT excited states shown are those pertinent to photoredox catalysis.

Steady state emission affects photocatalytic ability of a PC as well. In this case, visible light photon excites the PC into a short-lived singlet excited state (^{1}MLCT), which rapidly decays to a forbidden

triplet excited state (^{3}MLCT) through intersystem crossing. Emission maxima are used as first-order approximations of the energy difference between the ^{3}MLCT and ground state, E_0, which is associated with highest energy vibrational component of a spectrum at 77K. As mentioned, the redox activity depends on the redox potentials of both ground- and excited states. However, excited state potentials cannot be measured directly, rather, they are calculated using the energies of the excited states and ground state redox potentials.

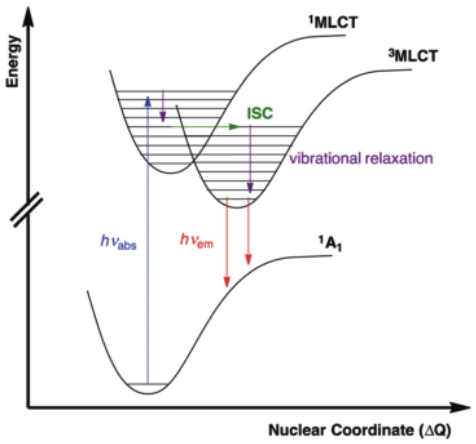

Figure 4: Simplified Potential Energy Surface Diagram

Source: Arias-Rotondo *et al*., 2016

The redox properties of polypyridyl metal complexes can be tuned by altering the ligands attached to the metal center. Generally, electron-withdrawing substituents on ligands make them easier to reduce while the metal becomes harder to oxidize. In contrast, with electron-donating substituents its harder to reduce the ligands and easier to oxidize the metal center. Comparison between Ru(II) and the less electron rich Ir(III) makes the latter harder to oxidize (e.g., $[Ru(bpy)_3]^{2+}$ versus $[Ir(bpy)_3]^{3+}$) while the bpy ligand becomes easily oxidizable (Arias-Rotondo *et al*., 2016).

2.9.1 Methoxytrifluoromethylation of alkenes

This is an example of a critical chemical transformation that allows selective difunctionalization of alkenes using visible-light-driven single electron transfer. Halofunctionalization of alkenes enables the rapid buildup of complex molecules starting from simple alkenes and facilitates a platform for further functionalization and elaboration (Griffin *et al.*, 2017). Organofluorine

compounds are increasingly vital in agrochemical, material sciences as well as in pharmaceutical fields. Particularly, the trifluoromethyl (CF_3) group is known to influence chemical and metabolic stability, polarity, membrane permeability, lipophilicity and binding selectivity in biologically active molecules. Hence new methodologies for highly efficient and selective insertion of CF_3 group into diverse skeletal structures have become popular among synthetic chemists (Yasu *et al.*, 2012; Ochola & Wolf, 2016). Trifluoromethylation can be classified into three modes; electrophilic, nucleophilic and radical which can be achieved using either Umemoto's reagent (S-(trifluoromethyl)dibenzothiophenium tetrafluoroborate), for electrophilic and radical transformations, or Togni's reagent (1-trifluoromethyl-1,2-benziodoxol-3-(1H)-one) as precursors to the CF_3 in presence of suitable photoredox catalysts. Selective difunctionalization of alkenes is a powerful chemical transformation yet only a limited number of reports involving trifluoromethylation have been published. Additionally, while trifluoromethylation of aromatic compounds has been extensively researched and effective methodologies established, the trifluoromethylation of alkenes is still at infancy (Yasu *et al.*, 2012). Studies have demonstrated that slight differences in structure of PCs have considerable effect on SET between the PC and substrates such as CF_3SO_2Cl but don't affect the rate of final product formation significantly (Ochola & Wolf, 2016).

2.9.2 Photodegradation of Morin

Morin (2′, 3,4′, 5,7-pentahydroxyflavone) is a non-toxic flavonoid polyphenolic dye, mainly present in tea, fruits and vegetables and ideal for studying catalytic processes in laundry detergents (Wieprecht *et al.*, 2004; Nemanashi and Meijboom 2015). Typically, the catalytic degradation/oxidation catalysis of Morin and related dyes has been studied under heterogeneous conditions using manganese oxide nanoparticle (NP) catalysts with H_2O_2 as the oxidant or Au NPs as a model reaction. The oxidative degradation of Morin can be studied by monitoring the maximum absorbance of Morin via time resolved UV-Vis spectroscopy. The maximum absorbance λ_{max} ideally observed at ca. 410nm at pH 10 should decrease with time. Isosbestic points obtained from the time-resolved spectra are an indication of oxidation of Morin to yield one product and no side products. Studies have reported the disappearance of these isosbestic which is attributable to an initiation of a secondary reaction where by the substituted benzofuranone

decomposes to 2,4-dihydroxybenzoic acid and 2,4,6-trihydroxybenzoic acid (Nemanashi & Meijboom, 2015).

2.9.3 Photooxidation of Alcohols

Photooxidation of alcohols using visible light potentially allows simple, selective and environmentally benign access to valuable carbonyls groups such as aldehydes and ketones, which are key in the manufacture of fine chemicals and intermediates under mild green conditions. Previous studies have utilized iridium and ruthenium phenyl pyridine complexes using molecular oxygen as an oxidant while others have utilized metal free conditions under visible light to achieve the desired transformations (Rueping *et al.*, 2012; Samanta & Biswas, 2015).

2.10 Selective Hydrogenation of 2-Furaldehyde to Furanmethanol and Tetrahydro-2-furanmethanol

Selective reduction of aldehydes to corresponding alcohols is vital since it furnishes compounds that are of economic value. In particular, furfural can be selectively hydrogenated to tetrahydro-2-furanmethanol, which is expensive to manufacture but has potential for use in production of fine chemicals.

2.10.1 2-Furaldehyde (Furfural)

2-Furaldehyde is produced from agricultural waste biomass that contain pentoses, which are aldose sugars, composed of small rings formed from short five-member chains, that constitute a class of complex carbohydrates, present in cellulose of many woody plants such as corn cobs, sugar cane bagasse, rice and oat hulls etc. Furfural is among the organic compounds derived from biomass that can replace the crude oil-based organics used in industry. Furfural is a clear, colorless liquid with a characteristic ‘almondbenzaldehyde’ odor (Brady *et al.,* 2000; Win, 2005).

Furfural is used in production of lubricating oils, specialist adhesives and plastics, and as solvent in fungicide and weed killer. It is used in the production of furfuryl alcohol, tetra hydro furfuryl alcohol (THFA), acetyl furane, methyl furane, furoic acid and tetrahydrofuran (THF), an important industrial solvent. Furfural and hydroxymethylfurfural (HMF) can serve as a building block for

other potential transportation fuels including dimethylfuran and ethyl levulinate (Win, 2005). The pathways for production of THFA and other products are shown in Scheme 6.

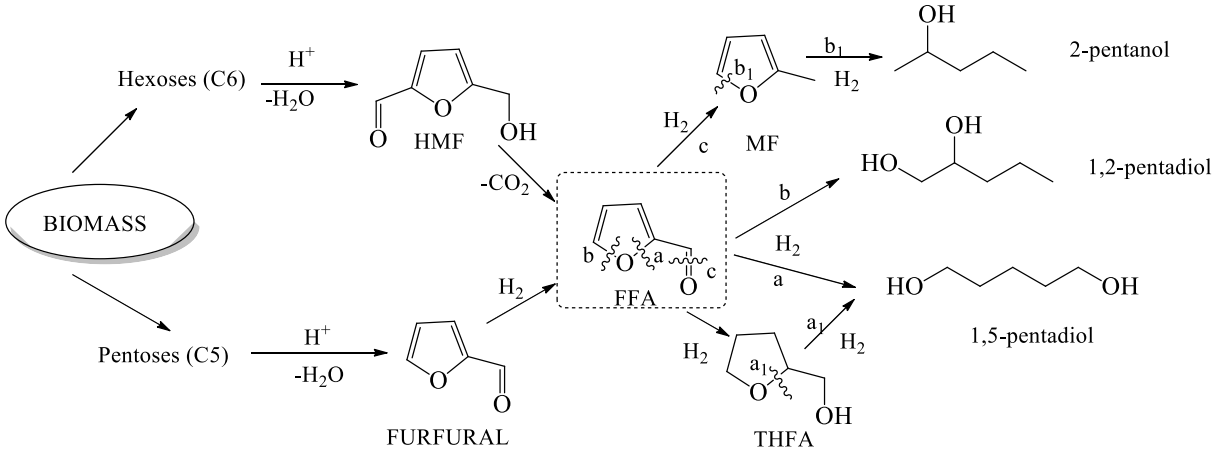

Scheme 6: Pathways for production of THFA and Diols from biomass

Hydrogenation of furfural has drawn a lot of interest since it leads to production of THFA, which has an extensive use as highly versatile, high purity solvent, as a chemical intermediate and due to its relatively benign nature and the fact that it's not oil-based, it is regarded as a green solvent in industrial applications.

The use of heterogeneous catalysts for the synthesis of fine chemicals has become popular. Hydrogenation reactions of α, β unsaturated aldehydes to produce unsaturated alcohols are of particular importance and involves the selective catalytic hydrogenation of carbonyl groups in the presence of olefin groups in a molecule which also contains C=C bond conjugated with the C=O bond which appears as a difficult task, since almost all metal catalysts usually give saturated compounds as main products (Reyes *et al.*, 2010). The aim is to hydrogenate the carbonyl group, keeping intact the olefinic function, in spite of the C=C double bond being easily hydrogenated over most conventional catalysts to give saturated aldehydes as the primary products (Rojas, 2010).

Various attempts have been carried out in order to improve the selectivity of heterogeneous supported metal catalysts in these reactions. Different metals and supports have been used to study the selective hydrogenation of unsaturated compounds. Thus, metals such as Ru, Rh, Co, Pt, Os and Ir have been studied, showing great differences in activity and selectivity. Metal supported catalysts have been modified by alloying, by adding promoters, by using strong metal-support

interaction and by inducing electronic effects. Despite the number of investigations in this field, there is not an agreement on the nature of the effect, which may have a more significant impact on the selectivity towards the unsaturated alcohol. Usually, the hydrogenation of furfural is done using copper chromite as catalyst. However, the toxicity and moderate activity of this catalyst has motivated the study of other alternative catalysts able to overcome the mentioned difficulties. Thus, different catalysts, such as, copper supported on activated carbon, Raney Ni, amorphous Ni alloys, Cu-Zn mixed oxides with Al, Mn and Fe, Cu-MgO and Pt dispersed on different supports have been used in the hydrogenation of furfural (Reyes *et al.*, 2010). Previous studies have shown that in the case of furfural hydrogenation, the best results (97 % yield, 100 % conversion, 98 % selectivity) were obtained in the presence of Ni and Cu. However, this catalytic mixture could not be recycled. In the case of furfuryl alcohol hydrogenation, there is need to continue searching for better and efficient systems to catalyze this reaction.

2.10.2 Tetrahydro-2-furanmethanol; Tetrahydrofurfuryl alcohol (THFA)

THFA is one of the promising compounds obtained by the hydrogenation of furfural and an important building block in the synthesis of polyols. Polyols, especially diols, have direct use as monomers in the polyester industry (Chatterjee, 2011).

The hydrogenation of furfuryl alcohol (FA) to give tetrahydrofurfuryl alcohol (THFA) is of great importance, since it's used as raw material for fine chemical synthesis and widely used as organic solvent in the production of paint and resins (Song, 2007), but little information is available in this regard. Studies show that nickel-based catalysts (alloys or Raney-nickel, promoted or supported) are used for this reaction because of high conversion of FA and high selectivity and yields of THFA but, drastic pressure and temperature conditions are required. Therefore, nobel metals (Ir, Pd, Pt and Rh) supported catalysts have been reported to be highly active in hydrogenation reactions under favorable conditions (Song, 2007; Vetere, 2010).

CHAPTER THREE

MATERIALS AND METHODS

3.1 Experimental section

All reactions and manipulations were carried out under standard inert atmosphere using Schlenk, high vacuum line or glove-box techniques. Solvents were dried by standard procedures. All reagents used were of analytical grade, purity >99%, and were obtained from commercial suppliers (Sigma-Aldrich, Alfa Aesar, Across, Strem and VWR).

Weighing for solid samples was done on a Sartorius TE 2145 analytical balance while for liquid samples graduated needles and pipettes were used. Purification was done using flash chromatography or preparative thin layer chromatography (TLC) on silica gel or silica gel 60 (F_{254}) plates. Percentage yield was calculated based on limiting reagents.

3.1.1 Instrumentation

The melting points for the complexes were determined using a Gallenkamp melting point apparatus, center of analysis and synthesis, Lund University, Sweden

High resolution mass spectrometer spectral data was obtained from Micromass Q-TOF spectrophotometer operated either in electrospray ionization (ESI) mode or for some other complexes, atmospheric pressure chemical ionization (APCI) mode constituting a needle with 5.0kV voltage, a heated capillary temperature of 150^{o}C, and sheath flow N_2 gas set at 25 arbitrary units. The syringe pump was operated at a flow rate between 3-5µl/min. Data was analyzed using Masslynx software.

NMR analyses for the ligands and complexes were done using deuterated CD_2Cl_2, $C_2D_2Cl_4$ and $CDCl_3$. ^{1}H NMR was performed using a Bruker Avance 400 FT-NMR operating at 400.1 MHz (1H), while ^{13}C and 2D COSY NMR was performed using a Bruker 500MHz NMR operating at 499.76 MHz for ^{1}H and 125.64 MHz for ^{13}C NMR spectroscopy. Multiplicities were abbreviated as follows: (s) singlet, (d) doublet, (t) triplet, (q) quartet and (m) multiplet.

UV-VIS and photoluminescence measurements were done on Varian Cary 100 Bio UV-VIS spectrophotometer and Varian Cary Eclipse fluorescence spectrophotometer, respectively. Quantum yields and emission lifetimes were measured using home-built epifluorescence microscope setup connected to CCD camera to measure luminescence intensity and to a time-correlated single photon counting (TCSPC, Picoharp 300, Picoquant) system.

Electrochemical measurements via cyclic voltammetry were made with EG&G Princeton Applied Research model 173 potentiostat−galvanostat equipped with a Sefram TGM 164 X-Y recorder. The measurements were performed using a glassy-carbon electrode as working electrode, with silver/silver chloride electrode as reference electrode and a platinum electrode as the counter electrode.

Mikroanalytisches Laboratorium KOLBE(Nachf.), Mülheim an der Ruhr, company in Germany was used to determine the carbon, hydrogen, nitrogen and fluorine content for the iridium complexes.

Single crystals were analyzed using X-ray Crystallography. Intensity data were collected with an Oxford Diffraction Excalibur 3 system, using ω-scans and Mo-Kα radiation (λ = 0.71073 Å). The data were extracted and integrated using Crysalis RED.

3.1.2 Reagents Preparations

In all cases, dry solvents used were obtained from dry solvent dispenser SPS system, MBraun7656 and used without any further manipulations.

Preparation of supporting electrolyte for CV measurements, 0.1M Tetra- (n-butyl)-ammonium hexafluorophosphate, nBu$_4$NPF$_6$, was done by weighing 9.69 g nBu$_4$NPF$_6$ and dissolving in CH_2Cl_2 in a 250 cm^3 volumetric flask.

For the photobleaching studies**,** a stock solution of 2 mM morin was freshly prepared for every catalytic run by weighing 0.00604 g of sigma morin and dissolving it in a carbonate buffer solution in a 10 cm^3 volumetric flask. From this, utilizing the equation $C_1V_1 = C_2V_2$, 0.1 mM solution were made hence 0.5 cm^3 of the stock solution was diluted further using carbonate buffer solution diluting to the mark in a 10 cm^3 volumetric flask. The carbonate buffer solution used for the studies was made by first diluting 0.2 M $NaHCO_3$, by weighing 1.68 g in 100 cm^3 H_2O and of 0.2 M

Na_2CO_3 by weighing 2.12 g in 100 cm^3 H_2O. This was followed by mixing 22.5 cm^3 of 0.2 M $NaHCO_3$ and 27.5 cm^3 of 0.2 M Na_2CO_3 at pH 10 and diluted to the mark using deionized water in a 200 cm^3 volumetric flask. Further, 100 mM H_2O_2 stock solution was made from 30% w/w H_2O_2 (30% w/w implies 30g H_2O_2 per 100 g solution meaning the concentration was 9.79 M). Hence using $C_1V_1 = C_2V_2$, 1.02 cm^3 of H_2O_2 (30%) was pipetted using a micropipette into 100 cm^3 deionized water to make 100 mM H_2O_2 stock solution. From this, 10 mM of the H_2O_2 was made by pipetting 1 cm^3 into 10 cm^3 volumetric flask and diluting to the mark with deionized water and this was subsequently used for the photobleaching reactions where necessary.

3.2 Synthesis of the Ligands

The synthesis protocols for the ligands (L_1-L_{10}) are summarized in Scheme 7. The cyclometalating ligands were synthesized via Suzuki-Miyaura cross-coupling protocol (Miyaura & Suzuki, 1995), which involves reaction of an aryl halide with aryl boronic acid for L_1-L_6 and 1-chloroisoquinoline and the appropriate phenylboronic acid for L_7-L_{10} in weak base, catalyzed by soluble palladium (0) complexes in organic solvents, in a homogeneous catalytic cycle (Tian et al., 2011). Characterization was done using MS, ^{1}H- and ^{13}C-NMR spectroscopy.

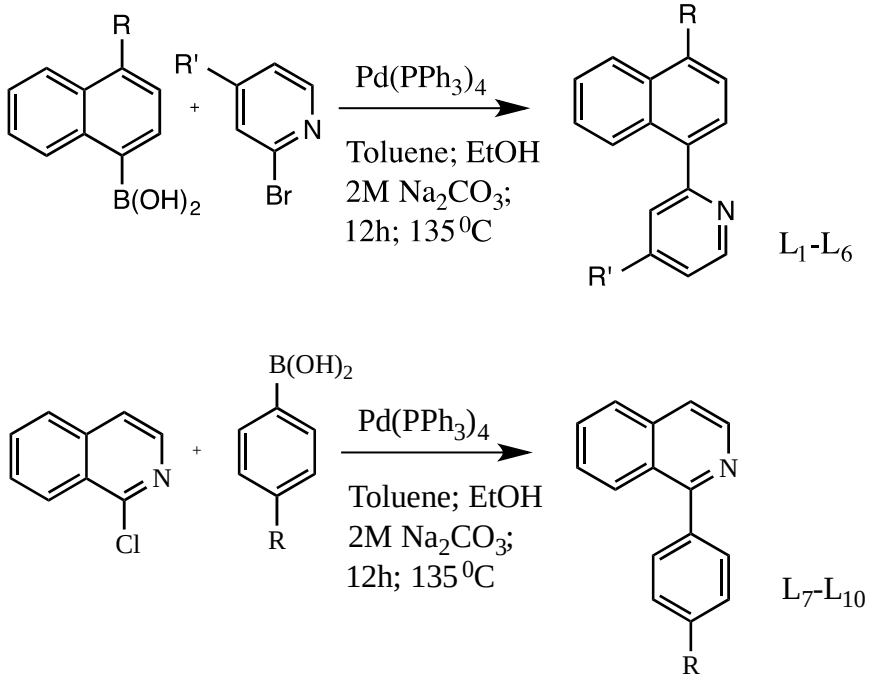

Scheme 7: Ligand Synthesis

3.2.1 Synthesis of 2-(1-Naphthyl) Pyridine (L_1)

Naphthalene-1-boronic acid (1.582 g, 9.2 mmol) and tetrakis(triphenylphosphine) palladium (0) (0.392 g, 4 mol%) were weighed and placed in a two-neck round bottomed flask. 30 cm^3 toluene was added while stirring the mixture at room temperature under nitrogen. 2-Bromopyridine (1.244 g, 7.9 mmol), 20 ml 2 M Na_2CO_3 and 10 cm^3 ethanol were added one after the other. The two main reagents naphthalene-1-boronic and 2-bromopyridine were weighed to make 1.1 and 1 equivalent respectively, such that the latter was limiting reagent. The solution was heated to reflux while stirring for 12 h at 135 $^{\circ}$C under inert conditions. The mixture was cooled to room temperature and extracted three times using 20 cm^3 ethyl acetate and the organic fraction dried over anhydrous $MgSO_4$, filtered through a pad of silica and concentrated using a rotary evaporator. TLC confirmed the product under UV lamp and the residue was purified using flash chromatography on silica gel with a solvent system of ethyl acetate: hexane (1:3) after which the appropriate portions collected, dried under vacuum, to give the product. Yield was determined and product confirmed using NMR spectroscopy and MS.

3.2.2 Synthesis of 2-(1-Naphthyl)-4-methoxy Pyridine (L_2)

4-methoxybenzene boronic acid (0.511 g, 3.4 mmol) and tetrakis(triphenylphosphine) palladium (0) (0.141 g, 4 mol%) were weighed and stirred in 30 cm^3 toluene at room temperature under nitrogen. 1-Isoquinoline (0.5 g, 3.1 mmol) together with 20 cm^3 2 M $Na_2CO_3$and 10 cm^3 ethanol were added one after the other. The solution was heated under N_2 to reflux while stirring for 12 h at 135 $^{\circ}$C. The mixture was cooled to room temperature, extracted three times using 20 ml ethyl acetate, the organic fraction dried over anhydrous $MgSO_4$, filtered through a pad of silica and concentrated using a rotary evaporator. The residue was purified using flash chromatography on silica gel with a solvent system of ethyl acetate: hexane in a ratio of 1:3. TLC confirmed the product under UV lamp and appropriate portions collected, dried under vacuum, to give the product. Yield was determined, and product confirmed by NMR spectroscopy and MS.

3.2.3 Synthesis of 2-(1-Naphthyl)-4-trifluoromethyl Pyridine (L_3)

The third ligand followed a similar procedure for preparation and purification where naphthalene-1-boronic acid (0.5 g, 2.9 mmol), 2-bromo-4-trifluoromethyl pyridine (0.597 g, 2.6 mmol) and tetrakis (triphenylphosphine) palladium (0) (0.122 g, 4 mol%) were weighed and mixed with 30 ml toluene, 20 ml 2 M $Na_2CO_3$and 10 ml ethanol and the mixture refluxed under N_2 for 12 h. The product was confirmed using TLC under UV lamp and appropriate portions collected, dried under vacuum to give the product. Yield was determined, and product was confirmed using NMR spectroscopy and MS.

3.2.4 Synthesis of 2-(1-Naphthyl)-4-methyl Pyridine (L_4)

Naphthalene-1-boronic acid (0.500 g, 2.9 mmol), tetrakis (triphenylphosphine) palladium (0) (0.1225mg, 4 mol%) and 2-bromo-4-methyl pyridine (0.455 g, 2.6 mmol) were weighed and mixed in 30 cm^3 toluene, 20 cm^3 2 M $Na_2CO_3$and 10 cm^3 ethanol. The solution was refluxed under N_2 with stirring for 12 h at 135 $^{\circ}$C. Extraction and purification were done in a similar way as preceding ligands. Product was collected, dried under vacuum, to give the product. Yield was determined and product confirmed using NMR spectroscopy and MS.

3.2.5 Synthesis of 2-(4-methylnaphthyl)-4-methyl Pyridine (L_5)

4-methylnaphthalene-1-boronic acid (0.500 g, 2.7 mmol), tetrakis (triphenylphosphine) palladium (0) (0.113 g, 4 mol%) and 2-bromo-4-methyl pyridine (0.420 g, 2.6 mmol) were weighed and stirred in 30cm^3 toluene, 20 cm^3 2M Na_2CO_3 and 10 cm^3 ethanol. The solution was refluxed under N_2 with stirring for 12 h at 135 $^{\circ}$C. Extraction and purification were done in a similar way as preceding ligands. The product was collected, dried under vacuum, to give the product. Yield was determined and product confirmed using NMR spectroscopy and MS.

3.2.6 Synthesis of 2-(4-methylnaphthyl) Pyridine (L_6)

4-methylnaphthalene-1-boronic acid (0.500 g, 2.7 mmol), tetrakis (triphenylphosphine) palladium (0) (0.113 g, 4 mol%) and 2-bromopyridine (0.386 g, 2.4 mmol) were weighed into a two-neck flask and the solution was refluxed under N_2 with stirring for 12 h at 135 $^{\circ}$C. Extraction and purification were done in a similar way as preceding ligands. The product was collected, dried

under vacuum, to give the product. Yield was determined and product confirmed using ^{1}H NMR spectroscopy and MS.

3.2.7 Synthesis 4-fluoro-1-phenyl isoquinoline (L_7)

4-fluorophenylboronic acid (0.25 g, 1.787 mmol), tetrakis (triphenylphosphine) palladium (0) (0.192 g, 0.166 mmol) and 1-chloroisoquinoline (0.209 g, 1.276 mmol) were weighed and stirred in 30 cm^3 toluene, 20 cm^3 2 M Na_2CO_3 and 10 cm^3 ethanol. The solution was refluxed under N_2 with stirring for 12 h at 135 $^{\circ}$C. Extraction and purification were done in a similar way as preceding npy-based ligands. The product was collected, dried under vacuum, to give the product Yield was determined and product confirmed using NMR spectroscopy and MS.

3.2.8 Synthesis 1-phenyl-4-(trifluoromethyl) isoquinoline (L_8)

4-(trifluoromethyl) phenyl boronic acid (0.300 g, 1.58 mmol), tetrakis (triphenylphosphine) palladium (0) (0.173 g, 0.15 mmol) and 1-chloroisoquinoline (0.185 g, 1.128 mmol) were weighed and stirred in 30 cm^3 toluene, 20 cm^3 2 M Na_2CO_3 and 10 cm^3 ethanol. The solution was refluxed under N_2 with stirring for 12 h at 135 $^{\circ}$C. Extraction and purification were done in a similar way as preceding ligands. The product was collected, dried under vacuum, give the product. Yield was determined and product confirmed using NMR spectroscopy and MS.

3.2.9 Synthesis 4-*tert*-butyl-1-phenyl isoquinoline (L_9)

4-*tert*-butyl phenylboronic acid (0.178 g, 3.362 mmol), tetrakis (triphenylphosphine) palladium (0) (0.141 g, 0.122 mmol) and 1-chloroisoquinoline (0.5 g, 3.1 mmol) were weighed and stirred in 30 cm^3 toluene, 20 cm^3 2 M Na_2CO_3 and 10 cm^3 ethanol. The solution was refluxed under N_2 with stirring for 12 h at 135 $^{\circ}$C. The product was collected, dried under vacuum, to give the product. Yield was determined and product confirmed using NMR spectroscopy and MS.

3.2.10 Synthesis 4-methyl-1-phenyl isoquinoline (L_{10})

4-p-tolylphenyl boronic acid (0.46 g, 3.36 mmol), tetrakis (triphenylphosphine) palladium (0) (0.141 g, 0.122 mmol) and 1-chloroisoquinoline (0.5 g, 3.1 mmol) were weighed and stirred in 30 cm^3 toluene, 20 cm^3 2 M Na_2CO_3 and 10 cm^3 ethanol. The solution was refluxed under N_2 with

stirring for 12 h at 135 °C. The product was collected, dried under vacuum, to give the product. Yield was determined and product confirmed using NMR spectroscopy and MS.

3.3 Characterization of Ligands

3.3.1 Yield determination

Prior to yield determination, for all ligands, the product was dried under vacuum for 12 h then the actual weight determined by getting the mass of the empty vial and subtracting it from the mass of vial and product. The percent yield was then calculated using the formula:

% Yield = (actual yield / theoretical yield) X 100 %

Where, theoretical yield = moles of limiting reagent X Molecular weight of product.

3.3.2 Solubility Tests

Solubility test for all the ligands was done by weighing ca. 1 mg of samples into series of test tubes each containing 2 cm^3 of solvent such as dichloromethane, trichloromethane, acetonitrile, diethyl ether and dimethyl sulfoxide etc. The mixture was shaken in the solvent or in some cases gently heated in an oil bath in consideration of the boiling point of the solvent used or sonicated.

3.3.3 UV/Vis spectroscopy

10 μM samples of select ligands were prepared in CH_2Cl_2 and measured between the ranges of 200 to 800 nm. The excitation wavelength was 200 nm and emission set between 250-600 nm. Calibration was done with a blank sample in 1 cm path length quartz cell before scanning the samples.

3.3.4 Mass spectroscopy

Mass spectra were obtained from Q-TOF Micromass spectrometer operated under ESI mode whose needle voltage was 5.0kV, and capillary temperature of 150 °C. 0.5 cm^3 of sample prepared in chloroform was analyzed and Masslynx software used to analyze data.

3.3.5 Proton (^{1}H) NMR spectroscopy

1mg of sample was dissolved in 0.5 cm^3 of deuterated solvent and transferred into an NMR tube. NMR spectra were obtained and analyzed using Mnova software. ^{1}H chemical shifts (δ) were reported in parts per million (ppm) relative to the residual solvent peak and referenced against trimethyl silane (TMS). Deuterated chloroform, $CDCl_3$ was used.

3.3.6 Carbon (^{13}C) NMR spectroscopy

^{13}C NMR spectra were obtained and analyzed using Mnova software. The chemical shifts were reported in ppm relative to the residual solvent peak and referenced against trimethyl silane Deuterated chloroform was used.

3.4 Synthesis of Homoleptic Iridium (III) Complexes

The tris homoleptic iridium complexes were synthesized in a one-step using a modified cyclometalating procedure (Singh *et al*., 2015), to yield 10 complexes (C-L_1 to C-L_{10}) corresponding to the respective ligands. The modifications involved using a Strauss flask and heating H_2O to 205 ^oC while in literature Parr reactor was used to heat H_2O to 260 ^oC. General procedure is shown in Scheme 8 for 2-(1-naphthyl) pyridine ligand to yield C-L_1 to C-L_6 and Scheme 9 for 1-phenyl isoquinoline ligand for C-L_7 to C-L_{10}. These complexes were characterized by NMR, MS, elemental analysis, and in the case of C1, X-ray diffraction. Photophysical and electrochemical studies were done using UV-VIS, Photoluminescence (PL), emission lifetimes, quantum yields and cyclic voltammograms (CV).

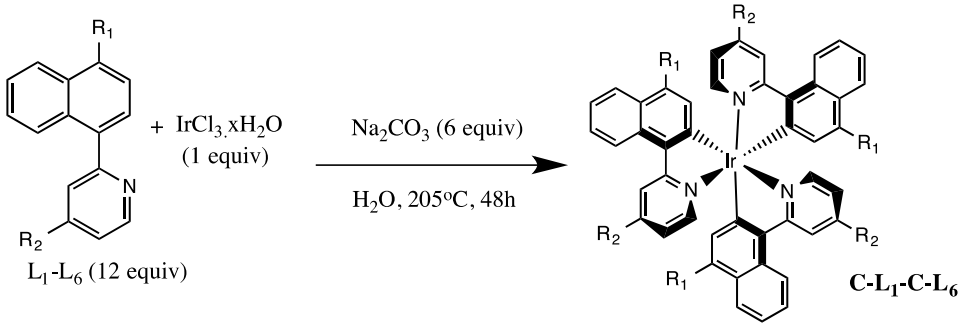

Scheme 8: Cyclometalation; Chemical Structures of C-L_1-C-L_6

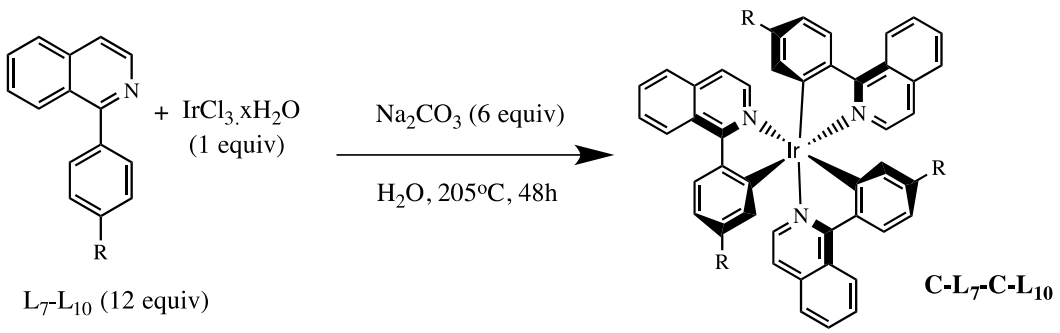

Scheme 9: Cyclometalation; Chemical Structures of C-L_7-C-L_{10}

3.4.1 Synthesis of *tris* 2-(1-naphthyl) pyridyl iridium using 2-(1-naphthyl) pyridine (C-L_1)

2-(1-naphthyl) pyridine (0.329 g, 1.6 mmol) and Na_2CO_3 (0.0846 g, 0.8 mmol) were weighed and mixed in a Strauss flask, which was evacuated on high vacuum line and filled with argon. This was taken to the glove box where iridium (III) chloride hydrate (0.0398 g, 0.133 mmol) was weighed and added. The reagents were 12, 6 and 1 equivalent respectively. 60 cm^3 deionized water, which had been degassed by bubbling N_2 for 2 hours, was transferred into the flask through canula using Schlenk techniques. The mixture was then refluxed under N_2 while stirring at 205 $^{\circ}$C for 48 h. After cooling to room temperature, the mixture was extracted three times with 20 cm^3 CH_2Cl_2. The organic phase was filtered through a pad of Celite and concentrated to give a crude product. Purification was done by flash chromatography through dry loading (where the crude compound is mixed with silica gel and packed into the column) due to poor solubility of the crude product. Two solvent systems were used, first a mixture of ethyl acetate: hexane in a 3:1 ratio was used to isolate the ligand, then the solvent system was then changed to 100 % CH_2Cl_2 to isolate the complex. A red crystalline product was obtained after concentration. The yield was determined, and the product confirmed using NMR and crystals subsequently grown for further analysis. Characterization for the complex was done using ^1H, ^{13}C, and 2D COSY NMR spectroscopy, HRMS, crystallography and elemental analyses.

3.4.2 Synthesis of *tris* 2-(1-naphthyl)-4-methoxy pyridyl iridium using 2-(1-naphthyl)-4-methoxy pyridine (C-L_2)

Tris 2-(1-naphthyl)-4-methoxy pyridyl iridium was prepared by first weighing 2-(1-naphthyl)-4-methoxy pyridine (0.35 g, 1.488 mmol) and Na_2CO_3 (0.079 g, 0.744 mmol) into a Strauss flask

and putting them under inert atmosphere then adding $IrCl_3.xH_2O$ (0.037 g, 0.124 mmol) inside the glove box. 60 $cm^3$of N_2 saturated deionized water was transferred into the flask using Schlenk line and the mixture refluxed for 48 h at 205 ˚C. Upon cooling, the mixture was extracted thrice using 20 cm^3 CH_2Cl_2, the organic phase filtered through a pad of Celite, and concentrated. The residue was then purified using preparative Thin Layer Chromatography (prep TLC) plates with UV254 organic indicator, using CH_2Cl_2 to yield red solid. The red layer was collected, dried, weighed and NMR done to confirm and check purity of the yield. Characterization for the complex was done using ^1H, ^{13}C and 2D COSY NMR spectroscopy, HRMS and elemental analyses.

3.4.3 Synthesis of *tris* 2-(1-naphthyl)-4-trifluoromethyl pyridyl iridium using 2-(1-naphthyl)-4-trifluoromethyl pyridine (C-L_3)

Tris 2-(1-naphthyl)-4-trifluoromethyl pyridyl iridium was prepared in a similar procedure as in section 3.4.1. $IrCl_3.xH_2O$ (0.032 g, 0.107 mmol), 2-(1-naphthyl)-4-trifluoromethyl pyridine (0.35 g, 1.28 mmol) and Na_2CO_3 (0.068 g, 0.64 mmol) were weighed and mixed in 60 cm^3 of N_2 saturated deionized water and refluxed for 48 h. Purification was done using preparative TLC plates with UV254 organic indicator in CH_2Cl_2. Characterization for the complex was done using ^1H, ^{13}C, and 2D COSY NMR spectroscopy, HRMS and elemental analyses.

3.4.4 Synthesis of *tris* 2-(1-naphthyl)-4-methyl pyridyl iridium using 2-(1-naphthyl)-4-methyl pyridine (C-L_4)

Tris 2-(1-naphthyl)-4-methyl pyridyl iridium was synthesized by weighing $IrCl_3.xH_2O$ (0.04 g, 0.133 mmol), followed by of 2-(1-naphthyl)-4-methyl pyridine (0.35 g, 1.6 mmol) and Na_2CO_3 (0.085 g, 0.8 mmol) in 60 $cm^3$of N_2 saturated deionized water and reaction, workup and purification carried out using similar procedure as in section 3.4.3 to yield red solid. Characterization for the complex was done using ^1H, ^{13}C, and 2D COSY NMR spectroscopy, HRMS and elemental analyses.

3.4.5 Synthesis of *tris* 2-(4-methylnaphthyl)-4-methyl pyridyl iridium using 2-(4-methylnaphthyl)-4-methyl Pyridine (C-L_5)

Tris 2-(4-methylnaphthyl)-4-methyl pyridyl iridium was synthesized by weighing$IrCl_3.xH_2O$ (0.0373 g, 0.125 mmol), 2-(4-methylnaphthyl)-4-methyl pyridine (0.35 g, 1.5 mmol), and Na_2CO_3

(0.08 g, 0.75 mmol) in 60 cm^3 of N_2 saturated deionized water and reaction, workup and purification carried out using similar procedure as in section 3.4.3 to yield red solid. Characterization for the complex was done using ^1H, ^{13}C, and 2D COSY NMR spectroscopy, HRMS and elemental analyses.

3.4.6 Synthesis of *tris* 2-(4-methylnaphthyl) pyridyl iridium using 2-(4-methylnaphthyl) pyridine (C-L_6)

Tris 2-(4-methylnaphthyl) pyridyl iridium was synthesized by weighing and mixing $IrCl_3.xH_2O$ (0.040 g, 0.133 mmol), 2-(4-methylnaphthyl) pyridine (0.350 g, 1.6 mmol), and Na_2CO_3 (0.085 g, 0.8 mmol) in 60 cm^3 of N_2 saturated deionized water and reaction, workup and purification carried out using similar procedure as in section 3.4.3 to yield red solid. Characterization for the complex was done using ^1H, ^{13}C, and 2D COSY NMR spectroscopy, HRMS and elemental analyses.

3.4.7 Synthesis of *tris* 4-fluoro-1-phenyl isoquinoline iridium using 4-fluoro-1-phenyl isoquinoline (C-L_7)

Tris 4-fluoro-1-phenyl isoquinoline iridium was synthesized by weighing $IrCl_3.xH_2O$ (0.025 g, 0.085 mmol), 4-fluoro-1-phenyl isoquinoline (0.228 g, 1.02 mmol), and Na_2CO_3 (0.054 g, 0.51 mmol) in 60 cm^3 of N_2 saturated deionized water and reaction, workup and purification carried out using similar procedure as in section 3.4.3 to yield red solid. Characterization for the complex was done using ^1H, ^{13}C, and 2D COSY NMR spectroscopy, HRMS and elemental analyses.

3.4.8 Synthesis of *tris* 4-trifluoromethyl-1-phenylisoquinoline iridium using 1-phenyl-4-(trifluoromethyl) isoquinoline (C-L_8)

Tris 4-trifluoromethyl-1-phenylisoquinoline iridium was synthesized by weighing $IrCl_3.xH_2O$ (0.0273 g, 0.092 mmol), followed by of 1-phenyl-4-(trifluoromethyl) isoquinoline (0.30 g, 1.1 mmol) and Na_2CO_3 (0.058 g,0.55 mmol) in 60 cm^3 of N_2 saturated deionized water and reaction, workup and purification carried out using similar procedure as in section 3.4.3 to yield red solid. Characterization for the complex was done using ^1H, ^{13}C NMR spectroscopy, HRMS and elemental analyses.

3.4.9 Synthesis of *tris* 4-tert-butyl-1-phenyl isoquinoline iridium using 4-tert-butyl-1-phenyl isoquinoline (C-L_9)

Tris 4-tert-butyl-1-phenyl isoquinoline iridium was synthesized by weighing $IrCl_3.xH_2O$ (0.033 g, 0.112 mmol), followed by of 4-tert-butyl-1-phenyl isoquinoline (0.35 g, 1.34 mmol) and Na_2CO_3 (0.071 g, 0.67 mmol) in 60 cm^3 of N_2 saturated deionized water and reaction, workup and purification carried out using similar procedure as in section 3.4.3 to yield red solid Characterization for the complex was done using ^1H, ^{13}C NMR spectroscopy, HRMS and elemental analyses.

3.4.10 Synthesis of *tris* 4-methyl-1-phenyl isoquinoline iridium using 4-methyl-1-phenyl isoquinoline (C-L_{10})

Tris 4-methyl-1-phenyl isoquinoline iridium was synthesized by weighing $IrCl_3.xH_2O$ (0.040 g, 0.133 mmol), followed by of 4-methyl-1-phenyl isoquinoline (0.35 g, 1.6 mmol) and Na_2CO_3 (0.085 g, 0.80 mmol) in 60 cm^3 of N_2 saturated deionized water and reaction, workup and purification carried out using similar procedure as in section 3.4.3 to yield red solid. Characterization for the complex was done using ^1H, ^{13}C NMR spectroscopy, HRMS and elemental analyses.

3.5 Characterization of Synthesized Complexes

3.5.1 Solubility tests

1mg samples were weighed into different test tubes and various 2 cm^3 solvents, MeOH, CH_2Cl_2, Toluene, Et_2O, CH_3CN and DMSO used to test the solubility of the complexes. Either shaking the tubes vigorously checked solubility, heating gently with shaking and/or sonication was done where necessary.

3.5.2 Melting point determination

The melting points for the complexes were determined using a melting point apparatus. 1 mg of sample was weighed and put into a sealed capillary tube and inserted into the instrument. The sample was then subject to gradual heating and any changes noted in the event of melting.

3.5.3 UV/Vis spectroscopy

10^{-5}M sample solutions were prepared for all complexes using CH_2Cl_2 and UV/ Vis spectra obtained on a Varian Cary 100 Bio spectrophotometer. 1 cm path length quartz curvettes were used in a double beam spectrophotometer with CH_2Cl_2 placed in the reference cell. The measurements were done using both UV and Visible range of 200-800 nm. Prior to measurements the samples were bubbled with nitrogen for 20 minutes.

3.5.4 Photoluminescence spectroscopy

Photoluminescence measurements were done on Varian Cary Eclipse fluorescence spectrophotometer using 10^{-5}M sample solutions of Ir(III) complexes in CH_2Cl_2. 1 cm path length fluorescence quartz curvettes were used with blank solvent first then the sample solution. The excitation wavelength was set as the maximum absorption wavelength (λ_{max}) of the MLCT band for each complex from the UV/Vis absorption spectra.

3.5.5 Quantum yield measurements

The quantum yields were measured using Laser microscope of 2.5 MHz and 50% power. The excitation wavelength was set at 485 nm. $1x10^{-6}$ M Ir(III) complex solutions were prepared in CH_2Cl_2 and degassed using freeze-pump-thaw on the high vacuum line. The solutions were then transferred in 7 cm^3 vials with screws and the inert solutions subjected to the laser microscopy. Solutions, which had not been degassed, were also measured as control. Analysis for quantum yields was then done using Image J software.

3.5.6 Lifetime measurements

The lifetime and relative luminescence quantum yield measurements were done using home-built epifluorescence microscope setup connected to CCD (charge-coupled device) camera to measure luminescence intensity and to a time-correlated single photon counting (TCSPC, Picoharp 300, Picoquant) system to record luminescence decay. The width of the instrumental response function for TCSPC was 150 ps. For the measurements, a spectroscopic curvette filled with the sample was placed in the microscope sample stage and observed with a low magnification objective lens (2X). Luminescence was excited by 485 nm pulsed diode laser (Picoquant) working at 2.5 MHz

repetition rate which limited the observation window of the luminescence decay to 400 ns. For each compound, the degassed solution and air-saturated solutions of the same concentration ($1x10^{-6}$ M in CH_2Cl_2) were measured.

The luminescence decay was calculated from the lifetime measured for the air-saturated solutions (which was much shorter due to quenching of the triplet state by oxygen) and the ratio between luminescence quantum yield of the degassed $\Phi_{degassed}$ and air-saturated solution (Φ_{air}):

$$\tau_{degassed} = \tau_{air} \frac{\phi_{degassed}}{\phi_{air}}$$

Since the excitation conditions and excitation geometry (front face excitation and detection) were kept the same and the samples were optically thick, the ratio $\Phi degassed$ / Φair is equal to the ratio of the luminescence intensities measured by the microscope camera.

3.5.7 High resolution mass spectroscopy

HRMS spectral data was obtained from Micromass Q-TOF spectrophotometer operated either in electrospray ionization (ESI) mode or for some other complexes, atmospheric pressure chemical ionization (APCI) mode constituting a needle with 5.0kV voltage, a heated capillary temperature of 150°C, and sheath flow N_2 gas set at 25 arbitrary units. The syringe pump was operated at a flow rate between 3-5 μl/min. Data was analyzed using Masslynx software.

3.5.8 Cyclic voltammetry

Measurements were performed using a glassy-carbon electrode as working electrode, with silver/silver chloride electrode as reference electrode and a platinum electrode as the counter electrode. All samples solutions were prepared in CH_2Cl_2 and degassed with nitrogen for 20 min prior to voltammetric studies. Tetra-(n-butyl)-ammonium hexafluorophosphate, nBu$_4$NPF$_6$, (0.1 M in CH_2Cl_2) was used as supporting electrolyte.

3.5.9 Proton (^{1}H) NMR spectroscopy

Proton NMR for the complexes was done using deuterated $C_2D_2Cl_2$ or CD_2Cl_2. Chemical shifts were reported in ppm downfield from TMS (δ = 0 ppm) using residual solvent peaks as internal reference. For all cases, ca. 1mg of sample was diluted in 0.5 cm^3 of the solvent, sonicated where

necessary and the measurement done. Multiplicities were abbreviated as follows: (s) singlet, (d) doublet, (t) triplet, (q) quartet and (m) multiplet.

3.5.10 Carbon (^{13}C) NMR spectroscopy

^{13}C NMR was done using the 500MHz NMR operating at 499.76 MHz (^{1}H). Chemical shifts were reported in ppm downfield from TMS (δ = 0 ppm) using residual solvent peaks as internal reference.

3.5.11 2D COSY NMR spectroscopy

All 2D NMR measurements were done on the 500 MHz NMR and were done concurrently (i.e., for H, C, and COSY) each sample at a time due to correlations involved between ^{1}H and ^{13}C.

3.5.12 Elemental analyses

Mikrolab Kolbe Company determined the carbon, hydrogen and nitrogen content for the iridium complexes. Ca. 0.7 mg of samples were weighed and dried over high vacuum line for 36 h prior to being sent to Germany for the elemental analyses.

3.5.13 Crystallography (XRD)

The crystals were grown by dissolving in CH_2Cl_2, filtering the solution using a micro filter then recrystallizing through vapor diffusion in diethylether to give red-orange crystals. A single crystal was mounted on a goniometer under a microscope and illuminated with finely focused beam of X-rays to produce a diffraction pattern, which was analyzed using Mercury software.

3.6 Photoredox Catalysis

The capacity of the six *tris*-Iridium (III) complexes C-L_1 to C-L_6 as catalysts in a photoredox mediated synthetic context was investigated using the three-component oxytrifluoromethylation of alkenes recently developed by Koike and Akita (Yasu et al., 2012). Further, the complexes were tested in photobleaching tests, which involved photodegradation of Morin and photooxidation of alcohols where oxidation of benzyl alcohol and 4-methoxybenzyl alcohols into corresponding aldehydes was attempted.

3.6.1 Oxytrifluoromethylation of styrene

An oven-dried microwave vial was cooled to room temperature under high vacuum. The vial was charged with 5-(trifluoromethyl)dibenzothiophenium tetrafluoroborate (Scheme 10) (Umemoto's reagent) (0.042 g, 1.1 equiv), catalyst (C-L_1 to C-L_6) (0.5 mol%) and styrene (0.010 4 g, 0.1 mmol), which had been filtered over a pad of basic Al_2O_3 prior to addition. The microwave vial was sealed and carefully degassed in 3 vacuum/nitrogen cycles. A 3 freeze-pump-thaw degassed (3 cycles) mixture of MeOH (0.2 cm^3) and CH_2Cl_2 (1.8 cm^3) was added. The reaction mixture was irradiated using blue LED light strip (7 W) at a distance of 2 cm under stirring for 4 hours. The vial was opened and the internal standard trimethoxybenzene was added. The reaction mixture with the internal standard was briefly stirred and subsequently transferred into a NMR tube equipped with a sealed D_2O capillary, which was used for locking and shimming of the spectrometer. The yield was determined using 128 scans with relaxation time of 60 sec. The yield was reported based on the integration of the most upfield signals (2.27 and 2.43 ppm) of the product. The experiments were performed twice and the conversions and yields were reported as average values. The control reaction was doing the reaction using $Ir(ppy)_3$ under the present conditions and comparing with the results from previous studies.

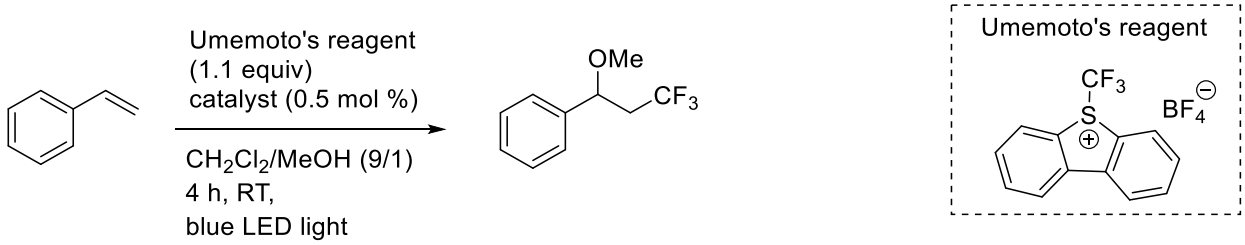

Scheme 10: Three-component Oxytrifluoromethylation of Styrene

3.6.2 Photocatalytic degradation/bleaching of Morin

Catalytic evaluation of the Ir (III) complexes was further studied via the oxidative degradation of Morin with visible blue LED lights (470 nm). The catalytic runs were performed in 1 cm^3 glass curvettes. The reactions were carried out in carbonate buffer. Calibration of the pH meter was done using pH 4.00 and pH 10.01 standard solutions. Before using the pH meter, pH 7 solution would be used to check if the meter was still calibrated.

The catalyst was prepared by weighing 0.3mg of the photocatalyst (C-L_1 to C-L_6) and dissolved in 10 cm^3 of the carbonate buffer followed by sonication. For all the complexes used the range used was 3.0-3.7x10^{-5} M.

The reaction was initiated by mixing the photocatalyst (500 µl), 0.1 mM freshly prepared Morin solution (500 µl). Time resolved UV/Vis spectra was then taken at t=0, then after every 1 min, after having illuminated the curvette with 470 nm visible light for 15-20 mins. Control experiments were performed by adding H_2O_2 (100 µl) into the reaction mixture then taking the UV/Vis spectra from 0 to 90 mins at a 10 min interval without the visible light and also with the visible light component. For all the runs, the reference cell contained the carbonate buffer.

3.6.3 Photooxidation of alcohols

The photocatalytic activity of the six Ir(III) complexes, C-L_1-C-L_6, was further investigated by utilizing them in photooxidation of alcohols into corresponding aldehydes specifically benzyl alcohol and 4-methoxybenzyl alcohol.

3.6.3.1 Photooxidation of Phenylmethanol (benzyl alcohol, BnOH)

In a microwave vial, the photoredox catalyst (1 mol%, 0.001 mmol), and phenylmethanol (1 equiv., 0.2 mmol) were dissolved in acetonitrile (1 cm^3) and ethyl viologen (1.2 equiv., 0.24 mmol) added into the mixture as shown in Scheme 11. The mixture was purged with N_2, and H_2O_2 (10 equiv.) added under inert conditions. The reaction was then stirred under irradiation with light source (blue light, distance ca. 0.5 cm) for 48 h. The reaction was quenched with MnO_2, then filtered through a pad of silica and cotton wool and analyzed by GC. Yields were related to internal standard, toluene. Several optimization reactions were carried out varying the solvent, amount of catalysts, reaction time and temperatures. With time, the lamp was also changed from white lamp to blue LED lights (λ= 470 nm) and all the results compared to determine the optimal conditions for the reaction.

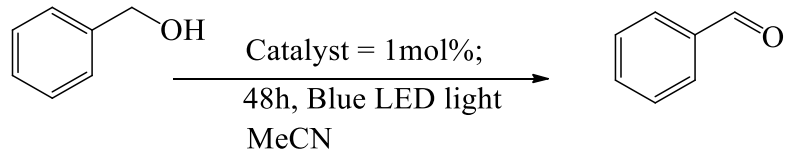

Scheme 11: Photooxidation of Phenylmethanol

3.6.3.2 Photooxidation of (4-Methoxyphenyl)methanol

A similar procedure as that in section 3.6.3.1 was followed where, the photoredox catalyst (1 mol %, 0.001 mmol), (4-Methoxyphenyl)methanol (1 equiv., 0.2 mmol) was dissolved in acetonitrile (1 cm^3) and ethyl viologen (1.2 equiv., 0.24 mmol) added into the mixture. The reaction was then stirred under irradiation with blue LED lights (λ= 470nm), at a distance ca. 0.5 cm from the vial for 48 h. The reaction was quenched with MnO_2, then filtered through a pad of silica and cotton wool and analyzed by GC. Yields were related to internal standard, toluene.

3.7 Hydrogenation of Furfural to THFA

The photocatalysts C-L_1 to C-L_6 (1 mol%), 10 mmol of the substrate were mixed with 2 cm^3 of solvent (CH_3CN) in a long glass vial and put in an autoclave where the mixture was purged with H_2 (5 bar) three times as shown in Scheme 12. The chamber was then filled with 50 bar H_2 and then completely sealed. The reaction was then stirred at this hydrogen pressure at 100 ^oC for 24 h. After cooling, n-tridecane, $CH_3(CH_2)_{11}CH_3$, which was the internal standard, was added, the mixture micro filtered into a vial and analyzed with GC. Yields were calculated from chromatograms.

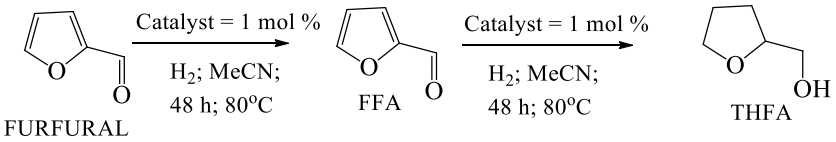

Scheme 12: Hydrogenation of Furfural to THFA

CHAPTER FOUR

RESULTS AND DISCUSSIONS

4.1 Synthesis of Ligands

A series of ten (10) ligands was prepared, six (L_1-L_6) of which were based on naphthalene moiety while the other four (L_7- L_{10}) were on isoquinoline moiety in order to compare their properties due to the similar structure

4.1.1 2-(1-Naphthyl) Pyridine (L_1)

2-(1-Naphthyl) Pyridine, $C_{15}H_{11}N$, molecular weight 205.2600, was the first unsubstituted ligand synthesized as per Section 3.2.1 and as shown in Scheme 13. Ninety two percent (1 g, 92%) yield was obtained, and it was determined to be soluble in polar organic solvents.

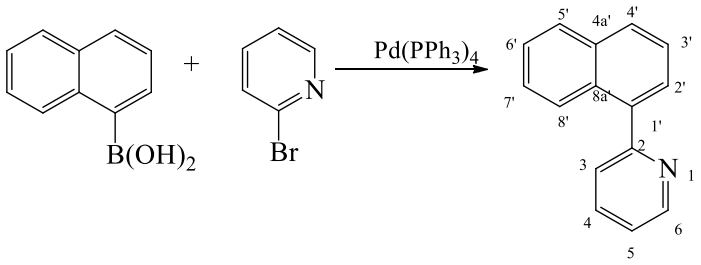

2-(1-Naphthyl) pyridine

Scheme 13: Synthesis of 2-(1-Naphthyl) Pyridine

High-resolution mass spectrometer data for L_1 obtained by electron spray ionization ESI, showed that the observed HRMS-ESI+ (*m/z*): $[M+H]^+$ of parent ion, which was 206.0950, corresponded with the calculated mass for $C_{15}H_{12}N$, 206.0970 as shown in Figure 5 suggesting the formulation of L_1.

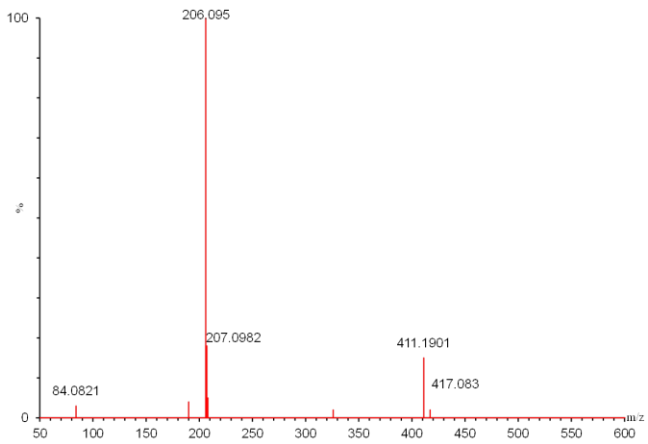

Figure 5: Mass spectrum for 2-(1-naphthyl) pyridine

A notable fragmentation peak is that at 411.1901 probably arising from the dimerization of the ligand. Figure 6 shows the major fragmentations of L_1 that corresponded to the expected formulations of this ligand.

UV-VIS measurements of the 2-(1-Naphthyl) Pyridine gave intense UV absorption bands below 300 nm with a λ_{max} of 294 nm. This was assigned to spin allowed intraligand (IL) or ligand-centered (^{1}LC) $^1\pi$-π^* transition of the conjugated π system confirming it was a pure ligand with no metal coordinated to it.

NMR was used to confirm the structure of all the ligands in this study. Figure 6 shows the ^{1}H NMR spectrum for L_1, which had 11 distinct peaks after integration, corresponding to the 11 protons on the ligand.

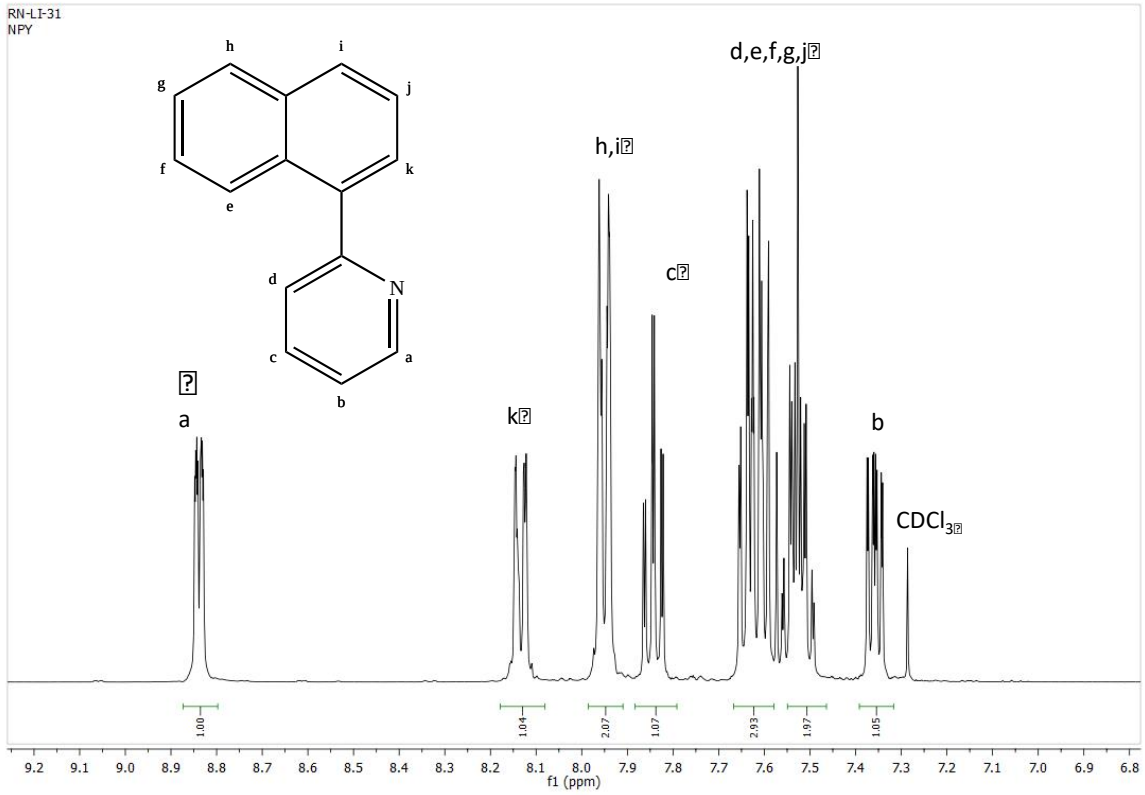

Figure 6: ^{1}H NMR Spectrum for 2-(1-naphthyl) pyridine

The chemical shifts for proton were found to be: ^{1}H NMR (400 MHz, Chloroform-d) δ 8.81 (ddd, J = 4.9, 1.9, 1.0 Hz, 1H), 8.11 (dd, J = 8.5, 1.3 Hz, 1H), 7.93 (dt, J = 7.2, 1.3 Hz, 2H), 7.82 (td, J = 7.7, 1.8 Hz, 1H), 7.63 – 7.54 (m, 3H), 7.54 – 7.46 (m, 2H), 7.33 (ddd, J = 7.6, 4.9, 1.2 Hz, 1H). This suggested that compound synthesized maybe 2-(1-naphthyl) pyridine (L_1). All the chemical shifts were shifted to the left (downfield), occurring between 7.33-8.81 ppm, corresponding to the aromatic region of the naphthyl-pyridine rings. Electronegativity of the nitrogen atom pulls the electron density towards itself from the neighboring carbon atoms hence the most deshielded proton is Ha since it is *ortho* to N on the pyridine ring (on C6 as numbered in Scheme 16) at δ=8.81 ppm and this is consistent with literature values of similar complexes (Tian, 2011).

In ^{13}C NMR, 15 distinct peaks were observed corresponding to 15 carbons on the ligand as presented; ^{13}C NMR (101 MHz, $CDCl_3$) δ 159.27, 149.56, 138.51, 136.44, 133.96, 131.18, 128.93, 128.39, 127.51, 126.52, 125.90, 125.62, 125.33, 125.09, 122.06. In this ligand carbon C2 and C6 were the most deshielded due to the electronegativity of nitrogen with C2 being more deshielded with δ = 159.27 than C6 with δ =149.56. The ^{13}C NMR spectrum is given in the Appendix1.1 and

this confirms that synthesized compound was L_1 since the data matches with the theoretically expected number of peaks.

The data from HRMS, UV-VIS, ^{1}H and ^{13}C NMR confirmed the synthesis of 2-(1-naphthyl) pyridine.

The proposed mechanism for the synthesis of L_1 is shown in Scheme 14A and 14B, entailing oxidative addition (OA) where palladium is oxidized from Pd(0) to Pd(II). It's been reported that oxidative addition is the rate-determining step and it proceeded by forming a complex between the Pd(0) catalyst and the first reagent, 2-bromopyridine. In the transmetallation step, the second reagent, the naphthyl-1-boronic acid was added with the loss of Br-$B(OH)_2$ moiety to generate a Pd(II) species, which became a Pd electrophile and performs a transmetallation on the organometallic component to form a di organopalladium (II) intermediate.

Presence of a base is a requirement for the coupling to happen since it aids in formation of a four-coordinate "ate" complex, which is required to facilitate efficient transfer of organic moiety from the organoboronic species to the metal center (Lennox & Lloyd-Jones, 2013). This then undergoes a reductive elimination to form the new C-C bond between the pyridine and naphthyl group or between phenyl and isoquinoline to give 2-(1-naphthyl) pyridine or 1-phenylisoqinoline ligand, which is reductively eliminated, and the catalyst regenerated and returns to Pd(0) oxidation state, thereby obeying the 18-electron rule. It can be concluded that the reaction mechanism follows Scheme 14A and 14B which agreed with Suzuki reactions.

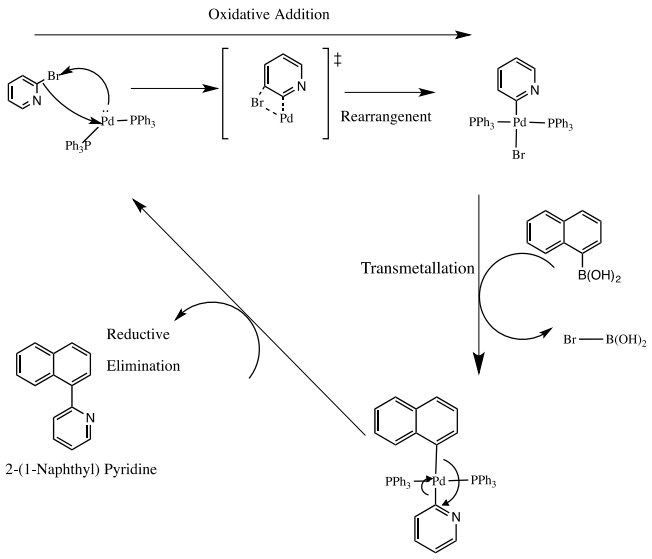

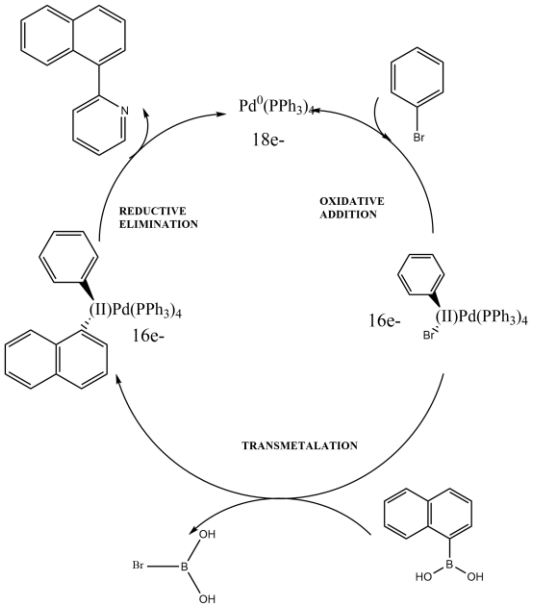

Scheme 14: A) Concerted Mechanism B) Schematic Representation of Suzuki Coupling for Ligands

4.1.2 2-(1-Naphthyl)-4-methoxy Pyridine (npy-OMe) (L_2)

2-(1-Naphthyl)-4-methoxy pyridine, $C_{16}H_{13}NO$, molecular weight 235.2860, was synthesized as described in Section 3.2.2 by introducing a strong electron-donating group, methoxy, on the *para* position of the pyridine ring, Scheme 15. The methoxy group has two competing effects; it can be an EDG through resonance within the conjugated ring where the lone pair on oxygen delocalizes

and increases electron density to the system making it electron rich and affects properties of the ligand especially the chemical shift values, which were upfield as compared to the unsubstituted ligand. Methoxy can also act as EWG inductively through sigma bonds due to the electronegative oxygen.

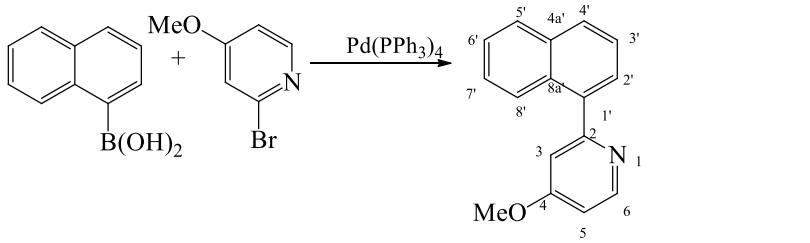

2-(1-Naphthyl)-4-methoxy pyridine

Scheme 15: Synthesis of 2-(1-Naphthyl)-4-MethoxyPyridine

Ninety percent (0.644 g, 90%) yield was obtained and the product was soluble in polar solvents. The structure of the L_2 was confirmed from mass spectrometer since the calculated peak for parent ion HRMS-APCI (m/z): $[M+H]^+$ for $C_{16}H_{14}NO$, 236.1075 corresponded to the observed peak, 236.1078 as shown in Figure 7, which confirmed the expected fragmentations of the ligand.

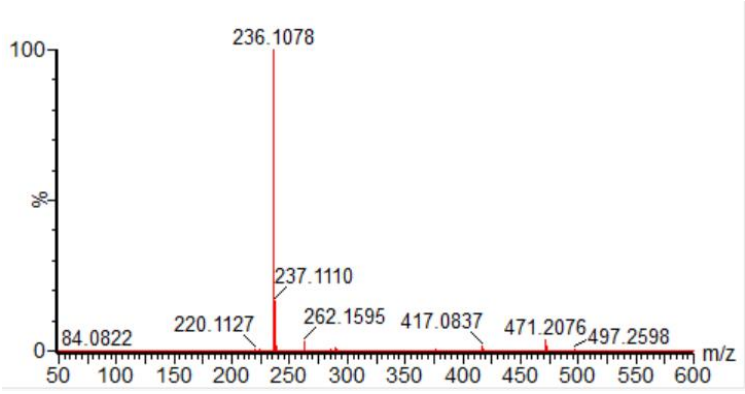

Figure 7: Mass Spectrum for 2-(1-Naphthyl)-4-Methoxy Pyridine

The fragmentation peak at 471.2076 is notable as well probably arising from the dimerization of the ligand.

UV-VIS measurements of the 2-(1-naphthyl)-4-methoxy pyridine gave intense UV absorption bands below 300 nm with a λ_{max} of 269 nm. This was assigned to spin allowed intraligand (IL) or

ligand-centered (^{1}LC) $^1\pi$-π^* transition of the conjugated π system. This confirmed it was a ligand without metal coordination and as consistent with literature (Tian, 2011).

Figure 8 shows the ^{1}H NMR for L_2 with the three chemically equivalent protons in the methoxy group being observed at δ=3.90 ppm. The proton NMR shifts were as follows: ^{1}H NMR (400 MHz, $CDCl_3$) δ 8.59 (d, *J* = 5.7 Hz, 1H), 8.15 (dd, *J* = 8.5, 0.9 Hz, 1H), 7.87 (d, *J* = 8.2 Hz, 1H), 7.70 – 7.64 (m, 3H), 7.61 (dd, *J* = 5.7, 0.6 Hz, 1H), 7.53 (ddd, *J* = 8.3, 6.9, 1.3 Hz, 1H), 7.09 – 7.03 (m, 2H), 3.90 (s, 3H) and the data suggested synthesis of 2-(1-naphthyl)-4-methoxypyridine.

The chemical shift occurring at 3.90 ppm was due to the electronegative oxygen shielding the protons from the external magnetic field, β_0.

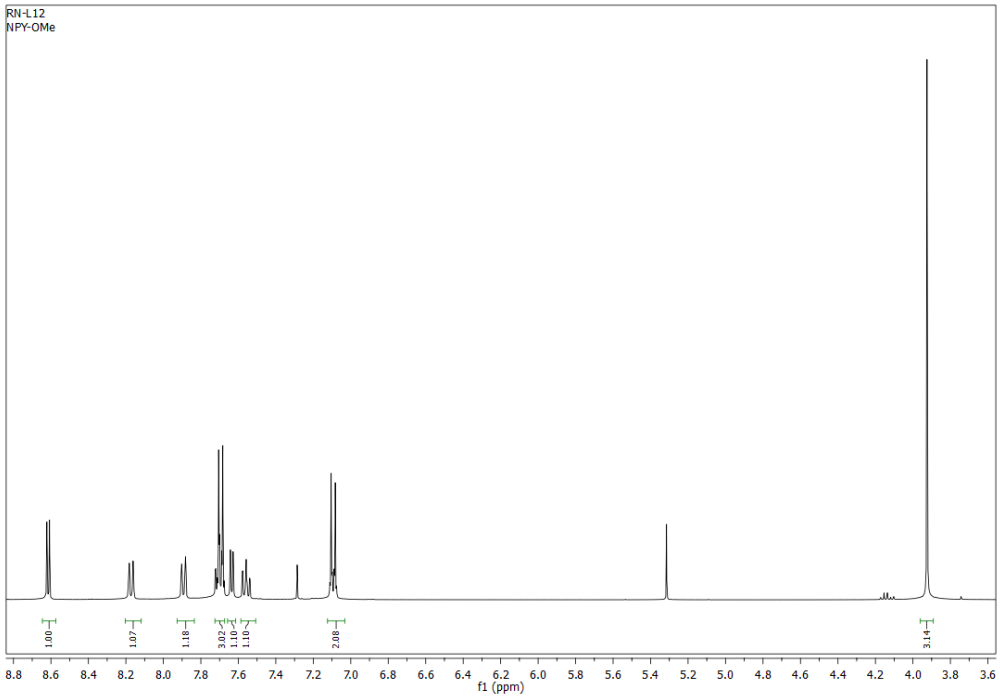

Figure 8: ^{1}H NMR Spectrum for 2-(1-Naphthyl)-4-Methoxy Pyridine

The most deshielded proton (δ= 8.59 ppm), on C6 consistent with numbering in Scheme 19 was upfield shifted in comparison to unsubstituted L_1, δ= 8.81 ppm, due to the electron donation of the O in methoxy group into the ring via resonance whereas the protons ortho to the methoxy group, on C3 δ= 7.09 and C5 δ= 7.03 ppm, were shifted slightly upfield 7.09-7.03 ppm as compared to L_1 and this was consistent with literature, which shows that protons *ortho* to an EDG portray

distinct upfield shift (Reich & Reich, 2018). There are 10 chemical shifts (δ= 8.59 -7.04 ppm) corresponding to 10 protons in the aromatic region of naphthalene and pyridine rings. From the work done by Hasan *et al.*, 2015 it was found that methoxy substituent shifts spectrum upfield due to electron donation and this was consistent with the results from this work.

In ^{13}C NMR, 16 distinct peaks were observed corresponding to 16 carbons on the ligand as presented; ^{13}C NMR (101 MHz, $CDCl_3$) δ 160.49, 160.13, 142.32, 137.04, 132.22, 131.41, 130.03, 127.76, 127.16, 127.09, 126.84, 119.64, 113.91, 55.52, 31.71, 22.78. The ^{13}C NMR spectrum is given in the Appendix 1.2 arising from expected L_2 shifts. Carbon C4 which is directly attached to methoxy was the most shifted to the left (deshielded) with δ =160.49 ppm due to the resonance effect of the oxygen as compared to that of L_1. This was closely followed by carbon C6 with δ =160.13 ppm due to the deshielding effect of the electronegative nitrogen. This ligand followed a similar concerted mechanism for Suzuki coupling as shown in Scheme 14A. The MS, UV-VIS, ^1H and ^{13}C NMR spectroscopy data confirmed the synthesis of 2-(1-naphthyl)-4-methoxy pyridine.

4.1.3 2-(1-naphthyl)-4-trifluoromethylpyridine (npy-CF_3) (L_3)

2-(1-naphthyl)-4-trifluoromethyl pyridine, $C_{16}H_{10}F_3N$, molecular weight 273.2582, Scheme 16, was synthesized by introducing trifluoromethyl group, a strong electron withdrawing group on the para position of the pyridine ring as summarized in Section 3.2.3. Ninety seven percent (0.750 g, 97%) yield was obtained and was soluble in polar solvents.

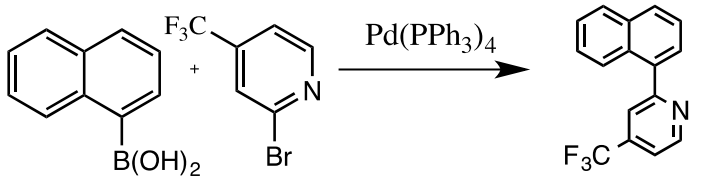

2-(1-naphthyl)-4-trifluoromethylpyridine

Scheme 16: Synthesis of 2-(1-naphthyl)-4-trifluoromethyl pyridine

In contrast to L_2, -CF_3 group withdraws electron density from the system making it electron deficient and affects the chemical shifts values, which were downfield shifted as compared to L_1.

The structure of the L_3 was confirmed where the calculated peak for parent ion HRMS-APCI (m/z): $[M+H]^+$ for $C_{16}H_{11}F_3N$, 274.0799 corresponded to the observed peak 274.0847 as illustrated on Figure 9.

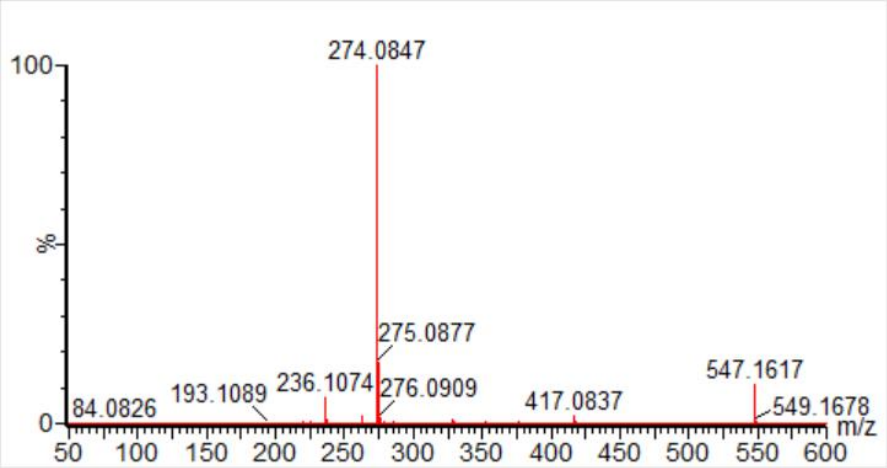

Figure 9: Mass Spectrum for 2-(1-naphthyl)-4-trifluoromethylpyridine

The fragmentation peak at 547.1617 was notable probably arising from the dimerization of the ligand. The data confirmed the expected fragmentations of the ligand.

UV-VIS measurements of the 2-(1-naphthyl)-4-trifluoromethyl pyridine gave intense UV absorption bands below 300 nm with a λ_{max} of 294 nm. This was assigned to spin allowed intraligand (IL) or ligand-centered (^{1}LC) $^1\pi$-π^* transition of the conjugated π system.

The proton NMR shifts were as follows: ^{1}H NMR (400 MHz, $CDCl_3$) δ 8.99 (d, *J* = 5.1 Hz, 2H), 8.07 – 8.03 (m, 2H), 7.99 – 7.92 (m, 4H), 7.83 (s, 2H), 7.64 – 7.49 (m, 5H) which corresponds to the spectrum in Figure 10 that showed 10 peaks in the only aromatic region since there were no other peaks, suggesting synthesis of 2-(1-naphthyl)-4-trifluoromethyl pyridine. The proton on the C6 in the pyridine ring, δ = 8.99 ppm, was the most downfield shifted as compared to L_1 δ = 8.81 ppm by + 0.18 ppm due to the electronegative trifluoromethyl substituent which removes electron density from ring leading to deshielding.

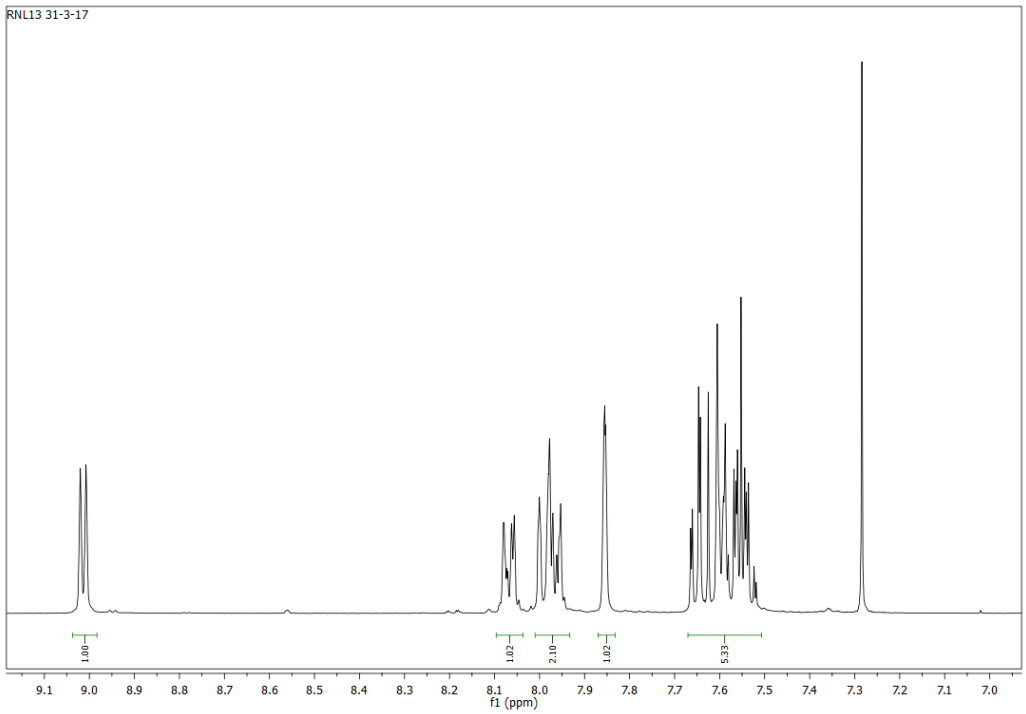

Figure 10: ^{1}H NMR Spectrum for 2-(1-naphthyl)-4-trifluoromethyl pyridine

The protons *ortho* to the EWG (C3, C5) should be shifted downfield this was observed in L_3 where a downfield shift of δ= 7.64 and 7.49 ppm respectively, was recorded as compared to L_1 and L_2. In ^{13}C NMR, 16 distinct peaks were observed corresponding to 16 carbons on the ligand as presented. ^{13}C NMR (101 MHz, $CDCl_3$) δ 160.88, 150.65, 137.23, 134.11, 130.98, 129.87, 128.69, 128.01, 127.10, 126.31, 125.41, 125.17, 120.75, 120.71, 117.73, 117.70 was in agreement of the theoretically expected L_3 peaks and the spectrum is given in the Appendix 1.3. Carbon C4, which is directly attached to trifluoromethyl group, had δ =134.11 was shifted to the right due to the bulkiness of the -CF_3 and the its ability to act as an electron donating group inductively although its an EWG. C2 and C6 were the most deshielded to due the electronegativity of nitrogen with C2 being more deshielded with δ=160.88 ppm than C6 with δ =150.65 ppm. The MS, UV-VIS, ^{1}H and ^{13}C NMR data confirmed the synthesis of 2-(1-naphthyl)-4-trifluoromethyl pyridine.

4.1.4 2-(1-Naphthyl)-4-methyl Pyridine (L_4)

2-(1-Naphthyl)-4-methyl pyridine, $C_{16}H_{13}N$, molecular weight 219.2870, Scheme 17, was synthesized from npy by introducing a methyl group, a weak electron donating group in the para

position of the pyridine ring as described in Section 3.2.4, giving ninety seven percent (0.589 g, 97%) yield, which was soluble in polar organic solvents. As expected, the chemical shifts were upfield shifted in comparison to L_1.

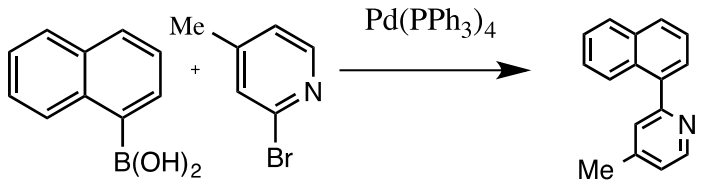

2-(1-naphthyl)-4-methylpyridine

Scheme 17: Synthesis for 2-(1-Naphthyl)-4-methylpyridine

The structure of the L_4 was confirmed where the calculated mass of the peak of the parent ion HRMS-APCI (*m/z*): $[M+H]^+$ 220.1082 corresponded with the observed 220.1126, as shown in Figure 11 conforming to the expected fragmentation pattern of the molecule. Another notable fragmentation peak is that at 439.2172 probably arising from the dimerization of the ligand.

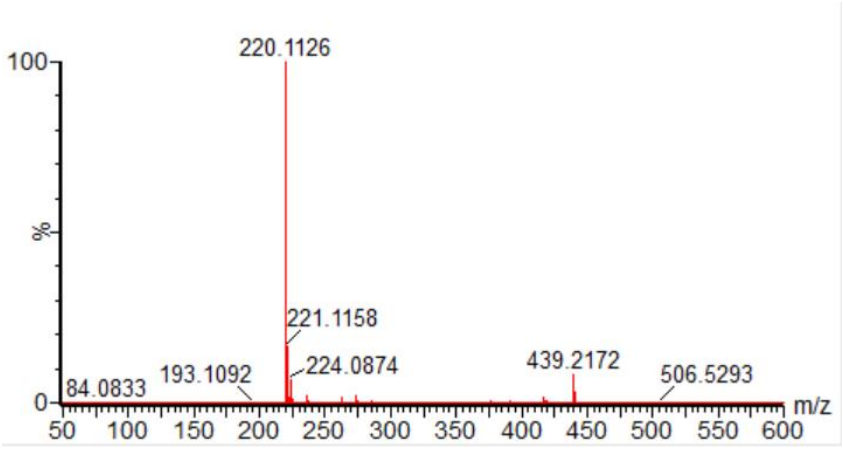

Figure 11: Mass Spectrum for 2-(1-Naphthyl)-4-methylpyridine

The proton NMR shifts were as follows: ^{1}H NMR (400 MHz, $CDCl_3$) δ 8.66 (dd, *J* = 5.1, 0.8 Hz, 1H), 8.12 – 8.08 (m, 1H), 7.93 – 7.88 (m, 2H), 7.63 – 7.51 (m, 2H), 7.53 – 7.45 (m, 2H), 7.41 (dq, *J* = 1.7, 0.8 Hz, 1H), 7.16 (ddd, *J* = 5.1, 1.7, 0.8 Hz, 1H), 2.44 (s, 3H), suggesting the synthesis of 2-(1-naphthyl)-4-methyl pyridine and the spectrum on is shown in Figure 12.

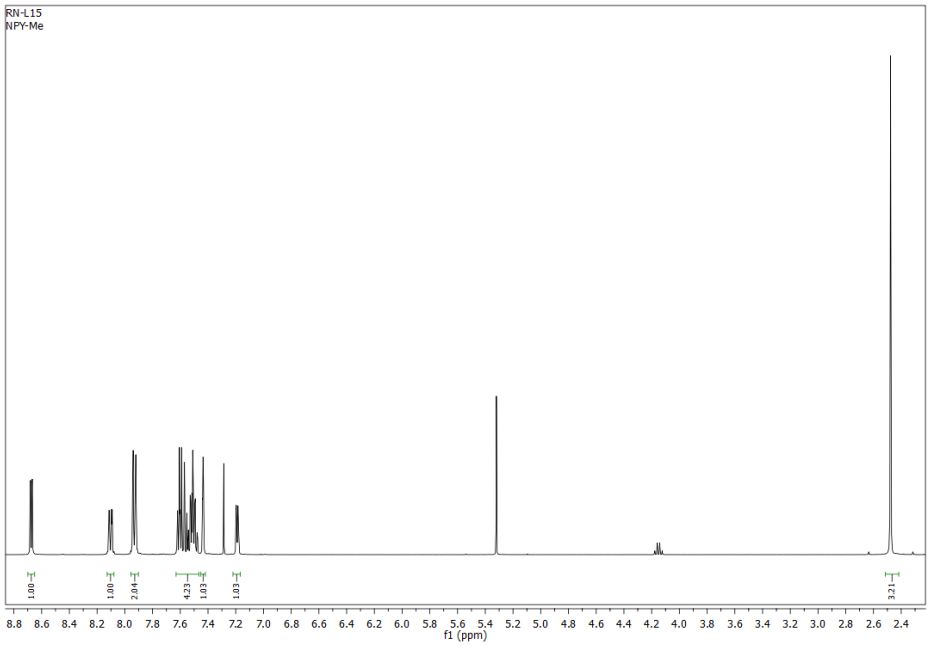

Figure 12: ^{1}H NMR Spectrum for 2-(1-Naphthyl)-4-methylpyridine

The methyl protons were quite shielded giving a singlet due to chemical equivalency at δ= 2.45 ppm, since methyl is a weak electron donating group. The proton on the C6 in the pyridine ring, δ = 8.66 ppm, was the upfield as compared to L_1 δ = 8.81 ppm by -0.15 ppm. The aromatic protons lay between δ= 8.66-7.16 ppm and they were shielded more than those in L_1 and L_3 due to the presence of weak electron donating group but deshielded more than L_2. This is because in L_3, -CF_3 is a stronger electron withdrawing group than methyl group, which is electron withdrawing through anisotropy hence more deshielded than L_4. Alkyl groups exhibit anisotropic effects, which could make them behave as if they are weakly electron withdrawing through anisotropy. This was consitent with report by Reich and Reich (2018). Comparing L_2 and L_4 shows the effect of the stronger EDG in L_2 i.e. -OMe since proton proximal to N is more shielded in L_2 (δ=8.59 ppm) than L_4 (δ=8.66 ppm). Similar to L_2, the protons *ortho* to the methyl group were upfield shifted due to the influence of EDG on that position as reported by Reich and Reich (2018).

Carbon 13 gave the corresponding 16 C peaks as shown; ^{13}C NMR (101 MHz, $CDCl_3$) δ 159.16, 149.32, 147.56, 138.72, 133.99, 131.33, 128.82, 128.38, 127.40, 126.46, 126.00, 125.88, 125.78, 125.34, 123.11, 21.24 again suggesting synthesis of L_4 with the spectrum given in the Appendix 1.4. Carbon C4, which is directly attached to methyl group, had δ =149.32 ppm was shifted to the

left as compared to that of L_1 since alkyl groups can act as weakly electron withdrawing. C2 and C6 were the most deshielded due to the electronegativity of nitrogen with C2 being more deshielded with δ=159.16 than C6 with δ =149.32 with these values being comparable to those of L_1. The MS ^{1}H and ^{13}C NMR data suggested the synthesis of 2-(1-naphthyl)-4-trifluoromethyl pyridine.

The MS, ^{1}H and ^{13}C NMR data confirmed the synthesis of 2-(1-naphthyl)-4-methyl pyridine.

4.1.5 2-(4-methylnaphthyl)-4-methyl Pyridine (npy-Me_2) (L_5)

2-(4-methylnaphthyl)-4-methyl pyridine, $C_{17}H_{15}N$, molecular weight 233.3140, Scheme 18, was synthesized by substituting two methyl groups on the pyridine and naphthyl ring as described in Section 3.2.5. A ninety percent (0.532 g, 90%) yield was obtained and the product was soluble in polar solvents.

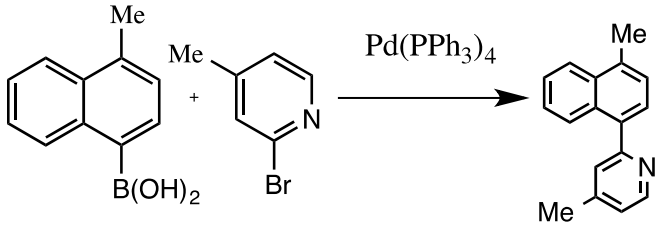

2-(-4-methyl naphthyl)-4-methylpyridine

Scheme 18: Synthesis of 2-(4-methylnaphthyl)-4-methyl pyridine

The structure of the L_5 was confirmed where the calculated mass of the peak of the parent ion HRMS-APCI (*m/z*): $[M+H]^+$ 234.1283 corresponded with the observed 234.1284, as shown in Figure 13 conforming to the expected fragmentation pattern of the molecule.

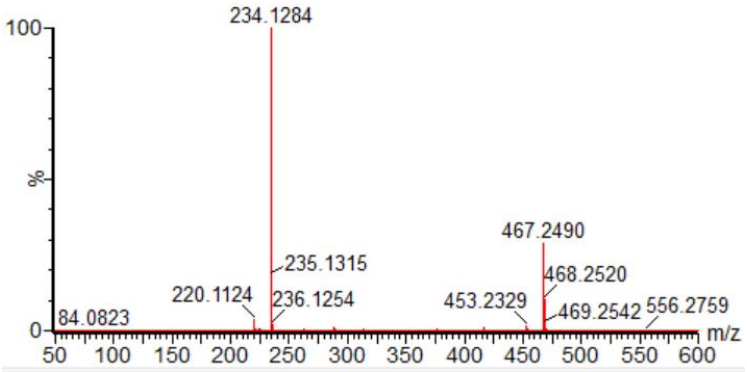

Figure 13: Mass Spectrum for 2-(4-methylnaphthyl)-4-methyl Pyridine

Another notable fragmentation peak is that at 467.490 probably arising from the dimerization of the ligand.

The proton NMR spectrum for L_5 gave the following chemical shifts values: ^{1}H NMR (400 MHz, $CDCl_3$) δ 8.64 (dd, *J* = 5.0, 0.8 Hz, 1H), 8.08 (dddd, *J* = 11.9, 8.4, 1.4, 0.7 Hz, 2H), 7.54 (ddd, *J* = 8.3, 6.8, 1.4 Hz, 1H), 7.51 – 7.45 (m, 2H), 7.41 – 7.38 (m, 2H), 7.14 (ddd, *J* = 5.1, 1.7, 0.8 Hz, 1H), 2.75 (d, *J* = 0.9 Hz, 3H), 2.44 (d, *J* = 0.8 Hz, 3H), corresponding to the spectrum shown in Figure 14 and suggesting the synthesis of 2-(4-methylnaphthyl)-4-methyl pyridine. It has two distinctive peaks upfield, corresponding to the two-methyl substitutions, with the three protons on each methyl being chemically equivalent. One of the peaks, on the naphthyl ring is slightly deshielded than that on pyridine ring due to resonance. Further, there are nine distinct chemical shifts downfield corresponding to the protons in the aromatic region of the ligand.

Once again considering the proton proximal to the nitrogen in the pyridine ring shows the effect of EDG since it is shielded, 8.64 ppm when compared to L_1 8.81 ppm and L_3 8.99 ppm but deshielded with comparison to L_2, 8.59 ppm. For the same proton there is a negligible difference of 0.02 ppm when compared to L_4, which has the same group on the same position. The protons on the ortho position of the methyl group on both rings are upfield, which is consistent with the work by Reich and Reich (2018).

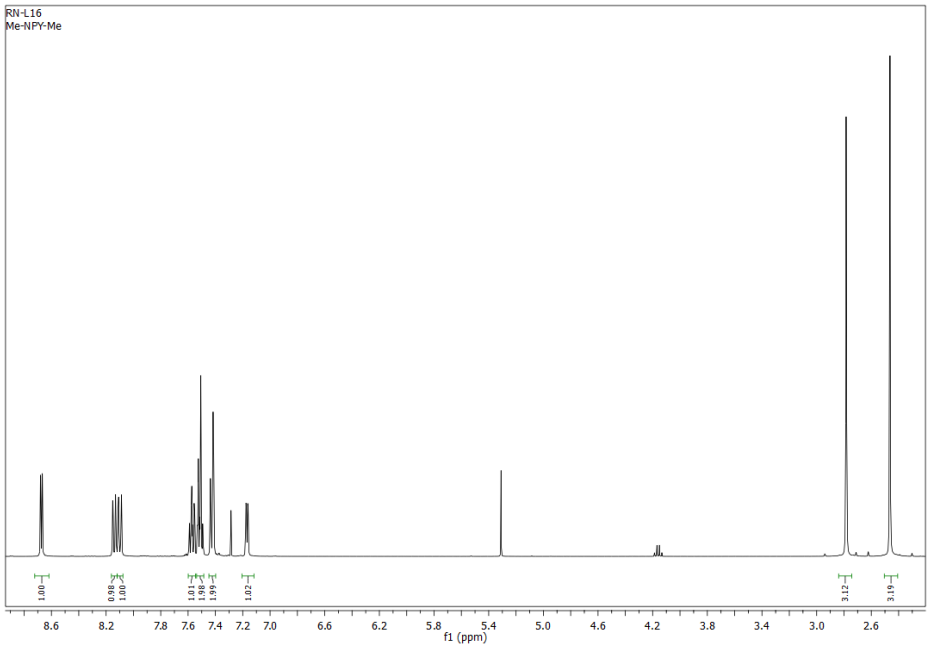

Figure 14: ^{1}H NMR Spectrum for 2-(4-methylnaphthyl)-4-methyl Pyridine

Carbon 13 gave the expected 17 peaks for the carbons in L_5 and data summarized as follows: ^{13}C NMR (101 MHz, $CDCl_3$) δ 159.52, 149.36, 147.49, 137.27, 135.13, 133.07, 131.43, 127.15, 126.45, 126.23, 126.12, 126.10, 125.76, 124.50, 122.97, 21.31, 19.85 suggesting the synthesis of 2-(4-methylnaphthyl)-4-methyl pyridine with the spectrum given in the Appendix 1.5. Carbon C4 had δ =149.36 ppm was shifted to the left as compared to that of L_1 since alkyl groups can act as weakly electron withdrawing. C2 and C6 were the most deshielded to due the electronegativity of nitrogen with C2 being more deshielded with δ=159.52 ppm than C6 with δ =149.36 ppm with these values being comparable to those of L_1.

The MS, ^{1}H and ^{13}C NMR data confirmed the synthesis of 2-(4-methylnaphthyl)-4-methyl pyridine.

4.1.6 2-(4-methylnaphthyl) Pyridine (Me-npy) (L_6)

2-(4-methylnaphthyl) pyridine, $C_{16}H_{13}N$, molecular weight 219.2870, was prepared by introducing a methyl group on para position of the naphthyl ring as described in Section 3.2.6 to form a Me-npy shown in Scheme 19. A ninety two percent (0.542 g, 96%) yield was obtained and the product was soluble in polar solvents.

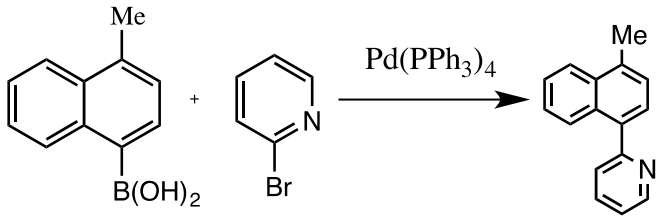

2-(4-methyl naphthyl) pyridine

Scheme 19: Synthesis of 2-(4-methylnaphthyl) Pyridine

The structure of the L_6 was confirmed where the calculated mass of the peak of the parent ion HRMS-APCI (*m/z*): $[M+H]^+$ 220.1126 corresponded with the observed 220.1127, as shown in Figure 15 conforming to the expected fragmentation pattern of the molecule. Another notable fragmentation peak is that at 439.2176 probably arising from the dimerization of the ligand.

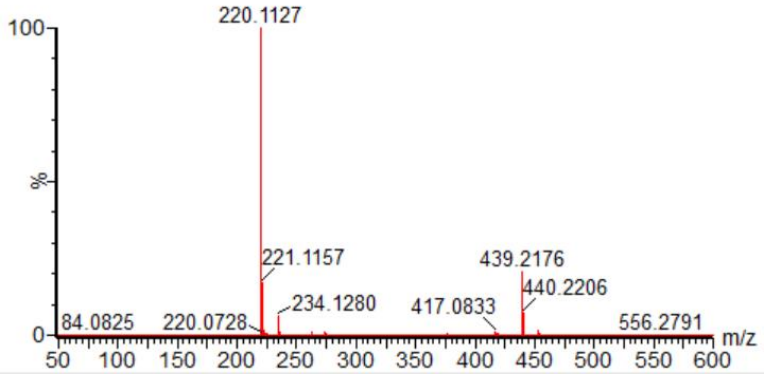

Figure 15: Mass Spectrum for 2-(4-methylnaphthyl) pyridine

The proton NMR for Me-npy gave the following chemical shifts values: ^{1}H NMR (400 MHz, $CDCl_3$) δ 8.80 (ddd, *J* = 4.9, 1.8, 0.9 Hz, 1H), 8.14 – 8.05 (m, 2H), 7.81 (td, *J* = 7.7, 1.8 Hz, 1H), 7.59 – 7.45 (m, 4H), 7.41 (dd, *J* = 7.2, 0.8 Hz, 1H), 7.32 (ddd, *J* = 7.6, 4.9, 1.2 Hz, 1H), 2.76 (d, J = 0.8 Hz, 3H) corresponding to spectrum shown in Figure 16, which exhibited a distinct singlet upfield at δ= 2.76 ppm that corresponded to the three protons of the methyl group. These protons are deshielded when compared to L_4 due to resonance in the naphthyl ring. The remaining aromatic protons' chemical shifts were in the range of 8.84-7.32 ppm. Here, the proton proximal to nitrogen has comparable chemicals shifts (δ = 8.80 ppm) with L_1 (δ = 8.81 ppm) due to absence of

substituents on the pyridine ring with the proton ortho to the methyl group being shielded (Reich & Reich, 2018).

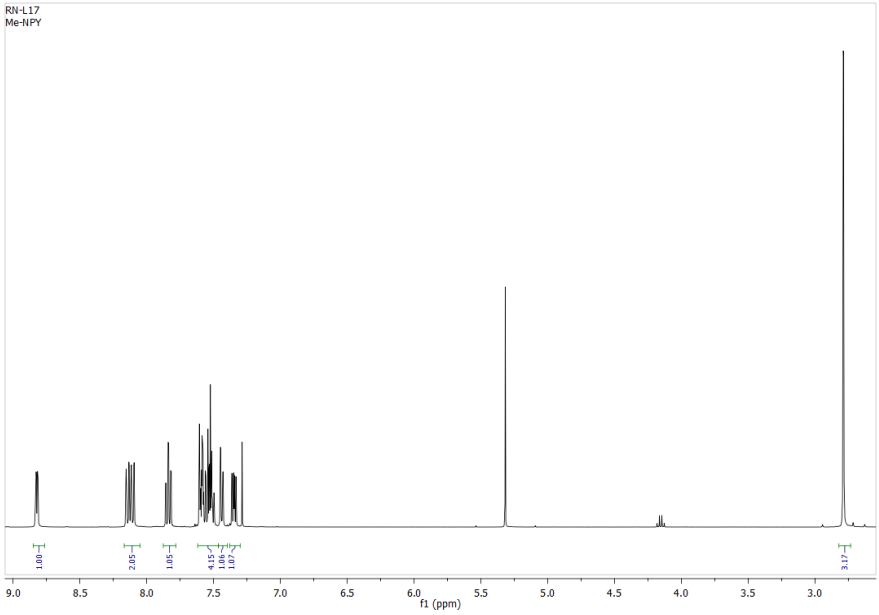

Figure 16: ^{1}H NMR Spectrum for 2-(4-methylnaphthyl) Pyridine

Carbon 13 gave the expected 16 peaks for the carbons in L_6 and data summarized as follows ^{13}C NMR (101 MHz, $CDCl_3$) δ 159.16, 149.32, 147.56, 138.72, 133.99, 131.33, 128.82, 128.38, 127.40, 126.46, 126.00, 125.88, 125.78, 125.34, 123.11, 21.24 confirming L6. The ^{13}C NMR spectrum is given in the Appendix 1.6. Carbon C4 had δ =147.56 ppm was shifted to the left as compared to that of L_1 due to alkyl group, which can act as weakly electron withdrawing. C2 and C6 were still the most deshielded due to the electronegativity of nitrogen with C2 being more deshielded with δ=159.16 ppm than C6 with δ =149.32 ppm with these values being comparable to those of L_1. The MS, ^{1}H and ^{13}C NMR data confirmed the synthesis of 2-(4-methylnaphthyl) pyridine.

4.1.7 4-Fluoro-1-phenyl isoquinoline (Piq-F) (L_7)

4-Fluoro-1-phenyl isoquinoline, $C_{15}H_{10}FN$, molecular weight 223.2450, was prepared by introducing a fluoro group on para position of the phenyl ring attached to isoquinoline backbone as described in Section 3.2.7 to form a Piq-F shown in Scheme 20.

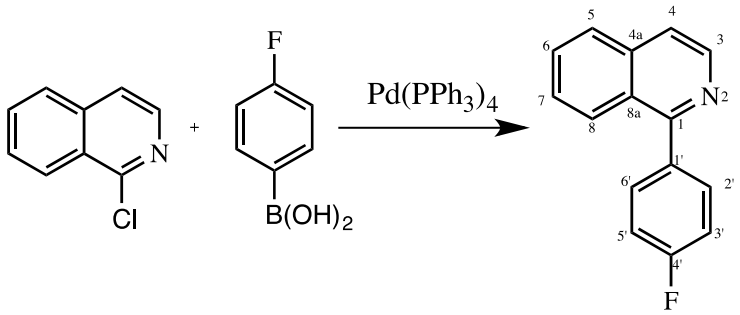

4-fluoro-1-phenyl isoquinoline

Scheme 20: Synthesis of 4-fluoro-1-phenyl isoquinoline

Eighty four percent (0.239 g, 84%) yield was obtained and the product was soluble in polar solvents. Its note worth that the yields of L_7-L_{10} were comparatively lower than for L_1-L_6 due to the use of 1-chloroisoquinoline (Ar-Cl) as starting material. The reactivity of Ar-Cl as compared to other halides is usually lower in Suzuki protocols under same conditions. The electronegativity decreases down the group as the atomic radius increases making the reactivity to increase down the group in the order Ar-I > Ar-Br > Ar-Cl (Tian, 2011). With respect to displacement of halides, Cl is harder to displace than Br and I hence the low yields.

The structure of the Piq-F was confirmed where the calculated mass of the peak of the parent ion HRMS-APCI (*m/z*): $[M+H]^+$ 224.0831 corresponded with the observed 224.0878, as shown in Figure 17 conforming to the expected fragmentation pattern of the molecule. A notable fragmentation peak was that at 206.0969 corresponding to the loss of the -F group.

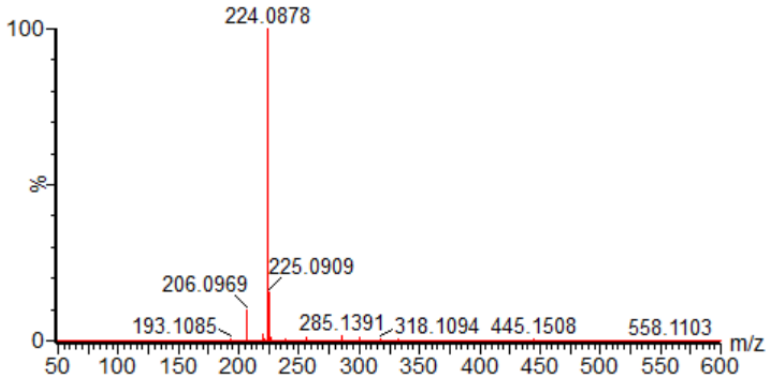

Figure 17: Mass Spectrum for 1-(4-fluorophenyl) isoquinoline

The proton NMR for Piq-F gave the following chemical shifts values as shown in Figure 18: ^{1}H NMR (400 MHz, $CDCl_3$) δ 8.67 (d, *J* = 5.7 Hz, 1H), 8.14 (d, *J* = 8.5 Hz, 1H), 7.97 (d, *J* = 8.2 Hz, 1H), 7.77 (ddd, *J* = 15.4, 8.4, 3.8 Hz, 4H), 7.68 – 7.60 (m, 1H), 7.35 – 7.28 (m, 2H). The low field compared to other protons all in the aromatic region. This was consistent to similar compounds in literature (Tian, 2011).

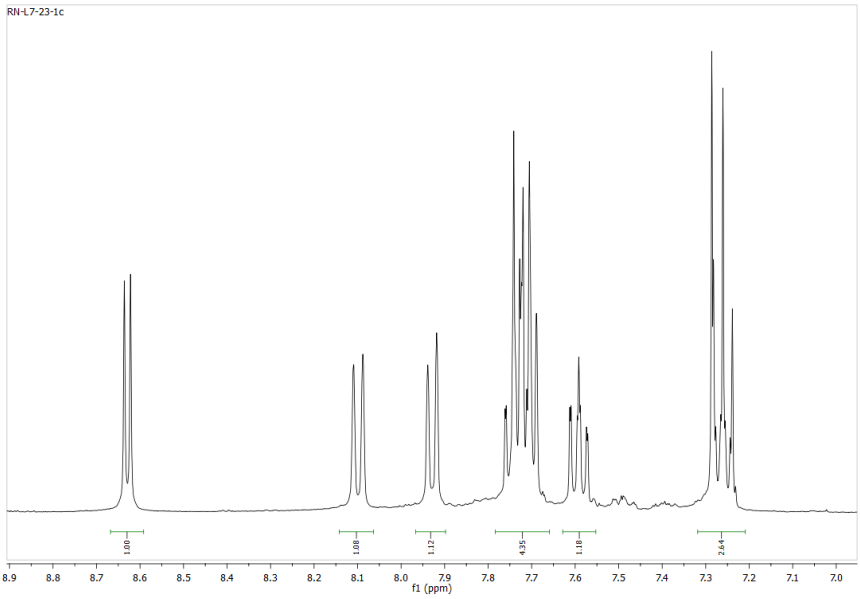

Figure 18: ^{1}H NMR Spectrum for 1-(4-fluorophenyl) isoquinoline

Tian (2011) reported the CH_2-N i.e., on carbon C3 doublet in unsubstituted 1-phenyl isoquinoline, is usually deshielded at 8.80 ppm. In our case the introduction of F group in the phenyl ring led to an upfield shift to 8.67 ppm.

The MS, ^{1}H and ^{13}C NMR spectroscopy data confirmed the synthesis of 4-fluoro-1-phenyl isoquinoline.

4.1.8 4-Trifluoromethyl-1-phenylisoquinoline (Piq-CF_3) (L_8)

4-Trifluoromethyl-1-phenyl isoquinoline, $C_{16}H_{10}F_3N$, molecular weight 273.2525, was prepared by introducing a trifluoromethyl group on *para* position of the phenyl ring attached to isoquinoline backbone as described in Section 3.2.8 to form Piq-CF_3 shown in Scheme 21. Eighty three percent (0.341 g, 83%) yield was obtained and the product was soluble in polar solvents.

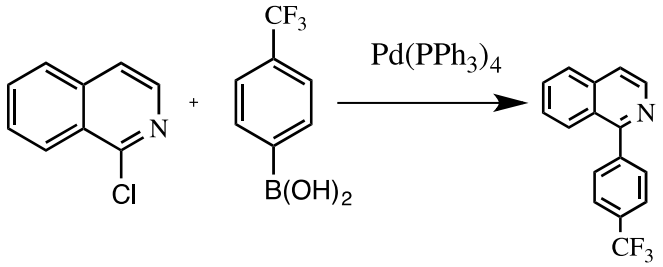

4-trifluoromethyl-1-phenyl isoquinoline

Scheme 21: Synthesis of 4-trifluoromethyl-1-phenyl isoquinoline

The structure of the Piq-CF_3 was confirmed where the calculated mass of the peak of the parent ion HRMS-APCI (*m/z*): $[M+H]^+$ 274.0799 corresponded with the observed 274.0847, as shown in Figure 19 conforming to the expected fragmentation pattern of the molecule.

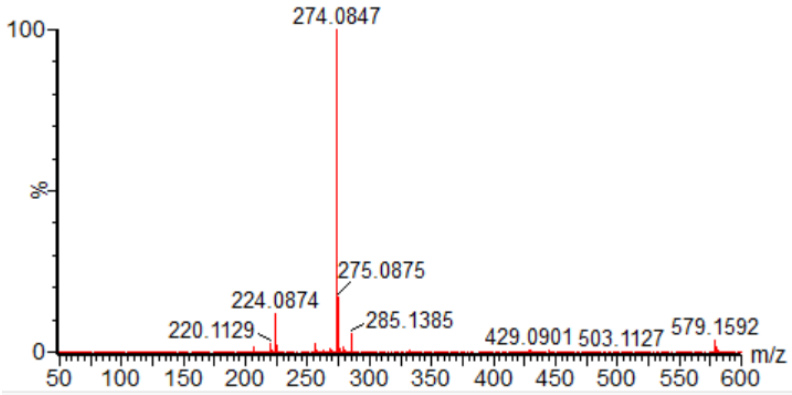

Figure 19: Mass spectrum 4-trifluoromethyl-1-phenyl isoquinoline

The proton NMR for Piq-CF_3 gave the following chemical shifts values as shown in Figure 20: ^{1}H NMR (400 MHz, $CDCl_3$) δ 8.66 (d, *J* = 5.7 Hz, 1H), 8.09 – 8.01 (m, 1H), 7.95 (d, *J* = 8.2 Hz, 1H), 7.89 – 7.80 (m, 4H), 7.79 – 7.70 (m, 2H), 7.60 (ddd, *J* = 8.3, 6.9, 1.2 Hz, 1H) suggesting the synthesis of 4-trifluoromethyl-1-phenyl isoquinoline.

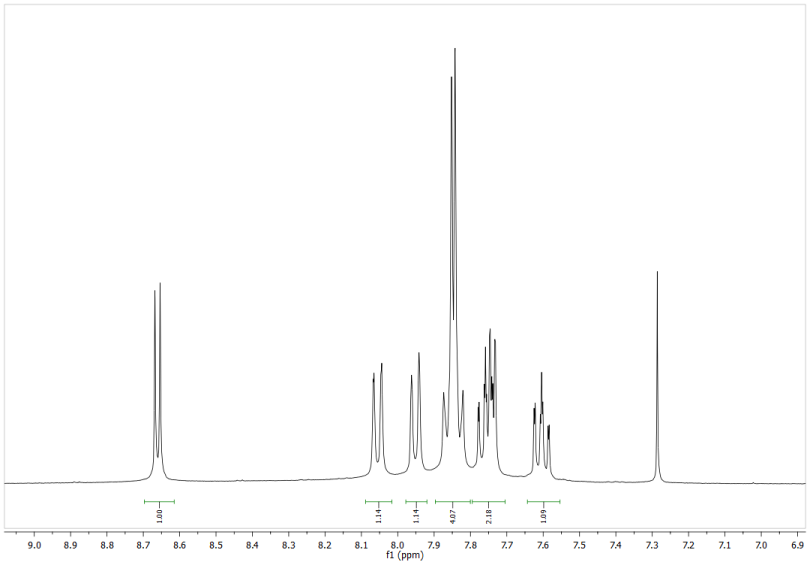

Figure 20: ^{1}H NMR Spectrum for 4-trifluoromethyl-1-phenyl isoquinoline

The MS, ^{1}H and ^{13}C NMR spectroscopy data confirmed the synthesis of 4-trifluoromethyl-1-phenyl isoquinoline.

4.1.9 4-*Tert*-butyl-1-phenyl isoquinoline (Piq-tBu$_3$) (L$_9$)

4-*tert*-butyl-1-phenyl isoquinoline, $C_{19}H_{19}N$, molecular weight 261.3609, was prepared by introducing a bulky 4-*tert*-butyl EDG group on para position of the phenyl ring attached to isoquinoline backbone as described in Section 3.2.9 to form a Piq-tBu$_3$ shown in Scheme 22. Sixty five percent (0.518 g, 65%) yield was obtained and the product was soluble in polar solvents.

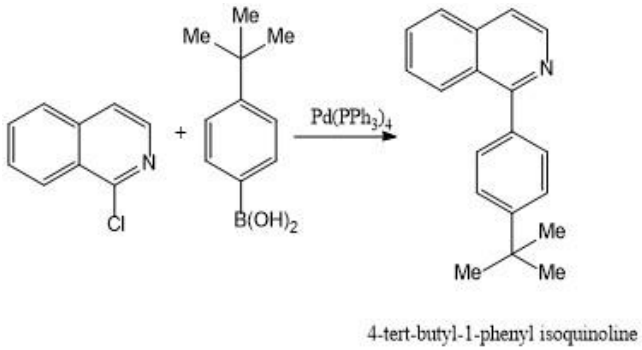

Scheme 22: Synthesis of 4-*tert*-butyl-1-phenyl isoquinoline

The structure of the Piq-tBu_3 was confirmed where the calculated mass of the peak of the parent ion HRMS-APCI (*m/z*): $[M+H]^+$ 262.1551corresponded with the observed 262.1596, as shown in Figure 21 conforming to the expected fragmentation pattern of the molecule.

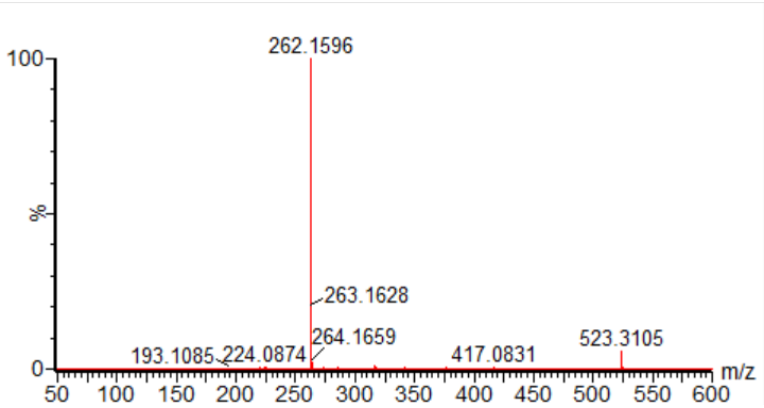

Figure 21: Mass Spectrum for 4-*tert*-butyl-1-phenyl isoquinoline

The proton NMR for Piq-tBu_3 gave the following chemical shifts values as shown in Figure 22: ^{1}H NMR (400 MHz, $CDCl_3$) δ 8.63 (d, *J* = 5.7 Hz, 1H), 8.21 (dd, *J* = 8.5, 0.7 Hz, 1H), 7.90 (d, *J* = 8.2 Hz, 1H), 7.69 (tdd, *J* = 9.8, 7.3, 3.4 Hz, 4H), 7.60 – 7.53 (m, 3H), 1.43 (s, 9H).

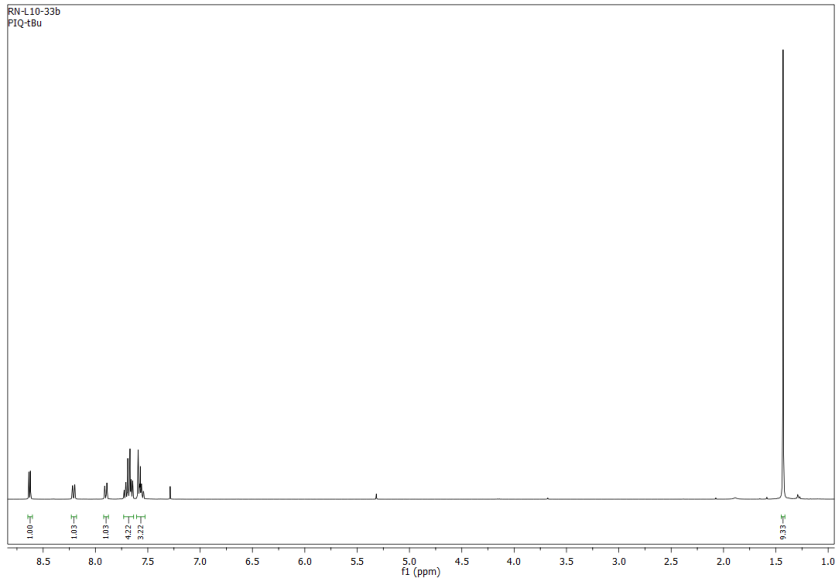

Figure 22: ^{1}H NMR Spectrum for 4-*tert*-butyl-1-phenyl isoquinoline

The MS, ^{1}H and ^{13}C NMR spectroscopy data confirmed the synthesis of 4-*tert*-butyl-1-phenyl isoquinoline.

4.1.10 4-Methyl-1-phenyl isoquinoline (Piq-Me) (L_{10})

4-methyl-1-phenyl isoquinoline, $C_{16}H_{13}N$, molecular weight 219.2811, was prepared by introducing a methyl group on para position of the phenyl ring attached to isoquinoline backbone as described in Section 3.2.10 to form a Piq-Me shown in Scheme 23. Eighty nine percent (0.593 g, 89%) yield was obtained and the product was soluble in polar solvents.

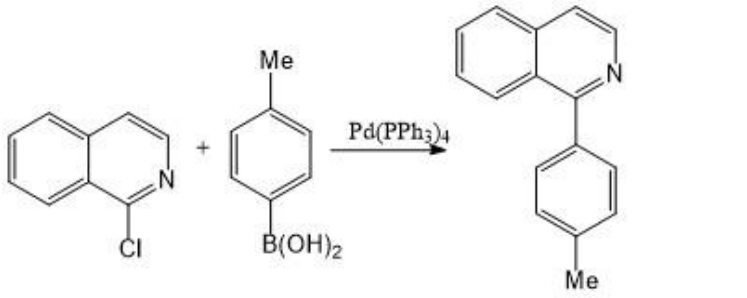

4-methyl-1-phenyl isoquinoline

Scheme 23: Synthesis of 4-methyl-1-phenyl isoquinoline

The structure of the L_{10} was confirmed where the calculated mass of the peak of the parent ion HRMS-APCI (*m/z*): $[M+H]^+$ 220.1082 corresponded with the observed 220.1130, as shown in Figure 23 conforming to the expected fragmentation pattern of the molecule.

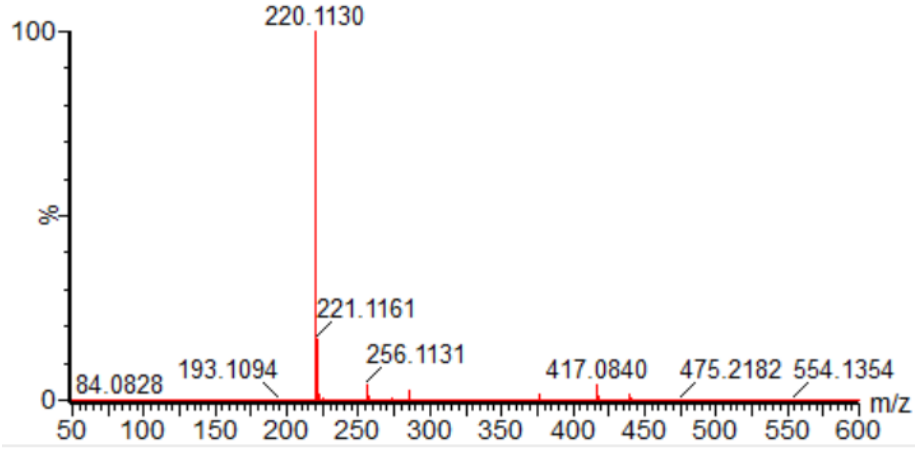

Figure 23: Mass Spectrum for 4-methyl-1-phenyl isoquinoline

The proton NMR for Piq-Me gave the following chemical shifts values: ^{1}H NMR (400 MHz, $CDCl_3$) δ 8.62 (d, *J* = 5.7 Hz, 1H), 8.16 (d, *J* = 8.5 Hz, 1H), 7.90 (d, *J* = 8.1 Hz, 1H), 7.70 (t, *J* = 7.5 Hz, 1H), 7.66 – 7.60 (m, 3H), 7.55 (t, *J* = 7.7 Hz, 1H), 7.37 (d, *J* = 8.2 Hz, 2H), 2.49 (s, 3H) confirming 4-methyl-1-phenyl isoquinoline as shown in Figure 24.

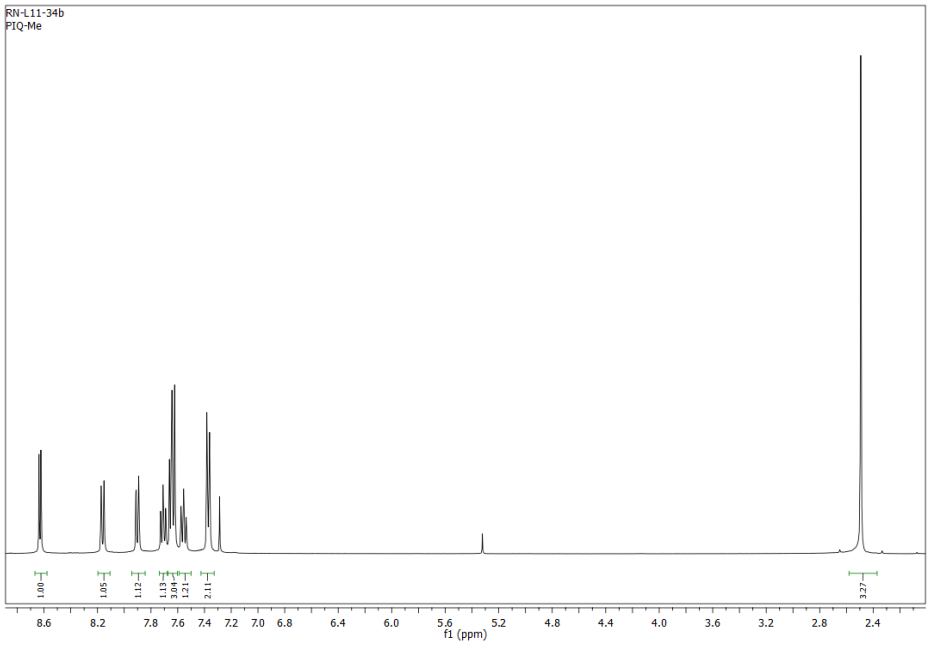

Figure 24: ^{1}H NMR Spectrum for 4-methyl-1-phenyl isoquinoline

The MS, ^{1}H and ^{13}C NMR data confirmed the synthesis of 4-methyl-1-phenyl isoquinoline.

4.2 Synthesis of *tris* cyclometalated homoleptic Ir (III) complexes

Ten *tris* homoleptic iridium(III) complexes, C-L_1-C-L_{10}, from each of the ten ligands were synthesized using the modified cyclometalation protocols as explained in section 3.4.

4.2.1 *Tris* 2-(1-naphthyl) pyridyl iridium (C-L_1); Ir(npy)$_3$

Tris 2-(1-naphthyl) pyridyl iridium, $C_{45}H_{30}IrN_3$, molecular weight 804.9730, was synthesized from npy (L_1) as described in Section 3.4.1 and is shown in Scheme 24. Forty four percent (0.047 g, 44%) yield as red crystals was obtained.

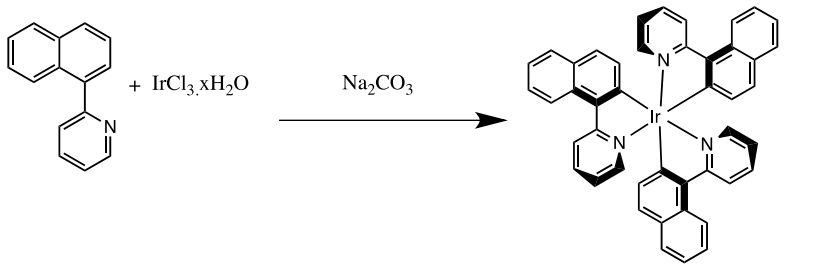

2-(1-Naphthyl) Pyridine

Tris 2-(1-naphthyl) pyridyl iridium

Scheme 24: Structure for *tris* 2-(1-naphthyl) pyridyl iridium

The solubility tests showed that the complex was not completely soluble in various solvents such as MeOH, CH_3CN, and DMSO even when heated or sonicated but was sufficiently soluble in CH_2Cl_2 and $C_2H_2Cl_4$.

Therefore, CH_2Cl_2 was used for subsequent studies such as photophysical and electrochemical measurements. C-L_1 was found to be air-stable, had high melting point (>300^{o}C), indicative of their thermal stability which was consistent with literature values of similar complexes (Tian, 2011).

The structure of the C-L_1 was suggested by HRMS. The calculated peak for parent ion obtained through Time of flight high-resolution mass spectroscopy; HRMS-ESI+ (*m/z*): $[M+H]^+$ for $C_{45}H_{31}IrN_3$ was 805.2069 and corresponded to the observed peak 805.2081 as illustrated in Figure 25.

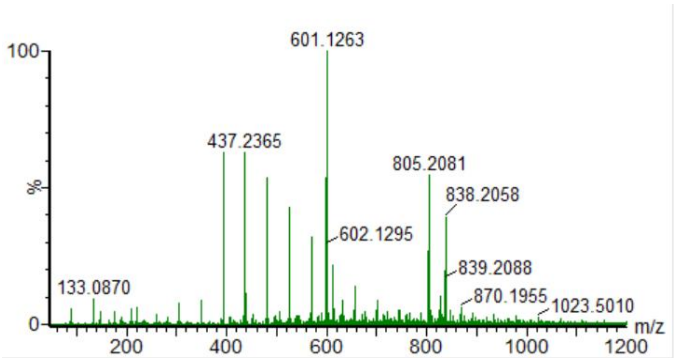

Figure 25: Mass Spectrum for *tris* 2-(1-naphthyl) pyridyl iridium

The fragmentation peak at 601.1263 was notable and corresponded to the complex after it had lost one ligand. The fragmentation patterns confirmed the expected formulations of the complexes.

The photophysical properties of C-L_1 were determined via UV-VIS spectroscopy and fluorescence spectroscopy as shown in Figure 26. The maximum absorption wavelength (λ_{max}) for C1 was observed to be 410 nm was used as the excitation wavelength for the fluorescence measurement giving emission maxima of 591 nm qualifying the specificity of this complex, C-L_1 behaving as a chromophore. The absorption and emission λ_{max} values proved that the ligand had coordinated with the Ir center.

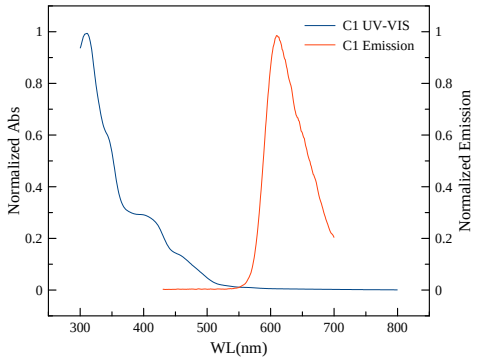

Figure 26: UV-VIS and PL Spectra for *tris* 2-(1-naphthyl) pyridyl iridium

From the UV-VIS spectrum, low energy absorption bands at ca. 348 nm were observed and ascribed to spin-allowed metal-to-ligand charge transfer transition (^{1}MLCT) in which an electron is promoted from a metal d orbital to a vacant π^* orbital on one of the ligands. The CT transition

are more likely to be MLCT than LMCT since the former occurs if the metal is in an oxidation state that allows it to be easily oxidized while the latter occurs if the metal is in an oxidation state that allows it to be easily reduced (House, 2018). The absorption above 400 nm with minimal extinction coefficient (usually 10-100$M^{-1}cm^{-1}$) could be attributed to $^3\pi$-π^* and ^{3}MLCT d - π^* transitions. Second band d-d transitions, which could be masked by the charge transfer transitions, can also be observed in this range albeit at low intensity with very low molar extinction coefficients since they are Laporte forbidden but are allowed due to SOC and vibronic coupling owing to their relatively low energy of transition. For C-L_1 d-d transition corresponded to 410 nm with 10Dq value of 24390 cm^{-1}. These observations were consistent with literature values of similar compounds (Greenwood & Earnshaw, 1998; Ulbricht, 2009; Pandey *et al.*, 2010; House, 2018).

The proton NMR of C-L_1 gave chemical shift values as: ^{1}H NMR (500 MHz, $C_2D_2Cl_4$) δ 8.43 (d, J = 8.7 Hz, 1H), 8.35 (d, J = 8.9 Hz, 1H), 7.66 – 7.56 (m, 2H), 7.46 (dd, J = 5.6, 1.0 Hz, 1H), 7.38 (ddd, J = 8.5, 6.8, 1.5 Hz, 1H), 7.23 (ddd, J = 7.9, 6.8, 1.0 Hz, 1H), 7.07 (d, J = 8.3 Hz, 1H), 6.96 (d, J = 8.3 Hz, 1H), 6.83 (ddd, J = 7.2, 5.5, 1.2 Hz, 1H) corresponding to Figure 27 and confirming C-L_1. The Carbon six (C6) value in C-L_1 shifted from 8.81 ppm in the ligand to 8.43 ppm in the complex due to coordination effect arising from C-H activation and subsequent cyclometalation. There were 10 peaks since all the ligands are chemically equivalent hence only one set of ten peaks, instead of eleven, Figure 6, as in the case of L_1 is observed.

Typically, homoleptic complexes tend to form facile complexes which, was evidenced by lack of isomers and subsequence chemical equivalency of the 3 C^N ligands in proton NMR spectroscopy due to C3 symmetry as opposed to meridional complexes which leads to formation of isomers. Similar to its respective ligand, electronegativity of the nitrogen atom created a deshielding effect of the proton *ortho* to N on the pyridine ring (on C6) at δ=8.43 ppm and this is consistent with literature values of similar complexes (Tian, 2011) although it was shifted upfield as compared to the ligand δ=8.81 ppm. This could be due to pi- back bonding/synergic bonding, where metal center receives electrons from the ligand into its empty d orbitals making it electron rich thus back-donates these electrons into the pi-antibonding orbitals of the ligand causing an upfield shift, δ 8.43-6.83 ppm.

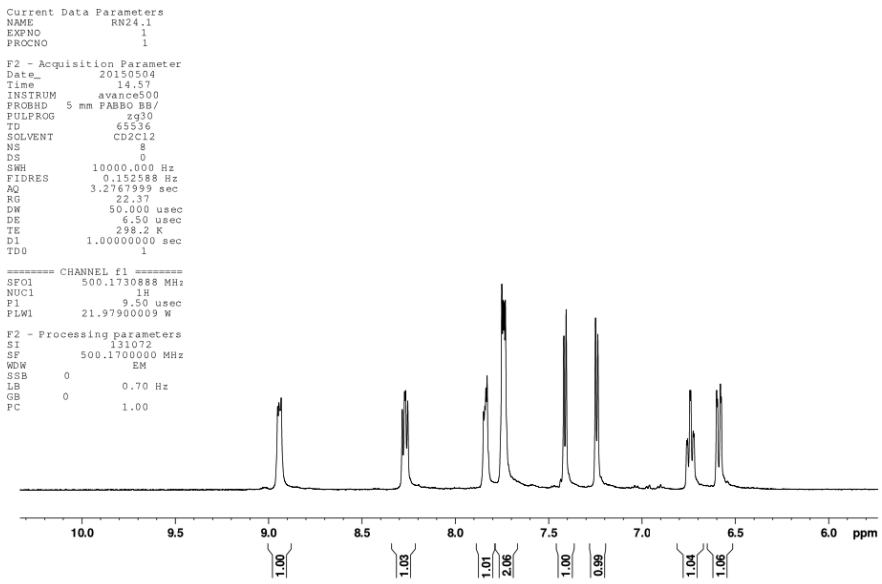

Figure 27: ^{1}H NMR Spectrum for *tris* 2-(1-naphthyl) pyridyl iridium

Carbon 13 gave 15 non-equivalent peaks: ^{13}C NMR (126 MHz, $C_2D_2Cl_4$) δ 168.13, 167.09, 148.05, 137.31, 136.95, 136.38, 132.18, 130.77, 129.73, 129.21, 126.35, 123.34, 122.43, 122.16, 121.5 suggesting the synthesis of *tris* 2-(1-naphthyl) pyridyl iridium and the ^{13}C NMR spectrum is given in the Appendix 1.7. C2 and C6 were still the most deshielded to due the electronegativity of nitrogen with C2 being more deshielded with δ= 168.13 ppm than C6 with δ =167.09 ppm with these values being more deshielded than L_1 showing the effects of the Ir metal center.

2D COSY NMR was used to further characterize where correlations between mutually coupled protons was established in the complex and the spectrum is given in the Appendix 1.8.

The elemental analysis for (C-L_1) showed that the calculated values $C_{45}H_{30}IrN_3$: C, 67.14; H, 3.76; N, 5.22 corresponded with the observed values of 67.11; H, 3.72; N, 5.25 suggesting the purity and composition of *tris* 2-(1-naphthyl) pyridyl iridium.

A single crystal for C1 was successfully grown and its structure elucidated from XRD *cf* Figure 28.

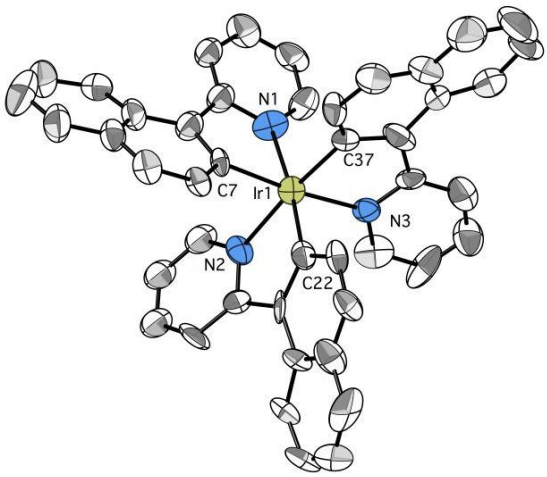

Figure 28: Crystal Structure for *tris* 2-(1-naphthyl) pyridyl iridium

The atom labeling corresponded with the crystal structure (Figure 28). The vital bond angles and cyclic bond lengths of the C and N atoms around the Ir center are: Ir-N1, 2.09(1); Ir-N2 2.14(1); Ir-N3, 2.13(1); Ir-C7, 2.03(1); Ir-C22, 2.00(2); Ir-C37, 2.03(1); Ir-N1-C1, 125(1); Ir-N1-C5, 119(1); Ir-N2-C16, 127(1); Ir-N2-C20, 116.3(9); Ir-N3-C31, 126(1); Ir-N3-C35, 115.3(9); N1-Ir-N2, 96.4(4); N1-Ir-N3, 95.8(4); N2-Ir-N3, 99.2(4). All the bond angles for the complex are summarized Appendix 4. This showed that the complex had a facial arrangement of the non-polymeric, three-cyclometalating ligands around the iridium center, through bidentate chelation with a 2-fold rotation axis proved that *tris* 2-(1-naphthyl) pyridyl iridium is octahedral structure complex. Moreover, ^{1}H NMR shifts was also found to be consistent with a facial structure, which corresponded to the number of coupled spins being equal to those of the protons on one ligand since all the 3 ligands are magnetically equivalent.

The HRMS, ^{1}H ^{13}C and 2D COSY NMR spectroscopy, elemental analysis and XRD data confirmed the synthesis of *tris* 2-(1-naphthyl) pyridyl iridium.

4.2.2 *Tris* 2-(1-naphthyl)-4-methoxy pyridyl iridium (C-L_2); Ir(npy-OMe)$_3$

Tris 2-(1-naphthyl)-4-methoxy pyridyl iridium, $C_{48}H_{36}IrN_3O_3$, molecular weight 895.2386, was synthesized from npy-OMe as described in Section 3.4.2 and shown in Scheme 25. Fifty percent (0.055 g, 50%) yield of red powder was obtained. The complex was found to be soluble in

halogenated solvents such as CH_2Cl_2 and $C_2H_2Cl_4$, and it was both air and thermally stable since it had a melting point of >300 ^oC. C-L_2 had better solubility than C-L_1, which was consistent with studies that have shown that addition of alkyl groups in the ancillary ligands of heteroleptic Ir(III) complexes can serve to improve the solubility of complexes in organic solvents (Tian, 2011).

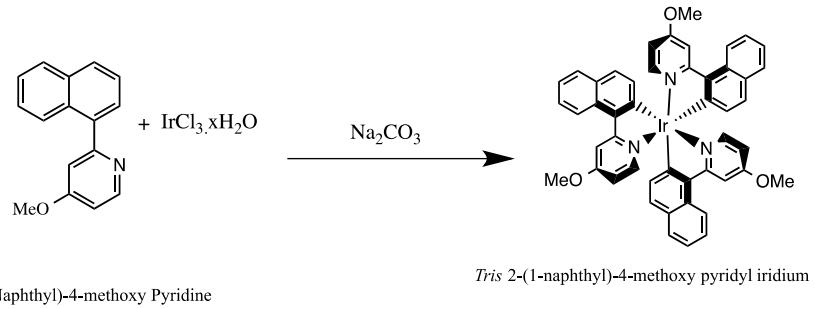

2-(1-Naphthyl)-4-methoxy Pyridine

Tris 2-(1-naphthyl)-4-methoxy pyridyl iridium

Scheme 25: Structure for *tris* 2-(1-naphthyl)-4-methoxy pyridyl iridium

The structure of the C-L_2 was confirmed where the calculated peak for parent ion obtained through time of flight high-resolution mass spectroscopy; HRMS-ESI+ (*m/z*): $[M+H]^+$ for $C_{48}H_{37}IrN_3O_3$ was 896.2419 and corresponded to the observed peak 896.2465 as illustrated in Figure 29.

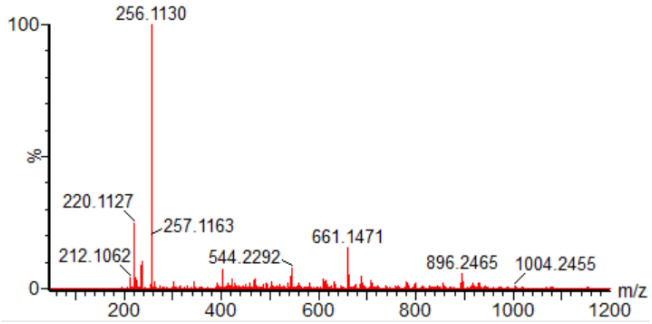

Figure 29: HRMS Spectrum for *tris* 2-(1-naphthyl)-4-methoxy pyridyl iridium

The fragmentation peak at 661.1471 was notable and corresponded to the complex after it had lost one ligand. The fragmentation patterns confirm the expected formulations of the complexes.

The photochemistry of Ir(npy-OMe)$_3$ as illustrated in Figure 30, gave λ_{max} as 418 nm and subsequently after excitation at this λ, the emission for the complex was found to be 610 nm, qualifying the specificity of this complex, C-L_2 behaving as a chromophore. The λ_{max} values proved

coordination with Ir(III) and were consistent with the expected literature values since substitution with electron donating methoxy group, albeit on the phenyl ring, should cause a red-shift of the emission energy (Hasan et al., 2015).

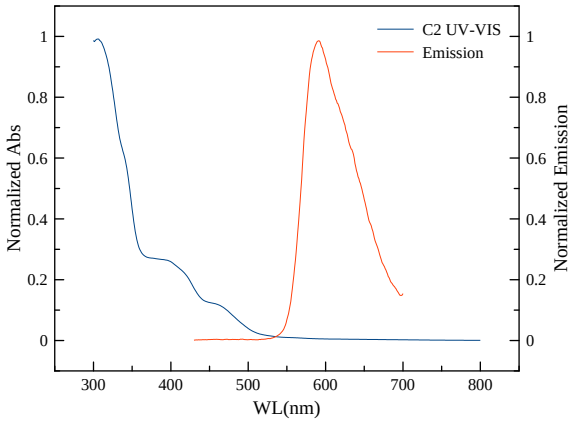

Figure 30: UV-VIS and PL spectra for *tris* 2-(1-naphthyl)-4-methoxy pyridyl iridium

The 343nm absorption bands are ascribed to spin-allowed metal-to-ligand charge transfer transition (MLCT) while the 418 nm band was ascribed to spin–orbit coupling (SOC) enhanced d-d transitions with a corresponding 10Dq value 23923 cm^{-1}.

The methoxy electron donating group raised the energy of the HOMO level hence reduced the HOMO-LUMO gap which led the emission to be red shifted to 610nm. This was consistent with reports in complexes based on the 2-phenylpyridine ligand that the HOMO level is strongly affected by substituents in the phenyl ring where the EDG raises the energy level of the HOMO hence reducing the HOMO-LUMO gap while EWG lowers HOMO level hence increasing the gap (Okada *et al.*, 2005; Hasan *et al.*, 2015).

The proton NMR of C-L_2 gave chemical shift values as: ^{1}H NMR (500 MHz, $C_2D_2Cl_4$) δ 8.92 – 8.88 (m, 1H), 8.16 (d, *J* = 8.8 Hz, 1H), 7.79 – 7.73 (m, 1H), 7.67 – 7.63 (m, 2H), 7.36 (d, *J* = 6.2 Hz, 1H), 7.11 (d, *J* = 6.2 Hz, 1H), 6.54 (dd, *J* = 8.8, 2.8 Hz, 1H), 6.47 (d, *J* = 2.8 Hz, 1H), 3.56 (s, 3H), corresponding to Figure 31, gave a sharp singlet upfield at δ= 3.56 ppm corresponding to the methoxy protons.

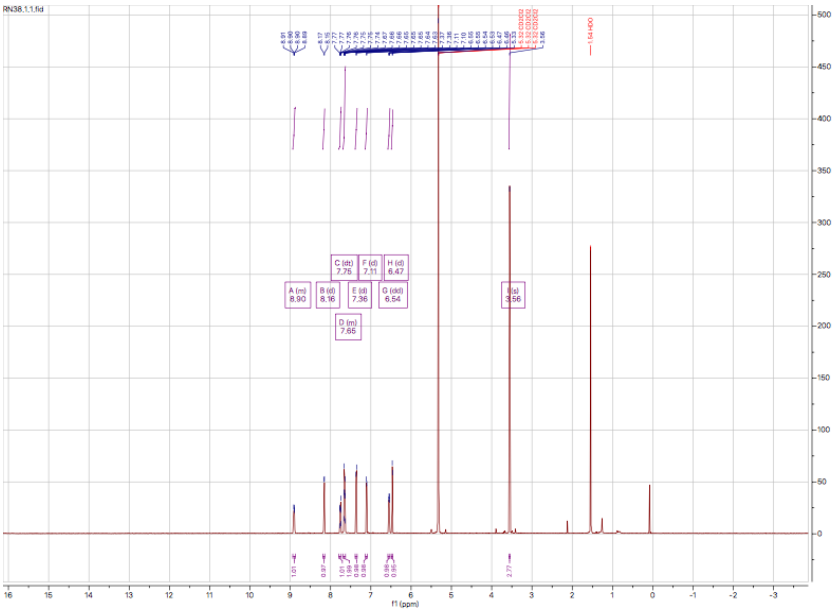

Figure 31: ^{1}H NMR Spectrum for *tris* 2-(1-naphthyl)-4-methoxy pyridyl iridium

The rest were observed as a set of nine chemically non-equivalent aromatic protons between 8.92-6.47 ppm as compared to 10 protons on npy-OMe. In C-L_2, the chemical shift values were deshielded with the most downfield value being 8.92 ppm in comparison to 8.43 ppm in C-L_1, which was not expected and contradicted the observed pattern of the ligands (L_1 vs. L_2). The strong electron donating methoxy group was expected to increase the electron density of the system leading to upfield shifts. However, downfield shifts were observed and this could be attributed to steric hindrances caused by the bulky -OMe group having a greater influence where steric compression forces protons to be close to each other and this typically leads to deshielding according to literature (Reich & Reich, 2018).

Carbon 13 gave 16 chemically non-equivalent peaks of the ligand as shown: ^{13}C NMR (126 MHz, $C_2D_2Cl_4$) δ 168.30, 167.34, 161.19, 140.33, 138.95, 137.21, 131.99, 130.68, 127.98, 127.89, 127.50, 126.61, 121.32, 119.70, 106.40. The δ were not affected by the steric hindrances as observed in ^{1}H NMRspectrum. The ^{13}C and COSY NMR spectra are given in Appendix 1.9 and Appendix 1.10 respectively with COSY giving correlations of mutually coupled protons in the complex and these suggested the synthesis of *tris* 2-(1-naphthyl)-4-methoxy pyridyl iridium. Carbon C4 which is directly attached to methoxy was the most deshielded with δ =168.30 ppm due to the resonance effect of the oxygen. This was closely followed by carbon C2 with δ =167.34

ppm and C6 with δ =161.19 ppm due to the deshielding effect of the electronegative nitrogen. These carbons were more deshielded than L_2 showing the effects of the Ir metal center.

The elemental analysis for C-L_2 showed that the calculated values C, 64.41; H, 4.05; N, 4.69 corresponded with the observed values of C, 64.69; H, 4.41; N, 4.34 suggesting the purity and composition of *tris* 2-(1-naphthyl)-4-methoxy pyridyl iridium.

C-L_2 did not form appropriate crystals for XRD.

The HRMS, UV-Vis, ^{1}H ^{13}C and 2D COSY NMR spectroscopy and elemental analysis data confirmed the synthesis of *tris* 2-(1-naphthyl)-4-methoxy pyridyl iridium.

4.2.3 *Tris* 2-(1-naphthyl)-4-trifluoromethyl pyridyl iridium (C-L_3); Ir(npy-CF_3)$_3$

Tris 2-(1-naphthyl)-4-trifluoromethyl pyridyl iridium, $C_{48}H_{27}F_9IrN_3$, molecular weight 1008.9676, was synthesized as described in Section 3.4.3 and as shown in Scheme 26. Thirty nine percent (0.042 g, 39%) red powder yield was obtained. The complex was air-stable with a melting point of >300^{o}C.

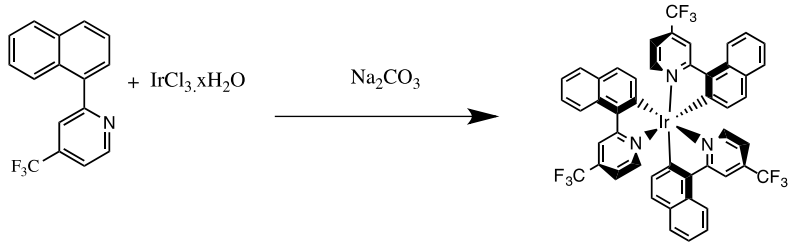

2-(1-Naphthyl)-4-trifluoromethyl Pyridine

Tris 2-(1-naphthyl)-4-trifluoromethyl pyridyl iridium

Scheme 26: Structure for *tris* 2-(1-naphthyl)-4-trifluoromethyl pyridyl iridium

The HRMS of Ir(npy-CF_3)$_3$ given in Figure 32 showed the main fragment to be m/z 274au which corresponds to a single ligand npy-CF_3 while the zoomed version Figure 33, showed the observed $[M+H]^+$ 1010.18 of the parent ion to correspond to the calculated mass of 1010. As summarized HRMS-ESI+ (*m/z*): $[M+H]^+$ calc for $C_{48}H_{28}F_9IrN_3$, 1010.1724; found, 1010.1780.

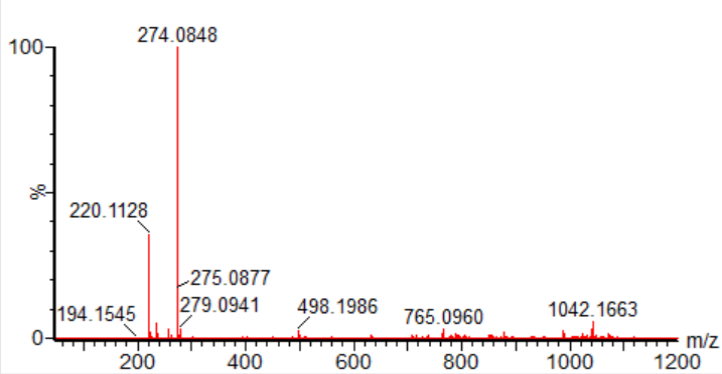

Figure 32: HRMS Spectrum for *tris* 2-(1-naphthyl)-4-trifluoromethyl pyridyl iridium

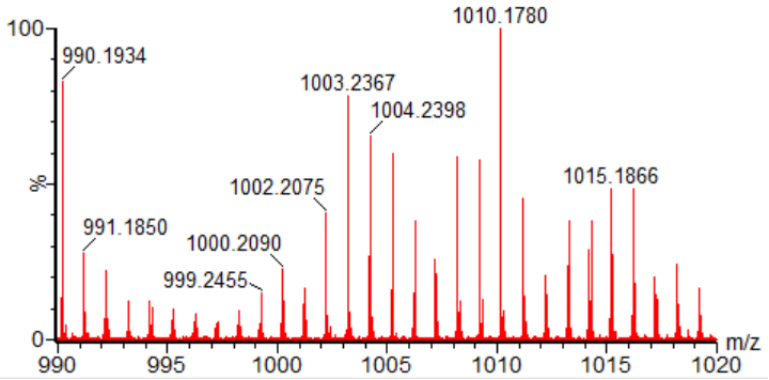

Figure 33: HRMS Spectrum for *tris* 2-(1-naphthyl)-4-trifluoromethyl pyridyl iridium

The absorption λ_{max} for C-L_3 as shown in Figure 34 was 435 nm and the emission corresponding to this excitation was found to be 603 nm qualifying the specificity of this complex, C-L_3 behaving as a chromophore. The 351 nm absorption bands are ascribed to spin-allowed metal-to-ligand charge transfer transition (MLCT) while the 435 nm band was ascribed to spin–orbit coupling (SOC) enhanced d-d transitions with the corresponding 10Dq value 22988 cm^{-1}, which was consistent with allowed d-d transitions for Ir(III) complexes bearing strong field ligands reported in literature (Pandey et al., 2010).

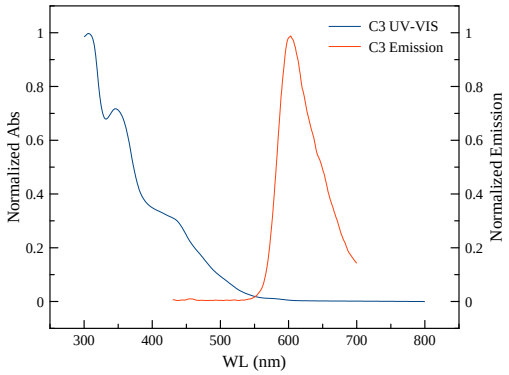

Figure 34: UV-VIS and PL for *tris* 2-(1-naphthyl)-4-trifluoromethyl pyridyl iridium

C-L_3 emission was blue shifted as compared to C-L_2 (610 nm) by 7 nm and this is consistent with its electron withdrawing nature. However, when compared to C-L_1 (591 nm) it is red shifted by 12 nm and this could be due to the inductive effects of CF_3 when it mimics CH_3 (Nagai et al., 1991).

The proton NMR of C-L_3 gave chemical shift values as: ^{1}H NMR (500 MHz, $C_2D_2Cl_4$) δ 8.73 (s, 1H), 8.50 (d, *J* = 8.5 Hz, 1H), 7.87 (d, *J* = 5.8 Hz, 1H), 7.77 (d, *J* = 8.3 Hz, 1H), 7.56 (d, *J* = 7.0 Hz, 1H), 7.39 (t, *J* = 7.0 Hz, 1H), 7.25 (d, *J* = 8.2 Hz, 1H), 7.14 (d, *J* = 5.9 Hz, 1H), 7.04 (d, *J* = 8.3 Hz, 1H) corresponding to the spectrum shown in Figure 35, exhibited a set of 10 peaks that were all chemically non-equivalent and corresponded to the aromatic protons with the values δ= 8.7-7.04 ppm. This suggested the synthesis of *tris* 2-(1-naphthyl)-4-trifluoromethyl pyridyl iridium.

C-L_3 δ were shifted downfield as compared to C-L_1, which is expected due to the electron withdrawing effects of CF_3. When compared to C-L_2, it was shifted upfield, which was unexpected since C-L_2 had an -OMe EDG substituent with less steric effect than CF_3 hence C-L_2 should have been more shielded. Therefore, the deviation could be attributed to CF_3's ability to display "mimic effect" where the steric requirement for F is similar to H hence CF_3 ends up behaving like CH_3 (an electron donor) thus the upfield shift (Nagai *et al.*, 1991). In addition, CF_3 is also known to have inductive-only nature (Coppo *et al.*, 2004). Moreover, the synergic bonding of the metal center here could serve to increase the electron density in the system, which had been depleted by EWG hence the upfield shift as compared to the corresponding ligand.

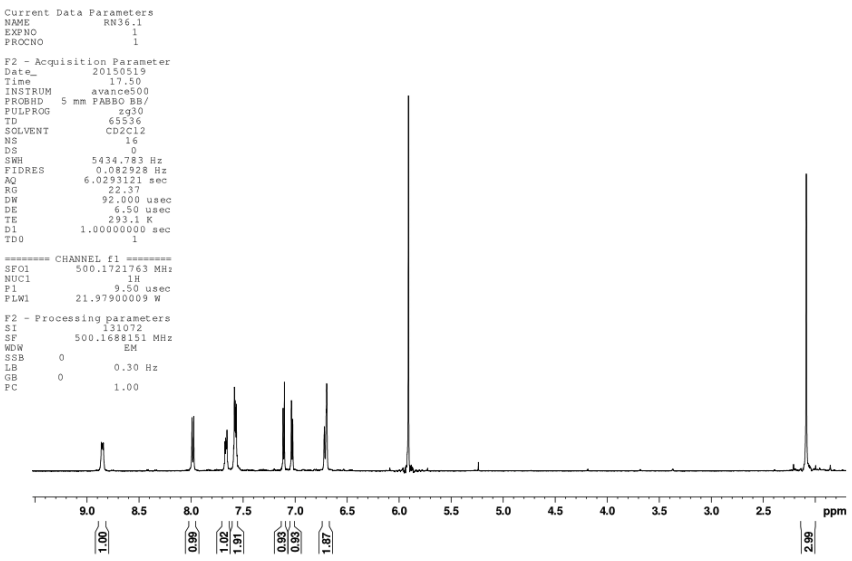

Figure 35: ^{1}H NMR Spectrum for *tris* 2-(1-naphthyl)-4-trifluoromethyl pyridyl iridium

The C-13 NMR of C-L_3 gave chemical shift values as: ^{13}C NMR (126 MHz, $C_2D_2Cl_4$) δ 168.52, 168.30, 149.28, 136.01, 132.54, 131.43, 130.84, 130.03, 127.31, 123.28, 121.45, 121.44, 119.03, 117.19 corresponding to the 16 peaks of the chemically equivalent ligands were consistent with theoretical peaks expected for C-L_3. Carbon C4 which was directly attached to trifluoromethyl group, was the most deshielded with δ =168.52 ppm due to the resonance effect of the -CF_3. This was closely followed by carbon C2 with δ =168.30 ppm and C6 with δ =149.28 ppm due to the deshielding effect of the electronegative nitrogen. These values being more deshielded than L_3 showing the effects of the Ir metal center.

The ^{13}C and COSY NMR spectra are given in the Appendix 1.11 and Appendix 1.12 respectively while ^{19}F NMR spectroscopy was done to confirm the presence of -CF_3 and the spectrum is given in Appendix 1.13.

The elemental analysis for C-L_3 showed that the calculated values to be C, 57.14; H, 2.70; N, 4.16; F, 16.95 corresponded with the observed values of C, 57.04; H, 2.87; N, 4.09; F, 16.83 suggesting the purity and composition of *tris* 2-(1-naphthyl)-4-trifluoromethyl pyridyl iridium
The HRMS, UV-Vis, ^{1}H ^{13}C, ^{19}F and 2D COSY NMR spectroscopy and elemental analysis data confirmed the synthesis of *tris* 2-(1-naphthyl)-4-trifluoromethyl pyridyl iridium.

4.2.4 *Tris* 2-(1-naphthyl)-4-methyl pyridyl iridium (C-L$_4$); Ir(npy-Me)$_3$

Tris 2-(1-naphthyl)-4-methyl pyridyl iridium, $C_{48}H_{37}IrN_3$, molecular weight 847.0540, was synthesized as described in Section 3.4.4 and summarized in Scheme 27. Forty-three percent (0.048 g, 43%) yield of red powder was obtained. The complex was air and thermally stable with its melting point being determined to be >300^{o}C.

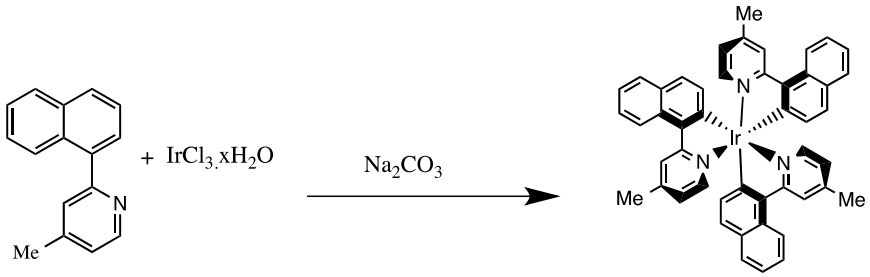

2-(1-Naphthyl)-4-methyl Pyridine

***Tris* 2-(1-naphthyl)-4-methyl pyridyl iridium**

Scheme 27: Structure for *tris* 2-(1-naphthyl)-4-methyl pyridyl iridium

The structure of the C-L$_4$ was confirmed where the calculated peak for parent ion obtained through Time of flight high-resolution mass spectroscopy; HRMS-ESI+ (*m/z*): $[M+H]^+$ was 847.2538 and corresponded to the observed peak 847.2541 as illustrated in Figure 36. The fragmentation patterns confirm the expected formulations of the C-L$_4$.

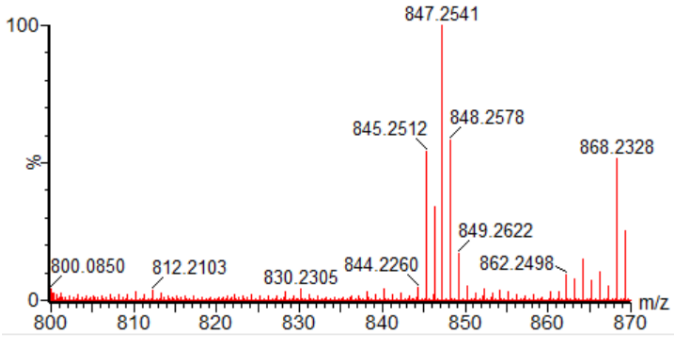

Figure 36: HRMS Spectrum for *tris* 2-(1-naphthyl)-4-methyl pyridyl iridium

The photophysical parameters for C-L$_4$ were measured and established to be λ_{max} 400 nm for UV-VIS absorbance and upon excitation of this an emission of 588 nm was observed as shown in

Figure 37, which qualified the specificity of this complex, C-L_4 behaving as a chromophore. The 345nm absorption bands are ascribed to spin-allowed metal-to-ligand charge transfer transition (MLCT) while the 400 nm band was ascribed to spin–orbit coupling (SOC) enhanced d-d transitions. Corresponding 10Dq value for absorption of C-L_4 was found to be 25000 cm^{-1} and was consistent with allowed d-d transitions for Ir(III) complexes bearing strong field ligands reported in literature (Pandey et al., 2010).

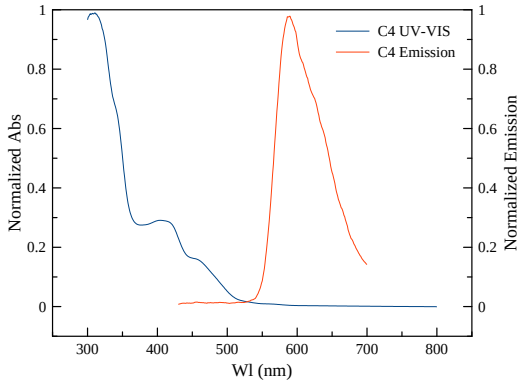

Figure 37: UV-VIS and PL for *tris* 2-(1-naphthyl)-4-methyl pyridyl iridium

Alkyl groups despite being electron donating can act as if they are weakly electron withdrawing through anisotropy hence emission for C-L_4 was strongly blue shifted than C-L_2 (610 nm) by 22 nm and even further than C-L_1 (591 nm) by 3 nm. This was consistent with literature according to Reich and Reich (2018).

The proton NMR of C-L_4 gave chemical shift values as: ^{1}H NMR (500 MHz, $C_2D_2Cl_4$) δ 8.53 (d, *J*= 8.7 Hz, 1H), 8.27 (s, 1H), 7.67 (d, *J* = 8.0 Hz, 1H), 7.50 (d, *J* = 5.7 Hz, 1H), 7.44 (t, *J* = 7.8 Hz, 1H), 7.27 (t, *J* = 7.4 Hz, 1H), 7.12 (d, *J* = 8.3 Hz, 1H), 7.00 (d, *J* = 8.3 Hz, 1H), 6.75 (d, *J* = 5.6 Hz, 1H), 2.46 (s, 3H) suggested the synthesis of *tris* 2-(1-naphthyl)-4-methyl pyridyl iridium, as shown in Figure 38**.** It had a singlet peak with δ= 2.45 ppm corresponding to the shielded methyl protons and a set of 10 aromatic protons at the range of 8.53-6.75 ppm. Comparison of C-L_2 and C-L_4 shows the expected trend where the chemical shift of C6 in C-L_4 8.53 ppm was upfield in comparison to 8.92 ppm of C6 in C-L_2 since despite C-L_2 having a stronger electron donating methoxy group, it is bulkier than the –Me group in C-L_4 hence the steric hindrances cause deshielding of C-L_2. This was consistent with literature according to Reich and Reich (2018).

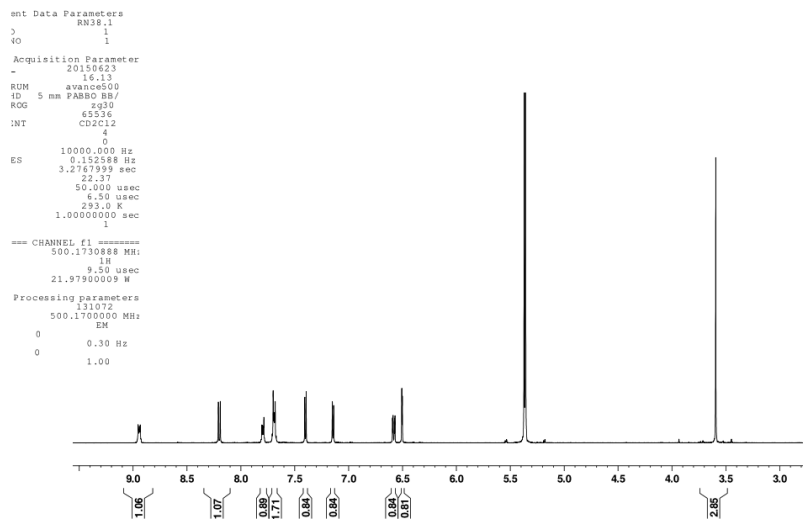

Figure 38: ^{1}H NMR Spectrum for *tris* 2-(1-naphthyl)-4-methyl pyridyl iridium

The carbon-13 NMR of C-L_4 gave expected chemical shift values that confirmed C4 as: ^{13}C NMR (126 MHz, $C_2D_2Cl_4$) δ 167.94, 166.31, 147.49, 147.30, 136.91, 136.21, 131.93, 130.73, 129.24, 128.52, 125.78, 123.72, 122.02, 121.80, 121.59, 21.26. The ^{13}C and COSY NMR spectra are given in the Appendix 1.14 and Appendix 1.15 respectively suggesting the synthesis of *tris* 2-(1-naphthyl)-4-methyl pyridyl iridium. Carbon C4, which is directly attached to methyl group, had δ =147.49 ppm was shifted to the right as compared to that of C-L_1. C2 and C6 were the most deshielded to due the electronegativity of nitrogen with C2 being more deshielded with δ= 167.94 ppm than C6 with δ = 166.31 ppm. These carbons were more deshielded than L_3 showing the effects of the Ir metal center.

The elemental analysis for C-L_4 showed that the calculated values to be C, 68.06; H, 4.28; N, 4.96 corresponded with the observed values of C, 68.35; H, 4.39; N, 4.82 suggesting the purity and composition of *tris* 2-(1-naphthyl)-4-methyl pyridyl iridium.
The HRMS, UV-Vis, ^{1}H ^{13}C and 2D COSY NMR spectroscopy and elemental analysis data confirmed the synthesis of *tris* 2-(1-naphthyl)-4-methyl pyridyl iridium.

4.2.5 *Tris* 2-(4-methylnaphthyl)-4-methyl pyridyl iridium (C-L_5); Ir(npy-Me_2)$_3$

Tris 2-(4-methylnaphthyl)-4-methyl pyridyl iridium, $C_{51}H_{42}IrN_3$, molecular weight of 889.1350, was synthesized as described in Section 3.4.5 and summarized in Scheme 28. Thirty nine percent

(0.043 g, 39%) yield of red powder was obtained. The complex was air and thermally stable with a melting point of > 300°C.

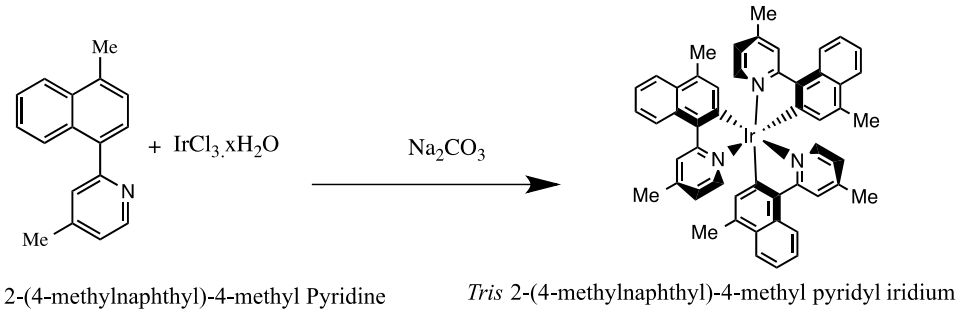

2-(4-methylnaphthyl)-4-methyl Pyridine

Tris 2-(4-methylnaphthyl)-4-methyl pyridyl iridium

Scheme 28: Structure for *tris* 2-(4-methylnaphthyl)-4-methyl pyridyl iridium

The structure of the C-L_5 was confirmed where the calculated peak for parent ion obtained through Time of flight high-resolution mass spectroscopy; HRMS-APCI+ (*m/z*): $[M+H]^+$ was 890.3086 and corresponded to the observed peak 890.2342 as illustrated in Figure 39. The fragmentation patterns confirmed the expected formulation of *tris* 2-(4-methylnaphthyl)-4-methyl pyridyl iridium.

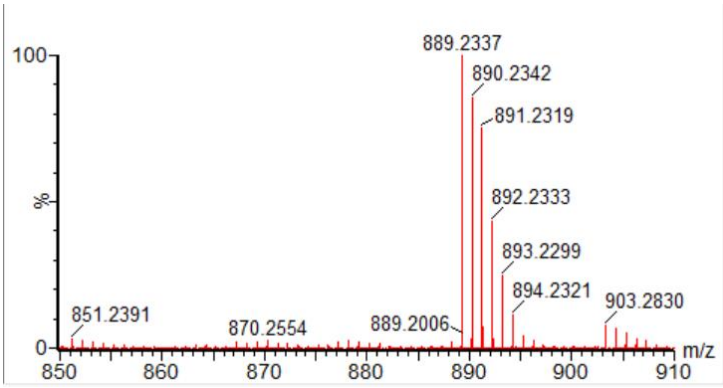

Figure 39: HRMS Spectrum for *tris* 2-(4-methylnaphthyl)-4-methyl pyridyl iridium

From the UV-VIS spectra, the λ_{max} was found to be 405 nm while from the fluorescence spectra the maximum emission was established to be at 603 nm qualifying the specificity of this complex, C-L_5 behaving as a chromophore as shown in Figure 40. C-L_5 emission is consistent with the expected red shift as compared to C-L_1 due to the electron donating methyl group. Additionally, the second methyl group in the naphthyl ring increased the red shift. This was consistent with

literature (Okada *et al.*, 2005, Hasan *et al.*, 2015). Corresponding 10Dq value for absorption of C-L_5 was found to be 24691 cm^{-1} and was consistent with allowed d-d transitions for Ir(III) complexes bearing strong field ligands reported in literature (Pandey et al., 2010). The 352nm absorption bands are ascribed to spin-allowed metal-to-ligand charge transfer transition (MLCT) while the 405 nm band was ascribed to spin–orbit coupling (SOC) enhanced d-d transitions.

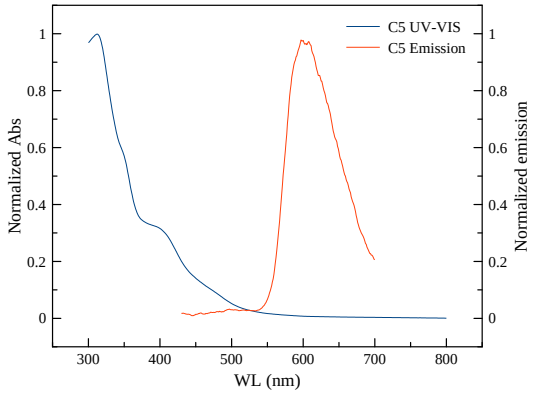

Figure 40: UV-VIS and PL Spectra for *tris* 2-(4-methylnaphthyl)-4-methyl pyridyl iridium

The proton NMR of C-L_5 gave expected chemical shift values as: ^{1}H NMR (500 MHz, $C_2D_2Cl_4$) δ 8.54 (d, J = 8.5 Hz, 1H), 8.19 (s, 1H), 7.86 (d, J = 8.2 Hz, 1H), 7.48 (d, J = 5.7 Hz, 1H), 7.43 (t, J = 7.7 Hz, 1H), 7.32 (t, J = 7.5 Hz, 1H), 6.99 (s, 1H), 6.68 (d, J = 5.7 Hz, 1H), 2.43 (s, 3H), 2.33 (s, 3H) suggesting the synthesis of *tris* 2-(4-methylnaphthyl)-4-methyl pyridyl iridium. The proton NMR obtained as given in Figure 41 showed two characteristic singlet peaks corresponding to the two -Me substituents on the naphthalene and pyridine rings at 2.76 ppm and 2.44 ppm respectively and a set of eight peaks of the aromatic protons at a range of 8.54 - 6.68 ppm.

C-L_5 chemical shifts were very similar to C-L_4 since they had the same substituent. The additional -Me in the naphthyl ring didn't not cause any significant effects in the δ values of the proton proximal to N; 8.53 vs.8.54 ppm. C-L_5 was more deshielded due to the weak anisotropic effects of -Me. This was consistent with literature (Reich & Reich, 2018).

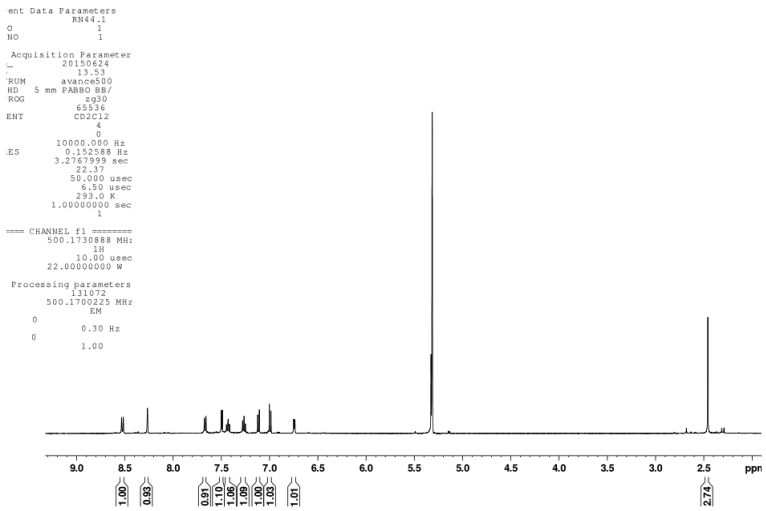

Figure 41: ^{1}H NMR Spectrum for *tris* 2-(4-methylnaphthyl)-4-methyl pyridyl iridium

^{13}C NMR (126 MHz, $C_2D_2Cl_4$) δ 168.94, 166.98, 147.80, 138.02, 136.23, 134.65, 132.48, 130.47, 125.85, 125.73, 123.99, 122.64, 122.15, 122.01, 30.23, 21.87, 19.96. The ^{13}C and COSY NMR spectra are given in the Appendix 1.16 and Appendix 1.17 respectively suggesting the synthesis of *tris* 2-(4-methylnaphthyl)-4-methyl pyridyl iridium. Carbon C4 had δ =147.80 ppm was shifted upfield as compared to that of C-L_1 due to the -Me electron donating effects. C2 and C6 were the most deshielded to due the electronegativity of nitrogen with C2 being more deshielded with δ=168.94ppm than C6 with δ =166.98ppm These values being more deshielded than L_5 showing the effects of the Ir metal center.

The elemental analysis for C-L_5 showed that the calculated values to be C, 68.29 H 4.76; N, 4.73 corresponded with the observed values of C, 68.26; H, 4.60; N, 4.97 suggesting the purity and composition of *tris* 2-(4-methylnaphthyl)-4-methyl pyridyl iridium.

The HRMS, UV-Vis, ^{1}H ^{13}C and 2D COSY NMR spectroscopy and elemental analysis data confirmed the synthesis of *tris* 2-(4-methylnaphthyl)-4-methyl pyridyl iridium.

4.2.6 *Tris* 2-(4-methylnaphthyl) pyridyl iridium (C-L_6); Ir(Me-npy)$_3$

Tris 2-(4-methylnaphthyl) pyridyl iridium, $C_{48}H_{37}IrN_3$, molecular weight of 847.0540, was synthesized according to Section 3.4.6 and is summarized in Scheme 29. Forty four percent

(0.0493 g, 44%) yield of red powder was obtained. The complex was thermal and air-stable with a melting point of >300ºC.

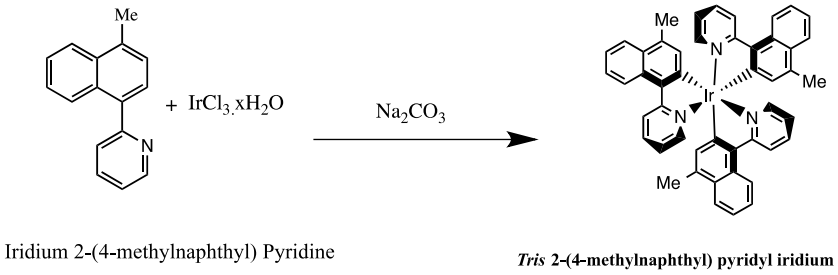

Iridium 2-(4-methylnaphthyl) Pyridine

***Tris* 2-(4-methylnaphthyl) pyridyl iridium**

Scheme 29: Structure for *tris* 2-(4-methylnaphthyl) pyridyl iridium

The structure of the C-L_6 was confirmed where the calculated peak for parent ion obtained through Time of flight high-resolution mass spectroscopy; HRMS-APCI+ (*m/z*): $[M+H]^+$ was 847.2617 and corresponded to the observed peak 847.2540 as illustrated in Figure 42. The fragmentation patterns confirm the expected formulations of C-L_6.

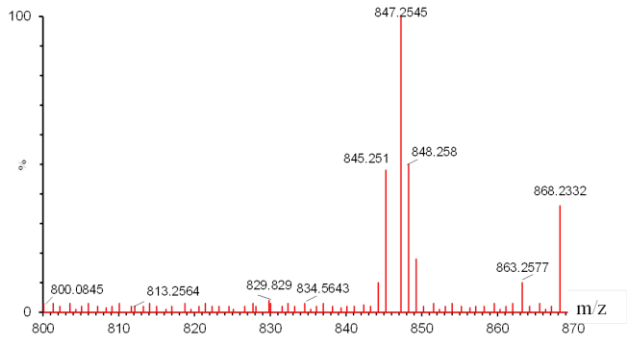

Figure 42: HRMS Spectrum for *tris* 2-(4-methylnaphthyl) pyridyl iridium

The photophysical properties of C-L_6 showed an absorption λ_{max} of 411 nm and emission maxima of 602 nm qualifying the specificity of this complex behaving as a chromophore as shown in Figure 43. The 354 nm absorption bands are ascribed to spin-allowed metal-to-ligand charge transfer transition (MLCT) while the 411 nm band was ascribed to spin–orbit coupling (SOC) enhanced d-d transitions. Corresponding 10Dq value for absorption of C-L_6 was found to be 24331 cm^{-1} and was consistent with allowed d-d transitions for Ir(III) complexes bearing strong field ligands reported in literature (Pandey et al., 2010). The emission maximum for C-L_6 was similar to C-L_5

probably indicating the influence of the -Me group in naphthyl group which is common for both complexes. The 350-400 nm absorption bands are ascribed to spin-allowed metal-to-ligand charge transfer transition (^{1}MLCT) and spin–orbit coupling (SOC) enhanced $^3\pi$-π^* and ^{3}MLCT t_{2g} d - π^* and d-d transitions for those above 400 nm.

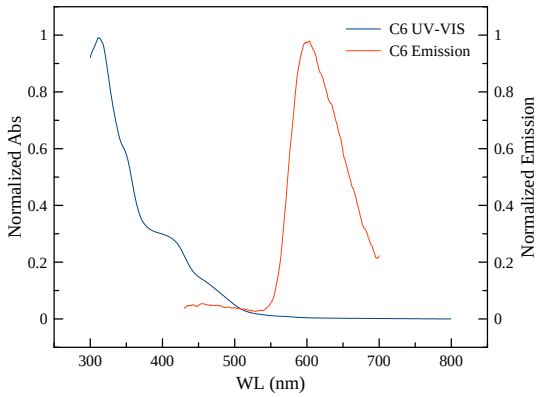

Figure 43: UV-VIS and PL Spectra for *tris* 2-(4-methylnaphthyl) pyridyl iridium

The proton NMR spectrum of C-L_6 gave chemical shift values as: ^{1}H NMR (400 MHz, $C_2D_2Cl_4$) δ 8.53 (d, *J* = 8.5 Hz, 3H), 8.36 (d, *J* = 8.2 Hz, 3H), 7.90 (d, *J* = 8.3 Hz, 3H), 7.67 – 7.60 (m, 3H), 7.54 (d, *J* = 5.5 Hz, 3H), 7.50 – 7.43 (m, 3H), 7.40 – 7.33 (m, 3H), 7.05 (s, 3H), 6.85 (t, *J* = 5.9 Hz, 3H), 2.37 (s, 9H). The spectrum is given in Figure 44 and it has a singlet peak with δ=2.37 ppm corresponding to the shielded methyl protons and a set of 10 aromatic protons at the range of 8.53-6.85 ppm. The data suggested the synthesis of *tris* 2-(4-methylnaphthyl) pyridyl iridium.

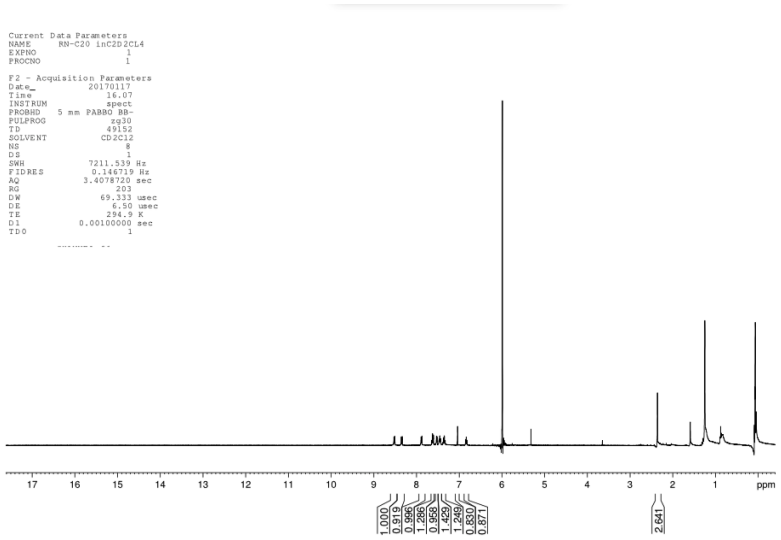

Figure 44: ^{1}H NMR Spectrum for *tris* 2-(4-methylnaphthyl) pyridyl iridium

The elemental analysis for C-L_6 showed that the calculated values to be C, 68.06; H, 4.28; N, 4.96 corresponded with the observed values of C, 68.40; H, 4.35; N, 4.87, suggesting the purity and composition of *tris* 2-(4-methylnaphthyl) pyridyl iridium.

The HRMS, UV-Vis, ^{1}H ^{13}C and 2D COSY NMR spectroscopy and elemental analysis data confirmed the synthesis of *tris* 2-(4-methylnaphthyl) pyridyl iridium.

4.2.7 *Tris* 4-fluoro-1-phenyl isoquinoline iridium (C-L_7); Ir(piq-F)$_3$

Tris 4-fluoro-1-phenyl isoquinoline iridium, $C_{45}H_{27}F_3IrN_3$, molecular weight 858.9442, was synthesized from L_7 as described in Section 3.4.7 and is shown in Scheme 30. Eighty six percent (0.05 g, 68%) yield of red crystals was obtained. The complex was thermal and air-stable with a melting point of > 300^{o}C. Despite this complex having the isoquinoline backbone, it showed similar properties as npy based complexes which was consistent to literature values (Tian, 2011).

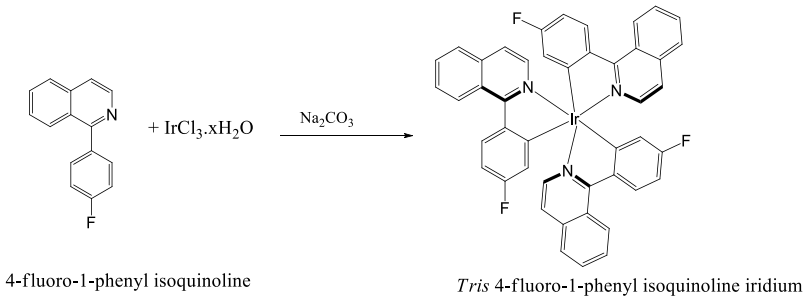

Scheme 30: Synthesis of *Tris* 4-fluoro-1-phenyl isoquinoline iridium

The structure of the C-L_7 was confirmed where the calculated peak for parent ion obtained through Time of flight high-resolution mass spectroscopy; HRMS-ESI+ (*m/z*): $[M+2H]^+$ was 860.1820 and corresponded to the observed peak 860.1848 as illustrated in Figure 45. The fragmentation patterns confirm the expected formulation of *tris* 4-fluoro-1-phenyl isoquinoline iridium.

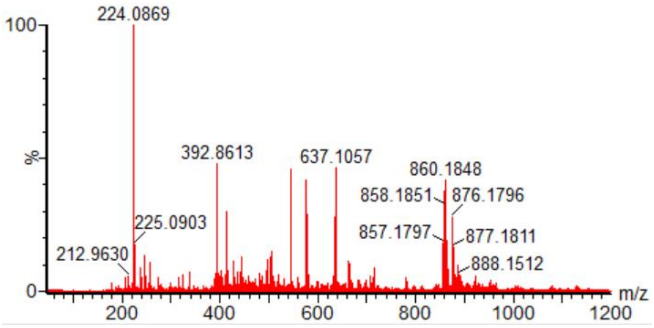

Figure 45: HRMS spectrum for *tris* 4-fluoro-1-phenyl isoquinoline iridium

From the UV-VIS spectrum, the λ_{max} was found to be 401 nm while from the fluorescence spectra the maximum emission was established to be 598 nm qualifying the specificity of the complex behaving as a chromophore. The spectra are given in Figure 46. Corresponding 10Dq value for absorption of C-L_7 was found to be 24938 cm^{-1} pointing to d-d transitions for Ir(III) complexes bearing strong field ligands. This was consistent with literature (Pandey *et al*., 2010).

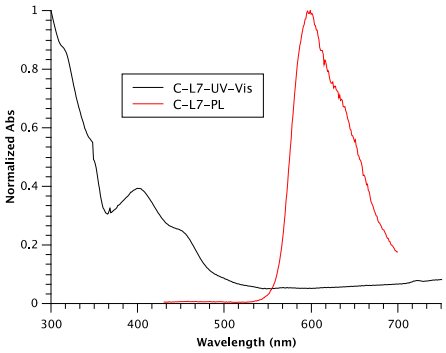

Figure 46: UV-VIS and PL Spectra for *tris* 4-fluoro-1-phenyl isoquinoline iridium

Phenyl isoquinolines moieties have been used extensively in tuning emission energy into the red-light emission, which leads to deep red emission. On the other hand, fluorine by its virtue of being a strong EWG is used to push emission towards blue region. This is why C-L_7 has a lower emission value than expected. However, C-L_7 is still red shifted by 8nm as compared to C-L_1 due to the influence of the isoquinoline backbone as well as the substitution being in the phenyl ring. This is supported in literature (Okada *et al.,* 2005, Hasan *et al.*, 2015).

The proton NMR of C-L_7 gave chemical shift values as: ^{1}H NMR (500 MHz, $C_2D_2Cl_4$) δ 9.43 – 9.34 (m, 1H), 8.72 (dd, *J* = 8.6, 5.9 Hz, 1H), 8.29 (dd, *J* = 6.0, 3.3 Hz, 1H), 8.19 (dd, *J* = 6.2, 3.2 Hz, 2H), 7.86 (d, *J* = 6.2 Hz, 1H), 7.69 (d, *J* = 6.2 Hz, 1H), 7.19 (td, *J* = 8.6, 2.2 Hz, 1H), 7.04 (dd, *J* = 10.1, 2.1 Hz, 1H) as shown in Figure 47 and suggested the synthesis of *tris* 4-fluoro-1-phenyl isoquinoline iridium.

Fluorine is the most electronegative element and attracts electrons to itself strongly leaving the system extremely electron deficient hence the chemical shifts are remarkably deshielded at 9.43 ppm. Moreover, F is attached directly to the phenyl ring hence the pπ-pπ bonding is prevalent which favors deshielding. This is consistent with literature values for similar complexes (Tian, 2011; Reich & Reich, 2018).

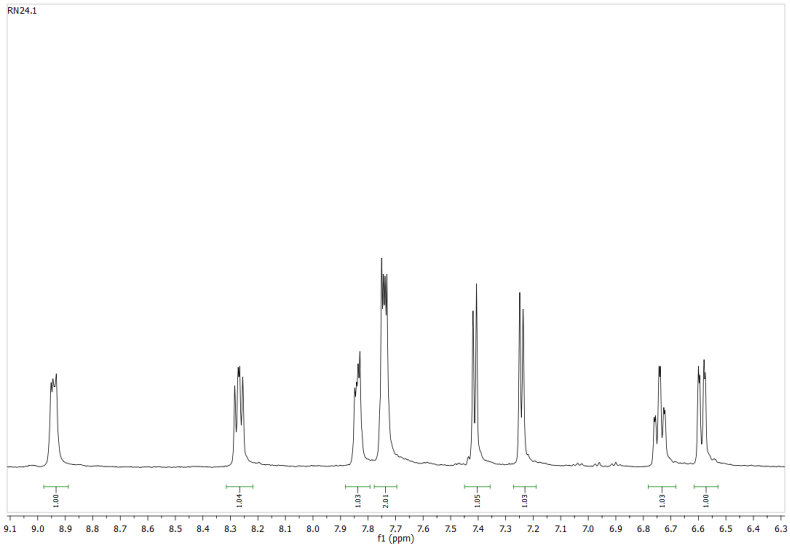

Figure 47: ^{1}H NMR Spectrum for *tris* 4-fluoro-1-phenyl isoquinoline iridium

The elemental analysis for C-L_7 showed the calculated values to be C, 62.93; H, 3.17; F, 6.64; N, 4.89 and corresponded with the observed values of C, 62.97; H, 3.20; F, 6.60; N, 4.87 suggesting the purity and composition of *tris* 4-fluoro-1-phenyl isoquinoline iridium.

The HRMS, UV-Vis, ^{1}H and ^{13}C NMR spectroscopy and elemental analysis data confirmed the synthesis of *tris* 4-fluoro-1-phenyl isoquinoline iridium.

4.2.8 *Tris* 1-phenyl-4-(trifluoromethyl) isoquinoline iridium (C-L_8); Ir(piq-CF_3)$_3$

Tris 1-phenyl-4-(trifluoromethyl) isoquinoline iridium, $C_{48}H_{27}F_9IrN_3$, molecular weight 1008.9676, was synthesized from L_8 as described in Section 3.4.8 and is shown in Scheme 31. Ninety five percent (0.075 g, 95%) yield of red crystals was obtained. The complex was thermal and air-stable with a melting point of > 300^{o}C.

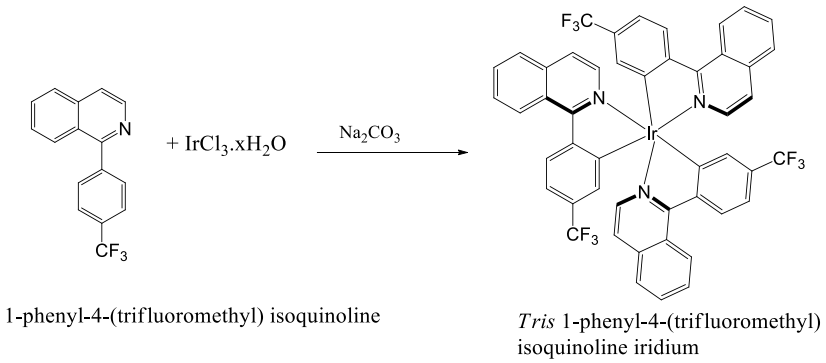

1-phenyl-4-(trifluoromethyl) isoquinoline

Tris 1-phenyl-4-(trifluoromethyl) isoquinoline iridium

Scheme 31: Synthesis of *Tris* 1-phenyl-4-(trifluoromethyl) isoquinoline iridium

The structure of the C-L_8 was confirmed where the calculated peak for parent ion obtained through Time of flight high-resolution mass spectroscopy; HRMS-ESI+ (*m/z*): $[M+2H]^+$ was 1010.1724 and corresponded to the observed peak 1010.1772 as illustrated in Figure 48. The fragmentation patterns confirm the expected formulation of *tris* 1-phenyl-4-(trifluoromethyl) isoquinoline iridium.

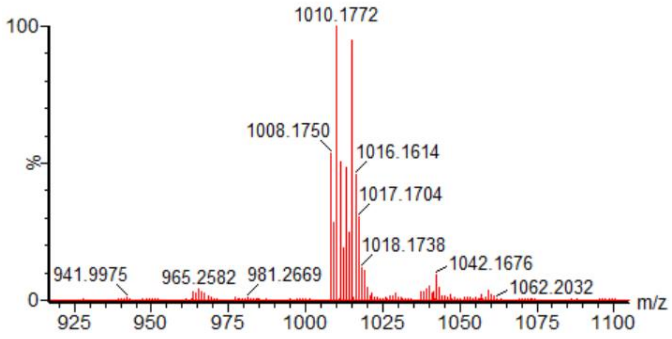

Figure 48: HRMS spectrum *tris* 1-phenyl-4-(trifluoromethyl) isoquinoline iridium

From the UV-VIS spectra, the λ_{max} was found to be 417 nm while from the fluorescence spectra the maximum emission was established to be at 612 nm qualifying the specificity of the complex behaving as a chromophore. The spectra are illustrated on Figure 49. Corresponding 10Dq value for absorption of C-L_8 was found to be 23981 cm^{-1} pointing to d-d transitions for Ir(III) complexes bearing strong field ligands. This was consistent with literature (Pandey *et al.*, 2010).

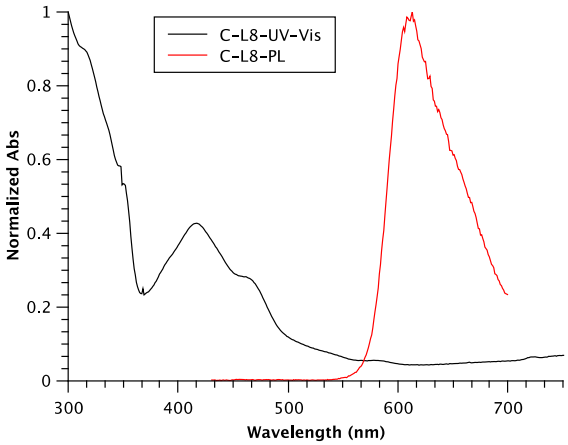

Figure 49: UV-VIS and PL Spectra for *Tris* 1-phenyl-4-(trifluoromethyl) isoquinoline iridium

Phenyl quinolines moieties have been used extensively in tuning emission energy into the red-shift emission, which leads to deep red emission. Additionally, $-CF_3$ tends to mimic $-CH_3$ hence C-L_8 was red shifted as compared to C-L_7 (598 nm) by 12 nm due to the aforementioned nature of $-CF_3$ as supported in literature (Nagai *et al.*, 1991; Coppo *et al.*, 2004; Reich & Reich, 2018).

The proton NMR spectrum of C-L_8 gave chemical shift values as: ^{1}H NMR (500 MHz, CD_2Cl_2) δ 8.71 (d, *J* = 5.3 Hz, 1H), 8.06 (d, *J* = 8.2 Hz, 1H), 7.69 – 7.60 (m, 1H), 7.57 (d, *J* = 4.2 Hz, 2H), 7.12 (d, *J* = 6.2 Hz, 1H), 7.05 (dd, *J* = 19.0, 9.6 Hz, 2H), 6.83 (d, *J* = 27.2 Hz, 1H) as shown in Figure 50 suggesting the synthesis of *tris* 1-phenyl-4-(trifluoromethyl) isoquinoline iridium.
The chemical shifts of C-L_8 are upfield as compared to C-L_7 despite the bulky and strong EWG substituent which is attributable to the inductive-only nature and "mimic" effects of CF_3 which makes it to behave as though it's an EDG and is supported by literature (Nagai *et al.*, 1991; Coppo *et al.*, 2004; Reich & Reich, 2018).

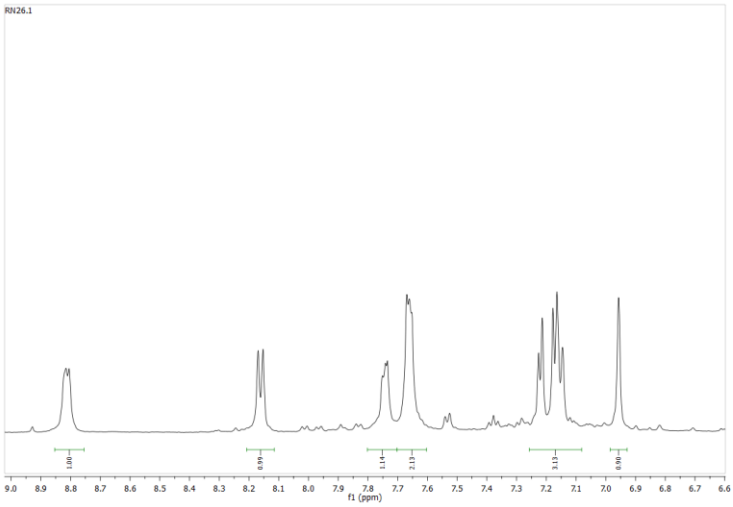

Figure 50: ^{1}H NMR Spectrum for*Tris* 1-phenyl-4-(trifluoromethyl) isoquinoline iridium

The elemental analysis for C-L_8 showed the calculated values to be C, 57.14; H, 2.70; F, 16.95; N, 4.16 and corresponded with the observed values of C, 57.17; H, 2.74; F, 16.92; N, 4.20, suggesting the purity and composition of *tris* 1-phenyl-4-(trifluoromethyl) isoquinoline iridium.
The HRMS, UV-Vis, ^{1}H and ^{13}C NMR spectroscopy and elemental analysis data confirmed the synthesis of *tris* 1-phenyl-4-(trifluoromethyl) isoquinoline iridium.

4.2.9 *Tris* 4-*tert*-butyl-1-phenyl isoquinoline iridium (C-L_9); Ir(piq-tBu_3)$_3$

Tris 4-*tert*-butyl-1-phenyl isoquinoline iridium, $C_{57}H_{54}N_3Ir$ molecular weight 973.2970, was synthesized from L_9 as described in Section 3.4.9 and is shown in Scheme 32. Forty nine percent (0.053 g, 49%) yield of red crystals was obtained.

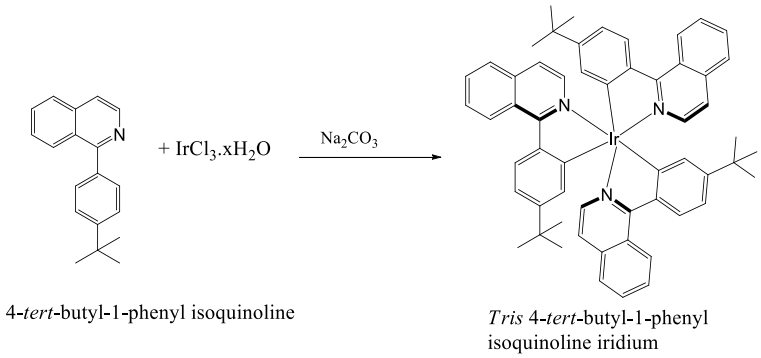

Scheme 32: Synthesis *Tris* 4-*tert*-butyl-1-phenyl isoquinoline iridium

The structure of the C-L_9 was confirmed where the calculated peak for parent ion obtained through time of flight high-resolution mass spectrometer; HRMS-ESI+ (*m/z*): $[M+H]^+$ was 974.3981 and corresponded to the observed peak 974.3978 as illustrated in Figure 51. The fragmentation patterns confirm the expected formulation of *tris* 4-*tert*-butyl-1-phenyl isoquinoline iridium.

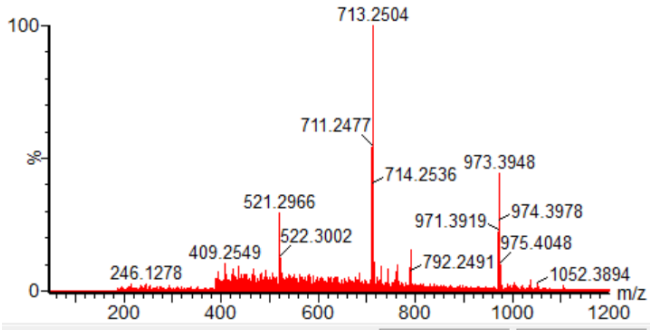

Figure 51: HRMS spectrum for *tris* 4-*tert*-butyl-1-phenyl isoquinoline iridium

From the UV-VIS spectra, the λ_{max} was found to be 424 nm while from the fluorescence spectra the maximum emission was established to be at 625 nm as shown in Figure 52, which is consistent with the deep red emission of phenyl isoquinoline moieties. Corresponding 10Dq value for absorption of C-L_9 was found to be 23585 cm^{-1} pointing to d-d transitions for Ir(III) complexes bearing strong field ligands. This was consistent with literature (Pandey et al., 2010). Additionally, -tBu_3 is a strong electron-donating group, which makes the HOMO-LUMO gap smaller adding the red shifted emission. This was consistent with literature values of similar compounds (Okada *et al.*,2005, Hasan *et al.*, 2015).

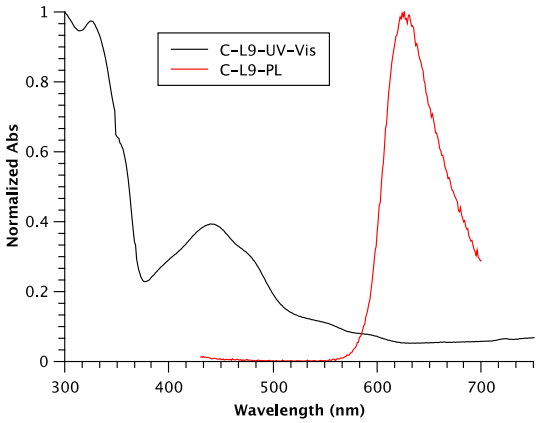

Figure 52: UV-VIS and PL Spectra for *Tris* 4-*tert*-butyl-1-phenyl isoquinoline iridium

The proton NMR of C-L_9 gave chemical shift values as: ^{1}H NMR (500 MHz, CD_2Cl_2) δ 8.85 – 8.75 (m, 1H), 7.95 (d, *J* = 8.6 Hz, 1H), 7.65 – 7.53 (m, 1H), 7.51 – 7.40 (m, 2H), 6.98 (dd, *J* = 14.5, 6.2 Hz, 2H), 6.83 (d, *J* = 8.5 Hz, 1H), 6.73 (s, 1H), 0.95 (d, *J* = 6.2 Hz, 9H) as shown in Figure 53 suggesting the synthesis of *tris* 4-*tert*-butyl-1-phenyl isoquinoline iridium.

The tert butyl group is a bulky EDG hence the steric hindrance effects are more than the electron donating effects hence chemical shift is shifted down field as compared to C-L_8. This is supported in literature (Reich & Reich, 2018).

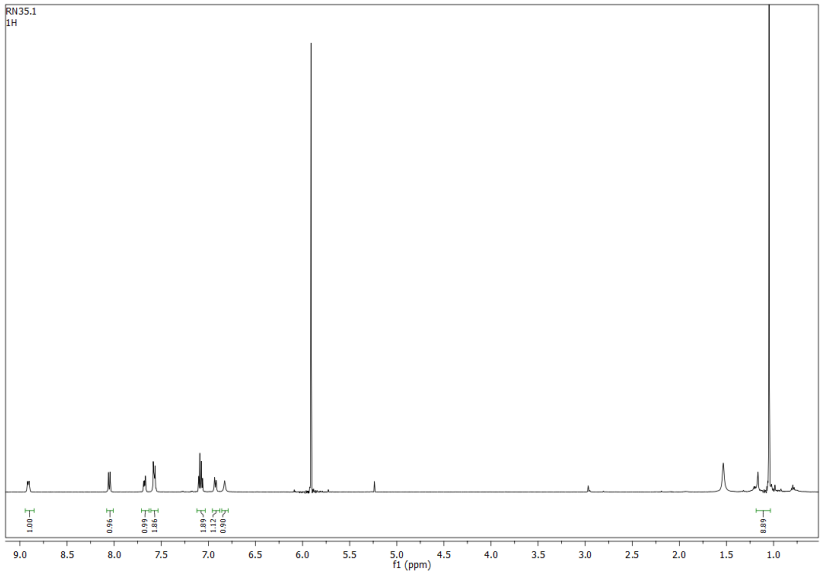

Figure 53: ^{1}H NMR Spectrum for *tris* 4-*tert*-butyl-1-phenyl isoquinoline iridium

The elemental analysis for C-L_9 showed the calculated values to be C, 70.34; H, 5.59; N, 4.32 and corresponded with the observed values of C, 70.30; H, 5.62; N, 4.36, suggesting the purity and composition of *tris* 4-*tert*-butyl-1-phenyl isoquinoline iridium.

The HRMS, UV-Vis, ^{1}H and ^{13}C NMR spectroscopy and elemental analysis data confirmed the synthesis of *tris* 4-*tert*-butyl-1-phenyl isoquinoline iridium.

4.2.10 *Tris* 4-methyl-1-phenyl isoquinoline iridium (C-L_{10}); Ir(piq-Me)$_3$

Tris 4-methyl-1-phenyl isoquinoline iridium, $C_{48}H_{36}N_3Ir$ molecular weight 847.0540, was synthesized from L_{10} as described in Section 3.4.10 and is shown in Scheme 33**.** Forty five percent (0.05 g, 45%) yield of red crystals was obtained.

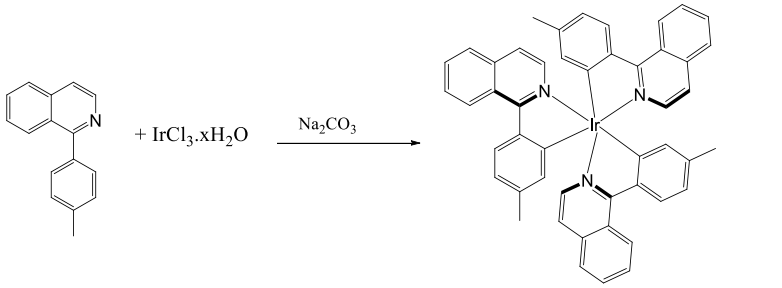

4-methyl-1-phenyl isoquinoline

Tris 4-methyl-1-phenyl isoquinoline iridium

Scheme 33: Synthesis of *Tris* 4-methyl-1-phenyl isoquinoline iridium

The structure of the C-L_{10} was confirmed where the calculated peak for parent ion obtained through time of flight high-resolution mass spectroscopy; HRMS-ESI+ (*m/z*): $[M+H]^+$ was 848.2572 and corresponded to the observed peak 848.2559 as illustrated in Figure 54. The fragmentation patterns confirm the expected formulation of *tris* 4-methyl-1-phenyl isoquinoline iridium.

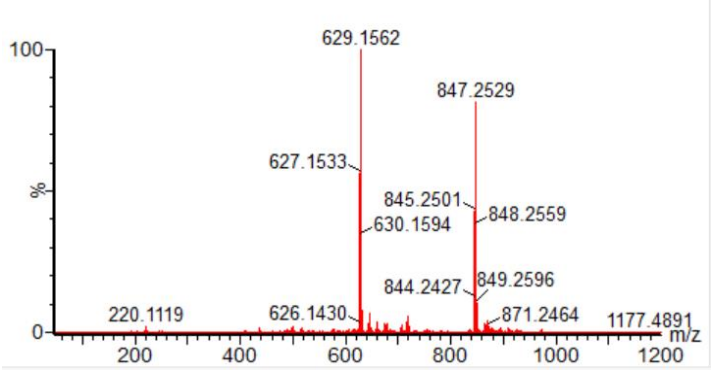

Figure 54: HRMS Spectrum for *tris* 4-methyl-1-phenyl isoquinoline iridium

From the UV-VIS spectra of C-L_{10}, the λ_{max} was found to be 440 nm while from the fluorescence spectra the maximum emission was established to be at 623 nm as shown in Figure 55, which was consistent with the deep red emission of phenyl quinolines moieties as well as the contribution of the -Me group which makes the HOMO-LUMO gap smaller adding the red shifted emission. Corresponding 10Dq value for absorption of C-L_{10} was found to be 22727 cm^{-1} pointing to d-d transitions for Ir(III) complexes bearing strong field ligands. This was consistent with literature (Pandey et al., 2010). C-L_9 and C-L_{10} depict the effects of EDG on phenyl ring have similar values which was supported in literature (Okada *et al.*, 2005; Hasan *et al.*, 2015).

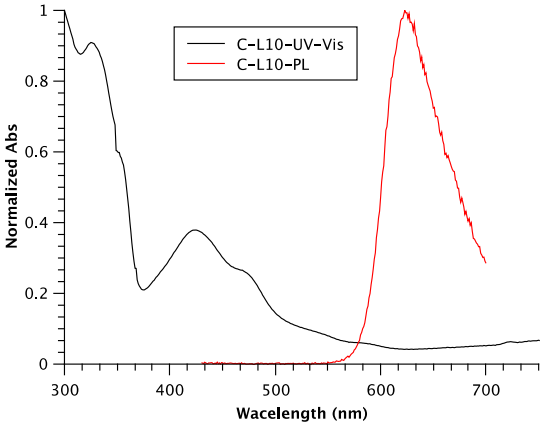

Figure 55: UV-VIS and PL Spectra for *Tris* 4-methyl-1-phenyl isoquinoline iridium

The proton NMR of C-L_{10} gave chemical shift values as shown in Figure 56: ^{1}H NMR (500 MHz, CD_2Cl_2) δ 8.79 – 8.70 (m, 1H), 7.88 (d, *J* = 8.1 Hz, 1H), 7.56 (dd, *J* = 6.2, 3.3 Hz, 1H), 7.47 (dd, *J* = 6.4, 3.3 Hz, 2H), 7.01 (d, *J* = 6.2 Hz, 1H), 6.93 (d, *J* = 6.2 Hz, 1H), 6.61 (d, *J* = 10.8 Hz, 2H),

1.99 (s, 3H) suggesting the synthesis of *tris* 4-methyl-1-phenyl isoquinoline iridium. The chemical shift of C-L_{10} is downfield as compared to C-L_9 due to the inductive effects of alkyl groups which is consistent with literature (Reich & Reich, 2018).

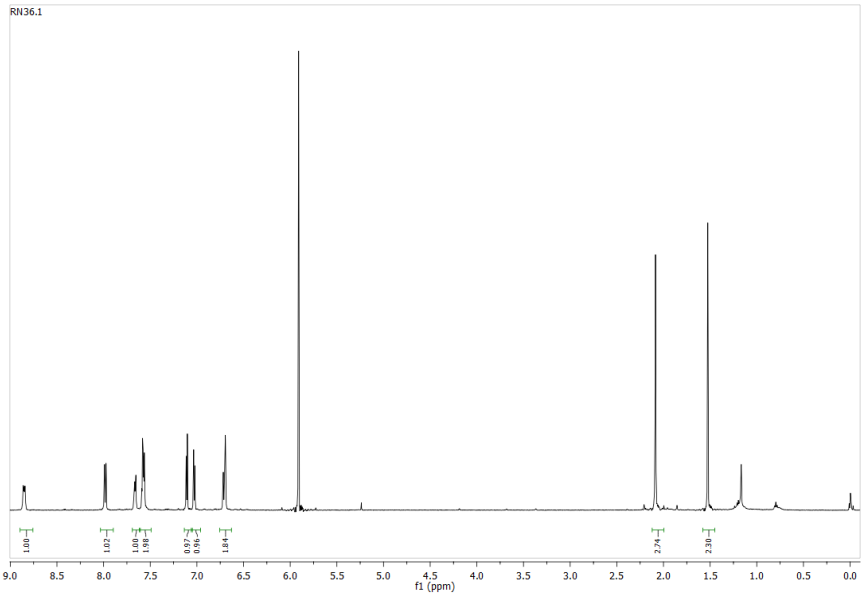

Figure 56: ^{1}H NMR Spectrum for *tris* 4-methyl-1-phenyl isoquinoline iridium

The elemental analysis for C-L_{10} showed that the calculated values to be: C, 68.06; H, 4.28; N, 4.96 and corresponded with the observed values of C, 68.02; H, 4.31; N, 4.97, confirming the purity and composition of *tris* 4-methyl-1-phenyl isoquinoline iridium.

The HRMS, UV-Vis, ^{1}H and ^{13}C NMR spectroscopy and elemental analysis data confirmed the synthesis of *tris* 4-methyl-1-phenyl isoquinoline iridium.

4.3 Photophysical Properties Variations of Ir(III) Complexes

The properties of varying structures of the first six complexes C-L_1 to C-L_6 were investigated. These included quantum yields and emission lifetimes based on the specific chemiluminescence properties of the complexes as described in section 3.5.5 and 3.5.6. Notable varying emission energies were for C-L_1, C-L_2, C-L_4 that were found to be 591, 588 and 610 nm respectively, while C-L_3, C-L_5, and C-L_6 had the values 603 nm, 603 nm and 602 nm respectively. The corresponding 10Dq values for C-L_1 to C-L_6 from absorption spectra were; 24390cm^{-1}, 23923 cm^{-1}, 22988 cm^{-1},

25000 cm^{-1}, 24691 cm^{-1} and 24331 cm^{-1} respectively. These values were consistent with expected 10Dq values for the crystal field splitting and were indicative of d-d transitions. The emission spectra were attributed to electronic transitions of 10Dq splitting of the *d* orbitals in the octahedral structure. Ir(III) complexes are d^6 low spin complexes, which typically experience high CFSE stabilization effect of the maximum possible value of $12/5_0$. The *tris* complexes were found to be octahedral (O_h) complexes based on XRD results of C-L_1.

The emission spectra were also influenced by nephelauxetic effect where the inter-electronic repulsion was reduced leading to increase in effective size of metal orbitals. This is due to contribution of negative charge by the ligands hence decreased effective positive charge on the Ir metal center and M-L covalent bond formed as a result of overlapping of metal and ligands evidenced by the MLCT transitions observed from emission energies.

In comparison to the unsubstituted C-L_1 (591 nm) with 10 Dq value of 24390 cm^{-1}, C-L_2 (610 nm) was the most shifted to longer wavelength hence lower energy, red/bathochromic shifts, by 19nm corresponding to a smaller splitting of the crystal field splitting in O_h field, 10Dq value 23923 cm^{-1}, while C-L_4 (588 nm) was shifted higher energy (blue/hypsochromic shifts) by 3 nm and a larger Dq10 value of 25000 cm^{-1}. This was indicative of the substituent effect on the ligand towards t_{2g} d_{xy}, d_{yz}, and d_{xz} orbitals lowering or increasing their energy.

This could have been further improved by the presence of EDG, which could have raised the HOMO energy through resonance and reduced the energy gap. This tendency identified with both the inductive and resonance effects of substituents of the other complexes, which largely affected the properties of the complexes as well. C-L_3, C-L_5 and C-L_6 displayed inductive effect influences on the crystal field hence the 8 nm, 8 nm and 7 nm shift to longer λ as compared to C-L_1. This could point to the HOMO stability and the emission energy gap being controlled by the nature of substituents either inductively or via resonance on the aromatic ring. The emission energies had the following trend, C-L_4>C-L_1>C-L_6>C-L_5>C-L_3>C-L_2, over the range of 588-610 nm as shown in Table 1. The npy, L_1, is an intermediate ligand in the spectrochemical series and its strength shifted depending on degree and strength of substitution. Introducing -CF_3 led to a strong field ligand and an increase in nephelauxetic effect in C-L_3 evidenced by the reduction in Δ_o splitting and longer emission λ_{max}. In C-L_4, the -Me made L_4 a weaker field ligand relative to L_1 and had a

decrease in nephelauxetic effect in C-L_4 as evidenced by the 3nm decrease in emission λ_{max}. The rest of the complexes were made into strong field ligands through substitution implying they had increased nephelauxetic effect and had longer emission λ_{max} than C-L_1. The introduction of these substituents on either the phenyl, the naphthyl or pyridyl ring, allowed for the tuning of the electronic and electrochemical properties of the resultant complexes.

For C-L_7 to C-L_{10} the emission energies were 598 nm, 612 nm, 624 nm and 652 nm respectively. The emission energies showed bathochromic shifts, longer λ and lower energy, of 7 nm, 21 nm, 33 nm and 34 nm for C-L_7, C-L_8, C-L_9 and C-L_{10} respectively as compared to C-L_1 indicative of the additional effect of the phenyl isoquinoline moiety ability to raise the t_{2g} d orbitals energy. In addition, the inductive and resonance effects of substituents affect the emission maxima such that C-L_7 had the lowest emission peak at 598 nm due to the effects of the EWG F while the EDGs led to the highest bathochromic shift although the bulkiness of -*t*Bu_3 led to C-L_9 not being as red shifted as would have been expected making C-L_{10} with -Me to be the most red shifted. The trend increased in the series C-L_7> C-L_8> C-L_9> C-L_{10} with the λ_{max} ranging between 598-625 nm.

4.3.1 Emission lifetimes, τ

The emission lifetimes of complexes C-L_1 to C-L_6 were determined through pulsed laser spectroscopy as described in section 3.5.6. The τ for C-L_1, C-L_2 and C-L_4 were 1.5 μs, 3.0 μs and 2.6 μs while for C-L_3, C-L_5 and C-L_6 were 3.7 μs, 1.4 μs and 2.6 μs respectively. These were due to luminescent triplet states of the complexes and since they fall in the microsecond range, they were indicative of phosphorescence lifetimes. The spectral assignment for the luminescent bands of these complexes could be categorized as fluorescent. Systematically, the substitution was observed to influence the excited state lifetime in a similar fashion as the emission energies due to heavy atom effect. All complexes had longer lifetimes than the unsubstituted C-L_1 with τ= 1.5 μs except C-L_5 with τ = 1.4 μs. Specifically, C-L_3 substituted with CF_3, a heavy atom had the longest τ= 3.7 μs, followed by the C-L_2 with τ =3.0 μs due to the heavy -OMe substitution. C-L_4 and C-L_6 both with the same -Me, substituent but on different positions, one on the pyridine ring and phenyl ring respectively had τ =2.6 μs. The trend could be indicative of the influence of substitutions heavy atom effect leading to longer lifetimes. This tendency also identified with both the inductive and resonance effects of substituents of the complexes, which affected the lifetimes of the complexes.

In aerated solutions of CH_2Cl_2 the values were low (τ =0.154-0.254 μs) due to quenching of excited states by molecular oxygen. However, these improved significantly (τ = 1.4-3.7 μs) in degassed solutions through pump-thaw-freeze system.

The luminescence decay of the degassed solutions was found to be too long, beyond the scope of the instrument, (decay time >> 400 *ns*), it was not possible to extract it accurately from the TCSPC measurement. Instead, it was calculated from the lifetime measured for the air-saturated solutions (which was much shorter due to quenching of the triplet state by oxygen) and the ratio between luminescence quantum yield of the degassed $\Phi_{degassed}$ and air-saturated solution (Φ_{air}).

Overall, the high τ ranged between 1.4 to 3.7 μs with the lifetime increasing in the series, C-L_5>C-L_1>C-L_4>C-L_6>C-L_2>C-L_3 as summarized in Table 1.

Ideally, excited state of the complex should persist long enough in order for the reaction to take place, essentially, long lifetimes, ensuring time to react with substrate before relaxation to ground state hence acts as an intrinsic timer for photoredox reactions (Arias-Rotondo et al., 2016). The complexes showed their immense potential of being effective in chemical transformations. Moreover, they had comparatively higher τ than the well-studied tris (2,2'-bipyridine) ruthenium $[Ru(bpy)_3]^{2+}$complex that has τ =1.1 μs (Liu et al., 2016) and $Ir(ppy)_3$ that has τ =1.6 μs both of which have been extensively used for photoredox processes.

4.3.2 Photoluminescence Quantum Yields, Φf

The Φ_f for complexes C-L_1 to C-L_6 was determined through absolute measurements as described in section 3.5.5. The Φ_f for C-L_1, C-L_2 and C-L_4 were 8.6, 22 and 19 while for C-L_3, C-L_5 and C-L_6 were 14, 9.4 and 16 respectively. The complexes exhibited these high Φ_f since they have rigid structures arising from the extended π-conjugated systems and further improved by the tris cyclometalation with Ir metal center. Moreover, they had predominantly MLCT transitions, which could have favored the high yields. Substitution could lead to heavy atom effect, which leads to higher yields and points to phosphorescence in a luminophore. This was observed in this case, whereby all complexes had higher quantum yields than the unsubstituted C-L_1 indicative of the significance of the heavy atom effect and essentially, leading to better conversion efficiency of absorbed photons into emitted photons as compared to C-L_1. Structural rigidity, substitution and transition type are among the factors that affect quantum yields of a luminophore (Omary & Patterson, 1999).

Overall, the complexes exhibited high quantum yields, which increased in the series, C-L_1>C-L_5>C-L_3>C-L_6>C-L_4>C-L_2 in the range of 8.6-22 for degassed solutions as summarized in Table 1.

Table 1: Summarized Photophysical and Electrochemical data for C-L_1-C-L_{10}

Compl	Absorption (molar coefficient given in brackets) (nm)	Emission			Electrochemistry (V)			
		Λmax (nm)	τ (μs)	Φ	E_{ox}(ΔEp)	E_{red}	$E_{1/2}$	[a)]$E_{III*/IV}$
			480nm					
C-L_1	236 (97833), 268 (68594), 302 (42774), 405 (8258), 457 (2763)	591	1.5	8.6	0.53(50)	0.46	0.50	– 1.38
C-L_2	237 (74822), 345 (10182), 391 (4312), 418 (1644)	610	3.0	22	0.68(50	0.63	0.66	– 1.37
C-L_3	235 (62338), 270 (53434), 311 (29402), 350 (20804), 435 (8240)	603	3.7	14	0.96(70)	0.89	0.93	– 1.13
C-L_4	237 (83509), 268 (49592), 400 (6445), 451 (1933)	588	2.6	19	0.65(50)	0.6	0.63	– 1.48
C-L_5	237 (77709), 267 (50547), 353 (1480), 405 (8039), 450 (2508)	603	1.4	9.4	0.60(60)	0.54	0.57	– 1.49
C-L_6	238 (55498), 270 (34124), 312 (17411), 355 (9424), 407 (4784), 455 (1396)	602	2.6	16	0.66(60)	0.6	0.63	– 1.43
C-L_7	286, 318, 348, 403, 452	598, 608			0.74	0.65	0.70	– 1.38
C-L_8	242, 318, 352, 416, 463	612			0.84	0.75	0.80	
C-L_9	296, 325, 251, 442, 476, 551,594	624			0.43	0.36	0.40	
C-L_{10}	253, 293, 327, 355, 423,472,583	625			0.46	0.39	0.43	
[b)] $Ir(ppy)_3$		519	1600	0.97[c]			0.77	–1.73

a) Approximated excited state redox potential in accordance with ref (Tucker & Stephenson, 2012)

b) (Hofbeck & Yersin, 2010)

c) (Sajoto et al., 2009)(Φ at 77K)

4.4 Electrochemical Properties of Complexes

The electrochemical properties of the iridium complexes C-L_1 to C-L_6 were probed via cyclic voltammetry (CV) as per Section 3.5.8 to establish the ground state redox potentials.

The oxidation potential $Eox_{½}$, for C-L_1, C-L_2 and C-L_4 were 0.74 V, 0.68 V and 0.65 V while for C-L_3, C-L_5 and C-L_6 were 0.96 V, 0.60 V and 0.66 V, respectively. The reduction potential $Ered_{½}$, for C-L_1, C-L_2 and C-L_4 were 0.69 V, 0.63 V and 0.60 V while for C-L_3, C-L_5 and C-L_6 were 0.89 V, 0.54 V and 0.54 V respectively. The vital data is summarized in Table 1. Redox trends involve electron moving to a lower energy level on another atom and typically involves the frontier orbitals (HOMO and LUMO) due to a linear relationship between them and redox potentials of the complexes.

Systematically, C-L_3 exhibited the highest ground state $Eox_{½}$ due to raising of HOMO-LUMO energy gap and had $Eox_{½}$ of +0.96 V whereas lower $Eox_{½}$ were observed for the neutral complex C-L_1, $Eox_{½}$ = +0.74 V and even lower potentials for complexes with electron donating groups of +0.68 V, +0.65 V, +0.60 V and +0.66 V for C-L_2, C-L_4, C-L_5 and C-L_6 respectively. For these with EDGs, the stronger the EDG, the higher the oxidation potential, C-L_2, while the position of substitution on either the phenyl or pyridyl ring did not affect the potential much as in the case of C-L_4 and C-L_5 but the degree of substitution lowers the oxidation potential further for C-L_5 since it is more substituted. This is because EDGs are expected to raise the HOMO energy level since they increase the electron density of the complexes, thus reducing HOMO-LUMO gap, making them more easily oxidizable (Liu *et al*., 2016).

The new family of *tris*-cyclometalated iridium complexes exhibited reversible oxidation waves as shown in Figure 57A during anodic scanning, ΔE_p=50-70 mV, which could be attributed to a single electron transfer (SET) event at the metal-centered Ir^{III}/Ir^{IV} oxidation couple, which pointed to their potential ability to serve as single electron oxidant or reductant. Similar compounds have successfully been utilized for this purpose (Koike & Akita, 2014). In their excited state, the complexes can act as an energy donor, an electron acceptor or an electron donor. For any given reaction, the process that dominates is usually determined by thermodynamic and kinetic factors associated with the reaction. Principally, in photoredox catalysis, the ground- and the excited-state redox potentials of a photocatalyst are utilized. The reversibility of complexes used as a photocatalyst is vital since they must be stable in their oxidized or reduced forms if they are to be

regenerated in a reaction and is typically based on the difference between anodic and cathodic peak potentials (Koike *et al.*, 2014; Arias-Rotondo *et al.*, 2016).

The $E_{ox½}$ of the complexes ranged between +0.60 V to +0.96 V in the series, C-L_5>C-L_4> C-L_6> C-L_2> C-L_1> C-L_3.

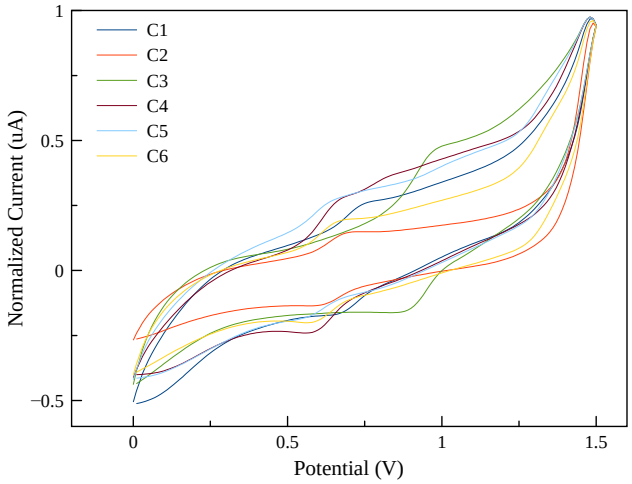

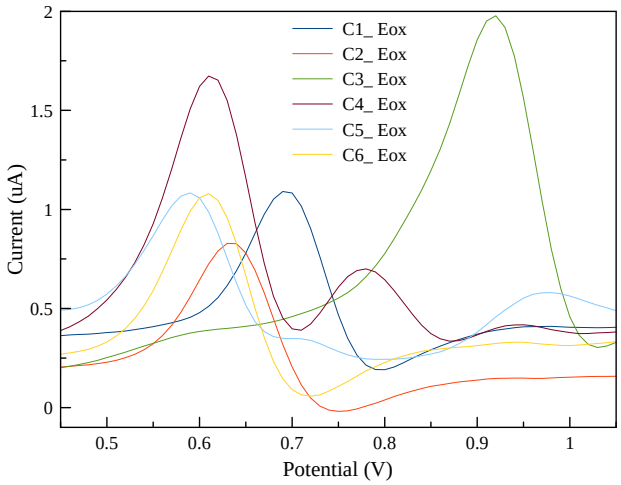

Figure 57: A) Cyclic Voltammograms for C-L_1-C-L_6 B) 1st Derivative for C-L_1-C-L_6

The first derivative for C-L_1 to C-L_6 is shown in Figure 57B. 1st derivative CVs is used to provide further proof of reversibility of a system based on peak heights, peak potential and peak widths. In a reversible process, the oxidation potentials in the 1st derivatives should be symmetric with respect to a symmetry axis and the peaks should be sharp and reach a maximum then decrease to a limiting value. Moreover, the peak potentials for original current (CV) should behave in a similar

fashion as the peak potentials for 1st derivative CVs, in a reversible system, which is the observed case (Figure 58B). In quasi-reversible and irreversible systems there is disappearance of symmetry of the peaks and the derivatives' peak potential is more negative than in original CV (Kim et al., 1993).

4.5 Applications of Iridium(III) Complexes

Photoredox catalysis proceeds via single electron transfer (SET) processes. They can either act as oxidants in oxidative quenching cycle or as reductants in reductive oxidative cycle. For C-L_1 to C-L_6, the expected mechanism of the SET process is proposed as depicted in Figure 58. In this study, it is proposed that the oxidative quenching cycle takes precedence in all the photoredox experiments done i.e., oxytrifluoromethylation of styrene, photodegradation of Morin and photooxidation of alcohols.

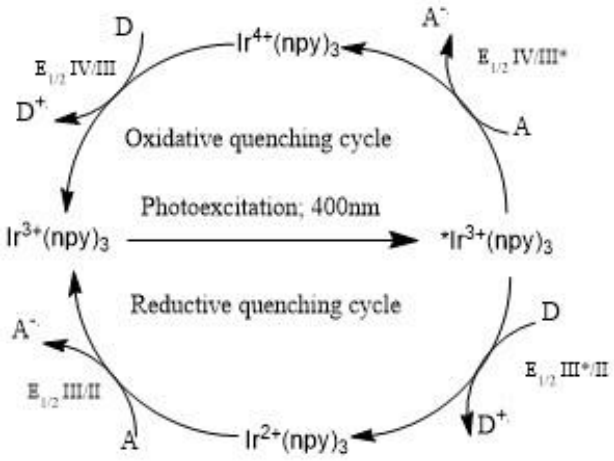

Figure 58: Oxidative and Reductive Quenching Cycles in SET processes for C-L_1

4.5.1 Oxytrifluoromethylation of Styrene

The photoredox catalytic activity of C-L_1 to C-L_6 was investigated using the challenging three-component oxytrifluoromethylation of styrene as per Section 3.6.1 and the results are tabulated in Table 2. C-L_1 to C-L_6 provided the corresponding products in yield ranging from 56% to 100%. Complexes C-L_1, C-L_2 and C-L_3 gave yields on the higher end of this range (97–100%) thus

proving to be more efficient for this specific transformation as compared to $Ir(ppy)_3$. Complex C-L_4 provided the product in the same yield as $Ir(ppy)_3$ (i.e., 87%). Complexes C-L_5 and C-L_6 gave the product in lower yields of 79% and 56%, respectively. It is noteworthy that the electronically neutral C-L_1, the most electron poor C-L_2 and the most electron rich C-L_3 complexes all provided the same yield of the product. Common for these complexes are the relatively high reduction potentials associated with the catalysts in the turnover event of the catalytic cycle (Ir^{IV}/Ir^{III} = 0.66-0.96 V). This indicated that reaction efficiency was coupled to the efficiency of the oxidation of the key benzyl radical intermediate. However, the other complexes C-L_4-C-L_6, all potent reductants in their excited states, had both reasonable reduction potential for the Ir^{IV}/Ir^{III} couple (0.57-0.63 V) and more than adequate excited state life times. Taken together, these characteristics did not greatly deviate from those of the better performing catalysts C-L_1, C-L_2 and C-L_3, which was especially clear when comparing with C-L_2. Therefore, catalyst deactivation could better explain the lower yields of C-L_4, C-L_5 and C-L_6. Deactivation of the catalyst is often observed in photoredox catalysis, and it originates from the reactions between intermediate high-energy radicals and the ligands of the catalysts. The lower performing complexes C-L_4, C-L_5 and C-L_6 in this work are all equipped with methyl substituents. H-atom abstraction from these substituents must be regarded as a very likely side reaction, which can commence deactivation of the catalysts. No side product associated with degradation of the catalysts could be observed, but this does not rule out radical based degenerative pathways for these catalysts. As such, in outperforming $Ir(ppy)_3$ as catalyst in the parent reaction, complex C-L_1, C-L_2 and C-L_3 provide an extension of current photoredox catalysts in terms of accessible redox window in the catalytic cycle.

Table 2: Oxytrifluoromethylation of Styrene under Visible Light

Entry	*Catalyst*	*Consumption (%) a, b*	*Yield (%) a, b*
1c	$Ir(ppy)_3$	100	99
2	$Ir(ppy)_3$	87	87
3	$C\text{-}L_1$	98	97
4	$C\text{-}L_2$	100	100
5	$C\text{-}L_3$	100	100
6	$C\text{-}L_4$	87	87
7	$C\text{-}L_5$	79	79
8	$C\text{-}L_6$	65	56

a) Average of two experiments; b) yield and consumption determined by ^{1}H-NMR using an internal standard; c) published data

4.5.2 Photocatalytic Degradation/bleaching of Organic Dye (Morin)

The photobleaching ability of the complexes $C\text{-}L_1$ to $C\text{-}L_6$ was studied through the oxidative degradation of Morin as per Section 3.6.2, as shown in Scheme 34 by monitoring the maximum absorbance using time-resolved UV-VIS.

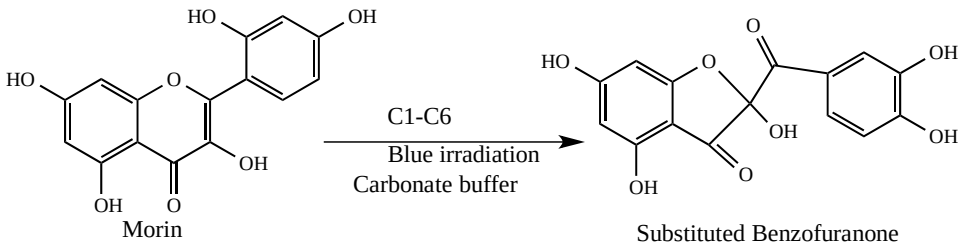

Scheme 34: Photodegradation of Morin with Ir(III) Complexes and Blue Light

4.5.2.1 Photodegradation of Morin using C-L1

Figure 59 shows the catalytic oxidation of Morin with C-L_1 and blue lights (470 nm) with the time-resolved measurement taken every minute for 12 minutes. Three peaks and three isosbestic points were observed on the spectra. The maximum absorbance for Morin observed at λ 410 nm decreased steadily along with that at λ 296 nm while λ 321 nm increased with time. The absorbance at 321 nm is associated with the formation of the substituted benzofuranone, which is the intermediate product of catalytic oxidation of Morin as shown in Scheme 34.

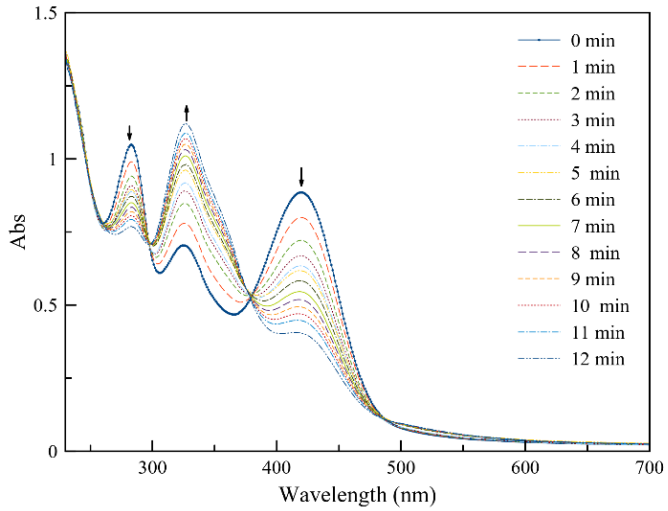

Figure 59: Time-resolved UV-VIS spectra of Morin solution with C-L_1 and blue lights

The peak at λ= 321 nm vanished after 30 minutes as shown in Figure 60, with new formation of a new peak at λ 332 nm from 80-180 minutes. Previous studies report the peak vanishes due to initiation of a secondary reaction which leads to further decomposition of the substituted benzofuranone into 2,4-dihydroxy benzoic acid and 2,4,6 trihydroxy benzoic acid (Polzer *et al.*, 2012). Three isosbestic points were observed at around λ 481 nm 365 nm and 290 nm, which indicated that oxidation of Morin, produced only one product without any side products for the observed period. This has been reported in previous studies using different catalysts (Polzer *et al.*, 2012; Nemanashi & Meijboom, 2015). Complexes C-L_2 to C-L_6 followed similar degradation patterns as C-L_1 for t=12 minutes and this is shown in appendix 3.8 to appendix 3.12, respectively.

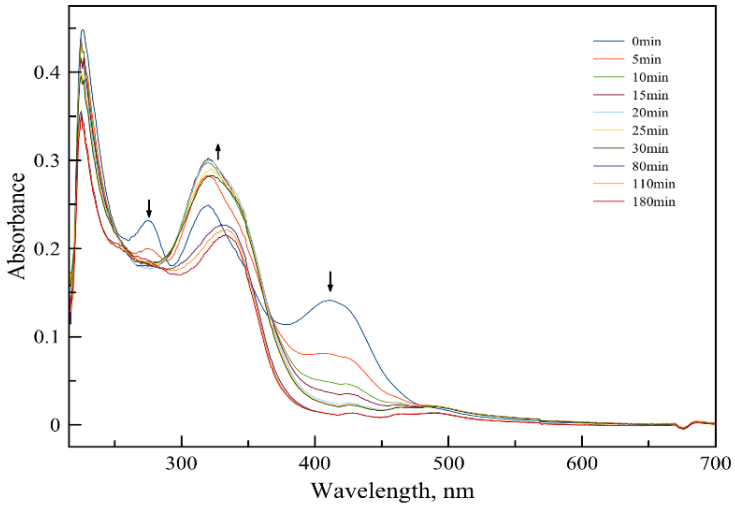

Figure 60: Time-resolved UV-VIS spectra of Morin showing formation of oxidation products

Control studies were carried out where the oxidation was done with C-L_1 and H_2O_2 without the irradiation. A similar oxidation profile, Figure 61, was observed. However, it took a longer time frame to completely degrade Morin t > 40 min as compared to the irradiation degradation which took t < 12min for the peak at λ 410 nm to completely disappear. It has been reported that in absence of a catalyst and with the peroxide, the maxima peak of Morin hardly decreases even after a long time, indicative of the critical role of the catalyst for the degradation. Further, morin degradation by oxygen has been proven not to be significant in presence of H_2O_2 (Polzer *et al.*, 2012; Nemanashi & Meijboom, 2015).

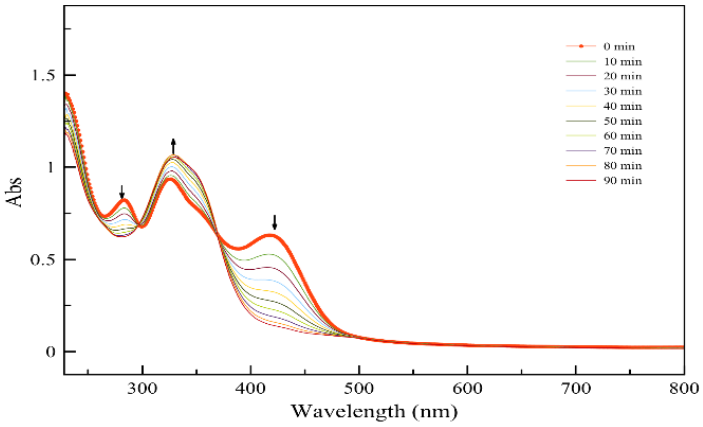

Figure 61: Time-resolved UV-VIS spectra of Morin Solution with C-L_1 and H_2O_2

Concentration of morin is directly proportional to decrease in absorption at λ= 410 nm after irradiation hence, absorption at this wavelength can be used in determining the kinetics of the reaction since the proportionality constant, observed rate constants, K_{obs}, gives a direct measure for morin's decrease in concentration. The performance of the six complexes can thus be evaluated by direct comparison of their respective rate constants. K_{obs} was computed using Equation 10 to give the degradation of morin with time at a fixed wavelength, λ= 410 nm, fitted to a three-parameter single exponential.

$$Abs_t = Abs_0 + (Abs_0 + Abs_\infty) * e^{-kt} \quad \text{----------(10)}$$

where Abs_t is the absorbance and Abs_0 and Abs_∞ are fitted parameters with the absorbance at time 0 and ∞ respectively.

Concentrations studies of C1 at 1 x10^{-5} M, 3 x10^{-5} M, 1 x10^{-4} M and 2 x10^{-4} M gave K_{obs} values of 0.22 s^{-1}, 0.026 s^{-1}, 0.019 s^{-1} and 0.015 s^{-1} respectively showing that low catalytic loading of the complexes, 3 x10^{-5} M gave the best degradation rates.

The observed rate constants were 0.026 s^{-1}, 0.028 s^{-1}, 0.028 s^{-1}, 0.036 s^{-1}, 0.029 s^{-1} and 0.023 s^{-1} for C-L_1 to C-L_6 respectively. C-L_4 had the fastest K_{obs} of 0.036 s^{-1} hence was the most efficient in degrading morin. This could be attributed to it being the most energetic amongst the complexes, λ= 588 nm, coupled with notable long τ =2.6 μs and lower Eox½ = 0.65V thus readily oxidizable lending it the capability to serve as single electron oxidant or reductant with ease. Conversely, complex C-L_6 had the lowest K_{obs} at 0.023 s^{-1} despite having comparable τ and Eox½ values. The emission wavelength for this complex was observed at 603 nm making it have lower energy as compared to C-L_4 hence the lower degradation rate. Both complexes C-L_4 and C-L_6 had -Me substitution. However, the positions of substitution for differed in that the former had -Me substituted in the pyridyl ring while the later -Me substitution was in the naphthyl ring.

On plotting the logarithmic absorbance against time, a linear relationship was obtained as shown in figure 62, implying that Morin degradation is a first order reaction. This observation was consistent with Nemanashi and Meijboom (2015) findings. Based on the K_{obs}, the effectiveness of our catalysts compared well with other catalysts that have been reported with the oxidation under O2 environment being faster than when H_2O_2 was utilized.

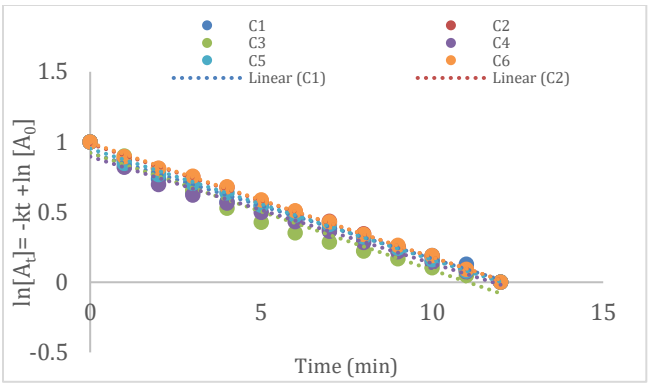

Figure 62: First-order plots for catalytic oxidation of Morin as a function of time for C-L_1 to C-L_6

4.5.3: Selective Photooxidation of Benzyl Alcohols to Aldehydes

The selective photooxidation of phenylmethanol (benzyl alcohol) and (4-Methoxyphenyl)methanol (4-methoxybenzene alcohol) to aldehydes was done as per Section 3.6.3. First, optimization studies were carried out at different reaction conditions i.e., catalyst loading, times and sacrificial electron donor or acceptor (additive), in order to obtain optimum conditions for the reaction using C-L_1 as shown in Table 3.

Table 3: Optimization Parameters for Benzyl alcohol using C-L_1

Entry	Time (h)	Cat loading	Additives	Yield % BzH	Conversion % BnOH
1	24	(0.5mol%)	Collidine	2	13
2	72	(0.5mol%)	Collidine	4	41
3	24	(0.5mol%)	diazonium	3	4
4	72	(0.5mol%)	diazonium	7	29
5	24	(1 mol%)	Ethyl viologen	9	31
6	48	(1 mol%)	Ethyl viologen	22	49
7	>100	(1 mol%)	Ethyl viologen	25	83
8	24	(1 mol%)	Methyl viologen	8	4
9	48	(1 mol%)	Methyl viologen	11	13
10	>100	(1 mol%)	Methyl viologen	8	69
11	24	(2.5 mol%)	Ethyl viologen	3	24
12	48	(2.5 mol%)	Ethyl viologen	5	35
13	>100	(2.5 mol%)	Ethyl viologen	15	52
14	24	(5mol%)	Ethyl viologen	0	25
15	48	(5mol%)	Ethyl viologen	4	32
16	>100	(5mol%)	Ethyl viologen	13	43
No cat	48	-	Ethyl viologen	-	-
In dark	48	(1mol%)	Ethyl viologen	-	-
No additive	48	(1mol%)	-	7	6

Key: phenylmethanol (BnOH); phenylmethanal (BzH); 2,4,6-trimethylpyridine (collidine); 1,1'-diethyl-4,4'-bipyridium dibromide (ethyl viologen); 1,1'-dimethyl-4,4'-bipyridium dichloride hydrate (methyl viologen); 4-nitrobenzenediazonium tetrafluoroborate (diazonium).

The calibration graphs for the p-MBH, 4-MBA, BnOH and BzH are given as appendices 3.4, 3.5, 3.6 and 3.7 respectively. The optimum conditions for the photooxidation catalysis experiments were found to be; 48 hours under 470 nm blue LED light strip (7 W) at a distance of 2 cm intensity,

with catalytic loading of 1 mol % and ethyl viologen as the sacrificial electron acceptor. These were used to investigate photooxidation reactions of C-L_1 to C-L_6 as shown in Table 4.

Table 4: Selective Photooxidation of Benzyl Alcohols

Entry	Yield (%)	
	BzH	p-MBH
C-L_1	30	58
C-L_2	11	57
C-L_3	25	50
C-L_4	18	50
C-L_5	4	11
C-L_6	28	26
No additive; C-L_1	7	-
In dark	-	-

The highest BzH yields achieved were 30%, 28% and 25% for complexes C-L_1, C-L_6 and C-L_3 respectively. The high yields of C-L_1 could be attributed to its unsubstitution hence no steric hindrances. The general trend for increasing yields for all the complexes was C-L_5>C-L_2>C-L_4>C-L_3>C-L_6>C-L_1. Experiment without the additive gave 7% of the BzH indicative of the significance of the catalyst's efficiency at the right loading. The highest p-MBH yields achieved were 58, 57 and 50% from complexes; C-L_1, C-L_2 and C-L_3 & C-L_4 respectively. The general trend for increasing yields for all the complexes was, C-L_5>C-L_6>C-L_4>C-L_3>C-L_2>C-L_1. The high yields of C-L_1 in both reactions could be due to its unsubstitution hence steric hindrances.

4.6 Selective Reduction of 2-furaldehyde to (tetrahydrofuran-2-yl) methanol (THFA)

The selective reduction of 2-furaldehyde (furfural) to 2-Furanmethanol (furfuryl alcohol) and (tetrahydrofuran-2-yl) methanol (tetrahydrofurfuryl alcohol, THFA) using C-L_1 to C-L_6 was carried out as described in section 3.7. First, optimization studies were carried out at different reaction conditions i.e., the time, temperature, hydrogen pressure effects, solvents and in order to obtain optimum conditions for the reaction using C-L_1 as shown in Table 5.

Table 5: Temperature and Pressure Optimization for Reduction of Furfural with C-L_1

S/No.	H_2 (bar)	T (^oC)	Time (h)	Solvent	Yield % (FOH)	Conversion%
1	30	50	24	*i*-PrOH; iPr_2NEt	1	14
2	30	60	24	*i*-PrOH	4	17
3	30	60	48	*i*-PrOH	4	16
4	40	60	24	*i*-PrOH; iPr_2NEt	1	5
5	40	60	24	CH_3CN; iPr_2NEt	1	1
6	40	60	48	CH_3CN; iPr_2NEt	3	8
7	40	60	67	CH_3CN; iPr_2NEt	1	1
8	40	80	24	CH_3CN; iPr_2NEt	1	14
9	40	100	24	Heptane	1	29
10	50	100	24	*i*-PrOH; iPr_2NEt	6	50
11	50	70	24	CH_3CN; iPr_2NEt	4	8
12	60	80	24	*i*-PrOH	6	6
13	60	80	48	*i*-PrOH	70	74
14	60	80	72	*i*-PrOH	20	25
15	60	80	48	*i*-PrOH; no catalyst	0	0
16	70	100	24	*i*-PrOH		1

Key: 2-Furanmethanol (FOH); isopropanol (*i*-PrOH); N, N-Diisopropylethylamine ($^iPr_2Net$)

The calibration curves for THFA, Furfuryl alcohol and Furfural are given in appendices 3.1, 3.2 and 3.3 respectively. The optimum conditions for the selective hydrogenation experiments were found to be: *i*-PrOH without any sacrificial electron acceptor or donor (additive), 60 H_2 bar, T= 80^oC and t = 48 h for this reaction. These were used to investigate hydrogenation reactions of C-L_1 to C-L_6 as shown in Table 6.

Table 6: Hydrogenation of Furfural with C-L_1 to C-L_6

Entry	Time (h)	Yield %	
		FOH	THFA
C-L_1	24	0.8	21.0
C-L_1	67	-	5.4
C-L_2	48	-	-
C-L_3	48	3.22	1.5
C-L_4	24	-	2.3
C-L_4	48	0.56	-
C-L_5	48	-	-
C-L_6	48	4.03	0.8
No catalyst	48	-	-

C-L_1, C-L_3 and C-L_4 gave the three highest yields for (tetrahydrofuran-2-yl)methanol with C-L_1 exhibiting ten times more yield at 21% as compared to 2.3% and 1.5% for C-L_3 and C-L_4. This could be due to C-L_1 being unsubstituted hence no steric hindrances that could be present in the substituted complexes. C-L_1 gave lower yields of THFA at 5.4% on increasing the reaction time by more than 2 times while FOH reduced from 0.8% to zero. The three highest yields for Furanmethanol were 4% for C-L_6, 3.2% for C-L_3 and 0.8% for C-L_1. An inverse relationship with respect to yields between the two expected products, (tetrahydrofuran-2-yl)methanol and Furanmethanol was observed. Experiments done in absence of the catalyst gave no yield indicating the vital role of the of the complexes as photocatalysts. Similar studies done with Ru (II) complexes have shown higher turnover numbers hence the reaction still needs to be optimized further for better results (Xuefeng et al., 2016).

CHAPTER FIVE

CONCLUSIONS AND RECOMMENDATIONS

5.1 CONCLUSIONS

Ten cyclometalating ligands (C^N) were synthesized using Suzuki-Miyaura cross-coupling reaction. Six of the synthesized ligands were based on the 2-(1-naphthyl) pyridine moiety and included the unsubstituted 2-(1-naphthyl) pyridine (L_1), 92% yield, 2-(1-naphthyl)-4-methoxy pyridine (L_2) 90% yield and 2-(1-naphthyl)-4-trifluoromethyl pyridine (L_3) 97% yield. Ligands L_4-L_6 gave yields ranging 90-97%, while L_7-L_{10} ligands, which were based on 1-phenyl isoquinoline moiety included 4-Fluoro-1-phenyl isoquinoline (L_7), 84% yield, 4-Fluoro-1-phenyl isoquinoline (L_8), 83% yield, 4-*tert*-butyl-1-phenyl isoquinoline (L_9), 65% yield and 4-methyl-1-phenyl isoquinoline (L_{10}), 89%) yield

UV-VIS spectroscopic measurements of the ligands gave excitation λ_{max} of ca. 260 - 294nm. These were intra-ligand π-π^* transitions.

Ten *tris*-homoleptic cyclometalated Ir(III) complexes were synthesized with the ligands. The yields obtained were: *Tris* 2-(1-naphthyl) pyridyl iridium (C-L_1), 44% yield, *Tris* 2-(1-naphthyl)-4-methoxy pyridyl iridium (C-L_2), 50% yield and *Tris* 2-(1-naphthyl)-4-trifluoromethyl pyridyl iridium (C-L_3), 39% yield. Complexes C-L_4 to C-L_6 gave yields ranging 39-44%, while C-L_7 to C-L_{10} had 45-95%.

The UV-VIS spectroscopic measurements of C-L_1 to C-L_{10} gave excitation λ_{max} range of 400-442 nm. On exciting at 400 nm the complexes exhibited varying emission λ_{max} between 588-625 nm i.e., C-L_1 emitted at 591 nm, C-L_2 610 nm, C-L_4 588 nm and C-L_{10} 625 nm. The varying emission λ_{max} values of the complexes showed their respective specificities. The 10Dq values of the octahedral complexes were C-L_1 24390 cm^{-1}, C-L_2 23923 cm^{-1}, C-L_4 25000 cm^{-1} and C-L_3 22988 cm^{-1}, resulting from d-d transitions.

Quantum yields, Φ_f, for C-L_1 to C-L_6 were C-L_1 8.6, C-L_2 22, C-L_3 14, C-L_4 19, C-L_5 9.4 and C-L_6 16. Subsequently, emission lifetimes, τ, for the complexes were between 1.4-3.7 μs where C-L_1

had 1.5 μs, C-L_2 had 3.0 μs, C-L_3 had 3.7 μs, and C-L_4 had 2.6 μs. The high Φ_f and long τ obtained were consistent with the phosphorescence of the luminophores.

C-L_2 with -OMe substitution at Carbon 4 had higher emission λ_{max} relative to C-L_1 by 19 nm, while C-L_3 with CF_3 increased by 12 nm relative to C-L_1, which reflected a reduction on Δ_o splitting. C-L_4 with -Me substitution decreased by 3 nm relative to C-L_1 reflecting an increase in Δ_o splitting. Cyclic voltammetry of the complexes C-L_1 to C-L_6 showed oxidation potential, $Eox_{1/2}$, ranging from +0.60 to +0.96 V during anodic scanning while reduction potential, $E_{red1/2}$, values were from +0.54 to +0.89 V during cathodic scanning. The $Eox_{1/2}$ values were a result of reversible, single electron transfer (SET) process at the metal-centered Ir^{III}/Ir^{IV}oxidation couple.

Crystallographic evaluations of C-L_1, showed it to be octahedral. Vital bond angles of C and N atoms around the Ir center were Ir-N1-C, 125; Ir-N1-C5, 119; Ir-N2-C16, 127; Ir-N2-C20, 116.3; Ir-N3-C31, 126; Ir-N3-C35, 115.3; N1-Ir-N2, 96.4; N1-Ir-N3, 95.8; N2-Ir-N3, 99.2 while the cyclic bond lengths were Ir-N1, 2.09; Ir-N2 2.14; Ir-N3, 2.13; Ir-C7, 2.03; Ir-C22, 2.00; Ir-C37, 2.03. These values were consistent with a facile arrangement of the non-polymeric, three-cyclometalating ligands around the iridium center through bidentate chelation with a 2-fold rotation axis showing that the complex was octahedral.

Complexes C-L_1 to C-L_6 were subsequently utilized in three photoredox catalysis applications using blue LED lights of 470 nm at 7 W. The first application on three-component methoxy trifluoromethylation of styrene, gave 97%, 100%, 100% yields for C-L_1, C-L_2, and C-L_3, respectively while the rest gave between the range 56 - 84%. The results showed the complexes were able to proficiently mediate single electron transfer (SET) events to achieve highly regioselective methoxytrifluoromethylation of styrene.

The second photoredox application was on photodegradation of Morin using blue light, as a model reaction. C-L_1 to C-L_6 were found to catalyse the degradation of morin in 12 minutes under ambient temperatures in O2 environment at pH 10 with degradation rate constants, K_{obs} 0.023 s^{-1} to 0.036 s^{-1}. C-L_4, exhibited the highest K_{obs} = 0.036 s^{-1}. The photoredox catalytic degradation reaction of Morin dye was found to follow first order kinetics.

The third photoredox application was on selective photooxidation of alcohols; phenylmethanol and (4-Methoxyphenyl) methanol to aldehydes. The highest phenylmethanal (BzH) yields achieved were 30, 28 and 25% from complexes; C-L_1, C-L_6 and C-L_3, respectively while the highest 4-methoxybenzaldehyde (p-MBH) yields achieved were 58, 57 and 50% from complexes; C-L_1, C-L_2 and C-L_3 and C-L_4 respectively. In both cases C-L_1 had highest yields compared to the rest of the complexes. The complexes selectively catalyzed the photooxidation and exhibited selectivity of 99% for both oxidation reactions.

The complexes selectively hydrogenated 2-furaldehyde into 2-Furanmethanol and Tetrahydrofuran-2-yl methanol giving 21% yield of Tetrahydrofuran-2-yl methanol with C-L_1 and gave 4% yield of 2-Furanmethanol with C-L_6.

5.2: RECOMMENDATIONS

1. Ir(III) complexes were successfully synthesized and they were utilized in photoredox catalysis and selective hydrogenation of furfural. The products of these applications can be used in manufacturing and pharmaceutical fields.
2. A prototype for photoredox catalysis should be developed using the 2-(napthalen-1-yl) pyridine *tris* homoleptic cyclometalated Ir(III) complexes C-L_1 to C-L_6.
3. A prototype process for selective hydrogenation of furfural to THFA utilized in the manufacture of fine organic chemicals should be developed using the 2-(napthalen-1-yl) pyridine *tris* homoleptic cyclometalated Ir(III) complexes C-L_1 to C-L_6.
4. Infrared, crystallographic measurements and DFT calculations should be done for the complexes. Complexes C-L_7 to C-L_{10} should be evaluated for their photoredox catalysis activity and selective hydrogenation.
5. Investigation of substitution positioning on the aromatic ring i.e. *ortho*, *meta*, *para* positions with weak field ligand substituents and strong field ligand substituents.

REFERENCES

Ahlstrand, D. A., Polukeev, A. V., Marcos, R., Ahlquist, M. S. G., & Wendt, O. F. (2017). Csp ^{3} −H Activation without Chelation Assistance in an Iridium Pincer Complex Forming Cyclometallated Products. *Chemistry - A European Journal*, *23*(8), 1748–1751. https://doi.org/10.1002/chem.201604469.

Albrecht, M. (2010). Cyclometalation using d-block transition metals: fundamental aspects and recent trends. *Chemical Reviews*, *110*(2), 576–623. https://doi.org/10.1021/cr900279a.

Anderson, J. R., Bendell, J. D., & Groundwater, W. P. (2004). *Tutorial Chemistry Texts: Organic Spectroscopic Analysis*. UK: The Royal Society of Chemistry.

Angnes, R. A., Li, Z.-J. Z.-F. Z., Correia, C. R. D., Hammond, G. B., Prier, C. K., Rankic, D. A., Correia, C. R. D. (2015). Recent synthetic additions to the visible light photoredox catalysis toolbox. *Org. Biomol. Chem.*, *13*(35), 9152–9167. https://doi.org/10.1039/C5OB01349F.

Arias-Rotondo, D. M., McCusker, J. K., Lytle, F. E., Hercules, D. M., Juris, A., Balzani, V., Zysman-Colman, E. (2016). The photophysics of photoredox catalysis: a roadmap for catalyst design. *Chem. Soc. Rev.*, *45*(21), 5803–5820. https://doi.org/10.1039/C6CS00526H.

Atkins, P. W. (1978). *Physical Chemistry* (1st ed.). Oxford: Oxford University Press, Inc.

Bae, H. J., Kim, H., Lee, K. M., Kim, T., Eo, M., Lee, Y. S., … Lee, M. H. (2013). Heteroleptic tris-cyclometalated iridium(III) complexes supported by an o-carboranyl-pyridine ligand. *Dalton Transactions (Cambridge, England : 2003)*, *42*(24), 8549–8552. https://doi.org/10.1039/c3dt51019k.

Ball, W. D., & Key, A. J. (2014). *Introductory Chemistry- 1st Canadanian Edition* (1st ed.). Retrieved from https://opentextbc.ca/introductorychemistry/front-matter/acknowledgments-2.

BASi Epsilon. (2009). *Instruction Manual for Basi Epsilon for Electrochemistry*. Retrieved from https://www.basinc.com/assets/library/manuals/EC_epsilon/EC_epsilon_Manual.pdf.

Brady, J., Russell, J., & Holum, J. (2000). *Chemistry-Matter and Its Changes* (3rd ed.). New York, NY USA: John Wiley & Sons Ltd.

Brown, J. M. (2015). New Trends in Cross-Coupling - Theory and Applications. Edited by Thomas J. Colacot. *Angewandte Chemie International Edition*, *54*(17), n/a-n/a. https://doi.org/10.1002/anie.201501713.

Bruce, M. I. (1977). Cyclometalation Reactions. *Angewandte Chemie International Edition in English*, *16*(2), 73–86. https://doi.org/10.1002/anie.197700731.

Brulatti, P. (2010). New luminescent iridium (III) complexes containing NCN cyclometallated ligands : synthesis , photophysical properties and emission tuning (University of Durham). Retrieved from http://etheses.dur.ac.uk/447.

Butschke, B., & Schwarz, H. (2012). "Rollover" cyclometalation – early history, recent developments, mechanistic insights and application aspects. *Chem. Sci.*, *3*(2), 308–326. https://doi.org/10.1039/c1sc00651g.

Chang, R. (2005). *Chemistry* (8th ed.; T. Timp, D. & S. Oberbroeckling, R., Eds.). New York, NY 10020: The McGraw-Hill Companies Inc.

Chatterjee, M. K. (2011). An attempt to achieve the direct hydrogenolysis of tetrahydrofurfuryl alcohol in supercritical carbon dioxide. *Catalysis Science & Technology*, *1*, 1466–1471.

Chen, L., You, H., Yang, C., Ma, D., & Qin, J. (2007). Novel, highly efficient blue-emitting heteroleptic iridium(III) complexes based on fluorinated 1,3,4-oxadiazole: tuning to blue by dithiolate ancillary ligands. *Chemical Communications (Cambridge, England)*, (13), 1352–1354. https://doi.org/10.1039/b616493e.

Cîrcu, V., & Micutz, M. (2011). *X-Ray Structural Characterization of Cyclometalated Luminescent Pt (II) Complexes*. *2*(II).

Colombo, M. G., Brunold, T. C., Riedener, T., & Gudel, H. U. (1994). Facial Tris Cyclometalated Rh3+ and Ir3+ Complexes: Their Synthesis, Structure, and Optical Spectroscopic Properties.

Inorganic Chemistry, *33*(3), 545–550.

Coppo, P., Plummer, E. A., De Cola, L., Hughes, H., Wang, R., Vos, J. G., … Thompson, M. E. (2004). Tuning iridium(iii) phenylpyridine complexes in the “almost blue” region. *Chem. Commun.*, *208*(15), 1774–1775. https://doi.org/10.1039/B406851C.

Crabtree, R. H. (2009). *The Organometallic Chemistry of the Transition Metals* (5th ed.). Retrieved from http://www.google.se/books.

Dedeian, K., Shi, J., Shepherd, N., Forsythe, E., & Morton, D. C. (2005). Photophysical and electrochemical properties of heteroleptic tris-cyclometalated iridium(III) complexes. *Inorganic Chemistry*, *44*(13), 4445–4447. https://doi.org/10.1021/ic050324u.

Ellis, A. M. (1999). Spectroscopic Selection Rules: The Role of Photon States. *Journal of Chemical Education*, *76*(9), 1291. https://doi.org/10.1021/ed076p1291.

Fadeeva, V. P., Tikhova, V. D., & Nikulicheva, O. N. (2008). Elemental analysis of organic compounds with the use of automated CHNS analyzers. *Journal of Analytical Chemistry*, *63*(11), 1094–1106. https://doi.org/10.1134/S1061934808110142.

Felici, M., Contreras-Carballada, P., Smits, J. M. M., Nolte, R. J. M., Williams, R. M., De Cola, L., & Feiters, M. C. (2010). Cationic heteroleptic cyclometalated iridium(III) complexes containing phenyl-triazole and triazole-pyridine clicked ligands. *Molecules (Basel, Switzerland)*, *15*(3), 2039–2059. https://doi.org/10.3390/molecules15032039.

Fihri, A., Bouhrara, M., Nekoueishahraki, B., Basset, J.-M., & Polshettiwar, V. (2011). Nanocatalysts for Suzuki cross-coupling reactions. *Chemical Society Reviews*, *40*(10), 5181. https://doi.org/10.1039/c1cs15079k.

Greenwood, N. N., & Earnshaw, A. (1998). *Greenwood - Chemistry of the Elements* (2nd ed.).

Griffin, J. D., Cavanaugh, C. L., & Nicewicz, D. A. (2017). Reversing the Regioselectivity of Halofunctionalization Reactions through Cooperative Photoredox and Copper Catalysis. *Angewandte Chemie International Edition*, *56*(8), 2097–2100.

https://doi.org/10.1002/anie.201610722.

Harvey, D. (2019a). Photoluminescence Spectroscopy. Retrieved June 12, 2019, from Chemistry LibreTexts website: https://chem.libretexts.org/Bookshelves/Analytical_Chemistry/Book%3A_Analytical_Chemistry_2.0_(Harvey)/10_Spectroscopic_Methods/10.6%3A_Photoluminescence_Spectroscopy.

Harvey, D. (2019b). UV/Vis and IR Spectroscopy. Retrieved June 12, 2019, from Chemistry LibreTexts website: https://chem.libretexts.org/Bookshelves/Analytical_Chemistry/Book%3A_Analytical_Chemistry_2.0_(Harvey)/10_Spectroscopic_Methods/10.3%3A_UV%2F%2FVis_and_IR_Spectroscopy.

Hasan, K., Bansal, A. K., Samuel, I. D. W., Roldán-Carmona, C., Bolink, H. J., & Zysman-Colman, E. (2015). Tuning the Emission of Cationic Iridium (III) Complexes Towards the Red Through Methoxy Substitution of the Cyclometalating Ligand. *Scientific Reports, 5*(1), 12325. https://doi.org/10.1038/srep12325.

Henderson, W., & McIndoe, J. S. (2005). *Mass spectrometry of Inorganic, Coordination, and Organometallic Compounds*. Retrieved from https://books.google.co.ke/books/about/Mass_Spectrometry_of_Inorganic_and_Organ.html.

Ho, C. L., Wang, E. I. C., & Su, Y. C. (2009). Tetrahydrofurfuryl Alcohol (THFA) Pulping of Rice Straw. *Journal of Wood Chemistry and Technology*, *29*, 101–118. https://doi.org/10.1080/02773810902796138.

Hofbeck, T., & Yersin, H. (2010). The Triplet State of fac -Ir (ppy) 3. *Inorganic Chemistry*, *49*(20), 9290–9299. https://doi.org/10.1021/ic100872w.

House, J. E. (2018). Chapter 12 - Spectroscopy of Metal Complexes. In J. E. House (Ed.), *Fundamentals of Quantum Mechanics (Third Edition)* (Third, pp. 297–314). https://doi.org/https://doi.org/10.1016/B978-0-12-809242-2.00012-7.

Housecroft, E. C., & Sharpe, G. A. (2005). *Inorganic Chemistry* (2nd ed.). England: Pearson Education Limited.

Huang, Z., Liu, B., He, Y., Yan, X., Yang, X., Xu, X., Wu, Z. (2015). Facilitating triplet energy-transfer in polymetallayne-based phosphorescent polymers with iridium(III) units and the great potential in achieving high electroluminescent performances. *Journal of Organometallic Chemistry*, *794*, 1–10. https://doi.org/10.1016/j.jorganchem.2015.06.030.

Jones, J. C. (2002). *Tutorial Chemistry Texts: d- and f-Block Chemistry*. British: Royal Society of Chemistry.

Kakani, S. L., & Kakani, A. (2004). *Material Science*. New Delhi: New Age International (P) Ltd.

Kemp, W. (1991). *Organic Spectroscopy* (3rd ed.). Hong King: Macmillan Education Ltd.

Khudyakov, I. V., Serebrennikov, Y. A., & Turro, N. J. (1993). Spin-orbit coupling in free-radical reactions: on the way to heavy elements. *Chemical Reviews*, *93*(1), 537–570. https://doi.org/10.1021/cr00017a023.

Kim, M.-H., Smith, V. P., & Hong, T.-K. (1993). First and Second-Order Derivative Polarography/Voltammetry for Reversible, Quasi-Reversible, and Irreversible ElectrodeProcesse. *J Electrochem. Soc*, *140*(3), 712–721.

Koike, T., & Akita, M. (2014). www.rsc.org/merckindex Visible-light radical reaction designed by Ru-and Ir-based photoredox catalysis. *Inorganic Chemistry Frontiers*, *1*, 562–576. https://doi.org/10.1039/c4qi00053f.

Koike, T., Akita, M., Yoon, T. P., Ischay, M. A., Du, J., Narayanam, J. M. R., … Ma, J.-A. (2014). Visible-light radical reaction designed by Ru- and Ir-based photoredox catalysis. *Inorganic Chemistry Frontiers*, *1*(8), 562–576. https://doi.org/10.1039/C4QI00053F.

Kondrashov, M., Raman, S., & Wendt, O. F. (2015). Metal controlled regioselectivity in the cyclometallation of 2-(1-naphthyl)-pyridine. *Chem. Commun.*, *51*, 911–913. https://doi.org/10.1039/C4CC07962K.

Kuhl, N., Hopkinson, M. N., Wencel-Delord, J., & Glorius, F. (2012). Beyond directing groups: transition-metal-catalyzed C-H activation of simple arenes. *Angewandte Chemie (International Ed. in English)*, *51*(41), 10236–10254. https://doi.org/10.1002/anie.201203269.

Labinger, J. a, & Bercaw, J. E. (2002). Understanding and exploiting C-H bond activation. *Nature*, *417*(May), 507–514. https://doi.org/10.1038/417507a.

Laporte, O., & Meggers, W. F. (1925). Some Rules of Spectral Structure. *Journal of the Optical Society of America and Review of Scientific Instruments*, *11*(5), 459–463. https://doi.org/10.1364/JOSA.11.000459.

Lees, A. J., & Lees, A. J. (1987). Luminescence properties of organometallic complexes. *Chem. Rev.*, *87*(4), 711–743. https://doi.org/10.1021/cr00080a003.

Lennox, A. J. J., & Lloyd-Jones, G. C. (2013). Transmetalation in the Suzuki-Miyaura coupling: the fork in the trail. *Angewandte Chemie (International Ed. in English)*, *52*(29), 7362–7370. https://doi.org/10.1002/anie.201301737.

Li, J. J. (2014a). C–H activation. In *Name Reactions* (pp. 112–122). https://doi.org/10.1007/978-3-319-03979-4_54.

Li, J. J. (2014b). Heck reaction. In *Name Reactions* (pp. 304–308). https://doi.org/10.1007/978-3-319-03979-4_129.

Li, J. J. (2014c). Hiyama cross-coupling reaction. In *Name Reactions* (pp. 316–317). https://doi.org/10.1007/978-3-319-03979-4_134.

Li, J. J. (2014d). Kumada cross-coupling reaction. In *Name Reactions* (pp. 357–359). https://doi.org/10.1007/978-3-319-03979-4_154.

Li, J. J. (2014e). Negishi cross-coupling reaction. In *Name Reactions* (pp. 430–431). https://doi.org/10.1007/978-3-319-03979-4_190.

Li, Z., Cui, P., Wang, C., Kilina, S., & Sun, W. (2014). Nonlinear Absorbing Cationic Bipyridyl

Iridium(III) Complexes Bearing Cyclometalating Ligands with Different Degrees of π-Conjugation: Synthesis, Photophysics, and Reverse Saturable Absorption. *The Journal of Physical Chemistry C*, *118*(49), 28764–28775. https://doi.org/10.1021/jp5073457.

Liddle, S. T., & van Slageren, J. (2015). Improving f-element single molecule magnets. *Chem. Soc. Rev.* https://doi.org/10.1039/C5CS00222B.

Littke, A. F., Dai, C., & Fu, G. C. (2000). Versatile Catalysts for the Suzuki Cross-Coupling of Arylboronic Acids with Aryl and Vinyl Halides and Triflates under Mild Conditions. *Journal of the American Chemical Society*, *122*(17), 4020–4028. https://doi.org/10.1021/ja0002058.

Liu, Y., Persson, P., Sundström, V., & Wärnmark, K. (2016). Fe *N* -Heterocyclic Carbene Complexes as Promising Photosensitizers. *Accounts of Chemical Research*, *49*(8), 1477–1485. https://doi.org/10.1021/acs.accounts.6b00186.

Livingtstone, S. E. (2017). *The chemistry of ruthenium, rhodium, pallodium, osmiun, iridium and platinum*. Retrieved from https://books.google.co.ke/books.

Ma, T. S., & Gutterson, M. (1970). Organic elemental analysis. *Analytical Chemistry*, *42*(5), 105–114. https://doi.org/10.1021/ac60287a024.

Mathey, F. (2013). *Transition Metal Organometallic Chemistry*. https://doi.org/10.1007/978-981-4451-09-3.

Miessler, L. G., Fischer, J. P., & Tarr, A. D. (2014). *Inorganic Chemistry* (5th ed.). Boston: Pearson Education Inc.

Miyaura, N., & Suzuki, A. (1995). Palladium-Catalyzed Cross-Coupling Reactions of Organoboron Compounds. *Chemical Reviews*, *95*(7), 2457–2483. https://doi.org/10.1021/cr00039a007.

Monos, T. M., & Stephenson, C. R. J. (2017). Photoredox Catalysis of Iridium(III)-Based Photosensitizers. In *Iridium(III) in Optoelectronic and Photonics Applications* (pp. 541–581). https://doi.org/10.1002/9781119007166.ch11.

Murakami, M., & Ishida, N. (2017). A shortcut to molecular complexity. *Nature Chemistry*, *9*(4), 298–299. https://doi.org/10.1038/nchem.2750.

Nagai, T., Nishioka, G., Koyama, M., Ando, A., Miki, T., & Kumadaki, I. (1991). The steric effect of a trifluoromethyl group. *Chemical & Pharmaceutical Bulletin*, *39*(1), 233–235. https://doi.org/10.1248/cpb.39.233.

Narayanam, J. M. R., Stephenson, C. R. J., Ciamician, G., Hoffmann, N., Fagnoni, M., Dondi, D., … Stephenson, C. R. J. (2011). Visible light photoredox catalysis: applications in organic synthesis. *Chemical Society Reviews*, *40*(1), 102–113. https://doi.org/10.1039/b913880n.

Nazeeruddin, M. K., Zakeeruddin, S. M., & Kalyanasundaram, K. (1993). Enhanced intensities of the ligand-to-metal charge-transfer transitions in ruthenium(III) and osmium(III) complexes of substituted bipyridines. *The Journal of Physical Chemistry*, *97*(38), 9607–9612. https://doi.org/10.1021/j100140a014.

Nemanashi, M., & Meijboom, R. (2015). Catalytic Behavior of Different Sizes of Dendrimer-Encapsulated Au_n Nanoparticles in the Oxidative Degradation of Morin with H_2O_2. *Langmuir*, *31*(33), 9041–9053. https://doi.org/10.1021/acs.langmuir.5b02020.

Nicholson, R. S. (1965). Theory and Application of Cyclic Voltammetry for Measurement of Electrode Reaction Kinetics. *Analytical Chemistry*, *37*(11), 1351–1355. https://doi.org/10.1021/ac60230a016.

Ochola, J. R., & Wolf, M. O. (2016). The effect of photocatalyst excited state lifetime on the rate of photoredox catalysis. *Org. Biomol. Chem.*, *14*(38), 9088–9092. https://doi.org/10.1039/C6OB01717G.

Okada, S., Okinaka, K., Iwawaki, H., Furugori, M., Hashimoto, M., Mukaide, T., … Ueno, K. (2005). Substituent effects of iridium complexes for highly efficient red OLEDs. *Dalton Transactions*, (9), 1583–1590. https://doi.org/10.1039/b417058j.

Okamura, N., Nakamura, T., Yagi, S., Maeda, T., Nakazumi, H., Fujiwara, H., & Koseki, S. (2016). Novel bis- and tris-cyclometalated iridium(iii) complexes bearing a benzoyl group

on each fluorinated 2-phenylpyridinate ligand aimed at development of blue phosphorescent materials for OLED. *RSC Adv.*, *6*(56), 51435–51445. https://doi.org/10.1039/C6RA09385J.

Omae, I. (2014). *Cyclometalation Reactions*. https://doi.org/10.1007/978-4-431-54604-7.

Omary, A. M., & Patterson, H. H. (1999). Luminescence Theory. *Encyclopedia of Spectroscopy and Spectrometry*, 1186–1207. https://doi.org/https://doi.org/10.1006/rwsp.2000.0160.

Pandey, R. N., Kumari, G., Kumar, A., & Kr Singh, R. (2010). Mixed-ligand organometallic complexes of pt-group metals with triphenyl phosphine and heterocyclic thioamides. In *Int. J. Chem. Sci* (Vol. 8).

Polukeev, A. V., Marcos, R., Ahlquist, M. S. G., & Wendt, O. F. (2015). Formation of a C–C double bond from two aliphatic carbons. Multiple C–H activations in an iridium pincer complex. *Chem. Sci.*, *6*(3), 2060–2067. https://doi.org/10.1039/C4SC03839H.

Polzer, F., Wunder, S., Lu, Y., & Ballauff, M. (2012). Oxidation of an organic dye catalyzed by MnOx nanoparticles. *Journal of Catalysis*, *289*, 80–87. https://doi.org/10.1016/j.jcat.2012.01.016.

Prier, C. K., Rankic, D. A., & MacMillan, D. W. C. (2013). Visible Light Photoredox Catalysis with Transition Metal Complexes: Applications in Organic Synthesis. *Chemical Reviews*, *113*(7), 5322–5363. https://doi.org/10.1021/cr300503r.

Rackus, D. G., Shamsi, M. H., & Wheeler, A. R. (2015). Electrochemistry, biosensors and microfluidics: a convergence of fields. *Chemical Society Reviews*, *44*(15), 5320–5340. https://doi.org/10.1039/c4cs00369a.

Reich, J., & Reich, H. J. (2018). 5-HMR-2 Chemical Shift. Retrieved January 19, 2019, from University of Wisconsin website: https://www.chem.wisc.edu/areas/reich/nmr/05-hmr-02-delta.html.

Reyes, P., Salinas, D., Campos, C., Oportus, M., Murcia, J., Rojas, H. F., … Fierro, J. L. G. (2010). Selective hydrogenation of furfural on Ir/TiO2 catalysts. *Quimica Nova*, *33*(4), 777–780.

https://doi.org/10.1590/S0100-40422010000400002.

Riess, F. J. (1985). Organometallic chemistry, coordination chemistry, main group chemistry. Where are the frontiers at present? *Journal of Organometallic Chemistry*, *281*(1), 1–14. https://doi.org/https://doi.org/10.1016/0022-328X(85)87085-6.

Rojas, H. M. (2010). Kinetic Behaviour in the Hydrogen of Furfural over Ir Catalysts Supported on TiO2. *Dyna*, *77*(163), 151–159.

Rueping, M., Vila, C., Szadkowska, A., Koenigs, R. M., & Fronert, J. (2012). Photoredox Catalysis as an Efficient Tool for the Aerobic Oxidation of Amines and Alcohols: Bioinspired Demethylations and Condensations. *ACS Catalysis*, *2*(12), 2810–2815. https://doi.org/10.1021/cs300604k.

Sajoto, T., Djurovich, P. I., Tamayo, A. B., Oxgaard, J., Goddard, W. A., & Thompson, M. E. (2009). Temperature Dependence of Blue Phosphorescent Cyclometalated Ir(III) Complexes. *Journal of the American Chemical Society*, *131*(28), 9813–9822. https://doi.org/10.1021/ja903317w.

Samanta, S., & Biswas, P. (2015). Metal free visible light driven oxidation of alcohols to carbonyl derivatives using 3,6-di(pyridin-2-yl)-1,2,4,5-tetrazine (pytz) as catalyst. *RSC Adv.*, *5*(102), 84328–84333. https://doi.org/10.1039/C5RA18151H.

Shaw, M. H., Twilton, J., & Macmillan, D. W. C. (2016). Photoredox Catalysis in Organic Chemistry. *The Journal of Organic Chemistry*, *81*(16), 6898–6926. https://doi.org/10.1021/acs.joc.6b01449.

Shi, L., & Xia, W. (2012). Photoredox functionalization of C–H bonds adjacent to a nitrogen atom. *Chemical Society Reviews*, *41*(23), 7687. https://doi.org/10.1039/c2cs35203f.

Singh, A., Teegardin, K., Kelly, M., Prasad, K. S., Krishnan, S., & Weaver, J. D. (2015). Facile synthesis and complete characterization of homoleptic and heteroleptic cyclometalated Iridium(III) complexes for photocatalysis. *Journal of Organometallic Chemistry*, *776*, 51–59. https://doi.org/10.1016/j.jorganchem.2014.10.037..

Sisodiya, S., Wallenberg, L. R., Lewin, E., & Wendt, O. F. (2015). Sonogashira coupling reaction over supported gold nanoparticles: Influence of support and catalyst synthesis route. *Applied Catalysis A: General*, *503*, 69–76. https://doi.org/10.1016/j.apcata.2015.07.001

Skoog, A. D. (stanford university), Holler, F. J. (university of K., & Nieman, A. T. (university of I. at U.-C. (1998). *Principles of Instrumental Analysis* (5th ed.). Publishers, Harcourt Brace College.

Skubi, K. L., Blum, T. R., & Yoon, T. P. (2016). Dual Catalysis Strategies in Photochemical Synthesis. *Chemical Reviews*, *116*(17), 10035–10074. https://doi.org/10.1021/acs.chemrev.6b00018.

Song, Y. L. (2007). Hydrogenation of furfuryl alcohol to tetrahydrofurfuryl alcohol on NiB/SiO2 amorphous alloy catalyst. *Frontiers of Chcemical Engineering in China*, *1*(2), 151–154.

Spessard, G. O., & Miessler, G. L. (2010). *Organometallic Chemistry* (2nd ed.). Oxford, New York: Oxford University Press, Inc.

Stauffer, E., Dolan, J. A., Newman, R., Stauffer, E., Dolan, J. A., & Newman, R. (2008). Gas Chromatography and Gas Chromatography—Mass Spectrometry. *Fire Debris Analysis*, 235–293. https://doi.org/10.1016/B978-012663971-1.50012-9.

Stein, A. L., Bilheri, F. N., & Zeni, G. (2015). Application of organoselenides in the Suzuki, Negishi, Sonogashira and Kumada cross-coupling reactions. *Chemical Communications*, *51*(85), 15522–15525. https://doi.org/10.1039/C5CC06347G.

Still, W. C., Kahn, M., & Mitra, A. (1978). Rapid chromatographic technique for preparative separations with moderate resolution. *The Journal of Organic Chemistry*, *43*(14), 2923–2925. https://doi.org/10.1021/jo00408a041.

Tian, N. (2011). *Phosphorescent iridium (III) complexes , copolymers and their applications*. University of Wuppertal.

Tian, N., Lenkeit, D., Pelz, S., Kourkoulos, D., & Hertel, D. (2011). Screening structure – property

correlations and device performance of Ir (III) complexes in multi-layer PhOLEDs †. *Dalton Transactions*, *40*, 11629–11635. https://doi.org/10.1039/c1dt11059d.

Tian, N., Thiessen, A., Schiewek, R., Schmitz, O. J., Hertel, D., Meerholz, K., & Holder, E. (2009). Efficient Synthesis of Carbazolyl- and Thienyl-Substituted -Diketonates and Properties of Their Red- and Green-Light-Emitting Ir (III) Complexes. *Journal of Organic Chemistry*, *74*(7), 2718–2725. https://doi.org/10.1021/jo8025516.

Trofimenko, S. (1968). Molybdenum complexes with non-inert-gas configuration. *Journal of the American Chemical Society*, *90*(17), 4754–4755. https://doi.org/10.1021/ja01019a059.

Tucker, J. W., & Stephenson, C. R. J. (2012). Shining Light on Photoredox Catalysis: Theory and Synthetic Applications. *The Journal of Organic Chemistry*, *77*(4), 1617–1622. https://doi.org/10.1021/jo202538x.

Ulbricht, C. (2009). *Phosphorescent systems based on iridium (III) complexes* (Technical University of Eindhoven). https://doi.org/9789038620503.

Vetere, V. M. (2010). Transition Metal-based Bimetallic Catalysts for the Chemoselective Hydrogenation of Furfuraldehyde. *J. Braz. Chem. Soc.*, *21*(5), 914–920.

Wadman, S. H., Kroon, J. M., Bakker, K., Havenith, R. W. A., van Klink, G. P. M., & van Koten, G. (2010). Cyclometalated Organoruthenium Complexes for Application in Dye-Sensitized Solar Cells. *Organometallics*, *29*(7), 1569–1579. https://doi.org/10.1021/om900481g.

Wadman, S. H., Lutz, M., Tooke, D. M., Spek, A. L., Hartl, F., Havenith, R. W. A., van Koten, G. (2009). Consequences of N,C,N'- and C,N,N'-coordination modes on electronic and photophysical properties of cyclometalated aryl ruthenium(II) complexes. *Inorganic Chemistry*, *48*(5), 1887–1900. https://doi.org/10.1021/ic801595m.

Wang, R., Deng, L., Zhang, T., & Li, J. (2012). Substituent effect on the photophysical properties, electrochemical properties and electroluminescence performance of orange-emitting iridium complexes. *Dalton Transactions*, *41*(22), 6833. https://doi.org/10.1039/c2dt12206e.

Wieprecht, T., Heinz, U., Xia, J., Schlingloff, G., & Dannacher, J. (2004). Terpyridine-manganese complexes: A new class of bleach catalysts for detergent applications. *Journal of Surfactants and Detergents*, *7*(1), 59–66. https://doi.org/10.1007/s11743-004-0289-7.

Willard, H. H., Merrit, J. L. L., Dean, A. J., & Settle, J. A. F. (1986). *Instrumental Methods of Analysis* (7th ed.). India: Satish Kumar Jain for CBS Publishers & Distributors.

Win, D. (2005). Furfural – Gold from Garbage. *AU Journal*, *8*(4), 185–190.

Wisser, M. D., Chea, M., Lin, Y., Wu, D. M., Mao, W. L., Salleo, A., & Dionne, J. a. (2015). Strain-Induced Modification of Optical Selection Rules in Lanthanide-Based Upconverting Nanoparticles. *Nano Letters*, *15*(3), 150218172610006. https://doi.org/10.1021/nl504738k.

Würth, C., Grabolle, M., Pauli, J., Spieles, M., & Resch-Genger, U. (2011). Comparison of Methods and Achievable Uncertainties for the Relative and Absolute Measurement of Photoluminescence Quantum Yields. *Analytical Chemistry*, *83*(9), 3431–3439. https://doi.org/10.1021/ac2000303.

Xuefeng, T., Wang, G., Zhu, Z., Ren, C., Zhou, J., Lv, H., Zhang, X. X. X. (2016). Hydrogenation of Aldehydes Catalyzed by an Available Ruthenium Complex. *Organic Letters*, *18*(7), 1518–1521. https://doi.org/10.1021/acs.orglett.6b00060.

Yasu, Y., Koike, T., & Akita, M. (2012). Three-component Oxytrifluoromethylation of Alkenes: Highly Efficient and Regioselective Difunctionalization of C□C Bonds Mediated by Photoredox Catalysts. *Angewandte Chemie International Edition*, *51*(38), 9567–9571. https://doi.org/10.1002/anie.201205071.

Zhuang, J., Li, W., Wu, W., Song, M., Su, W., Zhou, M., Cui, Z. (2014). Homoleptic tris-cyclometalated iridium(iii) complexes with phenylimidazole ligands for highly efficient sky-blue OLEDs. *New J. Chem.*, *39*(1), 246–253. https://doi.org/10.1039/C4NJ01316F.

APPENDICES

Appendix 1: NMR analyses for the Ligands and Complexes

Appendix 1.1 A^{13}C NMR for L_1

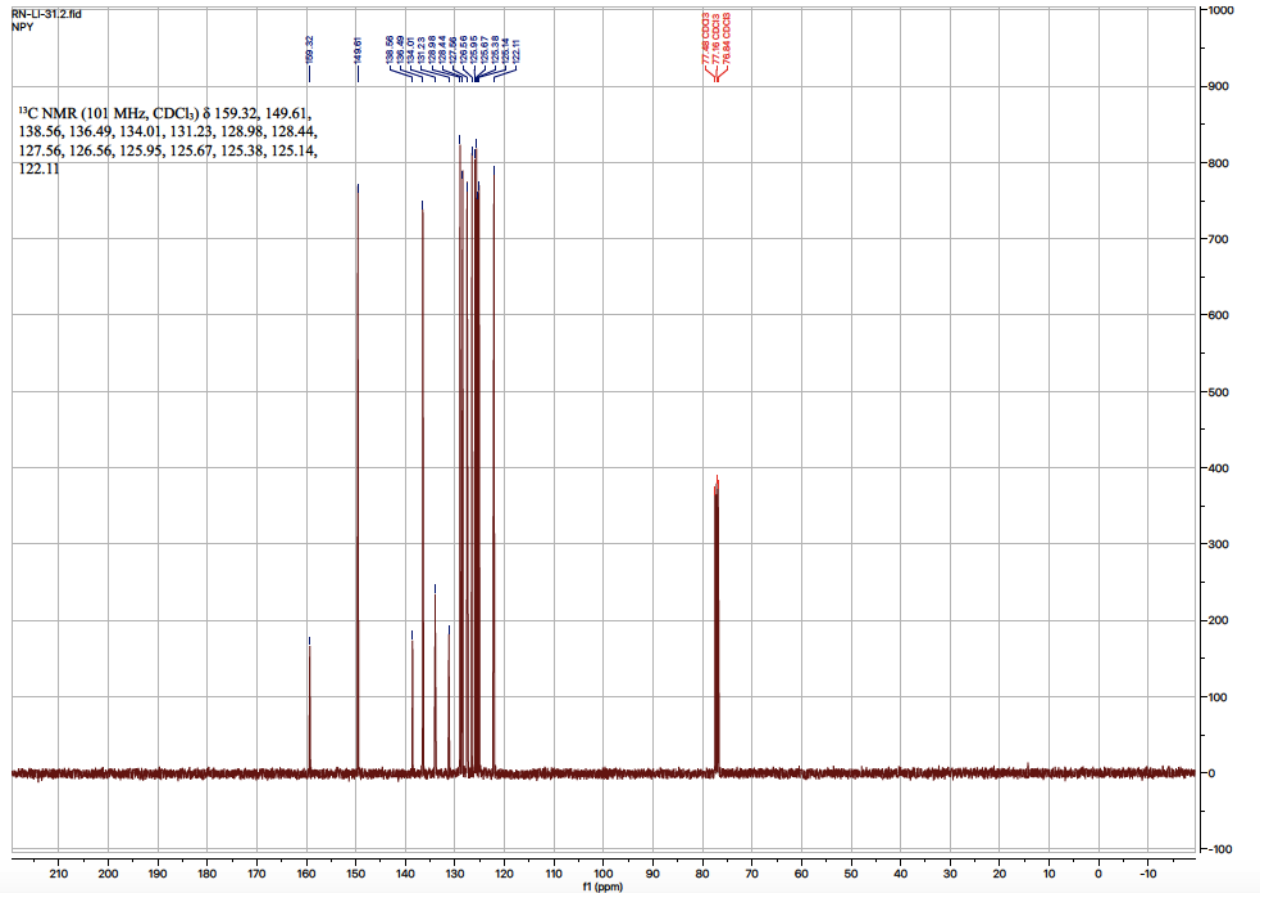

Appendix 1.2 ^{13}C NMR for L_2

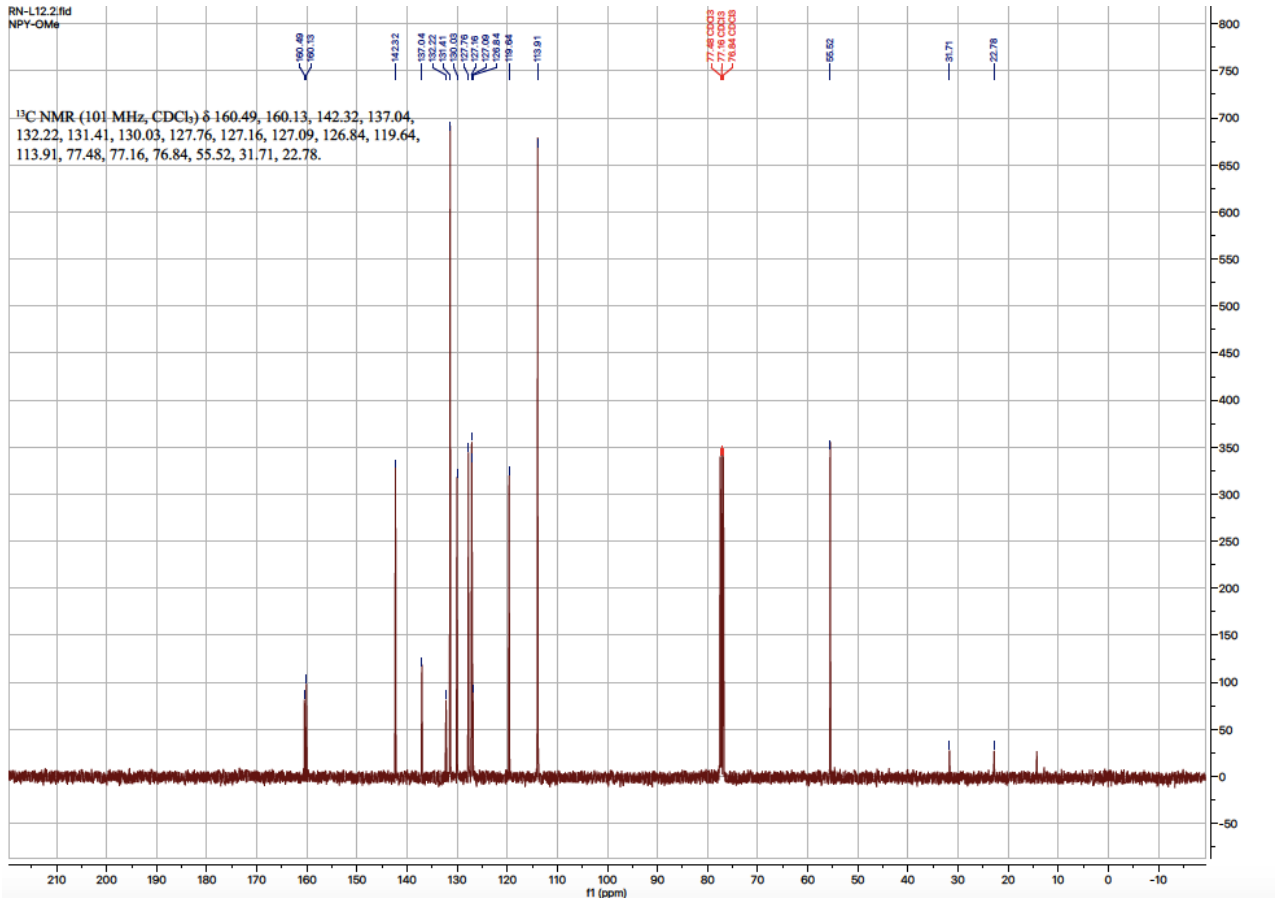

Appendix 1.3 ^{13}C NMR for L_3

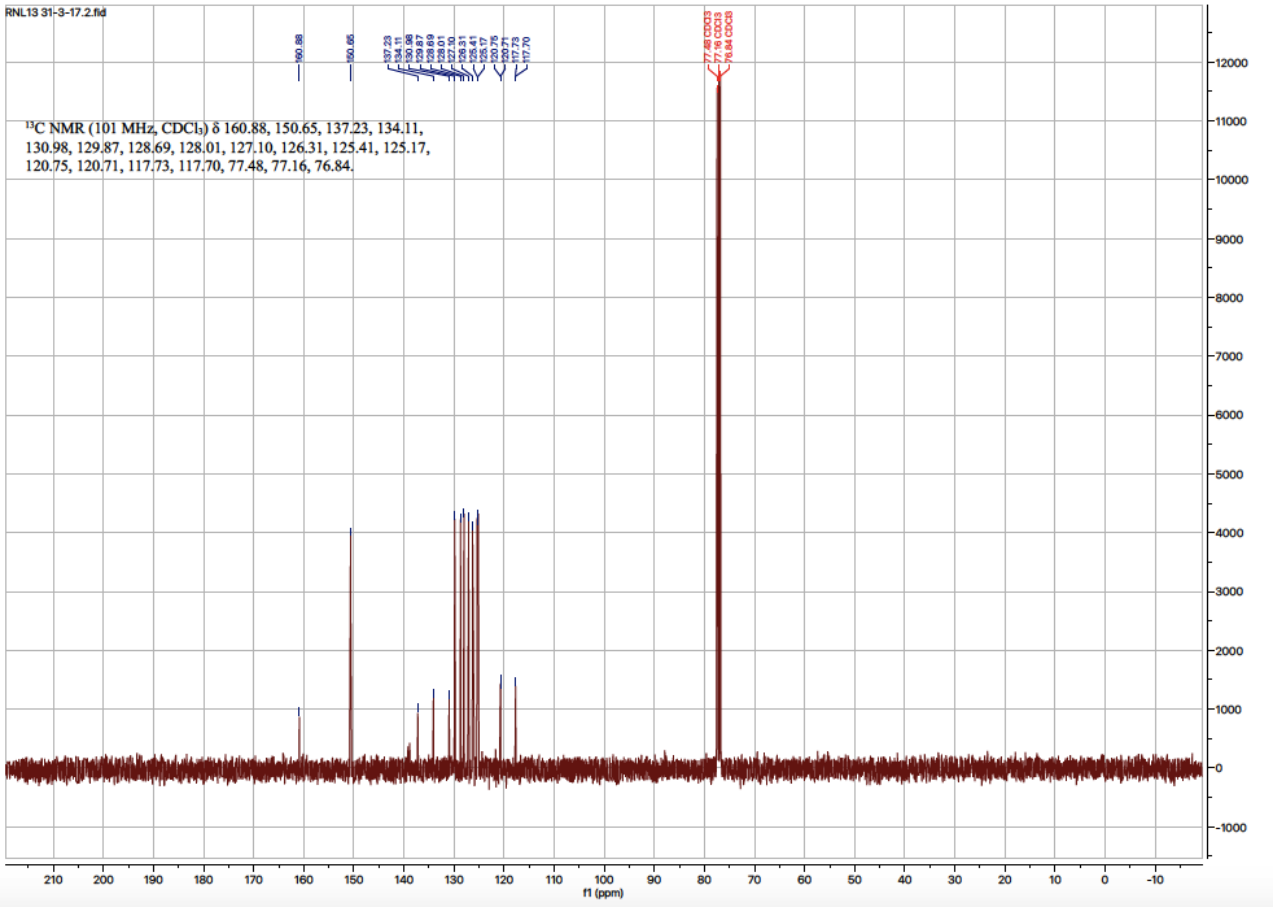

Appendix 1.4 ^{13}C NMR for L_4

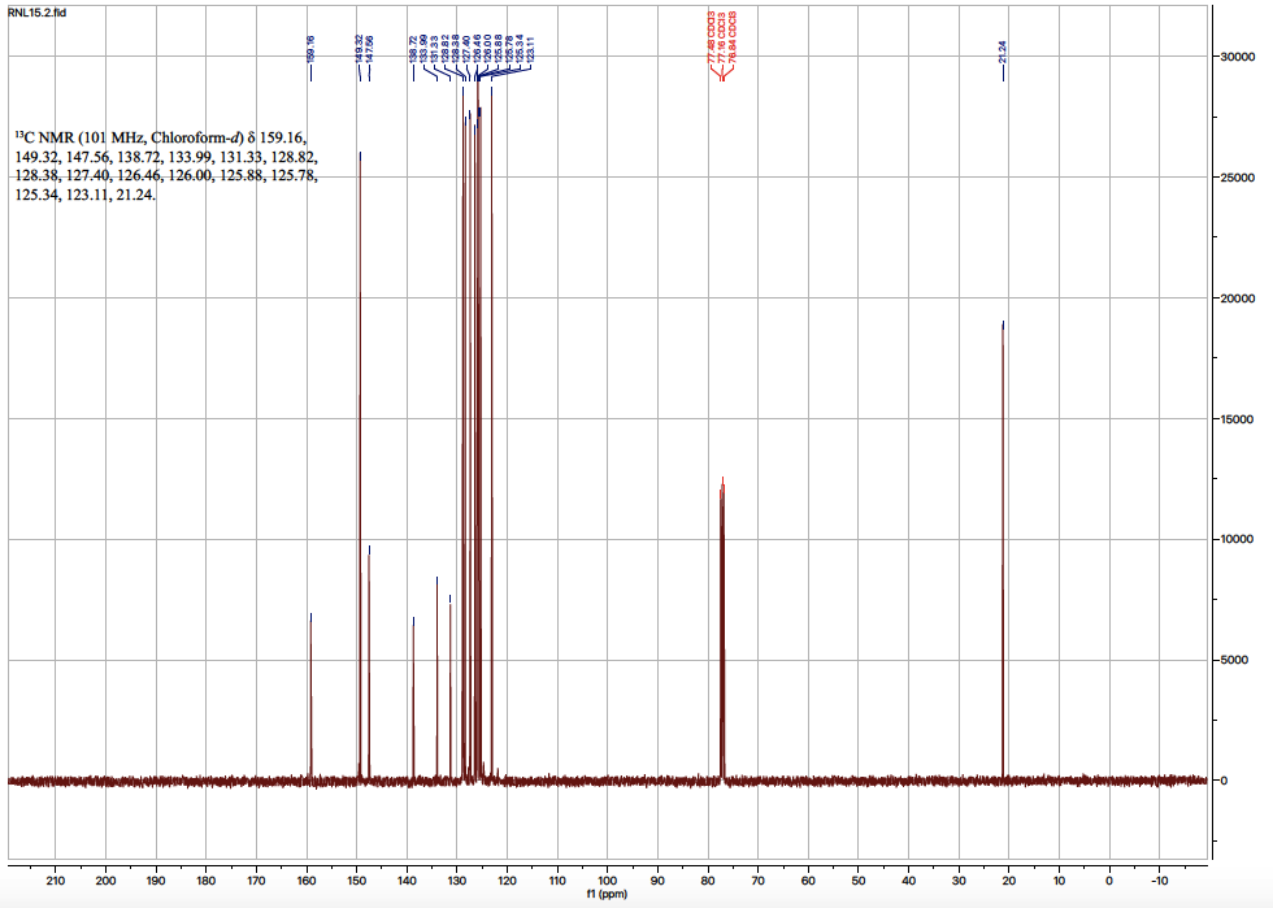

^{13}C NMR (101 MHz, Chloroform-*d*) δ 159.16, 149.32, 147.56, 138.72, 133.99, 131.33, 128.82, 128.38, 127.40, 126.46, 126.00, 125.88, 125.78, 125.34, 123.11, 21.24.

Appendix 1.5 ^{13}C NMR for L_5

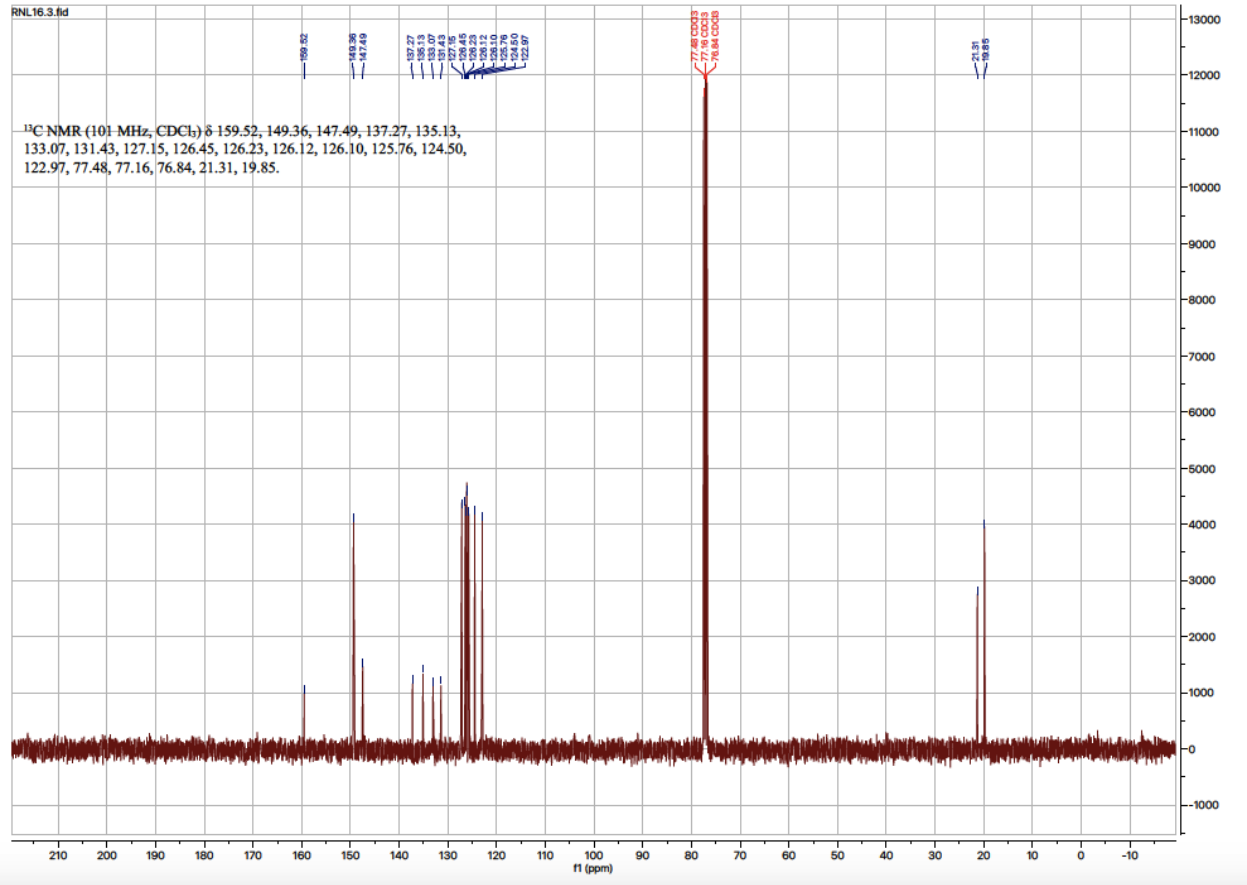

^{13}C NMR (101 MHz, $CDCl_3$) δ 159.52, 149.36, 147.49, 137.27, 135.13, 133.07, 131.43, 127.15, 126.45, 126.23, 126.12, 126.10, 125.76, 124.50, 122.97, 77.48, 77.16, 76.84, 21.31, 19.85.

Appendix 1.6 ^{13}C NMR for L_6

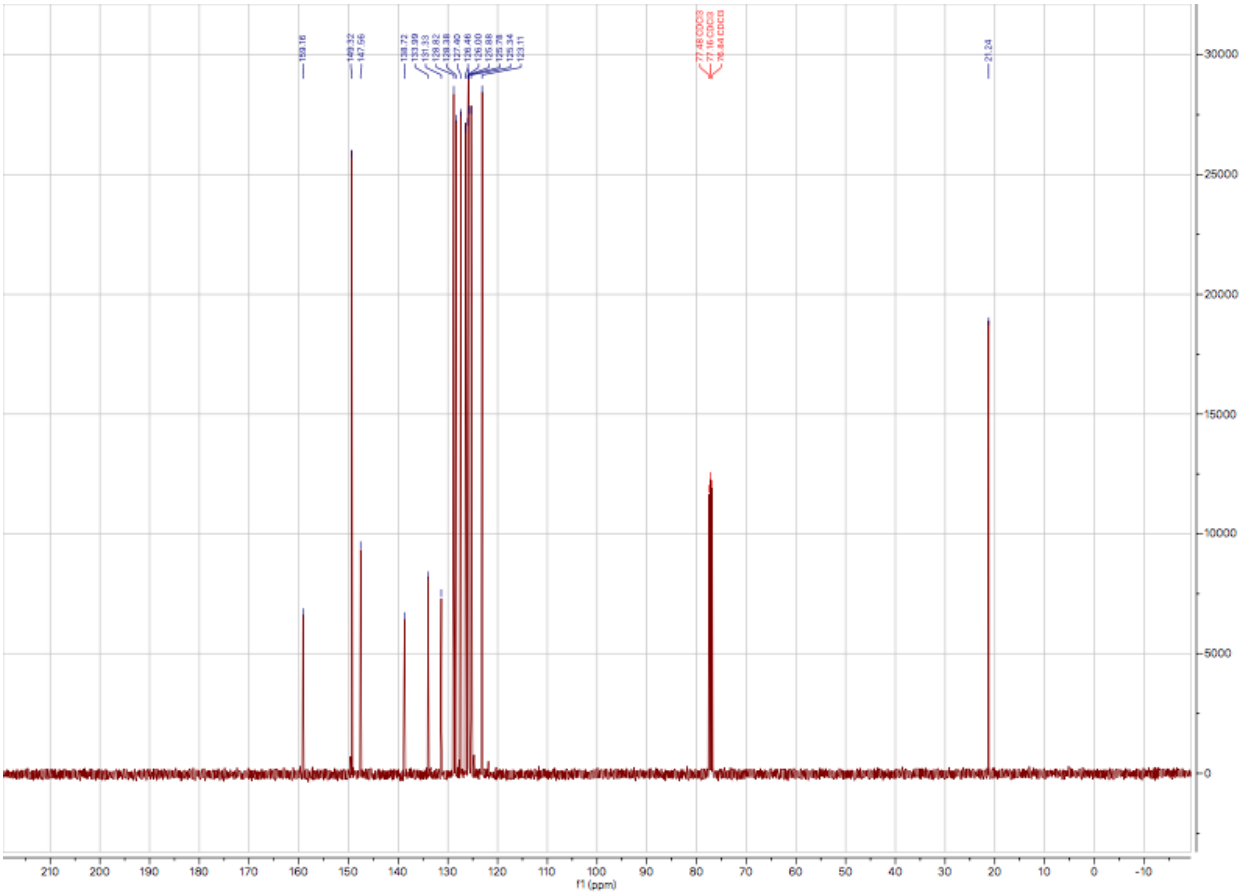

NMR spectra of complexes C-L_1-C-L_6

Appendix 1.7 ^{13}C NMR for C-L_1

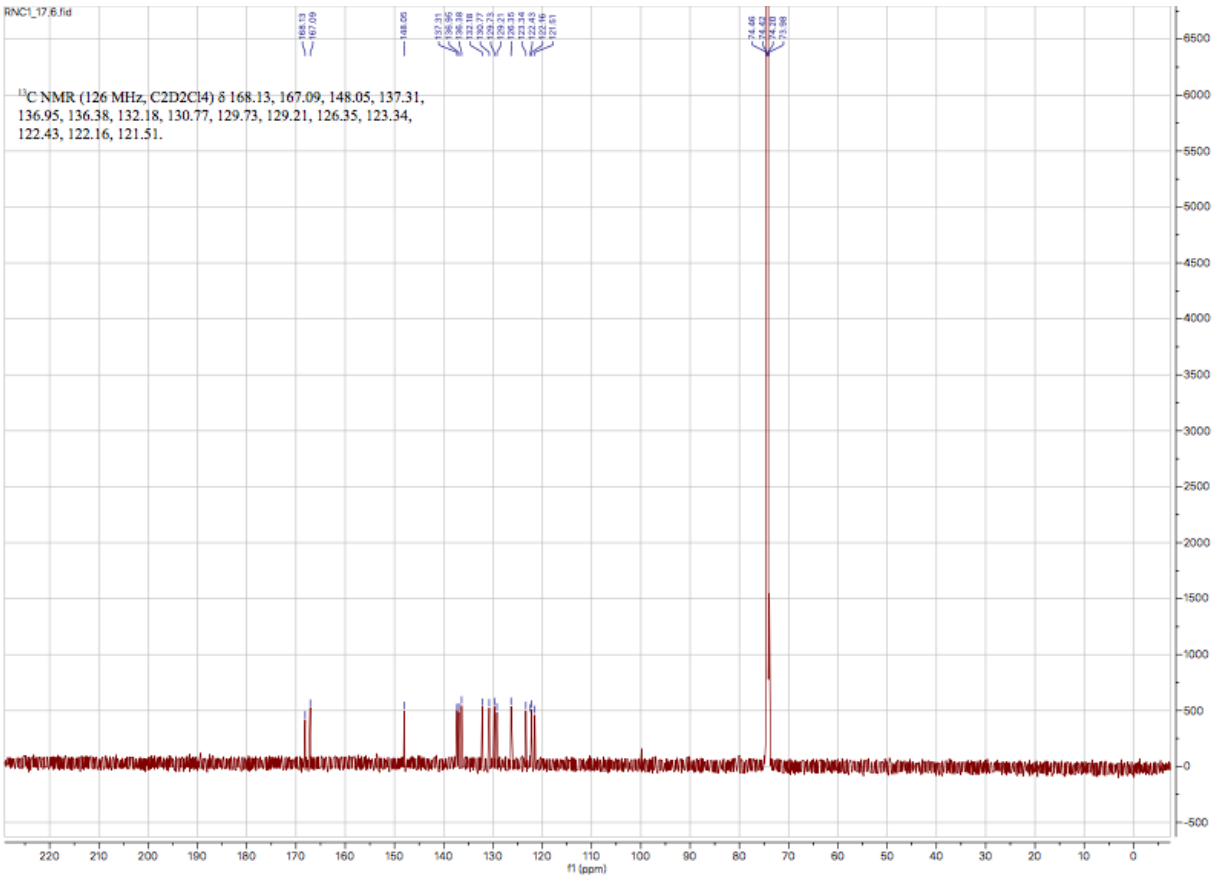

Appendix 1.8 COSY NMR for C-L_1

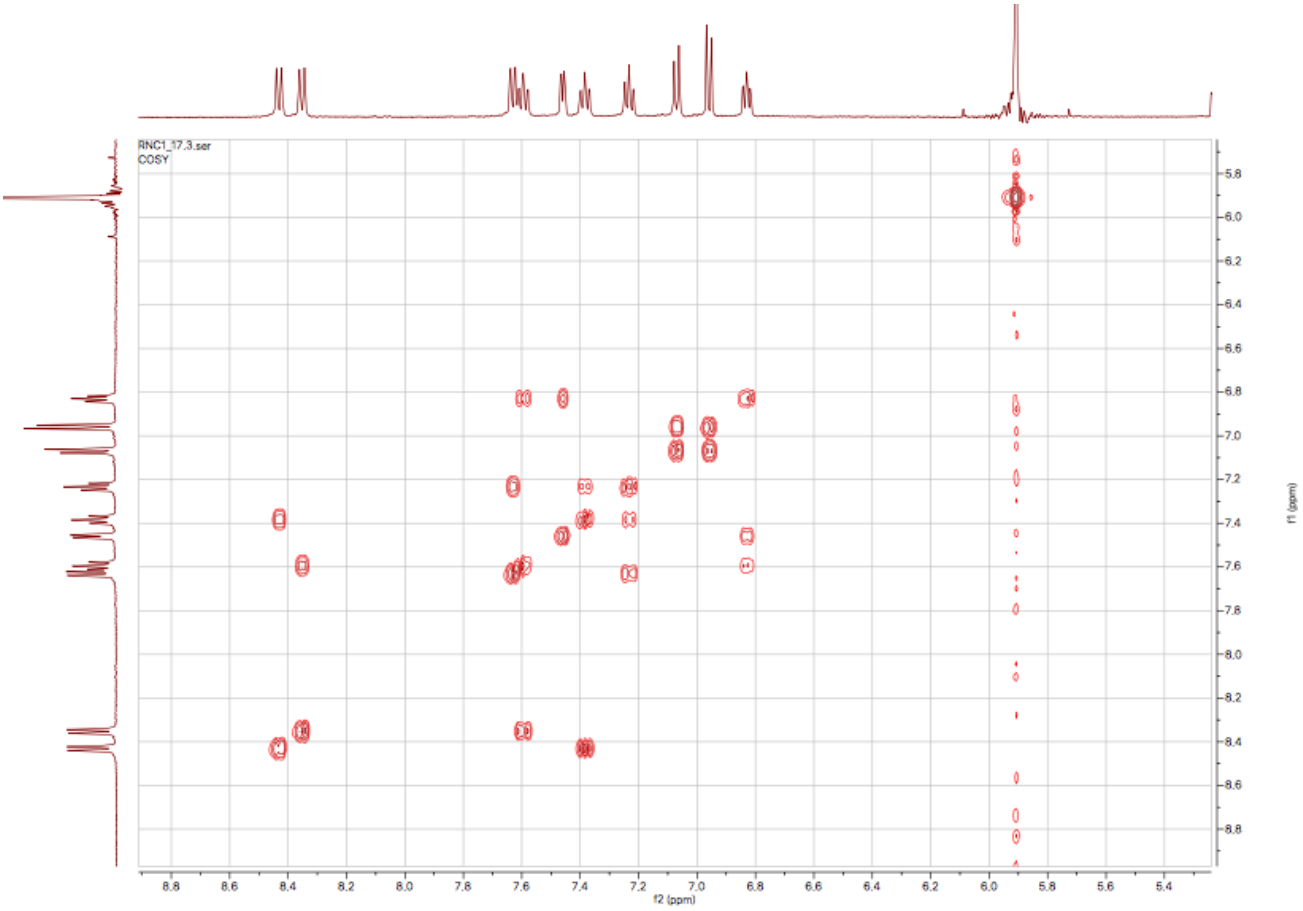

Appendix 1.9 ^{13}C NMR for C-L_2

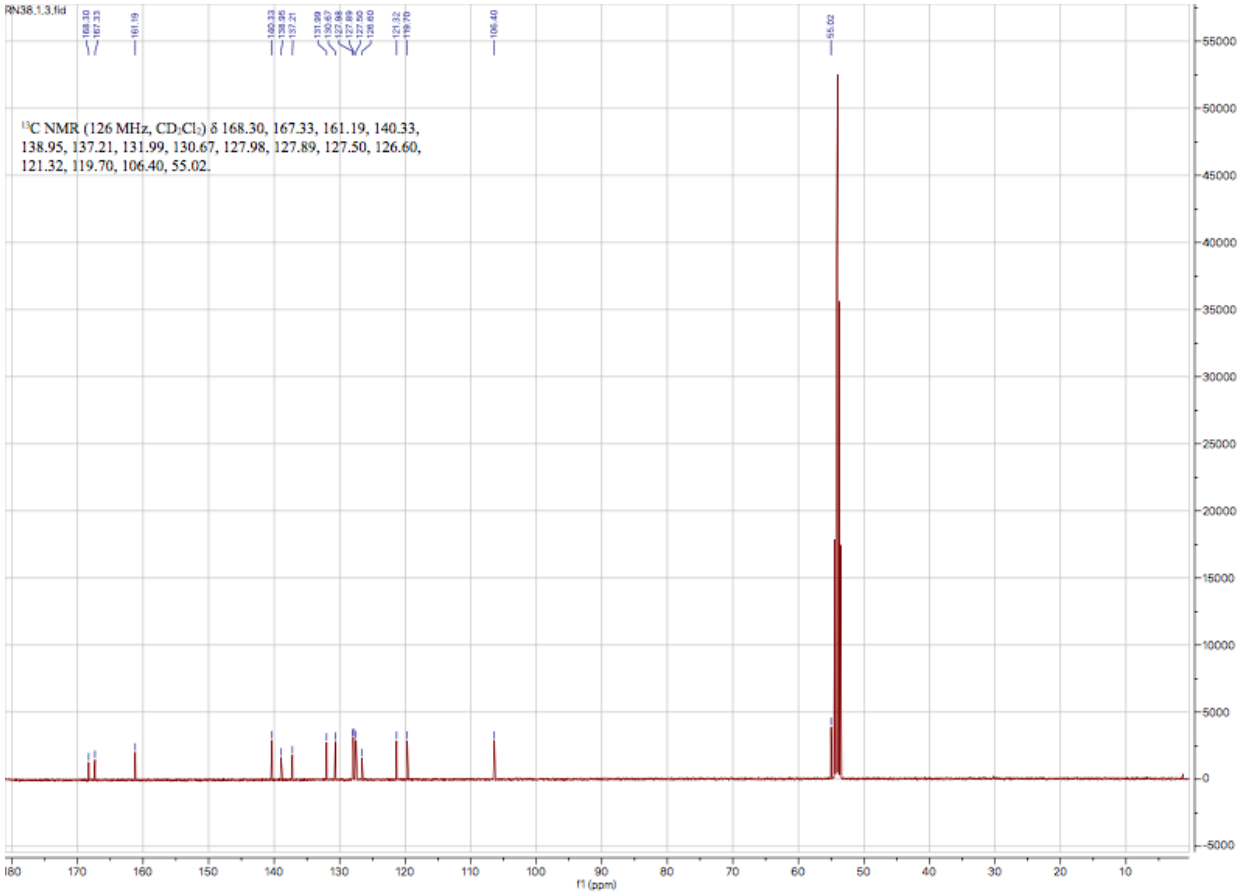

Appendix 1.10 2D COSY NMR for C-L_2

Appendix 1.11 ^{13}C NMR for C-L_3

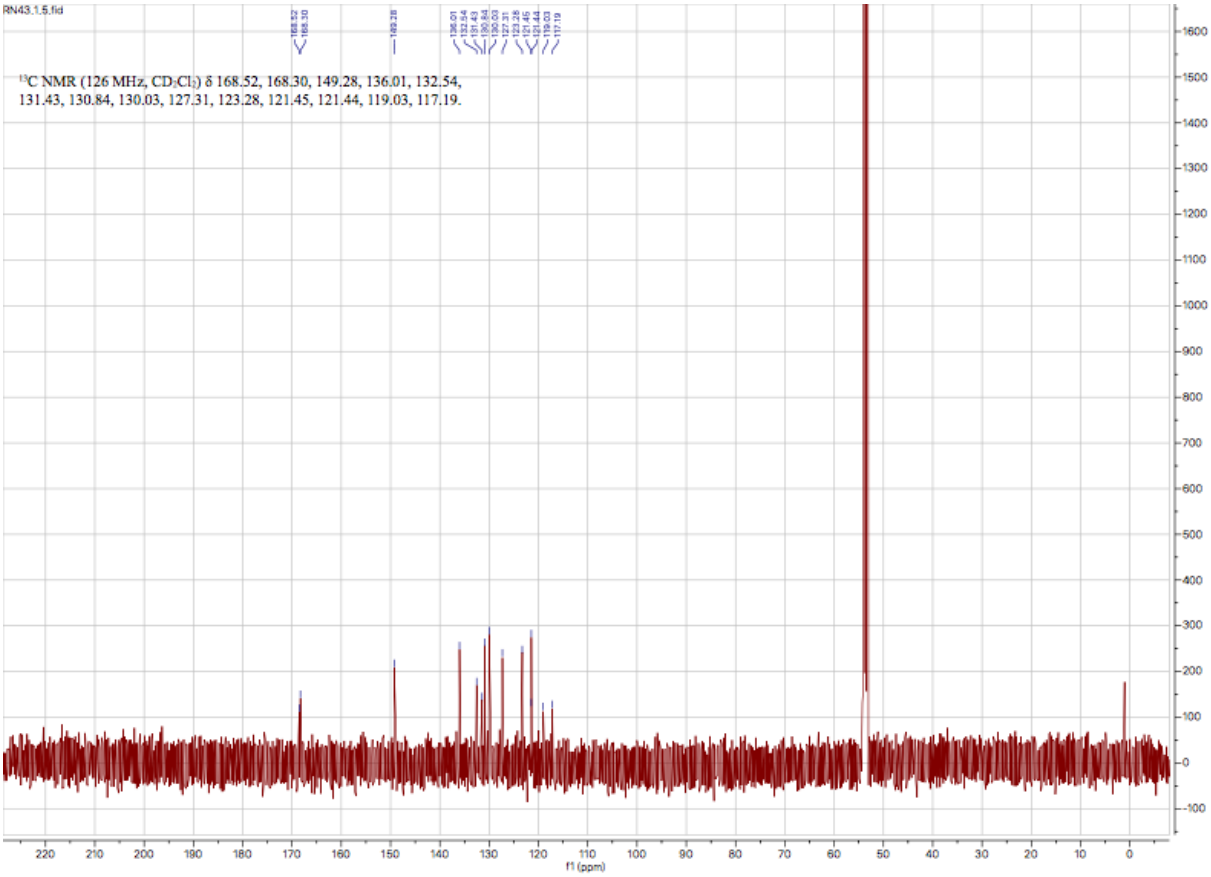

Appendix 1.12 2D COSY NMR for C-L_3

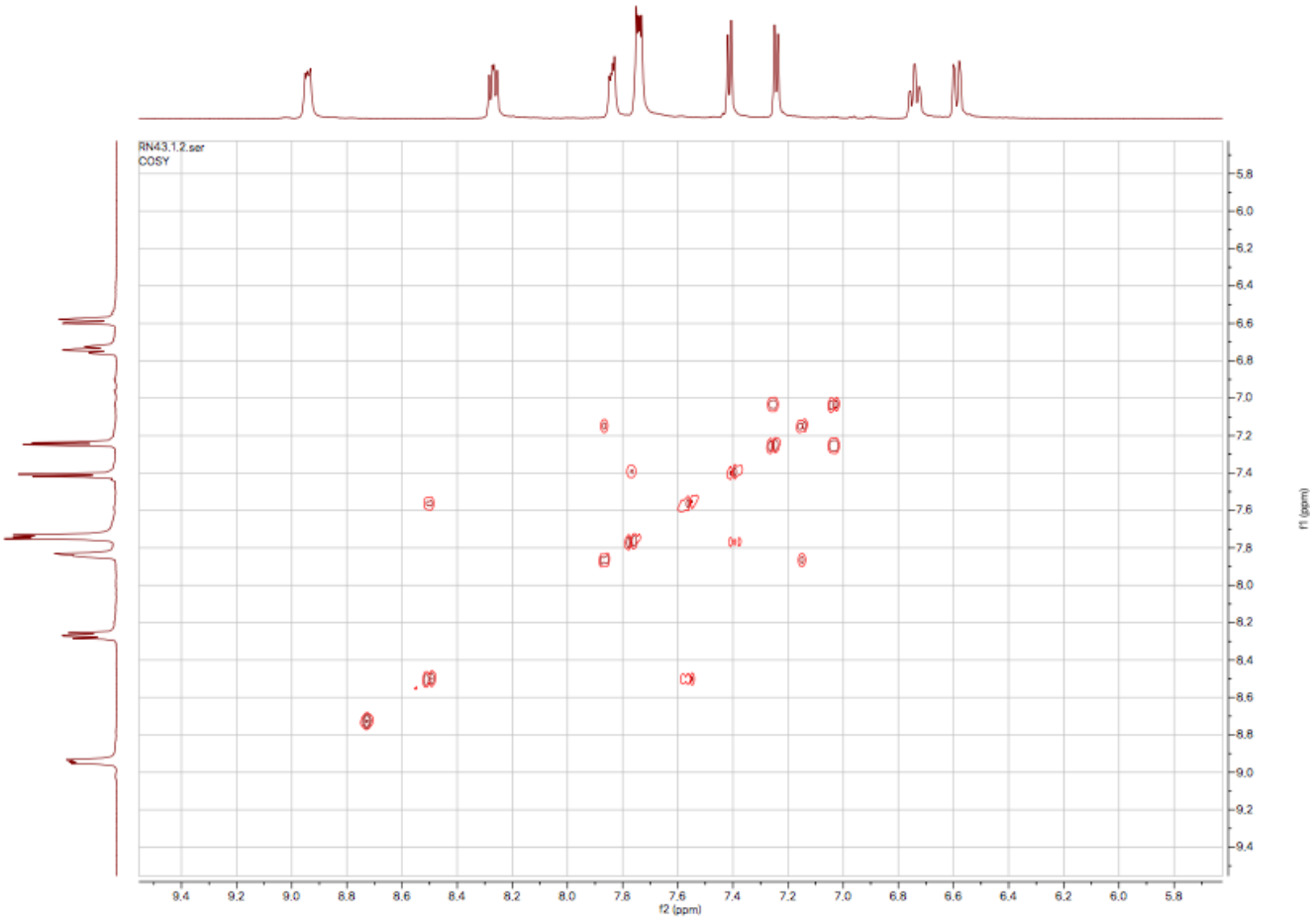

Appendix 1.13 19F NMR for C-L_3

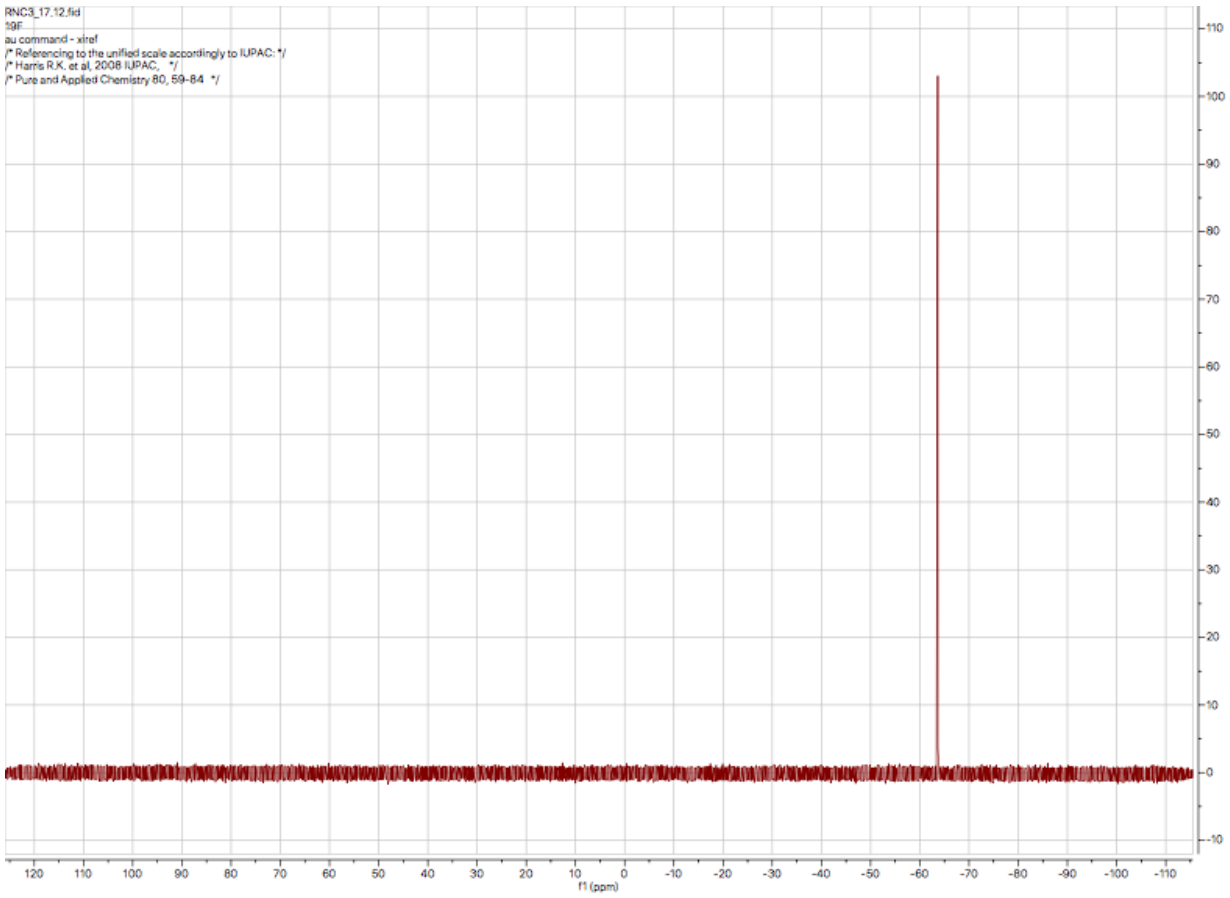

Appendix 1.14 ^{13}C NMR for C-L_4

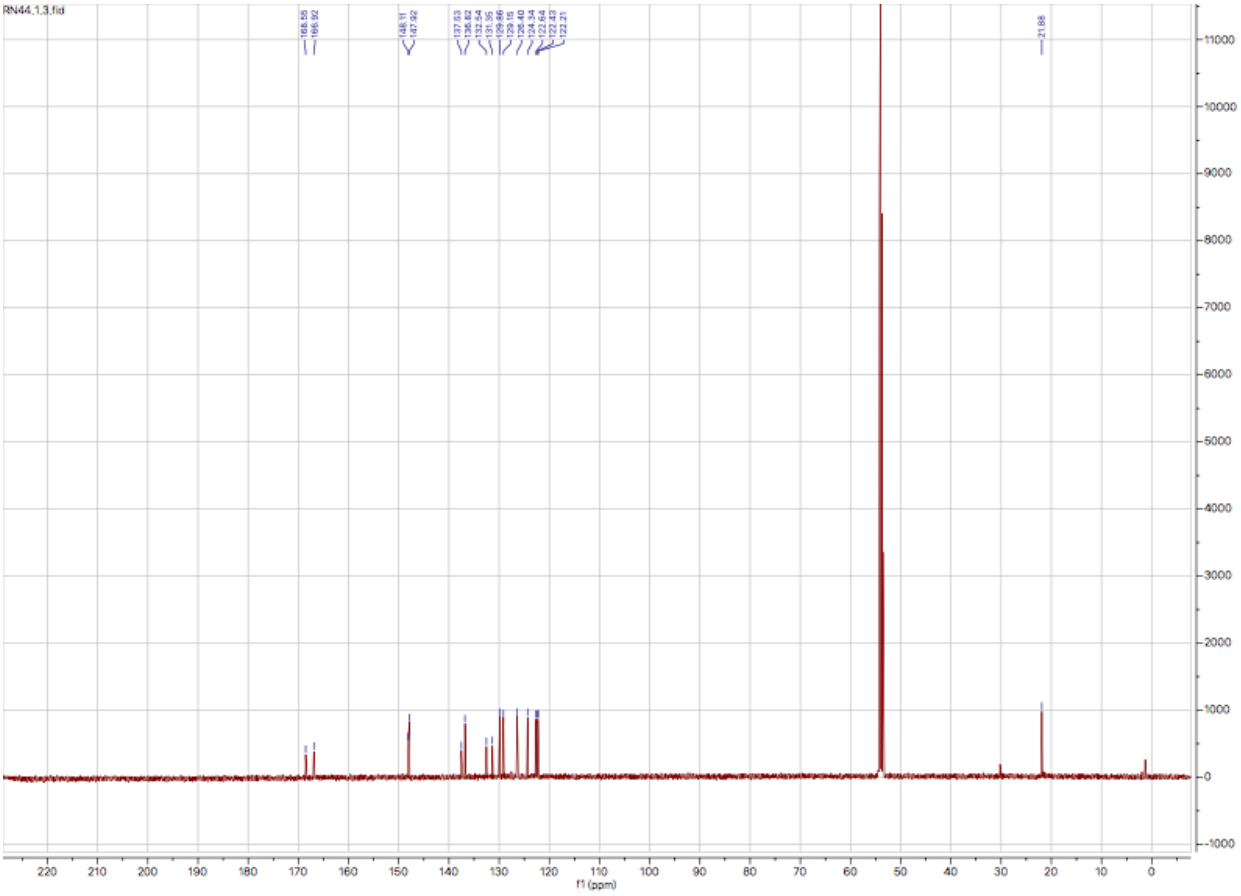

Appendix 1.15 2D COSY NMR for C-L_4

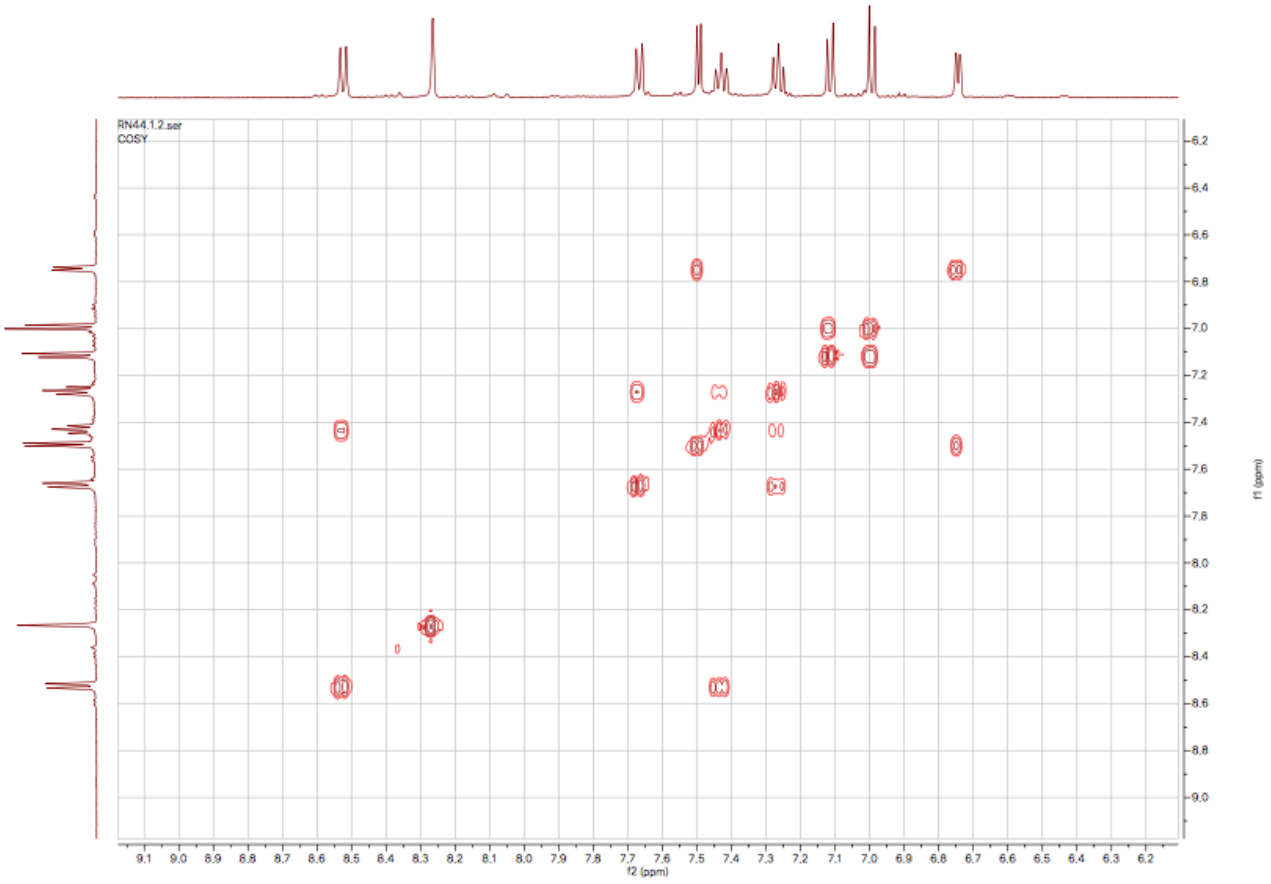

Appendix 1.16 ^{13}C NMR for C-L_5

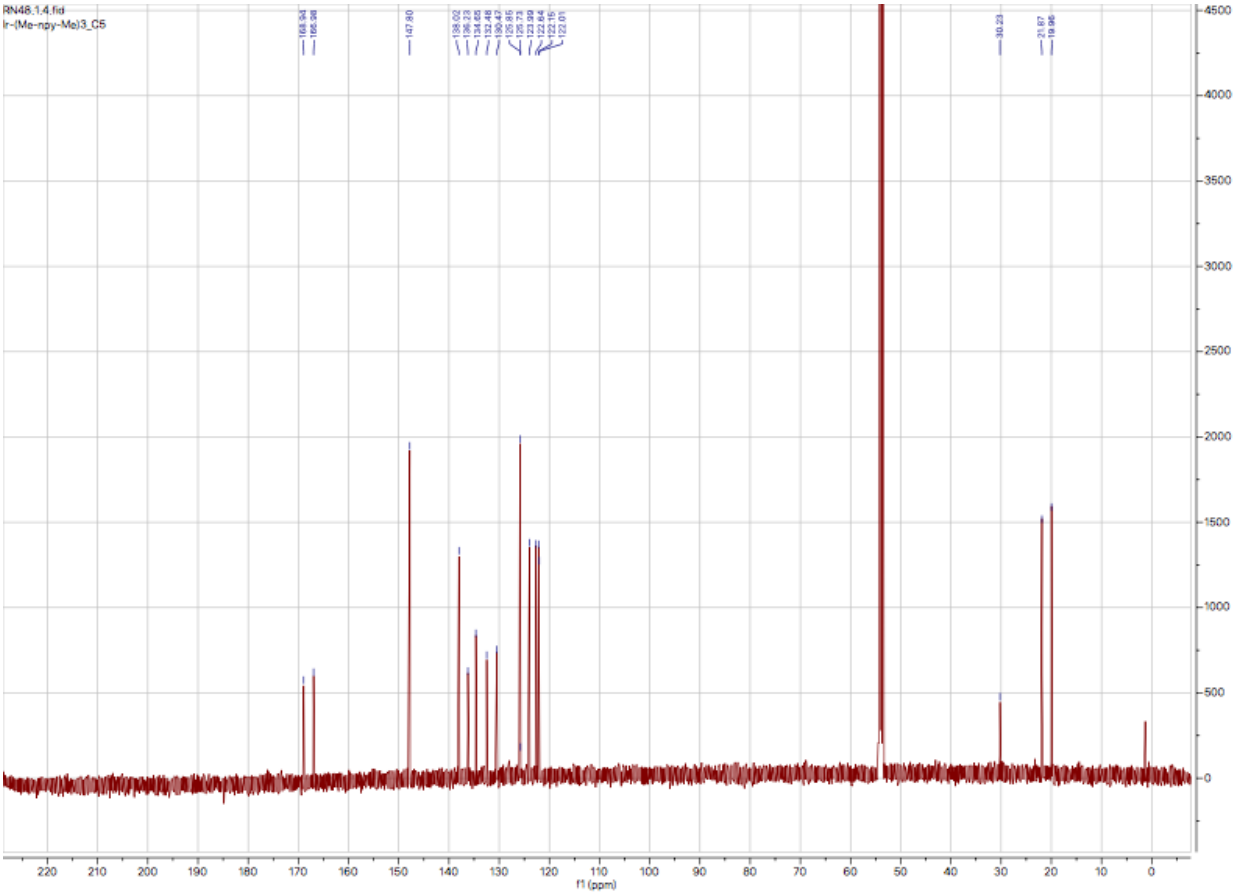

Appendix 1.17 2D COSY NMR for C-L_5

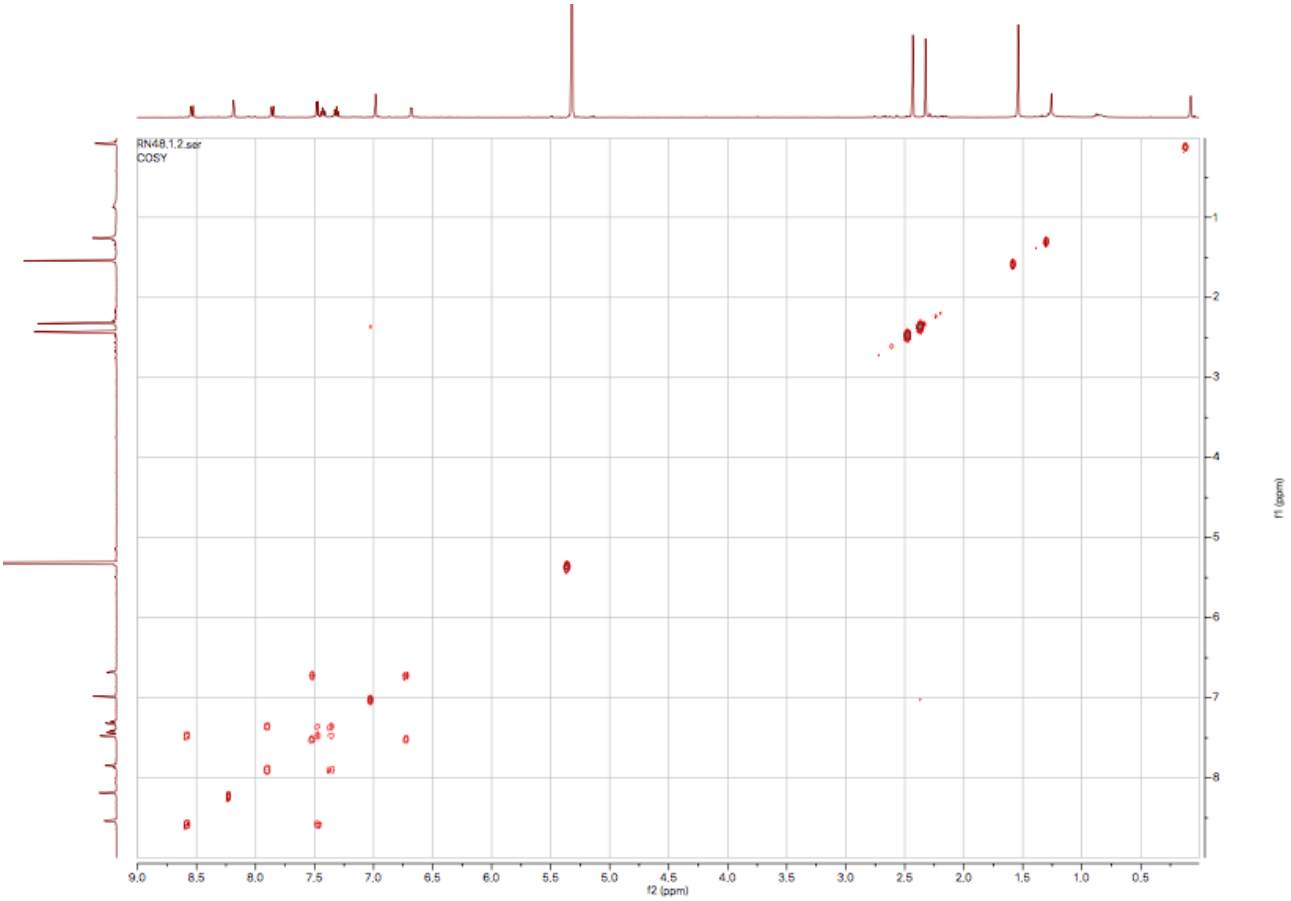

Appendix 2: Lifetime measurement Graph for C-L_1

PicoQuant FluoFit 10/29/2018

Model: Exp. [Tailfit] (Exponential)
Plotted Data Set #0 Decay: "\..\c1 in air 485 ex.phd" (0)
X²(reduced): 1.0079 ; Fitted Data Points: 0

Main Plot

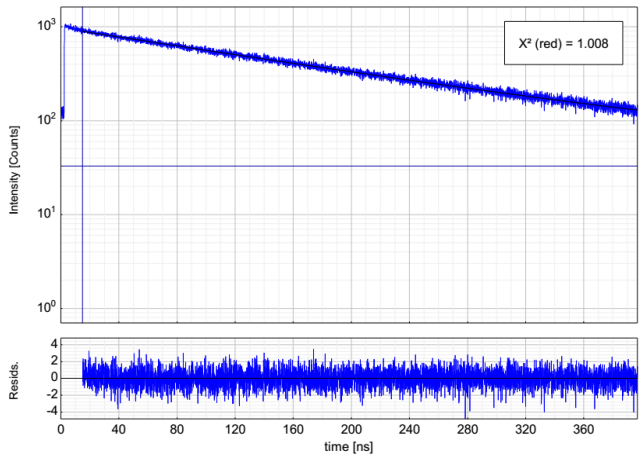

$$I(t) = \sum_{i=1}^{n} A_i \, e^{-\frac{t}{\tau_i}}$$

Parameter	Value	Conf. Lower	Conf. Upper	Conf. Estimation
A_1 [Cnts]	861.80	-7.65	+7.65	Fitting
τ_1 [ns]	174.55	-1.80	+1.80	Fitting
Bkgr. Dec [Cnts]	32.84	-2.68	+2.68	Fitting

Average Lifetime:

$\tau_{Av.1}$=174.55 ns (intensity weighted)
$\tau_{Av.2}$=174.55 ns (amplitude weighted)

Appendix 3 GC Calibration Graphs

Appendix 3.1 THFA calibration

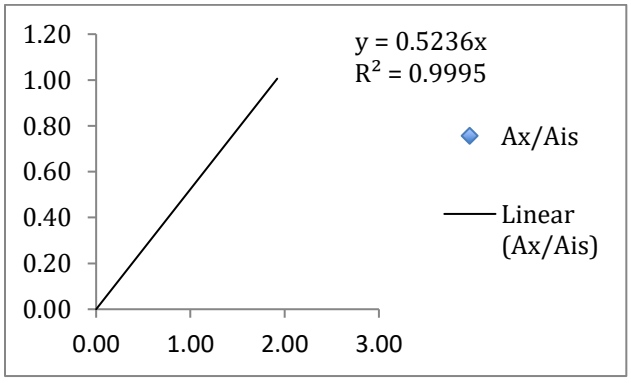

Appendix 3.2 Furfuryl Alcohol calibration

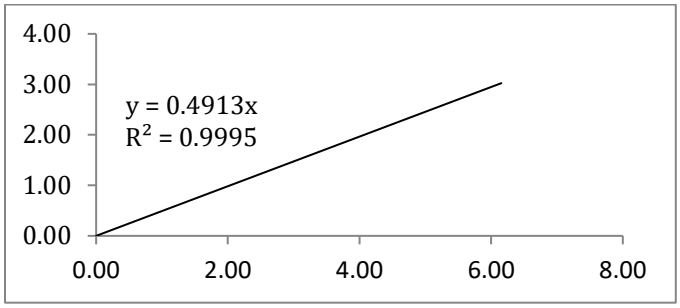

Appendix 3.3 Furfural calibration

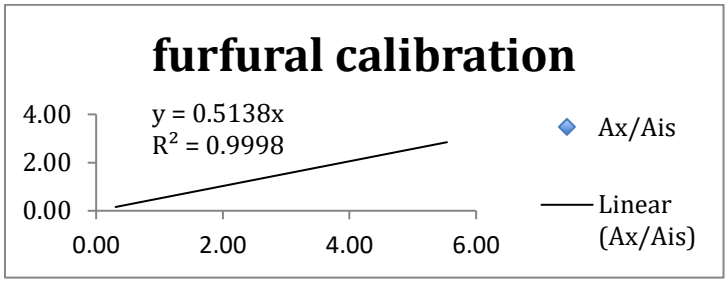

Appendix 3.4 p-anisaldehyde (p-MBH) calibration

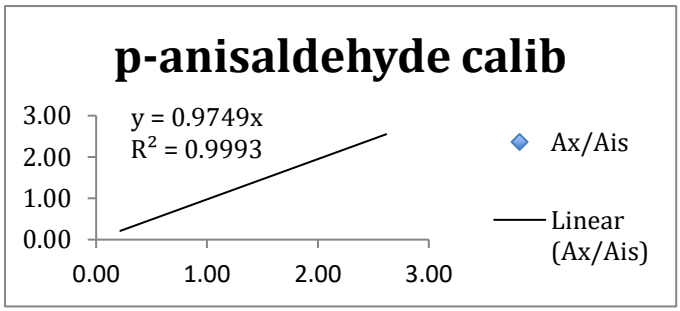

Appendix 3.5 4-methoxybenzene Alcohol (4-MBA) calibration

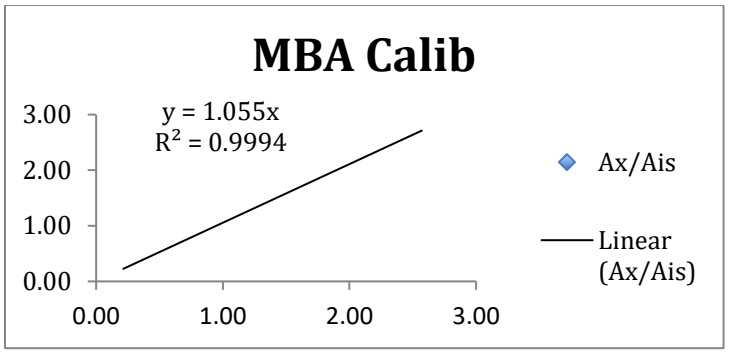

Appendix 3.6 Benzyl Alcohol calibration

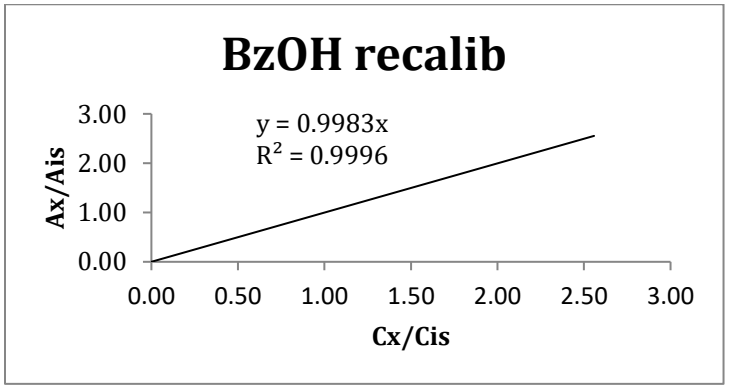

Appendix 3.7 Benzyl Aldehyde calibration

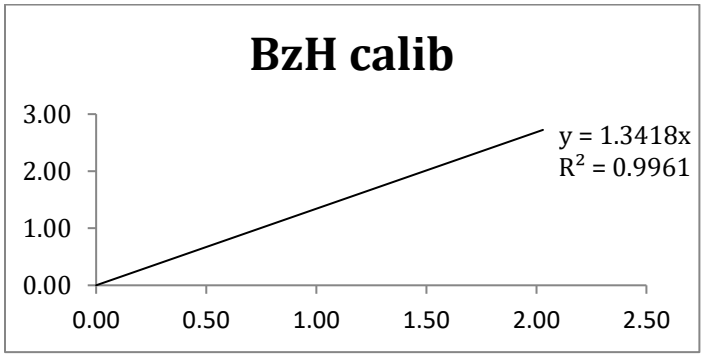

Appendix 3.8 Photodegradation of Morin using C-L_2

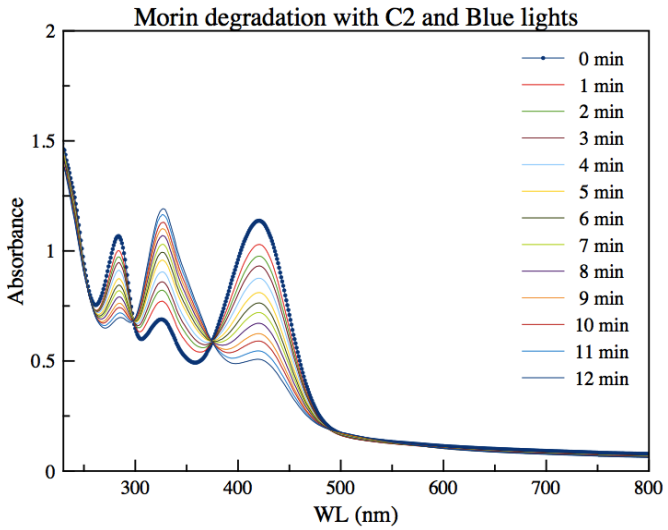

Appendix 3.9 Photodegradation of Morin using C-L_3

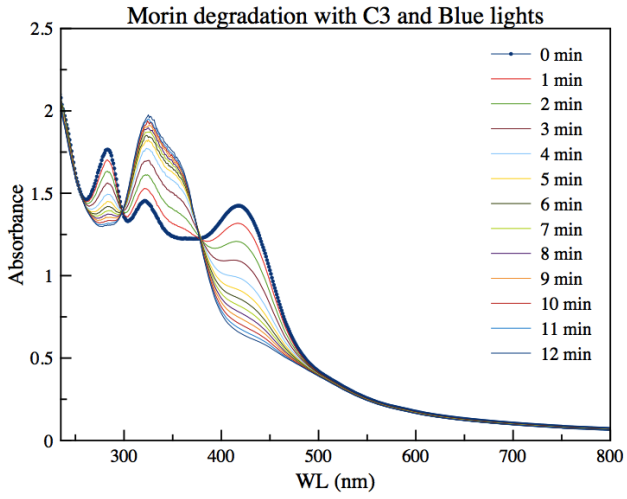

Appendix 3.10 Photodegradation of Morin using C-L_4

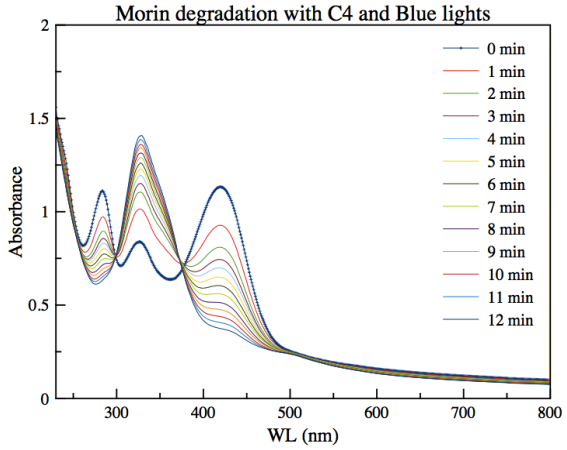

Appendix 3.11 Photodegradation of Morin using C-L_5

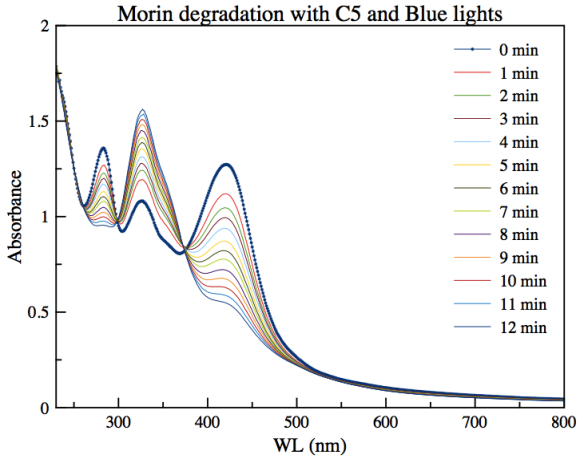

Appendix 3.12 Photodegradation of Morin using C-L_6

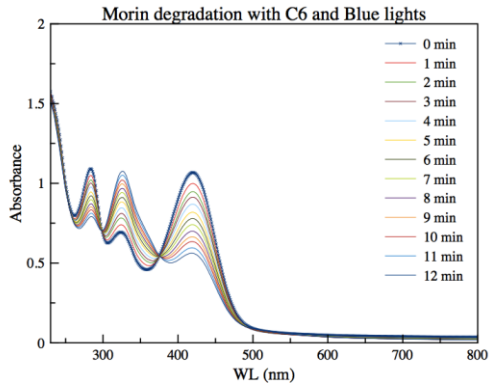

Appendix 4 Raw data for Crystallography

Table A.1: Bond Angles for C-L_1 from XRD Measurements

Number	Atom1	Atom2	Atom3	Angle	
1	Ir1	N1	C1	125(1)	
2	Ir1	N1	C5	119(1)	
3	C1	N1	C5	115(1)	
4	Ir1	N2	C16	127(1)	
5	Ir1	N2	C20	116.3(9)	
6	C16	N2	C20	116(1)	
7	Ir1	N3	C31	126(1)	
8	Ir1	N3	C35	115.3(9)	
9	C31	N3	C35	118(1)	
10	N1	Ir1	N2	96.4(4)	
11	N1	Ir1	N3	95.8(4)	
12	N1	Ir1	C7	77.2(5)	
13	N1	Ir1	C22	173.9(5)	
14	N1	Ir1	C37	89.0(5)	
15	N2	Ir1	N3	99.2(4)	
16	N2	Ir1	C7	83.6(5)	
17	N2	Ir1	C22	78.6(5)	
18	N2	Ir1	C37	174.3(5)	
19	N3	Ir1	C7	172.7(5)	
20	N3	Ir1	C22	88.4(5)	
21	N3	Ir1	C37	78.6(5)	
22	C7	Ir1	C22	98.7(6)	
23	C7	Ir1	C37	99.3(5)	
24	C22	Ir1	C37	96.1(6)	
25	N1	C1	H1		118
26	N1	C1	C2	125(1)	
27	H1	C1	C2		117
28	C1	C2	H2		120
29	C1	C2	C3	119(2)	
30	H2	C2	C3		120
31	C2	C3	H3		121
32	C2	C3	C4	117(2)	

33	H3	C3	C4		122
34	C3	C4	H4		118
35	C3	C4	C5	123(2)	
36	H4	C4	C5		119
37	N1	C5	C4	121(1)	
38	N1	C5	C6	108(1)	
39	C4	C5	C6	131(1)	
40	C5	C6	C7	115(1)	
41	C5	C6	C15	125(1)	
42	C7	C6	C15	120(1)	
43	Ir1	C7	C6	117(1)	
44	Ir1	C7	C8	123.5(9)	
45	C6	C7	C8	119(1)	
46	C7	C8	H8		120
47	C7	C8	C9	120(1)	
48	H8	C8	C9		120
49	C8	C9	H9		118
50	C8	C9	C10	124(1)	
51	H9	C9	C10		118
52	C9	C10	C11	125(1)	
53	C9	C10	C15	118(1)	
54	C11	C10	C15	117(1)	
55	C10	C11	H11		118
56	C10	C11	C12	125(2)	
57	H11	C11	C12		118
58	C11	C12	H12		122
59	C11	C12	C13	115(2)	
60	H12	C12	C13		122
61	C12	C13	H13		118
62	C12	C13	C14	124(2)	
63	H13	C13	C14		118
64	C13	C14	H14		120
65	C13	C14	C15	119(2)	
66	H14	C14	C15		120
67	C6	C15	C10	119(1)	
68	C6	C15	C14	121(1)	
69	C10	C15	C14	119(1)	
70	N2	C16	H16		118

71	N2	C16	C17	124(2)	
72	H16	C16	C17		118
73	C16	C17	H17		121
74	C16	C17	C18	119(2)	
75	H17	C17	C18		121
76	C17	C18	H18		120
77	C17	C18	C19	120(2)	
78	H18	C18	C19		120
79	C18	C19	H19		120
80	C18	C19	C20	120(1)	
81	H19	C19	C20		120
82	N2	C20	C19	120(1)	
83	N2	C20	C21	112(1)	
84	C19	C20	C21	127(1)	
85	C20	C21	C22	113(1)	
86	C20	C21	C30	124(1)	
87	C22	C21	C30	123(1)	
88	Ir1	C22	C21	118(1)	
89	Ir1	C22	C23	127(1)	
90	C21	C22	C23	115(1)	
91	C22	C23	H23		118
92	C22	C23	C24	124(1)	
93	H23	C23	C24		118
94	C23	C24	H24		119
95	C23	C24	C25	121(1)	
96	H24	C24	C25		119
97	C24	C25	C26	123(2)	
98	C24	C25	C30	120(2)	
99	C26	C25	C30	117(2)	
100	C25	C26	H26		120
101	C25	C26	C27	121(2)	
102	H26	C26	C27		120
103	C26	C27	H27		119
104	C26	C27	C28	122(2)	
105	H27	C27	C28		119
106	C27	C28	H28		121
107	C27	C28	C29	118(2)	
108	H28	C28	C29		121

109	C28	C29	H29		117
110	C28	C29	C30	126(2)	
111	H29	C29	C30		117
112	C21	C30	C25	116(1)	
113	C21	C30	C29	127(1)	
114	C25	C30	C29	116(1)	
115	N3	C31	H31		117
116	N3	C31	C32	125(2)	
117	H31	C31	C32		117
118	C31	C32	H32		122
119	C31	C32	C33	115(2)	
120	H32	C32	C33		122
121	C32	C33	H33		119
122	C32	C33	C34	122(2)	
123	H33	C33	C34		119
124	C33	C34	H34		119
125	C33	C34	C35	122(2)	
126	H34	C34	C35		119
127	N3	C35	C34	117(1)	
128	N3	C35	C36	114(1)	
129	C34	C35	C36	129(1)	
130	C35	C36	C37	115(1)	
131	C35	C36	C45	127(1)	
132	C37	C36	C45	118(1)	
133	Ir1	C37	C36	115(1)	
134	Ir1	C37	C38	126(1)	
135	C36	C37	C38	119(1)	
136	C37	C38	H38		119
137	C37	C38	C39	122(1)	
138	H38	C38	C39		119
139	C38	C39	H39		119
140	C38	C39	C40	121(2)	
141	H39	C39	C40		119
142	C39	C40	C41	122(2)	
143	C39	C40	C45	119(2)	
144	C41	C40	C45	119(2)	
145	C40	C41	H41		120
146	C40	C41	C42	120(2)	

147	H41	C41	C42		120
148	C41	C42	H42		119
149	C41	C42	C43	122(2)	
150	H42	C42	C43		119
151	C42	C43	H43		119
152	C42	C43	C44	121(2)	
153	H43	C43	C44		119
154	C43	C44	H44		120
155	C43	C44	C45	120(2)	
156	H44	C44	C45		120
157	C36	C45	C40	121(1)	
158	C36	C45	C44	122(1)	
159	C40	C45	C44	117(1)	